

**Energy Research and Development Division
FINAL PROJECT REPORT**

OPTIMIZING REFRIGERANT DISTRIBUTION IN EVAPORATORS



Prepared for: California Energy Commission

Prepared by: Purdue University



NOVEMBER 2011

CEC-500-2013-089

PREPARED BY:

Purdue University
Eckhard A. Groll,
James E. Braun,
Christian K. Bach

West Lafayette, Indiana, 47907
Commission Contract No. PIR-08-017
Commission Work Authorization No: NA

Prepared for:

Public Interest Energy Research (PIER)
California Energy Commission

Bradley C. Meister
Contract Manager

Virginia Lew
Office Manager
Energy Efficiency Research Office

Laurie ten Hope
Deputy Director
ENERGY RESEARCH AND DEVELOPMENT DIVISION

Robert P. Oglesby
Executive Director

DISCLAIMER

This report was prepared as the result of work sponsored by the California Energy Commission. It does not necessarily represent the views of the Energy Commission, its employees or the State of California. The Energy Commission, the State of California, its employees, contractors and subcontractors make no warrant, express or implied, and assume no legal liability for the information in this report; nor does any party represent that the uses of this information will not infringe upon privately owned rights. This report has not been approved or disapproved by the California Energy Commission nor has the California Energy Commission passed upon the accuracy or adequacy of the information in this report.

ACKNOWLEDGEMENTS

The authors would like to thank the California Energy Commission for the funding of this project. Furthermore the help of a number of students was greatly appreciated; these include Friedrich Welck (EXV test stand), Mira Weymann and Tom Faussett (large room cooling system), Timo Mueller, Andrew L. Hjortland and Woohyun Kim (rooftop air conditioning unit). We also would like to thank Kirill Ignatiev, Jean-Luc Caillat and Kok-Hiong Kee from Emerson Climate technologies which supported this project with advice and components.

PREFACE

The California Energy Commission Energy Research and Development Division supports public interest energy research and development that will help improve the quality of life in California by bringing environmentally safe, affordable, and reliable energy services and products to the marketplace.

The Energy Research and Development Division conducts public interest research, development, and demonstration (RD&D) projects to benefit California.

The Energy Research and Development Division strives to conduct the most promising public interest energy research by partnering with RD&D entities, including individuals, businesses, utilities, and public or private research institutions.

Energy Research and Development Division funding efforts are focused on the following RD&D program areas:

- Buildings End-Use Energy Efficiency
- Energy Innovations Small Grants
- Energy-Related Environmental Research
- Energy Systems Integration
- Environmentally Preferred Advanced Generation
- Industrial/Agricultural/Water End-Use Energy Efficiency
- Renewable Energy Technologies
- Transportation

Optimizing Refrigerant Distribution in Evaporators – Final Report is the final report for the Optimizing Refrigerant Distribution in Evaporators project contract number PIR-08-017 conducted by Purdue University. The information from this project contributes to Energy Research and Development Division's Buildings End-Use Energy Efficiency Program.

For more information about the Energy Research and Development Division, please visit the Energy Commission's website at www.energy.ca.gov/research/ or contact the Energy Commission at 916-327-1551.

ABSTRACT

This report presents the effects of air and refrigerant side maldistribution for three different applications. Maldistribution refers to a non-uniform flow of media. These applications were a three-ton large room cooling system, a five-ton domestic heat pump and a four-ton rooftop air conditioning unit with an airside economizer. Each system was tested with an electronic expansion valve control scheme that does not allow for individual control of the refrigerant side flowrate, and was then modified to include individual circuit refrigerant flow control using a hybrid control system. Indications of refrigerant side maldistribution were found for all applications using the electronic expansion valve control scheme, even with negligible airside maldistribution. The refrigerant flow was controlled to obtain similar exit superheats for each circuit using the hybrid control scheme. Small airside maldistribution led to relatively small (less than five percent) performance improvements. Significant improvements in terms of coefficient of performance and capacity were achieved if airside maldistribution was applied. Airside maldistribution occurs in practice in the form of fouling (all systems), frost build up (large room cooling system, heat pump), and temperature and flow maldistribution (rooftop unit, heat pump). Bin analyses were conducted for all systems to estimate the achievable annual performance improvement based on the measured performance improvement and using assumptions for the applicable maldistribution. Future work should include a statistical assessment of the maldistribution levels that are found in practice to determine a better estimate of the achievable performance improvement as well as the simple payback period.

Keywords: Evaporator maldistribution, air-side maldistribution, refrigerant-side maldistribution, hybrid control, large room cooling system, rooftop unit, domestic air-source heat pump

Please use the following citation for this report:

Eckhard A. Groll, James E. Braun, Christian K. Bach, Purdue University. 2011. *Optimizing refrigerant distribution in evaporators – final report*. California Energy Commission. Publication number: CEC-500-2013-089.

TABLE OF CONTENTS

Acknowledgements	i
PREFACE	ii
ABSTRACT	iii
TABLE OF CONTENTS.....	iv
LIST OF FIGURES	vii
LIST OF TABLES	xvii
EXECUTIVE SUMMARY	1
Introduction	1
Project Purpose.....	1
Project Results.....	1
Project Benefits	5
Chapter 1: Introduction and Literature Review	6
1.1..... Introduction.....	6
1.1.1 Organization of Report.....	6
1.2.....Significance and Motivation.....	6
1.2.1 Large Room Cooling System (LRCS)	6
1.2.2 Domestic Heat Pump (HP)	6
1.2.3 Rooftop Air Conditioning Unit (RAC).....	7
1.3.....Introduction to Hybrid Control and Related Control Approaches	8
1.4.....Objectives.....	10
1.4.1 Procedure of Investigation.....	10
1.5.....Literature Review	11
Chapter 2: Large Room Cooling System	16
2.1.....Controls.....	17
2.2.....Instrumentation	17
2.3.....Performance Indices	19
2.4.....TXV Control Scheme	20

2.4.1	Steady State Tests	21
2.4.2	Cyclic Test	23
2.4.3	Frost-Up Tests.....	25
2.4.4	Conclusions for TXV Test Results.....	28
2.5.....	EXV Control Scheme	29
2.5.1	Steady State Tests, System Behavior	29
2.5.2	Steady State Tests, Performance	34
2.5.3	Cyclic Test	35
2.5.4	Frost-Up Test	36
2.5.5	Tests with Different Levels of Coil Blockage	39
2.5.6	Conclusions, EXV	42
2.6.....	Hybrid Control Scheme	43
2.6.1	Steady State Tests, System Behavior	43
2.6.2	Steady State Tests, Performance	47
2.6.3	Frost-Up Test	47
2.6.4	Tests with Coil Blockage	50
2.6.5	Determination of Maldistribution Using Balancing Valves as Virtual Flow Sensors ..	51
2.6.6	Performance	53
2.7.....	Performance Comparison.....	53
2.8.....	Analysis.....	56
2.8.1	Bin Analysis	57
2.8.2	Results.....	60
2.9.....	Refrigerant Maldistribution Effects for Clean-Coil.....	62
	Optimized Distributor Versus Employed Distributor.....	68
2.9.2	Estimate of Performance Penalty for Distributors.....	70
2.9.3	Case A: Semi-Empirically Determined Distribution Factors	71
2.9.4	Case B: Simulated Distribution Factors	72
2.10....	Conclusions, Future Work and Recommendations	74

Chapter 3: Domestic Heat Pump	75
3.1.....System Description	75
3.1.1 Controls	76
3.1.2 Instrumentation, Cycle	77
3.1.3 Instrumentation, Outdoor Unit.....	79
3.1.4 Instrumentation, Indoor Unit.....	79
3.1.5 Performance Indices	81
3.1.6 Selection of Control Schemes	81
3.2.....Steady State Tests.....	82
3.3.....EXV Control Scheme	84
3.3.1 Steady State Tests.....	84
3.3.2 Steady Test, Performance.....	91
3.3.3 Tests with Controlled Air Maldistribution.....	92
3.3.4 Results of Testing, Performance.....	95
3.3.5 Frost-up Test	96
3.3.6 Coil Maldistribution	97
3.3.7 Conclusions, EXV	101
3.4.....Hybrid Control Scheme and Comparison.....	101
3.4.1 Steady State Tests, System Behavior	102
3.5.....Steady State Tests, Performance and Comparison to EXV	106
3.5.1 Frost-up Test	108
3.6.....Bin Analysis	113
3.6.1 Modifications Compared to Method Implemented in ANSI/AHRI 210/240	114
3.6.2 Results.....	115
3.7.....Conclusions and Recommendations.....	118
Chapter 4: Rooftop Air-Conditioning Unit.....	119
4.1.....System Schematics and Instrumentation.....	120
4.1.1 Control Schemes.....	123

4.1.2 Limitations of Experimental Setup/Facilities	123
4.1.3 Effects of Air-Side Economizer onto Maldistribution.....	124
4.1.4 Overall System behavior - Superheat.....	139
4.1.5 COP and Capacity	141
4.2.....EXV Control Scheme	142
4.2.1 COP and Capacity improvement.....	144
4.3.....Building Capacity and COP	147
4.4.....Building Bin Analysis.....	149
4.4.1 Case A: Minimum Damper Position of 10 percent (22 percent OAF)	151
4.4.2 Case B: Damper position of 52 percent (50 percent OAF).....	154
4.4.3 Additional Considerations for Free Cooling.....	155
4.5.....Conclusions and Recommendation.....	155
Chapter 5: Estimation of Simple Payback Period	157
Chapter 6: Summary and Conclusions.....	160
6.1 Recommendations and Future Work.....	161
References.....	164
Glossary	169
APPENDIX A: Large Room Cooling System	A-1
APPENDIX B: Domestic Heat Pump.....	B-1
APPENDIX C: Rooftop Unit	C-1

LIST OF FIGURES

Figure 1: Uneven Frost Build Up, Air-Inlet of Evaporator, Side View	2
Figure 2: Uneven Frost Build-Up, Air-Inlet of Evaporator, Frontal View	2
Figure 3: Conventional Superheat Control Scheme (Same For TXV or EXV)	8
Figure 4: Individual Circuit Flow Control.....	10
Figure 5: Hybrid Flow Control Method.....	10
Figure 6: Reduced Hybrid Flow Control Method	10

Figure 7: Distributor Valve	10
Figure 8: Large Room Cooling System.....	16
Figure 9: Evaporator Circuitry Schematic	17
Figure 10: Instrumentation Overview LRCS.....	18
Figure 11: Large Room Cooling System Instrumentation.....	19
Figure 12: Evaporator Exit Superheat as Measured for Different Operating Conditions, TXV ...	21
Figure 13: Cooling Capacity and COP for Different Operating Conditions.....	22
Figure 14: Measured Return-Bend Temperatures for Steady State TXV-Tests	22
Figure 15: Evaporator Coil, Connection Side with TXV	23
Figure 16: COP, Superheat and Evaporation Dew Point During Cyclic Tests.....	24
Figure 17: Comparison of Operating Dynamics of Cyclic and Steady State Tests	25
Figure 18: Temperatures During Frost-Up Tests.....	26
Figure 19: Individual Circuit Surface Usage Based on 1.5 K Threshold, TXV	26
Figure 20: TXV Frost Build-Up, 2.7 hrs after Start of Experiment.....	27
Figure 21: . Individual and Overall Superheat, Average Surface Usage Based on 1.5 K Threshold, TXV	28
Figure 22: COP and Capacity During Frost-Up Test, TXV	28
Figure 23: Primary Expansion Valves with (Right) and without Coil (Left) and Junction before Distributor.....	29
Figure 24: Evaporation Temperature and Evaporator Superheat, Condenser Air Inlet Temperature 2°C, EXV	30
Figure 25: Sight Glass Before Expansion Valve for Sufficient and Insufficient Subcooling	30
Figure 26: Evaporation Temperature and Evaporator Superheat, Condenser Air Inlet Temperature 12°C, EXV	31
Figure 27: Evaporation Temperature and Evaporator Superheat, Condenser Air Inlet Temperature 22°C, EXV	31
Figure 28: Evaporation Temperature and Evaporator Superheat, Condenser Air Inlet Temperature 35°C, EXV	31
Figure 29: Evaporation Temperature and Evaporator Superheat, Condenser Air Inlet Temperature 46°C, EXV	32

Figure 30: Measured Return-Bend Temperatures for Steady EXV-Tests At 2°C And 12°C Condenser Air Inlet Temperature, EXV.....	33
Figure 31: Measured Return-Bend Temperatures for Steady EXV-Tests at 22°C and 35°C Condenser Air Inlet Temperature, EXV.....	33
Figure 32: Measured Return-Bend Temperatures for Steady EXV-Tests At 46°C Condenser Air Inlet Temperature, EXV.....	34
Figure 33: Cooling Capacity and COP for Different Operating Conditions, EXV Control Scheme	35
Figure 34: COP, Superheat and Evaporation Dew Point During Cyclic Tests, EXV.....	36
Figure 35: Air Inlet Temperature and Refrigerant Exit Dew Point Temperature, EXV	36
Figure 36: Air Inlet Temperature, Superheat and Evaporation Temperature During Frost-Up Test, EXV	37
Figure 37: Superheat and Surface Usage, EXV	38
Figure 38: Average Individual Circuit Superheat, Overall Superheat, and First Superheated Position, EXV	38
Figure 39: COP and Capacity During Frost-Up Test, EXV	39
Figure 40: Blockage of Coil, EXV	39
Figure 41: Return-Bend Temperatures with Blockage to Coil, EXV	40
Figure 42: System Performance Indices with Different Levels of Airside Maldistribution, EXV.	41
Figure 43: System Performance Indices with Different Levels of Airside Maldistribution, EXV.	41
Figure 44: System Performance Indices Change with Different Levels of Airside Maldistribution, EXV	42
Figure 45: Hybrid Control Scheme, Evaporator	43
Figure 46: Measured Return-Bend Temperatures for Steady Hybrid-Tests at 12°C and 22°C Condenser Air Inlet Temperature, Hybrid.....	44
Figure 47: Measured Return-Bend Temperatures for Steady Hybrid-Tests at 35°C and 46°C Condenser Air Inlet Temperature, Hybrid.....	44
Figure 48: Measured Return-Bend Temperatures for Steady Hybrid-Test with Primary Valve Fully Open at 46°C Condenser Air Inlet Temperature, Hybrid	45
Figure 49: Evaporation Temperature and Evaporator Superheat, Condenser Air Inlet Temperature 12°C, Hybrid	46

Figure 50: Evaporation Temperature and Evaporator Superheat, Condenser Air Inlet Temperature 22°C, Hybrid	46
Figure 51: Evaporation Temperature and Evaporator Superheat, Condenser Air Inlet Temperature 35°C, Hybrid	46
Figure 52: Evaporation Temperature and Evaporator Superheat, Condenser Air Inlet Temperature 46°C, Hybrid	47
Figure 53: COP and Capacity as Function of Condenser Air Inlet Temperature, Steady State, Hybrid.....	47
Figure 54: Evaporation Dew Temperature, Room Temperature, and Superheat During Frost-Up Test, Hybrid	48
Figure 55: Capacity and COP as Function Of Time During Frost-Up Test, Hybrid.....	49
Figure 56: Superheat and Surface Usage During Frost-Up Test, Hybrid.....	49
Figure 57: Frost Build-Up 6.95 hrs after Startup	50
Figure 58: Frost Build-Up 10.6 hrs After Startup.....	50
Figure 59: Measured Return-Bend Temperatures for Tests with Coil Blockage, 35°C Condenser Air-Inlet Temperature, Hybrid	51
Figure 60: Individual Circuit Mass Flow Rates for Clean-Coil, 46°C	52
Figure 61: Individual Circuit Mass Flow Rates for Type B Blocked-Coil (2/3 blockage), 46°C	52
Figure 62: Performance as a Function of Condenser Air Inlet Temperature, Hybrid.....	53
Figure 63: Performance Change as a Function of Condenser Air Inlet Temperature, Hybrid	53
Figure 64: Influence of Ambient Temperature and Control Scheme on Performance Indices	54
Figure 65: Influence of Coil Blockage onto Capacity for EXV and Hybrid.....	55
Figure 66: Influence of Operating Time on Capacity and Evaporator Fan Power Consumption for Frost Build-up Test	56
Figure 67: Bin Temperature Comparison Region IV Versus Sacramento Municipal Airport	59
Figure 68: Measured COP and Capacity Data and Inter/Extrapolated Data.....	59
Figure 69: . COP and Capacity Ratios for Hybrid Compared to EXV Control	60
Figure 70: Annual Energy Consumption, LRCS.....	61
Figure 71: Annual Energy Consumption for Different Ambient Temperature Profiles, LRCS....	62
Figure 72: Estimated Energy and Cost Savings, LRCS	62
Figure 73: Return-Bend Temperatures, 35°C Ambient Temperature	63

Figure 74: Manually Estimated End of 2-Phase Section for EXV Control Scheme, 35°C Ambient Temperature	64
Figure 75: Semi-Empirical Approach to Calculate Flowrate Distribution	65
Figure 76: Estimated Refrigerant Distribution Factors, TXV, no Airside Maldistribution.....	66
Figure 77: Estimated Refrigerant Distribution Factors, EXV, no Airside Maldistribution.....	66
Figure 78: Estimated Refrigerant Mass Flow Maldistribution Performance Index, TXV, no Airside Maldistribution.....	66
Figure 79: Estimated Refrigerant Mass Flow Maldistribution Performance Index, EXV, no Airside Maldistribution.....	66
Figure 80: Connection Side of Evaporator, TXV Control Scheme.....	67
Figure 81: Distributor and Tandem Primary EXV's; Same Setup (Without Balancing Valves) Used for EXV Control Scheme	67
Figure 82: Location of Expansion Port Exits in Different Expansion Valves (Indicated by Arrow).	68
Figure 83: Two-Phase Simulation, Several Distributors, Horizontally Installed, Data Adopted from Graph 7 of Li et al. 2005; Estimated Maximum Uncertainty Caused by Reading from Graph 0.1%.....	70
Figure 84: Two-Phase Simulation, Several Distributors, Vertically Installed With Orifice 3.7° Misaligned, Data Adopted from Graph 7 of Li et al. 2005; Estimated Uncertainty Caused by Reading 0.2%	70
Figure 85: Simulation Results Compared to Equally Distributed Flow	72
Figure 86: Experimental Results Compared to Hybrid Base Case.....	72
Figure 87: COP And Capacity Change Residual	72
Figure 88: COP Degradation for Vertically Oriented Distributors with Misaligned Orifice	73
Figure 89: COP Degradation for Horizontally Aligned Distributors with Non-Misaligned Orifice	73
Figure 90: Capacity Degradation for Vertically Oriented Distributors with Misaligned Orifice .	73
Figure 91: Capacity Degradation for Horizontally Aligned Distributors with Non-Misaligned Orifice	73
Figure 92: Heat Pump Outdoor Unit.....	76
Figure 93: Indoor Unit and Instrumentation.....	76
Figure 94: Heat Pump System Schematic with Instrumentation, Cycle Level	78

Figure 95: Evaporator Circuitry and Return-Bend Temperature Measurement Points.....	80
Figure 96: Heat Pump With 50% of Air Inlet Grille Blockage by Plastic Foil.....	83
Figure 97: Spacing between Air Inlet Grille and Coil	83
Figure 98: Coil Blockage on a University maintained AC-Unit	83
Figure 99: Superheat and Evaporation Temperature, -20°C ambient, EXV.....	84
Figure 100: Superheat and Evaporation Temperature, -8.33°C ambient, EXV.....	85
Figure 101: Superheat and Evaporation Temperature, 8.33°C Ambient, EXV	85
Figure 102: Return-Bend Temperatures, -20°C Outdoor, 21.1°C Indoor Temperature	86
Figure 103: Measured Return-Bend Temperature for 6th Return-Bend, EXV, -20°C Outdoor/21.1°C Indoor Temperature.....	87
Figure 104: Standard Deviation of Return-Bend Measurements, EXV,	88
Figure 105: . Circuit Two-Phase Section End, EXV, 21.1°C Indoor Temperature	88
Figure 106: Circuit Two-Phase Section End, EXV, 21.1°C Indoor Temperature, 8.33°C Ambient Temperature	89
Figure 107: Distributor And Distribution Lines	90
Figure 108: Distributor Details.....	90
Figure 109: Individual Circuit Exit Superheat for Different ambient Temperatures.	91
Figure 110: COP and Capacity, Clean-Coil, Steady State, EXV	92
Figure 111: Coil Maldistribution for Blocked-Coil Cases, EXV	93
Figure 112: Individual Circuit Exit Superheats for Blocked-Coil Cases, EXV.....	93
Figure 113: Idealized Development of Superheat: Exponential Behavior	94
Figure 114: COP and Capacity for Blocked and Unblocked Cases, EXV, Steady State	95
Figure 115: Outdoor Room Conditions, Frost-Up Test, EXV.....	96
Figure 116: COP and Heating Capacity, Frost-Up Test, EXV	96
Figure 117: Superheat and Evaporation Temperature, Frost-Up Test, EXV.....	97
Figure 118: Circuit Two-Phase Section End, Frost-Up Test, EXV	98
Figure 119: Individual Circuit Exit Superheat During Frost-Up Test, EXV	99
Figure 120: Pictures of Coil Inlet During Frost-Up Test, EXV	100
Figure 121: Modification for Hybrid Control Scheme	101

Figure 122: Superheat and Evaporation Temperature, -20°C Ambient, Hybrid.....	102
Figure 123: Superheat and Evaporation Temperature, -8.33°C Ambient, Hybrid.....	102
Figure 124: Superheat and Evaporation Temperature, 8.33°C Ambient, Hybrid.....	103
Figure 125: Circuit Exit and Overall Superheat, 8.3°C ambient temperature, Hybrid and EXV	103
Figure 126: Circuit Two-Phase Section End, Hybrid, Clean-Coil.....	104
Figure 127: Individual Circuit Exit Superheats, Hybrid, Clean-Coil.....	104
Figure 128: Circuit Two-Phase Section End, Hybrid, Clean-Coil.....	105
Figure 129: Exit Superheats For High Temperature, Blocked-Coil.....	105
Figure 130: Circuit Exit Superheat, Hybrid, Blocked.....	106
Figure 131: COP and Capacity for Blocked and Unblocked Cases, Hybrid, Steady State.....	106
Figure 132: COP and Capacity Change Between EXV and Hybrid Control Scheme.....	107
Figure 133: Subcooling for heat pump tests	108
Figure 134: Corrected COP	108
Figure 135: Outdoor Room Conditions, Frost-Up Test, Hybrid.....	108
Figure 137: Superheat and Evaporation Temperature, Frost-Up Test, Hybrid.....	110
Figure 138: Circuit Exit Superheat During Different Time Ranges, Frost-Up Test, Hybrid	111
Figure 139: Circuit Two-Phase Section End During Different Time Ranges, Frost-Up Test, Hybrid.....	111
Figure 140: Balancing Valve Opening During Frost-Up Test, Hybrid	111
Figure 141: Individual Circuit Exit Superheats During Frost-Up Test, Hybrid.....	112
Figure 142: COP and Capacity, Frost-Up Test, EXV and Hybrid.....	113
Figure 143: Fractional Bin Hours per Region.....	113
Figure 144: Bin Hours per Region.....	113
Figure 145: Weighting Factors for Maldistributed Coil Case	114
Figure 146: Design Heating Requirement	115
Figure 147: Electricity Savings per Year, Relative Hybrid Compared to EXV	115
Figure 148: Electricity Cost Savings per Year, Absolute Hybrid Compared to EXV	116
Figure 149: Electricity Savings per Year, Absolute Hybrid Compared to EXV	116

Figure 150: Electricity Savings Potential in M\$/Year, Assuming Entire Estimated Installed Heat Pump Capacity of California is Installed in Each Region	117
Figure 151: Electricity Savings Potential in Gwh/Year, Assuming Entire Estimated Installed Heat Pump Capacity of California is Installed In Each Region.....	117
Figure 152: Schematic of a Rooftop Unit, Carrier Corporation (2006).....	119
Figure 153: Refrigerant Side Schematic of RTU	120
Figure 154: Air Side Instrumentation of Rooftop Unit	121
Figure 155: Supply Air Flowrate, RAC, EXV Control Scheme	124
Figure 156: Economizer and Coil Cross Section	125
Figure 157: Measurement Positions for Temperature (16 grid) and Velocity (Numbered Positions)	125
Figure 158: Economizer Section of Unit.....	127
Figure 159: Closed Economizer.....	127
Figure 160: 50% Open Economizer, View Angle 1	127
Figure 161: 50% Open Economizer, View Angle 2.....	127
Figure 162: Fully Open Economizer, View Angle 1	128
Figure 163: Fully Open Economizer, View Angle 2.....	128
Figure 164: Evaporator Coil Circuitry	129
Figure 165: Distributor and Expansion Valve	129
Figure 166: Velocity Distribution along Coil, 60 Hz Supply Fan Frequency, Different Economizer Positions	130
Figure 167: Velocity Distribution along Coil, Nominal Supply Fan Frequency Of 41.2 Hz, Different Economizer Positions	130
Figure 168: Handheld Anemometer	130
Figure 169: TXV, 52°C Ambient Temperature, Closed Damper.....	131
Figure 170: TXV, 28°C Ambient Temperature, Damper Closed.....	131
Figure 171: EXV, 52°C Ambient Temperature, Closed Damper.....	131
Figure 172: EXV, 28°C Ambient Temperature, Closed Damper.....	131
Figure 173: EXV, 52°C Ambient Temperature, Closed Damper, Individual and Overall Exit Superheat.....	132

Figure 174: TXV, 52°C Ambient Temperature, Closed Damper, Individual and Overall Exit Superheat.....	132
Figure 175 EXV, 27.8°C Ambient Temperature, Closed Damper.....	133
Figure 176: EXV, 27.7°C Ambient Temperature, Half Open Damper	133
Figure 177: EXV, 27.8°C Ambient Temperature, Fully Open Damper.....	133
Figure 178: Individual Circuit Exit Superheat and Avg. Mixed Air Temperature at Nominal Fan Frequency, EXV, 52°C Ambient Temperature, Half Open Damper	134
Figure 179: Individual Circuit Exit Superheat and Avg. Mixed Air Temperature at Nominal Fan Frequency, EXV, 52°C Ambient Temperature, Fully Open Damper.....	134
Figure 180: Individual Circuit Exit Superheat and Avg. Mixed Air Temperature at Nominal Fan Frequency, EXV, 10°C Ambient Temperature, Closed Damper	135
Figure 181: Individual Circuit Exit Superheat and Avg. Mixed Air Temperature at Nominal Fan Frequency, EXV, 10°C Ambient Temperature, Half Open Damper	135
Figure 182: 20 Individual Circuit Exit Superheat and Avg. Mixed Air Temperature at Nominal Fan Frequency, EXV, 15°C Ambient Temperature, Fully Open Damper	135
Figure 183: Individual Circuit Exit Superheat and Avg. Mixed Air Temperature at Nominal Fan Frequency, Hybrid, 52°C Ambient Temperature, Half Open Damper	136
Figure 184: Individual Circuit Exit Superheat and Overall Superheat, Hybrid, 52°C Ambient Temperature, Half Open Damper	136
Figure 185: Exit Superheat Measurement Position	137
Figure 186: Refrigerant Flow Rates for Closed Damper Position for 28°C Ambient Temperature	137
Figure 187: FMI for Closed Damper Position, 28°C Ambient Temperature.....	138
Figure 188: FMI for Closed Damper Position, 52°C Ambient Temperature.....	138
Figure 189: FMI for Half Open Damper Position, 52°C Ambient Temperature	138
Figure 190: FMI for Fully Open Damper Position, 52°C Ambient Temperature	138
Figure 191: Overall Evaporator Superheat, Nominal Fan Speed	139
Figure 192: Overall Superheat, EXV, as Function of Air Inlet Temperature with Different Damper Positions.....	139
Figure 193: Overall Superheat, EXV, as Function of Mixed Air Temperature with Different Damper Positions.....	140

Figure 194: Overall Superheat, Hybrid, as Function of Mixed Air Temperature with Different Damper Positions.....	140
Figure 195: Subcooling for EXV Tests	140
Figure 196: Subcooling for Hybrid Tests	140
Figure 197: COP for RAC, EXV Control Scheme.....	142
Figure 198: Capacity for RAC, EXV Control Scheme.....	142
Figure 199: Capacity as Function of Mixed Air Temperature, RAC, EXV Control Scheme.....	143
Figure 200: Flowrate of Moist Air as Function of Mixed Air Temperature, RAC, EXV Control Scheme	143
Figure 201: COP for RAC, Hybrid Control Scheme	144
Figure 202: Capacity for RAC, Hybrid Control Scheme.....	144
Figure 203: Capacity as Function of Mixed Air Temperature, RAC, Hybrid Control Scheme...	144
Figure 204: Flowrate Of Moist Air as Function of Mixed Air Temperature, RAC, Hybrid Control Scheme	144
Figure 205: Capacity Improvement for Hybrid Control Scheme	145
Figure 206: COP Improvement for Hybrid Control Scheme	145
Figure 207: COP Improvement for Hybrid Control Scheme, Considering Additional Power Consumption of Hybrid Control	146
Figure 208: Simplified schematic for rooftop unit and building.....	147
Figure 209: Capacity Difference for Hybrid Capacity if Building Capacity Rather than Vapor Compression System Capacity is Used.....	148
Figure 210: COP Building Change for Hybrid Control Compared to EXV Control Tests	148
Figure 211: Free Cooling COP	149
Figure 212: Free Cooling Capacity.....	149
Figure 213: Flowchart for bin calculation model.....	150
Figure 214: Outdoor Air Fraction as function of damper position	151
Figure 215: Bin-wise power consumption reduction, Sacramento, 10% minimum damper position	152
Figure 216: Bin wise power consumption reduction, Bakersfield, 10% minimum damper position	152

Figure 217: Annual power consumption reduction as function of roof offset, 10% minimum damper position	153
Figure 218: Annual % power consumption reduction as function of roof offset, 52% minimum damper position	153
Figure 219: Rooftop Units Mounted on Dark-Colored Roof Of a University Owned Building (2012).....	153
Figure 220: Bin-wise power consumption reduction, Sacramento, 52% minimum damper position	154
Figure 221: Bin wise power consumption reduction, Bakersfield, 52% minimum damper position	154
Figure 222: Annual power consumption reduction as function of roof offset, 52% minimum damper position	155
Figure 223: Annual % power consumption reduction as function of roof offset, 52% minimum damper position	155
Figure 224: Estimate of Additional Cost for Hybrid Control per System before Markup.	158

LIST OF TABLES

Table 1: Boundary Conditions for Distributor in Simulation and Reality	68
Table 2: Overall Superheat Settings for Simulation	71
Table 3: Measurements and Accuracy	121
Table 4: Flow Meter Specification.....	130
Table 5: Cost Estimates for Components.....	157
Table 6: Simple Payback Period for Analyzed Systems for Several Operating Conditions	159

EXECUTIVE SUMMARY

Introduction

Electricity to operate commercial air conditioning equipment contributes to about 12 percent of the electricity usage for the sector in California (Itron, 2006). Approximately 33 percent is used for cooling along and about 32 percent is used for heating in the residential sector (EIA, 2013a). Expectations and minimum standards for equipment efficiency have been rising due to growing concerns about environmental impacts and electricity consumption, creating significant challenges for heating, ventilation, air conditioning and refrigeration (HVAC&R) equipment manufacturers. At some point it becomes necessary to incorporate changes to the basic vapor compression cycle in order to achieve higher efficiencies. One such modification involves individual control of refrigerant flow within each circuit of the evaporator.

For a given overall superheat exiting the evaporator of a vapor compression system, close to optimum capacity and efficiency are achieved when each of the refrigerant circuits within the evaporator has the same exit superheat. Non-uniform superheat of multi-circuit evaporators can be caused by many factors, including: 1) uneven air flow distribution due to air-side fouling, and/or improper design and installation of evaporators; 2) uneven refrigerant flow distribution due to uneven circuit flow resistance and/or uneven separation of liquid and vapor refrigerant within the refrigerant distributor; and 3) uneven air-inlet temperature distribution caused by air recirculation and/or air side economizers.

Project Purpose

The first goal of this project was to conduct a literature review on flow maldistribution and its effects on equipment performance as well as mitigation of the issue by adjusting the refrigerant side flowrates. The second goal was to assess three potential systems and analyze potential performance improvements in each system from reduced maldistribution using experiments and simulation. The extent of system-level performance improvement in the selected systems was previously unknown but was expected to be significant. The specific objective of the project was to determine the achievable performance improvement for a hybrid control as compared to an electronic expansion valve (EXV) control without any flow balancing.

Project Results

Three applications were selected that could have significant air side maldistribution in field operation: 1) a three-ton large room cooling system where uneven frost build up and fouling could lead to airside maldistribution; 2) a five-ton domestic heat pump that was subject to the same issue in a more severe manner due to smaller fin spacing and operation in the outside; and 3) a four-ton commercial rooftop unit equipped with an airside economizer that could cause significant temperature and flow maldistribution. Each system was tested without individual circuit flow control and with an EXV as well as with individual circuit flow control in order to evaluate the achievable performance improvement.

The three-ton large room cooling system consisted of a condensing unit that is typically mounted outdoors and an indoor evaporator unit. The indoor unit for the chosen system was

operated at a two degrees centigrade ($^{\circ}\text{C}$) (35.6° Farenheit) ($^{\circ}\text{F}$) air-inlet temperature. These types of systems are used to store perishable food products such as fresh meat (short-term) as well as vegetables and fruit (long- and short-term). Due to the low room temperature, the evaporation temperature is below the freezing point, which can lead to uneven frost build up under certain operating conditions. This effect is shown in Figure 1 and Figure 2 for the air inlet side of the system tested in this report.project. The system cycles through periods with frost build up (cooling on) and defrosting (cooling off) while the fan is operating continuously if the dew point of the air in the room is above the fin temperature. The duration of these cycles depends upon cooling load and ambient temperature. As a result, minor influence of frost build up in low load periods and larger influence in high load periods was to be expected.

Steady-state clean-coil tests at various ambient temperatures from $2\text{-}46^{\circ}\text{C}$ ($35.6\text{-}115^{\circ}\text{F}$) and frost build up tests were conducted to capture the effect of frost build up on performance as well as on possible performance improvement when using the hybrid control. Additional steady-state tests with different levels of coil blockage were conducted to achieve better repeatability for the performance comparison.



Figure 1: Uneven Frost Build Up, Air-Inlet of Evaporator, Side View



Figure 2: Uneven Frost Build-Up, Air-Inlet of Evaporator, Frontal View

Steady-state clean-coil tests with the hybrid control approach and EXV baseline were conducted. The large room cooling system (LRCS) capacity and coefficient of performance (COP) increased for the hybrid control scheme by about six percent and four percent respectively with little dependence on the ambient temperature. The original thermostatic expansion valve (TXV), which is still used in this type of application to save initial cost, led to a COP reduction of one percent and a capacity reduction of more than four percent for 22°C ambient temperature when compared to the EXV baseline.

The indoor room was kept at high humidity to simulate fresh and moist produce that has to be chilled to storage temperature for the frost build up tests. The frost build up led to severe hunting of the TXV after only 2.5 hours of operation. This was caused by increasing air side maldistribution that led to overfeed of liquid on some circuits, causing a steeper reaction of the superheat to changes of the refrigerant mass flowrate. It was possible to adjust the superheat according to the operating conditions to obtain less superheat fluctuations for the EXV. It was also possible to adjust the mass flowrates in the individual circuits for the hybrid control

approach, which increased the overall effectiveness of the coil and resulted in a more even and slower frost build up.

Blocked-coil tests were conducted with two different levels of blockage using the hybrid and EXV control schemes. These blockage levels led to a performance reduction that was comparable to very light and intermediate frost build up. COP and capacity were compared to the EXV clean-coil tests for the applicable ambient temperature. COP was increased by one percent for one operating point and decreased by up to eight percent for other operating points for the hybrid control scheme. COP reduction was much larger for the EXV control scheme, ranging from nine to 29 percent. The capacity for the hybrid control scheme was reduced by zero percent to eight percent, while it was reduced by 16 percent to 31 percent using the EXV only control scheme. The hybrid control therefore recovered a significant amount of the performance penalties caused by maldistribution.

A bin analysis was conducted to evaluate the annual performance improvement. The clean-coil data from EXV and hybrid control was used for the simulation, using the EXV control as the baseline since no reliable data on the maldistribution over the course of a year was available. The result of this simulation was a minimum achievable performance improvement for a system without any refrigerant or air side fouling. Energy savings of 2.1 percent (condensing unit and room subject to outdoor conditions) and 2.2 percent (condensing unit subject to outdoor conditions or within building, room in building) were found for Sacramento Executive AP typical meteorological year (TMY) 3 data. Fouling and frost build up will lead to larger achievable energy savings. The payback period required for simple payback will therefore be shorter than the approximately nine years evaluated in the economic analysis based on clean coil conditions.

Heat pumps offer significant potential for more energy efficient use of electricity. Air-source heat pumps can deliver two to four units of heat depending on ambient temperature, in contrast to resistance heating, where only one unit of heat is available for each unit of electricity. Moreover, if the building will be equipped with an air conditioning (AC) system, the system changes that are necessary to make it work as a heat pump are relatively small, which can lead to a lower overall installation cost as compared to a gas or oil furnace. Electricity can be generated using renewable resources that do not interfere significantly with food production, such as wind and solar power, in contrast to fuels used for a furnace.

Air-source heat pumps are subject to ambient air that carries dust and organic material, inevitably leading to coil fouling. The transport of salt particles leads to additional significant corrosion of heat exchangers in coastal regions. Furthermore, uneven frost build up can lead to a reduction of the air flow on parts of the coil if the ambient air temperature is low enough. In addition to these operating-based sources of air side maldistribution, design constraints lead to circuits with different tube numbers and airflow rates as well as maldistribution on the refrigerant side. A five-ton domestic heat pump was tested with an EXV as well with the hybrid control scheme to evaluate the range of possible performance improvements. Steady-state tests were conducted for -20°C, -8.33°C, and 8.33°C ambient temperature. These tests were conducted with a clean outdoor heat exchanger as well as with a partially blocked air-inlet grille of the

outdoor unit to simulate a repeatable air side maldistribution. The blockage level was based on additional frost-up tests.

The clean-coil tests indicated that capacity and COP increases for the domestic heat pump (DHP) with the hybrid control method were on the order of one percent and 0.6 percent, respectively. However, these numbers did not include savings due to a potential extension of the runtime between defrost cycles and the effects of frost build-up or coil fouling. A four percent to 26 percent improvement in capacity along with a four percent to 20 percent COP improvement was observed for the blocked air inlet grille when using the hybrid control method. The hybrid control system extended the runtime by more than 30 percent for the frost-up tests, which could be increased even further by optimized control of the balancing valves.

A bin analysis was conducted to evaluate the potential benefits of the hybrid control system. The energy savings ranged from 2.8 percent to 3.5 percent depending on the climate zone for an estimated effective maldistribution. These results did not include potential savings that could be achieved by using a reduced number of defrosting cycles. The estimated simple payback period (SPP) exceeded the system lifetime for most operating conditions, except for climate zone 5. The hybrid control may not be economically viable for California's climate at this time. However, the SPP estimate did not include additional savings due to a reduced number of defrosts. Therefore the hybrid control should be considered further for cold climate heat pumps, including an in-depth evaluation of the assumptions for the maldistributed coil and an evaluation of a reduced hybrid control scheme.

In the tested system, the defrost cycles themselves were based on compressor runtime below approximately zero°C rather than on actual frost build up, which offered additional potential for energy savings.

Rooftop units (RTUs) with economizers use a damper system to exhaust return air and in exchange bring in fresh air before the evaporator. A large benefit of RTUs is their compact design that does not require any field installation of refrigerant circuitry; only return, supply air, power and controls need to be connected.

However, the compact design of RTUs leads to significant maldistribution of temperature, humidity, and velocity at the inlet to the coil, especially if the economizer damper position is partially open. A four-ton rooftop unit with economizer was tested with ambient temperatures of 10°C (50°F), 27.77°C (82°F), and 52°C (126°F) to assess these effects. Significant temperature maldistribution and flow maldistribution between the different circuits was found. The measurements conducted with the balancing valves of the hybrid control as virtual sensors indicated an increase of 45 percent refrigerant flow at the top of the coil and a 56 percent decrease at the bottom of the coil to obtain equal circuit exit superheats for the most extreme condition.

The achievable COP improvement as defined in the 2008 Air-Conditioning, Heating, and Refrigeration Institute (AHRI) 210/240 standard was in the range of 1.5 percent for the closed damper position operation at 28°C (82 F) ambient temperature to 16.6 percent for a half open damper at 51.5°C (125°F) ambient temperature if the hybrid control rather than an EXV control

scheme was used. Since the rooftop unit was equipped with an economizer, the actually available cooling capacity for the building differed from the cooling capacity available on the refrigerant side. For low ambient temperature the net cooling capacity available for cooling the building was larger than the refrigerant side capacity, while for high ambient temperature it was smaller than the refrigerant side capacity. A building COP was defined as the ratio of available cooling for the building to the total power input of the rooftop unit. For a closed damper, the differences between the two COPs were relatively small, while they were quite significant for a half open and fully open damper. A nearly 65 percent building COP improvement resulted for the hybrid control at the most extreme condition (fully open damper, 51.5°C [125°F] ambient temperature).

A bin analysis for Sacramento Executive AP and Bakersfield Meadows Field was conducted to evaluate the yearly benefits of the systems. This analysis showed that actual electrical energy consumption reduction using the building COP was in the range of 0.8 percent to 6.6 percent depending on climate zone, minimum damper position, and the increase of local temperature due to solar irradiation. Solar irradiation was considered to be a constant roof temperature offset that affects the condenser and ventilation air inlet temperature. The simple payback period was estimated to be 10.7 years with 10 percent minimum damper position and no roof temperature offset for Bakersfield. The simple payback period with a minimum damper position of 52 percent and a roof temperature offset of 9° Kelvin (K) was one year. The simple payback period was estimated to exceed the typical equipment lifetime with 22 years for a 10 percent minimum damper position and no roof temperature offset for Sacramento. The simple payback period with a minimum damper position of 52 percent and a roof temperature offset of 9°K was 2.5 years. These numbers did not include any additional coil maldistribution caused by uneven fouling over the lifetime of the system. Future work should include an assessment of this issue since the roof temperature offset was only approximated. Even without this assessment, the hybrid control system led to significant improvements, especially if a large outdoor air fraction is required.

Project Benefits

The research conducted in this project helped to advance the understanding of how air and refrigerant side maldistribution in HVAC&R systems contributes to excess electricity usage. Resolving these issues could lead to reduced energy use, which would reduce greenhouse gas emissions that cause climate change as well as other emissions that contribute to air pollution.

Chapter 1:

Introduction and Literature Review

1.1 Introduction

Air-source vapor compression systems of a size of 3.5 kW (1 ton) or larger generally use multiple circuits for the evaporator. While this leads to benefits in terms of capital cost and efficiency, it also inherently opens up another problem: maldistribution. Maldistribution in evaporators can be caused by heat transfer degradation and flow maldistribution on both refrigerant and air sides of the evaporator. Kim et al. (2008a) investigated the effects of flow maldistribution on the performance of a 10.55 kW (3 ton) domestic heat pump by using a simulation model. They found that COP degraded by about 4 percent and capacity by about 6 percent, if airside maldistribution was applied. When applying equal superheat control to the two evaporator branches of their model, they found that most of the performance degradation can be recovered. Kim et al. (2008a) furthermore suggested the use of a hybrid control of expansion valves, where the main expansion valve provides most of the pressure drop while small balancing valves control the flow in each individual circuit. The hybrid control was believed to be of lower cost than using individual circuit expansion valves

1.1.1 Organization of Report

This report starts with a literature review on flow maldistribution and its effects on equipment performance as well as mitigation of the issue by adjusting the refrigerant side flowrates. After that experimental results are provided for three systems. The simulation and data analysis is followed by the conclusions and recommendations. The chapter for each system is written in a way that the content can be understood without knowledge of the other chapters.

1.2 Significance and Motivation

For each of the three selected systems, there are different causes of maldistribution. These lead to a performance reduction of the system which can be recovered in part by using the hybrid control approach. The extent of system-level performance improvement in actual systems of the selected type was previously unknown, but expected to be significant. Therefore it was assessed using experiments and simulation.

1.2.1 Large Room Cooling System (LRCS)

EIA (2006) states that 436 billion kWh (1489 trillion Btu) of electricity are used in the USA for walk-in units, which includes freezers. The large room cooling system (LRCS) operates close to the freezing point and is therefore subject to frost build-up, while it does not have a dedicated defrost system as freezers do. Under high load operation it can frost-up significantly.

1.2.2 Domestic Heat Pump (HP)

About 70 percent of the energy used for space heating of residential buildings in the US comes from natural gas (DOE, 2012). In 2005, space heating amounted to 4.3 quadrillion Btu (1260 TWh) or nearly 41 percent of the total energy consumed in the residential sector (DOE, 2012).

Since fossil fuels contribute significantly to global warming, it is necessary to reduce the energy used for space heating. This can be done by reducing the heating load or by using more energy efficient heating equipment. Improving the insulation and air tightness of existing buildings is not without challenges, as outlined by Lstiburek (2012a) and Lstiburek (2012b). Installation of more efficient heating systems is likely a simpler retrofit. Isaac and van Vuuren (2009)¹ predicted a more than 50 percent increase of the heating energy demand in US between the years 2000 and 2050, along with more than double the usage of AC. While the increased usage of AC, partially a result of global warming, is unfortunate, it also represents a huge opportunity for air-source heat pumps (ASHPs). ASHPs are, in their simplest configuration, modified AC systems and can therefore replace AC systems at relatively small additional cost. One advantage is that they run on electricity, which means that any primary energy source can be used. Ideally, a natural gas furnace should be combined with a HP. Using real time availability data, the HP could then be run if sufficient renewable energy (e.g. wind) is available. In times of limited renewable energy supply the gas furnace can be used as a backup. Unfortunately, ASHPs are subject to the environment and therefore are subject to outdoor coil fouling and under certain operating conditions, uneven frost build-up. Frost buildup is of increased significance for cold climate heat pumps. While theoretical investigations to investigate the effects of maldistribution for heat pumps existed previously (e.g. Kim et al. 2008a, Kim et al., 2009a), the goal of the HP investigation described in this report was to determine the range of the associated performance penalties and the possibility of improvement when using an actual system.

1.2.3 Rooftop Air Conditioning Unit (RAC)

Based on EIA (2006), 463 billion kWh (4578 trillion Btu) of electricity for cooling in commercial buildings (excluding malls) is consumed by packaged air conditioning systems, which includes rooftop units. Kaern (2011) numerically investigated the effects of maldistribution for a residential air conditioning unit, which has similar evaporation and condensing temperatures as a rooftop air conditioning (RAC) unit having a closed outside ventilation damper. He found, that for the worst case airflow maldistribution, the COP penalty was reduced from 43.2 percent to 5.7 percent if individual circuit flow control was applied. In contrast to split system residential air conditioning units, rooftop units are not only subject to refrigerant and airside flow maldistribution, but also to airside temperature and humidity maldistribution. This becomes very significant, if fresh air economizers are used, which mix ambient air and return air directly in front of the evaporator coil. Another issue with fresh air economizers is also that they can fail, which can lead to unnecessarily large outdoor air fractions. Indeed, faulty economizers are common in practice, Jacobs et al. (2003) states that 62 percent of the tested RTUs had faulty economizers, a result which is comparable to Cowan (2004) which states that 64 percent of the tested RTU's needed economizer service. It is therefore expected, that a significant potential for performance improvement exists if hybrid control is applied to rooftop units with economizers.

¹ Calculated based on Figure 5 in Isaac and van Vuuren (2009).

1.3 Introduction to Hybrid Control and Related Control Approaches

The evaporator superheat is used in vapor compression systems as a measure of the two-phase coil utilization. In practice, however, the issue is somewhat more complicated, since multiple circuits are used in parallel to increase the efficiency while optimizing the cost of the evaporator. Figure 3 shows a vapor compression cycle with 3 circuits and a conventional overall superheat control, which is either done using a thermal expansion valve (TXV) or electronic expansion valve (EXV). While this control scheme can control the overall superheat, it cannot control the distribution of refrigerant to individual circuits. If refrigerant side and airside flowrates are uniform and no fouling occurs on either side, then this is not an issue. In practice, however, maldistribution occurs, which degrades the performance as described in more detail in the literature review. This maldistribution can be caused, on the refrigerant side, by:

- unequal heat transfer degradation caused by fouling or
- refrigerant flow maldistribution caused by
 - i) different pressure drop in feeder tubes and/or in coil or
 - ii) quality maldistribution at the distributor.

On the air side, maldistribution can be caused by

- unequal heat transfer degradation caused by fouling, frost build-up or corrosion or
- temperature maldistribution at the inlet to the coil, or
- airside flow rate maldistribution caused by
 - i) unequal airside fouling or
 - ii) unequal frost build-up or
 - iii) limitations in the coil design.

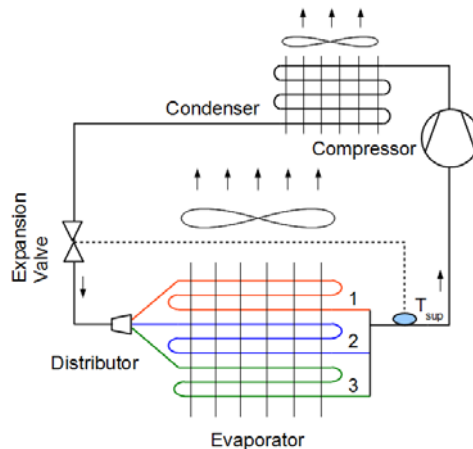


Figure 3: Conventional Superheat Control Scheme (Same For TXV or EXV)

Depending on application and design, multiple factors can occur at the same time leading to significant penalties. To overcome the associated performance penalties, it is desirable to control the superheat in the individual circuits of the evaporator. Using existing technology, a

straightforward approach would be to use individual valves for each circuit as shown in Figure 4. The disadvantages of this approach are that (a) the circuit capacity is sometimes smaller than the smallest available expansion valve on the market and (b) there would be a significant increase in cost. Figure 5 shows the cycle with hybrid control, as introduced by Kim et al. (2008b). The basic idea behind the hybrid control is a primary valve that provides for most of the pressure drop, which is followed by balancing valves that control the flow to the individual circuits. The hybrid control was expected to be a more cost effective option than individual expansion valves, since they do not need to have a wide actuation range. The biggest disadvantage of the hybrid control is that additional components, electronic controls and sensors need to be mounted in the system. This leads to additional possible leakage points as well as a more complex and potentially less reliable control scheme for the system. The goal of this project was to determine whether the achievable advantages in terms of COP and capacity are worth the additional investment. Figure 6 shows a reduced hybrid control scheme, which is a compromise between the full benefit of individual circuit control and the cost of it. Mader et al. (2010) and Funder-Kristensen et al. (2012) introduced an expansion device that, at the same time implements the function of a distributor and therefore reduces the number of components as shown in Figure 7.

Further details on the effects of flow control on the performance of evaporators and the effects and reasons for maldistribution can be found in the literature review.

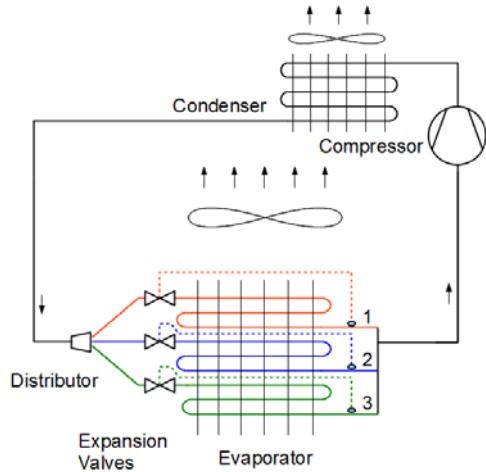


Figure 4: Individual Circuit Flow Control

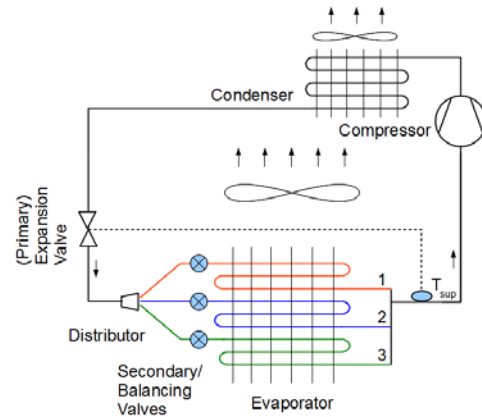


Figure 5: Hybrid Flow Control Method

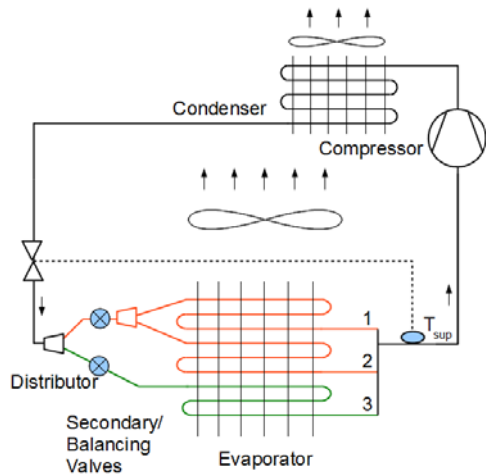


Figure 6: Reduced Hybrid Flow Control Method

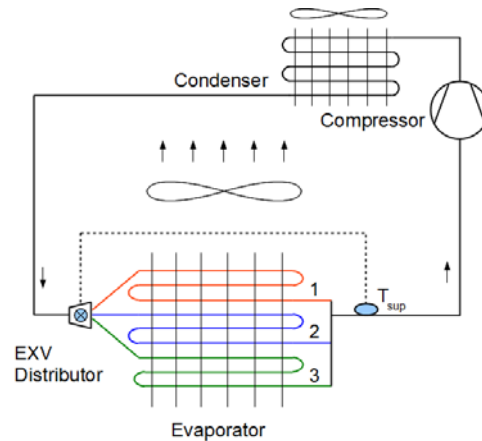


Figure 7: Distributor Valve

1.4 Objectives

The objective of this project was to determine the achievable performance improvement for the hybrid control – as compared to an EXV control without any flow balancing. This was done using an experimental study for the aforementioned systems which was augmented by simulations and annual performance evaluations using a bin-type analysis for the TMY3 temperature data for California as given by NREL (2012).

1.4.1 Procedure of Investigation

The following configurations and tests were considered for the HP and LRCS:

- Clean-coil:
 - i) Determine effects of initial refrigerant and airside maldistribution for the evaporator coil, and

- ii) determine performance benefits (COP, capacity) of individual circuit flow.
- Frost build up:
 - i) Determine effects of control scheme on evenness of frost build-up and superheat stability, and
 - ii) determine direct performance benefits as well as indirect performance benefits of individual circuit flow control (e.g. possible delay of defrost cycles).
- Blocked-coil tests
 - i) Determine performance penalties of a defined airside maldistribution, and
 - ii) determine performance advantages for the individual circuit flow control.

For the RAC, the performance penalties were evaluated as a function of different economizer openings and ambient temperatures.

1.5 Literature Review

The following review intends to give an overview of work that was previously done to assess the effects of flow maldistribution in multi circuited evaporators.

Janghoo (1997) developed a model to simulate the capacity of finned tube evaporators with one dimensional airside maldistribution. Their model considered cross fin conduction and refrigerant side distribution based on pressure drop. Fin conduction was considered between directly neighboring tubes. Dependent on the simulated airside velocity profile and type of coil, they found a capacity degradation of up to 63 percent for R407C and their coil C, if refrigerant distribution was assigned based on pressure drop. They furthermore found that capacity decreases if the refrigerant side distribution is assigned based on pressure drop. For their coil A, for example, they found a capacity degradation of 5 percent (R22) if refrigerant side distribution was based on pressure drop rather than assuming uniform refrigerant flow distribution. If airside maldistribution was applied, the capacity for the same refrigerant and coil dropped by 9 percent with uniform refrigerant flow while it dropped by 39 percent if refrigerant side flowrate was assigned based on pressure drop.

Payne and Domanski (2002) evaluated the potential benefits if refrigerant distribution is controlled to achieve equal exit superheats. In the experimental part of their study, they found capacity reductions of up to 41 percent and 32 percent for the wavy and wavy lanced fin evaporator if overall superheat was held constant while the individual circuit superheat was allowed to vary. For non-uniform air flow tests, it was found that the capacity was recovered to within 2 percent of the original value if superheats were controlled to the original value. In parallel to the experiments, they used their evaporator model EVAP5 to predict possible savings in evaporator core volume if a smart distributor was used. They found that, in extreme cases, the savings in core volume can be up to 40 percent. Using a combination of experimental and simulation results, it was found that the impact of cross fin conduction is negligible for tests with a low uniform individual circuit exit superheat of 5.6°C (10 F). For tests that had high individual circuit exit superheats of 16.7°C (30 F), the influence of cross fin conduction was found to be significant.

Domanski et al. (2004) developed a model which used an evolutionary algorithm to optimize evaporator circuitry for uniform and nonuniform airflow, termed ISHED. It was found that for a 3 bank evaporator with 12 tubes each, the capacity of the design for uniform airflow operated at uniform airflow was slightly smaller than the one obtained for non-uniform airflow when operating in non-uniform airflow (both approximately 5.25 kW). The capacity of the design obtained for uniform airflow under nonuniform airflow dropped to 4.82 kW.

Domanski and Yashar (2007) used a newer version of ISHED to optimize evaporator and condenser circuitries for different refrigerants. For the evaporator designs, it was found that the ISHED generated design outperformed the best manually generated design for all refrigerants. For the condenser designs, it was found that the ISHED generated design performed equally well or better than the best manually generated design. They furthermore found, that for an A-type evaporator coil, as found in residential AC-systems, the capacity improved by 4.2 percent, if the ISHED optimized circuitry was compared to the original circuitry. For this simulation, the velocity profile was based on particle velocity measurements and CFD simulation. Due to the effects of the condensate pan, it included points with very small air velocities as well as backflow. While not directly connected to evaporators, it should be mentioned that the same issue of flow maldistribution also exists for liquid to air finned tube heat exchangers.

T'Joel (2006) investigated the effects of airflow maldistribution on the performance of a 3 row air-to water finned tube heat exchanger. Using different velocity profiles, he found that the overall heat transfer coefficient dropped by up to 8 percent, if a quadratic velocity profile was applied. De Paepe (2006) mentions the work of Rabas (1987), who numerically studied the performance degradation of condensers, if airside maldistribution was applied by using a relatively simple model for the heat transfer. According to De Paepe (2006), Rabas (1987) found that, even for extremely nonuniform inlet velocity profiles, the main effectiveness degraded by less than 7 percent. Bury (2012) numerically and experimentally investigated water coolers. He found a deterioration factor of about 15 percent if nonuniform airflow was applied in the simulation.

Kim et al. (2008b) introduced the hybrid control scheme for evaporators, suggested possible balancing valves and evaluated possible performance benefits using a numerical model. Kim et al. (2008a) describes the modeling approach and results in a more concise form. The hybrid control scheme uses a primary expansion valve that provides most of the pressure drop and flow balancing valves in each individual circuit to achieve uniform individual circuit exit superheat. They numerically investigated an upstream flow balancing method, where the valves are placed between the distributor and circuit inlet, and a downstream flow balancing method, where the valves are placed at the exit of each circuit. The effects of air flow maldistribution on the COP and capacity were investigated for a 10.55 kW (3 ton) residential R410A heat pump. They verified their model against measurement data for the heat pump without additional airside maldistribution. The model split up the evaporator into one section with 2 passes (C1) and a second section with 3 passes (C2). The flow distribution

factor V_{C1}/V_{C2} was varied while the overall flow rate through the evaporator was held constant. This was done for the cases of (a) no refrigerant side flow control, (b) upstream flow balancing method, and (c) downstream flow balancing method. The simulations were done for 35°C (95 F) ambient temperature and 26.6°C (80 F) indoor temperature under dry coil conditions. They found that the downstream flow balancing method leads to a larger degradation of COP and capacity for air flow distribution factors 0.9 to 0.7. For the upstream flow balancing method, they found that most of the performance degradation caused by uneven airside flow was recovered when individual circuit superheats were balanced. Specifically, for an air distribution factor of 0.6, capacity degraded by about 6 percent and COP by about 4 percent without balancing superheats. If the upstream flow balancing method was applied, most of the losses were recovered. In their paper, they stated that more than 99.9 percent of the losses were recovered; however, from their Figure 8 and 9, which shows the results, about 90 percent of the losses were recovered.

Kim et al. (2009a) explain the model used in Kim et al. (2008a) in greater detail. Kim et al., (2009b) investigates additional cases of maldistribution for the same model as previously described, considering R410A, R134A and R22 as refrigerants. In a parametric study, they found that a reduction of the feeder tube diameter to the circuits of section C1 led to a cooling capacity degradation of 13 percent and a COP degradation of 9 percent. The effective feeder tube diameter can be changed as a result of bends in the feeder tubes. Void fraction in individual circuits can decrease as a result of maldistribution at the distributor. They found that a void fraction increase of section C1 by 5.7 percent from the initial value of 0.8995 to 0.9505 leads to a cooling capacity degradation of 12 percent and a COP degradation of 8 percent. For an air flow maldistribution factor of 0.6, corresponding to a flow distribution factor V_{C1}/V_{C2} of 0.4, they found a cooling capacity degradation of 16 percent and a COP degradation of 11 percent. Additionally they considered combinations of airside and refrigerant maldistribution. They found that for all considered cases, most of the capacity and COP degradation was recovered, if the upstream flow balancing method is applied.

Kaern and Elmgaard (2009) described a simulation model for air conditioning systems, which uses a two-pass evaporator to study the effects of maldistribution. Similar to the model of Kim et al. (2008a-b), it considers feeder line pressure drop and quality maldistribution at the distributor. They found that, a quality distribution factor of $F_x = x_2/x_{in} = 0.1$, incurred a COP degradation of 15 percent. If different feeder line bends were considered by multiplying the pressure drop as calculated for a straight by a factor of 6, the COP degradation was 5 percent. Additionally they considered airside flow velocity distribution using a factor $F_{air} = V_{fr,1}/V_m = 0.1$ and found the COP degradation was 38 percent. If the individual circuit superheats were controlled with applied airside distribution factor of 0.1, the COP degradation decreased from 38 percent to 7 percent. Their overall conclusion was that the conductance (UA) and COP reduction become significant when full evaporation is not reached in one of the circuits.

Kaern et al. (2011a) found that non-uniform airflow distribution leads to a COP reduction of up to 43.2 percent and quality maldistribution in the distributor leads to a COP

reduction of up to 13 percent. Kaern et al. (2011b) confirmed their previous result, that most of the capacity and COP degradation, for a wide range of airside maldistribution, can be recovered if the individual circuit exit superheat is uniform. However, uniform exit superheat did not coincide with the maximum performance recovery, which was obtained at unequal exit superheats. Additionally they found, that a 19 percent increase in evaporator size leads to a similar COP improvement as uniform exit superheat control. Kaern et al. (2011a-b) do not consider fan power in the calculation of capacity and COP, therefore the results with consideration of fan power will look slightly different.

Mader et al. (2010) and Funder-Kristensen et al. (2012) describe an expansion distribution device, which controls the flow to each individual circuit by using a rotating disc. It replaces a conventional expansion valve and distributor. Experimental results for the efficiency improvement of this device compared to EXVs could not be found in open literature. Sales brochures of the manufacturer, however, e.g. Danfoss (2011a) claim a COP improvement of 25 percent for HP mode or 1 SEER point for AC systems. Kaern et al. (2011) describe this valve in more detail and also attempted to simulate the valve within the system. In the simulation study, they found that the valve leads to a degradation of performance if no maldistribution is applied, due to pressure fluctuations. For the face-split evaporator, the performance was found to increase compared to the uncompensated EXV case, if the air distribution factor was larger than or equal to 0.5. The results have to be taken with caution, since the pressure fluctuations were about 3 times larger than the ones obtained from measurements. Furthermore, steady-state heat transfer correlations were considered, which did not consider the unsteady flow patterns generated by the pulsing action of the valve.

The previous publications showed the effects of flow maldistribution and the chances to gain a significant reduction of performance degradation if flow rates to individual circuits are controlled appropriately. However, to save cost it is preferable to design the refrigerant circuitry of the evaporator coil for the initial air side maldistribution while having an accurately working distributor to ensure the intended equal flow distribution. Therefore additional efforts were taken by numerous researchers to improve the distribution characteristics of distributors.

Nakayama et al. (2000) developed a 3-pass distributor for a split system room air conditioner with 5 kW (1.4 ton) cooling capacity. Instead of the orifice used at the inlet to their baseline distributor, a capillary mixing space was used. They found that the distribution characteristics were independent of the capillary mixing space's length if it was larger than 3 times the diameter of the capillary mixing space. The difference between minimum and maximum circuit cooling capacity was reduced to 1/5 of the difference of the original design. As a result, the cooling capacity of the air conditioner increased by 1.2 percent compared to the baseline. Additionally, a smaller dependency of the cooling capacity on the inclination of the distributor axis by 15° away from the perpendicular was noticed; the capacity using the new distributor degraded by 0.4 percent, compared to the 1.5 percent measured with the original design. Unfortunately the authors did not give any indication of measurement uncertainties in their results.

Li et al. (2005) came to the conclusion that, for a 4 branch distributor, depending on the type of refrigerant distributor and considering a misalignment of 3.7° of the flow into the distributor, the flowrate in each branch can change by as much as +22-35 percent. Furthermore, it was found that gravity can influence the distribution if the distributor is aligned horizontally. An alternative design was suggested that is less vulnerable to misalignment of the orifice at the inlet of the distributor. Note that Li et al. (2005) assumed uniform quality across the orifice and uniform exit pressures of the distributor exit ports, which is likely not the case in actual systems - presenting an additional source of refrigerant side maldistribution.

Prior to the current study there were no experimental results available on the effects of flow maldistribution on the performance of the three systems selected for this report.

Chapter 2: Large Room Cooling System

For the large room cooling system, experiments were conducted with a clean-coil and blocked-coil. Additionally, frost build up tests were conducted. This chapter describes the setup, the experiments and their results. An estimate of the achievable yearly energy savings is given, based on a bin calculation method. An estimate of the achievable performance improvement using an improved distributor is given based on simulations.

The large room cooling system consists of a condensing unit with scroll compressor and receiver tank, Figure 8 (a) and an evaporator unit with TXV, Figure 8 (b). The 6 fans of the evaporator unit are equipped with high efficiency electronically commutated motors (ECM).



(a) Condensing Unit



(b) Evaporator Unit

Figure 8: Large Room Cooling System

Figure 9 shows the evaporator, which is the main object of interest in this study. The refrigerant flow is split up into 8 circuits, using a venturi type distributor. These circuits have a slightly different airside area, due to the nonmatching number of bores and tubes. The superheated gas is collected in a header. Between each of the 6 fans, there are separation sheets, so that each fan generates the airflow for a sixth of the coil face on the air outlet side of the coil.

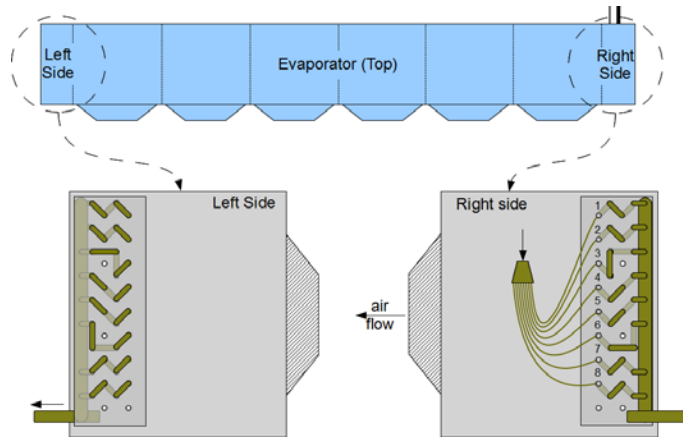


Figure 9: Evaporator Circuitry Schematic

2.1 Controls

The temperature control of the room is achieved with a thermostat that controls the liquid line solenoid valve of the evaporator while the fans run continuously. For the purpose of testing, this thermostat was replaced with a control switch, which was in the on position during the steady-state tests. The condenser fan is switched with the compressor and additionally controlled by a low pressure cut out switch to keep the condensing temperature high enough to prevent damage to the compressor as well as insufficient capacity due to low inlet pressure to the expansion valve. The compressor is equipped with a crankcase heater that is always on. All fans and the compressor are constant speed. The inbuilt expansion device is a TXV with limited maximum operating pressure (MOP).

2.2 Instrumentation

Refrigerant pressure and temperature were measured at the points indicated in Figure 10 to determine the refrigerant states. For the positions indicated in the diagram, immersion thermocouples type Omega TMQSS with an accuracy of 0.5°C were used. Pressures were measured with Setra type 207 gauge pressure transducers with an accuracy of 0.13 percentFS, where 500 PSIG transducers were used on the high pressure side and 250 PSIG transducers were used on the low pressure side of the system. Subcooled refrigerant mass flowrate was measured at the condensing unit outlet with a Coriolis mass flow meter of type Micromotion CMF025 with an accuracy of 0.1 percent of measured flowrate. Compressor power consumption was measured with an Ohio Semitronics, Inc. three-phase two element watt meter type PC5-062-C with an accuracy of 0.04 kW. Evaporator fan power consumption was measured with an Exceltronic XLC5A2-8-1 watt meter with an accuracy of 0.3 percent for the measured fan power. Condenser fan voltage and current were measured once with an Extech EX505 multimeter with a base accuracy of 0.5 percent. A power factor of 0.7 ± 0.1 was assumed for the calculation of the real fan power.

Figure 11 (a) shows the airside and refrigerant side measurements of the evaporator unit. Air inlet and outlet temperature is measured at six positions with T-type thermocouples, where each position is the middle of the area that is covered by a specific fan. Inlet temperature is

measured at the middle of each position, while outlet temperature is measured at the upper quarter of the fan guard. Air inlet humidity is measured with a General Eastern dew point monitor model D2 with an accuracy of 0.2°C. As a backup, the relative humidity at the inlet is also measured with a Vaisala HMP233 relative humidity sensor with an accuracy of 1 percentRH. Refrigerant temperature is measured at the inlet and outlet of the unit with T-type immersion thermocouples, together with the refrigerant pressure. The temperatures of the individual circuits are measured at inlet, outlet and return-bends with surface mount T-type thermocouples. The thermocouples are wound around the pipe to reduce stem conduction, and the measurement tip is glued in close contact with the pipe using thermally conductive epoxy type Omegabond 101. The pipe is then insulated with 3/8 inch insulation with a conductivity of 0.27 Btu/(hr·ft·F) to reduce measurement error due to heat transfer with the surrounding air. The temperature of the equalization line of the TXV is measured in the same way. This measurement is reallocated for the Hybrid control approach to measure the saturation temperature after the first expansion process. The return-bend measurements are used to conclude whether or not the refrigerant in a specific circuit and position is superheated or not. Since the return-bends are made of copper, they conduct heat from the fins along their length. This leads to heat transfer from the return-bend to the refrigerant. Therefore tube surface might be above saturation temperature at the measurement position while the core of the flow still entrains (some) liquid particles. Therefore the conclusion on the state within the tubes, based on the surface measurements, has to be interpreted with some caution.

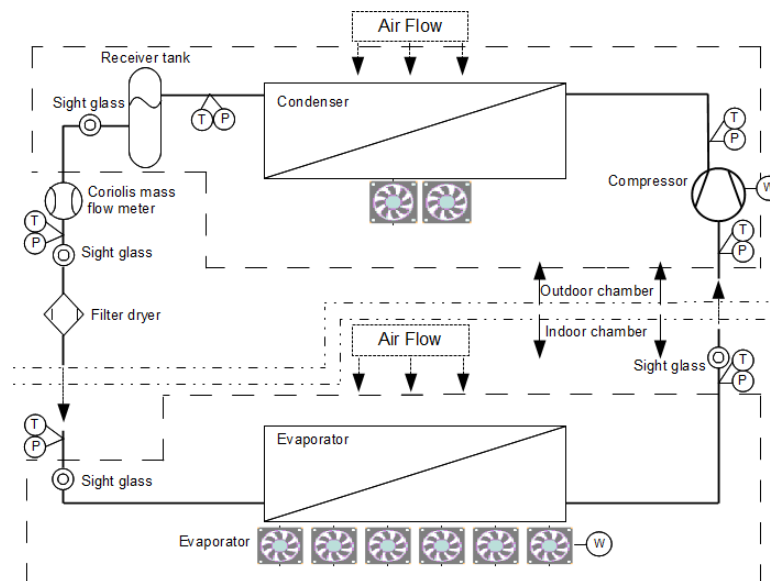


Figure 10: Instrumentation Overview LRCS

Figure 11 (b) shows the air- and refrigerant side measurements of the condensing unit. Air temperature is measured at the inlet and outlet of the condenser. At the inlet, an equally

spaced 2 by 2 grid is used. At the exit, the sensors are mounted at the fan guard, two for each of the fans.

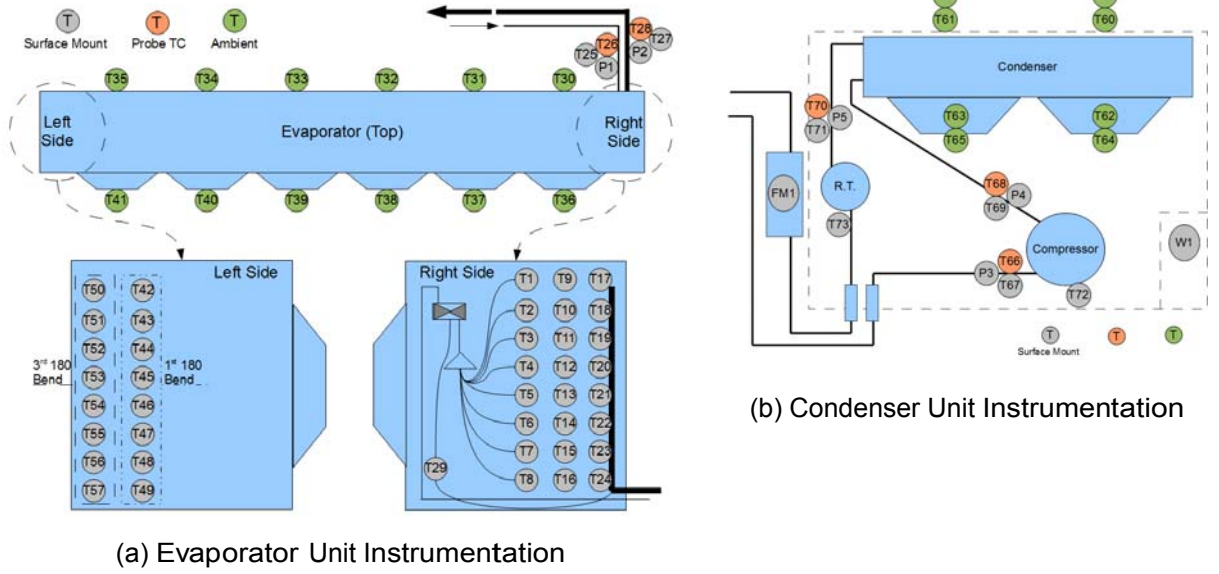


Figure 11: Large Room Cooling System Instrumentation

2.3 Performance Indices

Performance indices represent cooling capacity and efficiency. The following performance indices are used: Refrigerant side cooling capacity q_{ref} is calculated as

$$q_{ref} = \dot{m}_{ref} \cdot (h_{evap,out} - h_{evap,in}), \quad (1)$$

where \dot{m}_{ref} is the average refrigerant mass flowrate in kg/s and $h_{evap,out}$ and $h_{evap,in}$ are the average enthalpy of refrigerant leaving and entering the evaporator unit in kJ/kg. The cooling capacity q_{ss} is calculated as

$$q_{ss} = q_{ref} - W_{e-fans} - W_{slnd}, \quad (2)$$

where W_{e-fans} is the average evaporator fan power consumption in kW and W_{slnd} is the liquid line solenoid power consumption in kW. The applicable standard, AHRI 1251 (AHR, 2009) specifies that the total power consumption of the unit has to be included in the calculation of the coefficient of performance (COP). For the LRCS, the COP is therefore defined as

$$COP = \frac{q_{ss}}{W_{comp} + W_{e-fans} + W_{slnd} + W_{ccht}}, \quad (3)$$

where W_{c-fans} is the condenser fan power consumption in kW and W_{ccht} is the crankcase heater power consumption in kW. The power consumption of the expansion valves were not included since their power consumption is not representative of the very low power consumption that would be expected for optimized devices. For the cyclic and frost-up tests, it is not appropriate to use average values for cooling capacity, compressor and fan power consumption due to different runtimes (cyclic) and largely changing system efficiency (both). In this case the capacity is calculated as

$$q_{cyc} = \frac{\sum_{\tau_{on}} \left[m_{ref} \cdot (h_{evap,out} - h_{evap,in}) - W_{slnd} \right] \cdot \Delta \tau - \sum_{\tau_{tot}} W_{e-fan} \cdot \Delta \tau}{\tau_{on}}, \quad (4)$$

where τ_{on} is the time where the liquid line solenoid valve is switched on, τ_{tot} is the total duration of the cyclic test and $\Delta \tau$ is the time step between individual data points. The COP is calculated as

$$COP = \frac{q_{cyc} \cdot \tau_{on}}{\sum_{\tau_{tot}} (W_{e-fan} + W_{ccht}) \cdot \Delta \tau + \sum_{\tau_{on}} (W_{c-fan} + W_{comp} + W_{slnd}) \cdot \Delta \tau}. \quad (5)$$

For all tests, a constant value was used for the condenser fan, the crankcase heater and the liquid line solenoid. These values were measured without the entire system running.

2.4 TXV Control Scheme

The original TXV control scheme uses a valve with external pressure compensation. The superheat of the valve was adjusted to give about ± 2 K of hunting at 22°C ambient temperature, as shown in Figure 12. For higher ambient temperature, e.g. 35°C, the hunting is barely noticeable due to changed system behavior. For this temperature, the TXV also shows excellent stability for cyclic operation. In contrast to that, with a frosted up coil, the TXV begins to hunt extremely. In the frosting test the superheat hunts between 1 and 11.5 K after 4.3 hours of operation. The reason for this is the changed system response in conjunction with the constant control behavior of the TXV that did not adapt to it. This incapability of the TXV to adjust to different conditions leads to a higher superheat than necessary for high ambient temperatures. Ideally, one should adjust the valve for different operating conditions or use two different expansion valves that have an optimized superheat setting for the main operating ranges. Due to the additional labor and/or material cost, neither of these options is usually employed; the TXV is therefore run with a constant superheat setting.

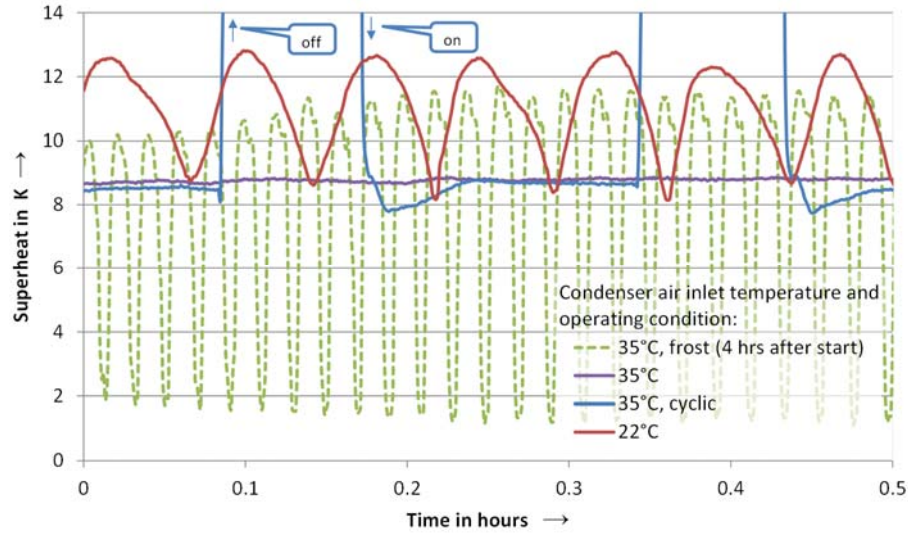


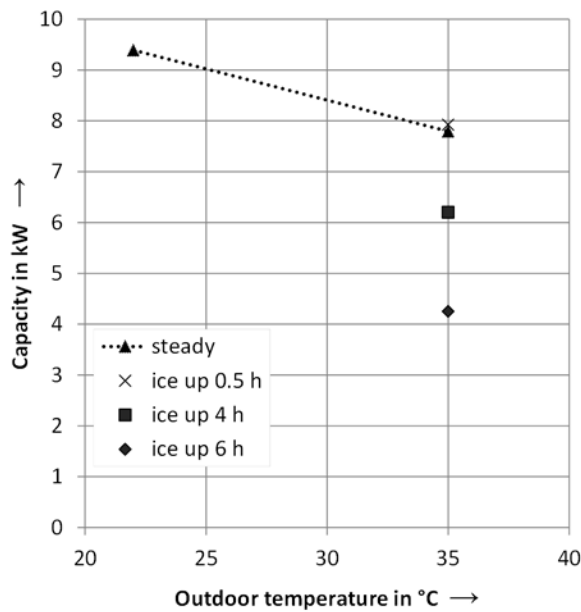
Figure 12: Evaporator Exit Superheat as Measured for Different Operating Conditions, TXV

2.4.1 Steady State Tests

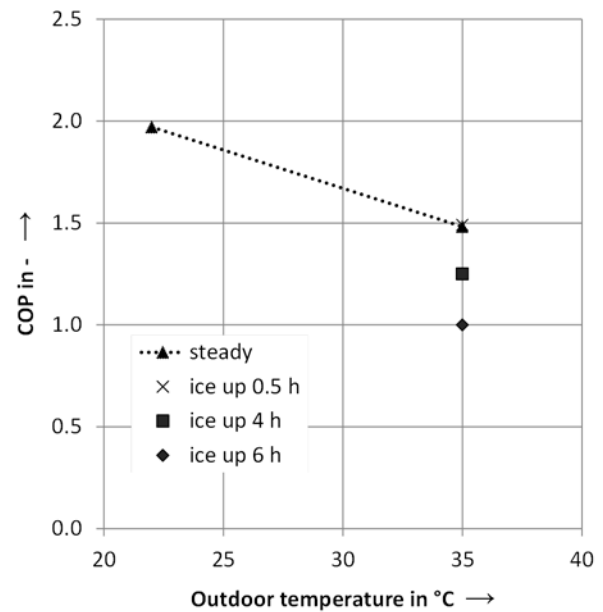
For the steady-state tests, the room conditions were held constant. The system was run until there was no trend noticeable in any of the measured variables, including the calculated COP. From that point on, at least 30 minutes of data were taken to be used for the calculation of the performance values. Figure 13 shows that COP and capacity decrease with increasing ambient temperature for the steady-state tests. At 22°C ambient temperature, capacity and COP are 9.4 kW and 2.0, decreasing to 7.8 kW and 1.5 for 35°C condenser air inlet temperature. Figure 14 shows the measured return-bend temperatures, a significant amount of maldistribution is noticeable: For 22°C condenser air inlet temperature, the point where the refrigerant starts to appear superheated varies between after the first return-bend and after the third return-bend, depending on the circuit. This documents the non-optimum use of the refrigerant side surface area of the evaporator. Furthermore, by comparing the graphs for 22°C and 35°C condenser air inlet temperature it should be obvious that the distribution of the refrigerant is highly dependent upon operating conditions. Circuit 7, for example, gets very well supplied with refrigerant in the 35°C case: It starts superheating after the 3rd return-bend, which means about 75 usage of the refrigerant side area for evaporation. In the 22°C case, however, it starts superheating after the 1st return-bend, which, based on the shape of the curve means only about 30 percent usage of its refrigerant side area for evaporation.

Possible causes for this maldistribution were identified after opening the lid on the connection side of the evaporator, Figure 15. The flow leaving the TXV may have a very non-uniform distribution of refrigerant quality. Since the connection between the TXV and the distributor is very short and not straight, there is not enough length for the quality maldistributed flow exiting the TXV to fully develop and additional maldistribution can be caused by the non-straight connection of the distributor. This quality maldistribution leads to different mass flowrates at the exiting distributor tubes. The distributor tubes themselves are bent in different shapes, which can lead to different pressure drops.

However, different feeder tube pressure drop as a sole factor can already lead to maldistribution as shown by Kaern (2009).

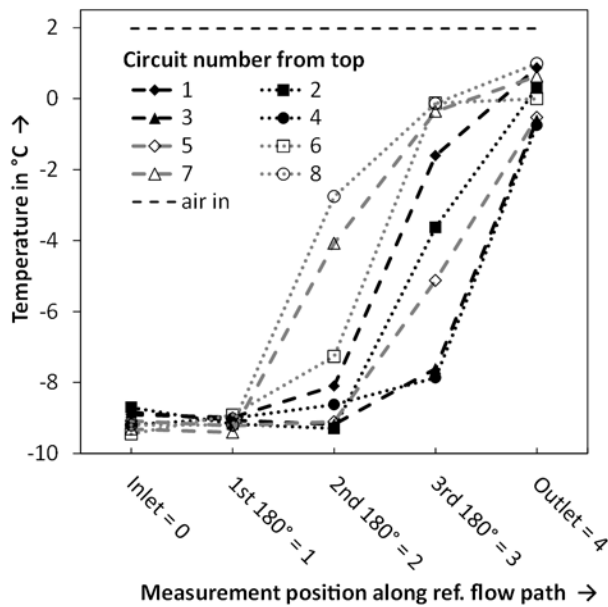


(a) Cooling Capacity

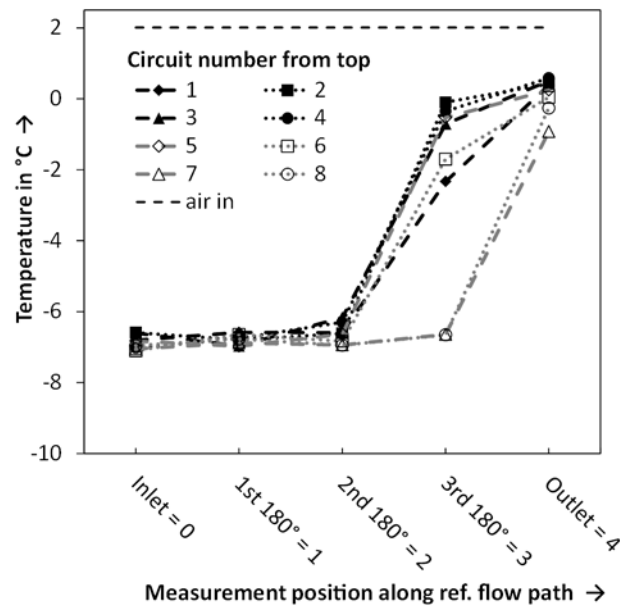


(b) Coefficient of Performance (COP)

Figure 13: Cooling Capacity and COP for Different Operating Conditions



(a) 22°C Condenser Air Inlet Temperature



(b) 35°C Condenser Air Inlet Temperature

Figure 14: Measured Return-Bend Temperatures for Steady State TXV-Tests

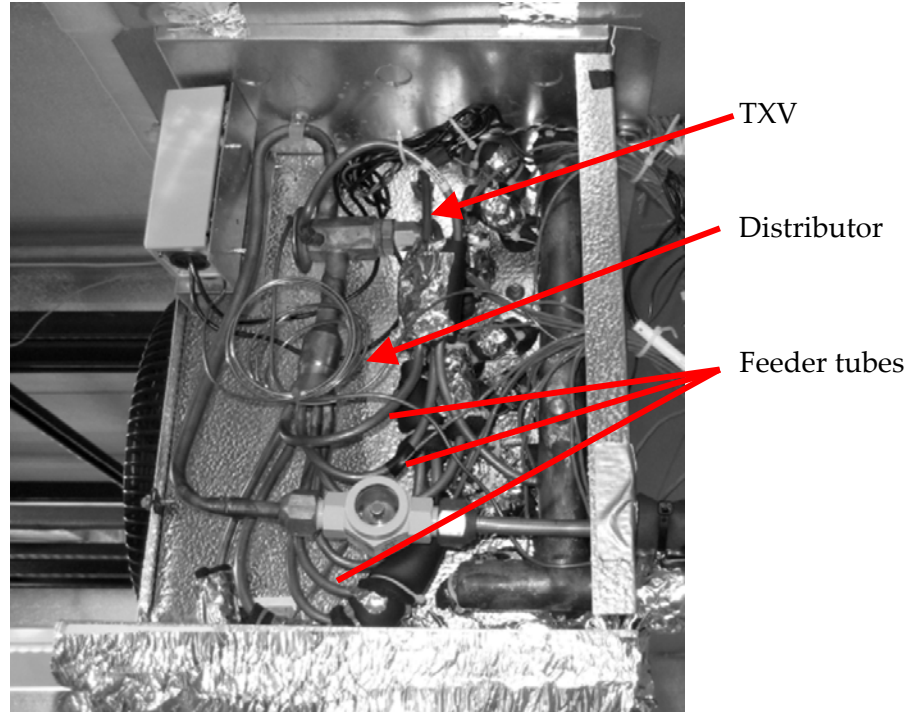


Figure 15: Evaporator Coil, Connection Side with TXV

2.4.2 Cyclic Test

For the cyclic test at 35°C ambient temperature, the refrigerant solenoid, compressor, and evaporator fan were on for 10 minutes and then off for 5 minutes, to determine the cyclic behavior of the unit. This procedure was repeated until the pattern of COP and Capacity between different cycles did not change significantly. Figure 17 shows that, at the beginning of each on-cycle, the superheat was about 25 percent smaller than the steady-state superheat. As a result, the superheat is slightly lower at the beginning of each cycle, as previously shown in Figure 12 on page 20. It was found that the compressor COP and capacity during each on cycle are 1 and 3 percent higher than for the corresponding steady-state test. The reason for this is mainly the dynamic behavior of the system: The condensing coil cools down during the off cycle, while the evaporator coil is heated up to within 2 K of the room temperature. Figure 12 shows that as a result, during the first 30-50 percent of each duty cycle, the condensing temperature is lower than for the steady-state case while it is not exceeded significantly during the rest of the duty cycle. Additionally the evaporating temperature is higher during the very first part of the duty cycle where the condensing temperature is lower. After that it is only slightly lower than for the steady-state case. This results in a better compressor COP if the power consumption of the indoor and outdoor fan is not taken into consideration. However, the evaporator fans are always running with the manufacturers control scheme. As a result, the actual system COP is 5 percent lower than for the steady-state case when considering both the on, and off cycles. Closer examination of the results revealed that the cyclic tests do not represent the operating conditions in terms of air inlet temperature to the evaporator and condenser very well. Figure 17 (a) shows that once the compressor and condenser fan are

switched off², the measured air inlet temperature drifts towards the refrigerant dew temperature. The room temperature sensor experiences a similar trend, and as a result, reduces the reheat for the air handling unit supplying the psychrometric rooms. This results in a lower room temperature, which becomes visible as a sudden drop of air inlet temperature once the compressor and with it the condenser fan are switched on again. Figure 17 (b) shows that, for the evaporator, the fluctuations are smaller. The reason for this is that the evaporator fans run continuously. Therefore the cooling capacity of the LRCS is the driving factor for the air inlet temperature fluctuations on the evaporator side. Due to the fluctuations of the air inlet temperature on both the evaporator side and condenser side, the calculated change in COP should not be taken as a measure for part load degradation. Therefore the results were not indicated in Figure 13.

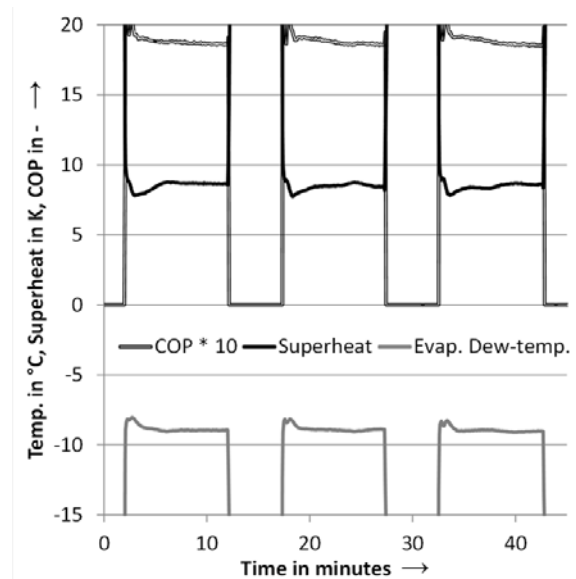
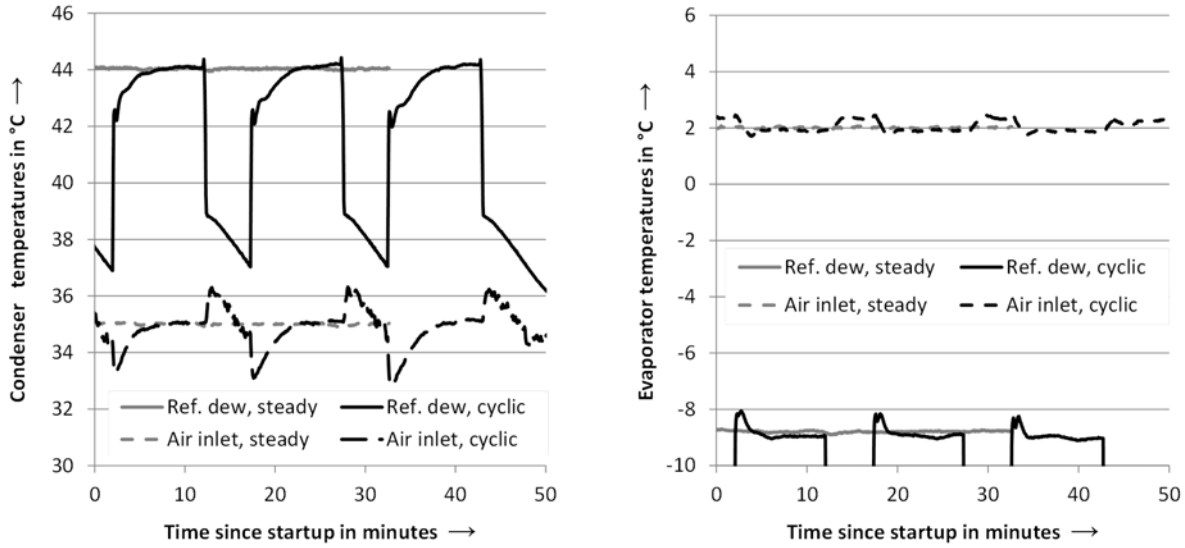


Figure 16: COP, Superheat and Evaporation Dew Point During Cyclic Tests

² This is visible in a sudden drop of refrigerant dew temperature.



(a) Condenser Temperatures

(b) Evaporator Temperatures

Figure 17: Comparison of Operating Dynamics of Cyclic and Steady State Tests

2.4.3 Frost-Up Tests

For the frost-up test, the air inlet temperature and average relative humidity to the evaporator were 2°C and 79 percent RH, respectively. The air inlet temperature to the condenser was 35°C. A defrost of the cooling coil of the psychrometric rooms was necessary during the testing. Figure 18 shows that this leads to an increase of the room temperature by about 1 K between 3 and 4 hours after the start. Figure 18 also shows that superheat and evaporation temperature remain very steady until approximately 2.5 hrs after the start of the experiment. After that, the frost reached a sufficient thickness to noticeably decrease the heat transfer - the evaporation temperature starts dropping, the system behavior changes and the expansion valve starts hunting while keeping a constant average superheat value.

Figure 19 shows the first superheated position for selected individual circuits based on a threshold of 1.5 K. This threshold means that for each measurement, and each circuit, the downstream temperature was compared with the upstream temperature and if the difference was larger than 1.5 K, the refrigerant in the tube was considered superheated. The first superheated position is set to 5, if the threshold is not reached at the end of the circuit. Up to about 4.2 hrs after the start of the experiment, there are only occasional changes of the start of superheat for some circuits. This means that it might be possible to control the distribution with a fixed setting, e.g. by pinching the distribution lines for tuning. Unfortunately this works only for applications that have constant indoor and outdoor temperatures (e.g., compare Figure 19(a) to Figure 14(b) for circuit 7). Furthermore, uneven frost build-up, as shown in Figure 20 leads to increased air side maldistribution. This is very visible in the change of the stability of the superheat at about 4.2 hrs after startup, Figure 18. Figure 19 shows that additionally, the first superheated positions change more rapidly and with higher amplitude. Some circuits are periodically already superheated at the 1st return-bend (e.g. circuit 2 at about 4.2 hrs, Figure

19(b)), while towards the end of the experiment, circuit 8 does periodically not superheat at all. Furthermore the span of where the first superheated position occurs during one hunting cycle of the valve increases, e.g. as shown in Figure 19(b) for circuit 6 at the end of the experiment it ranges from the 1st return-bend to the circuit exit, position 4.

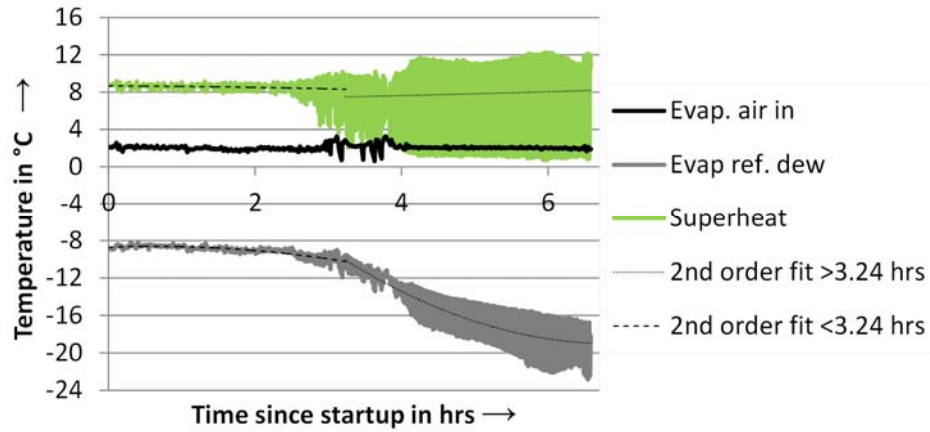
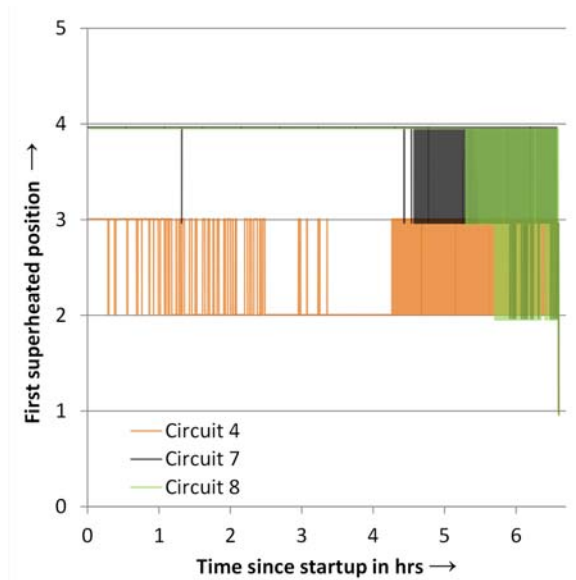
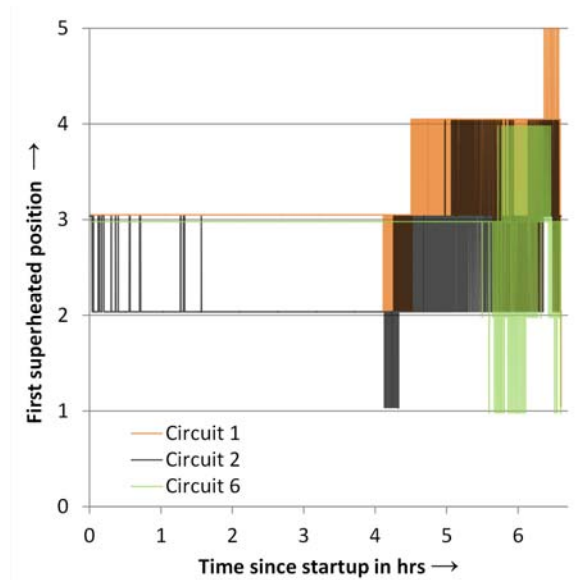


Figure 18: Temperatures During Frost-Up Tests



(a) Circuits 4, 7, and 8



(b) Circuits 1, 2, and 6

Figure 19: Individual Circuit Surface Usage Based on 1.5 K Threshold, TXV



(a) Side View

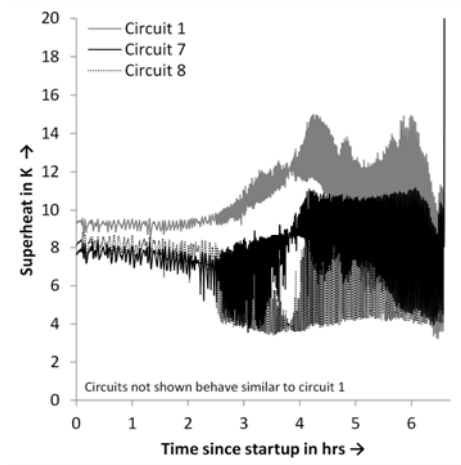


(b) Frontal View

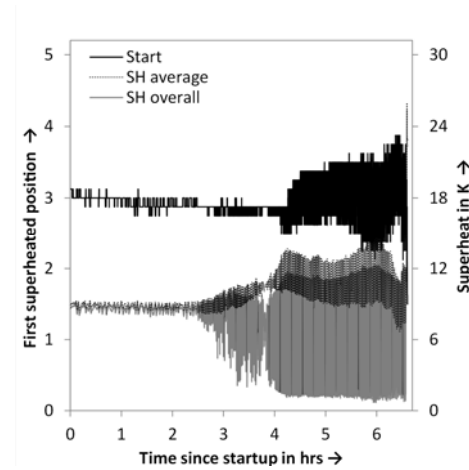
Figure 20: TXV Frost Build-Up, 2.7 hrs after Start of Experiment

The main reason for the unstable behavior of the TXV is that some of the individual circuits start feeding liquid into the exit header. This can be seen in Figure 21(b) by comparing the average of the individual circuit exit superheat (average superheat) and the measured overall exit superheat. While both superheats are the same within the measurement error until about 2.5 hrs after startup, they increasingly differ due to liquid exiting some circuits after that point in time.

Figure 22 shows COP and capacity as a function of time. Capacity and COP behave in a similar fashion as the evaporation temperature in Figure 18. The reduction of COP from start to end is about 30 percent, while the reduction in capacity is 39 percent. While a reduced COP means increased energy consumption, reduced capacity might mean that the system will not be able to maintain the required room temperature under full load and near full load conditions. Under part load conditions, the solenoid and compressor will be switched off by the thermostat for a long enough time fraction to allow for sufficient air defrost of the coil. If the heat and humidity load increases due to high ambient temperature and/or storage of fresh goods the time fraction will not be sufficient for a full defrost and partial defrost occurs. This will, at some point lead to excessive frost-build up on portions of the coil, resulting in even larger deviations of the first superheated position due to much higher differences in the heat transfer to individual circuits. To overcome this, the system has to be oversized, which leads to higher initial and operating costs.



(a) Individual Circuit Superheat of Circuits 1, 7, and 8



(b) Average Individual Circuit Superheat, Overall Superheat, and First Superheated Position

Figure 21: . Individual and Overall Superheat, Average Surface Usage Based on 1.5 K Threshold, TXV

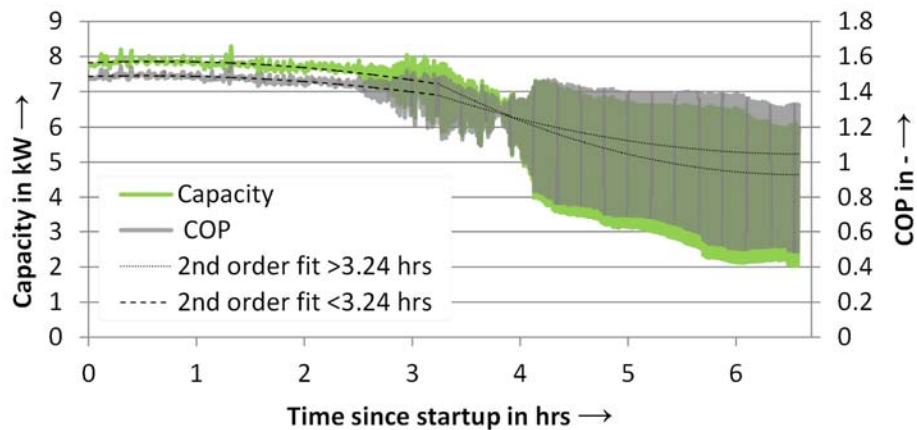


Figure 22: COP and Capacity During Frost-Up Test, TXV

2.4.4 Conclusions for TXV Test Results

For practical applications, the superheat of thermostatic expansion valves can be adjusted only once. The chosen superheat value has to be sufficiently high to ensure stable operation even for operating conditions with significant frost build-up and/or low ambient temperatures. This leads to reduced capacity and COP when compared to electronically controlled solutions, which can adapt to different operating conditions. The fraction of each of the coils circuits that is used for evaporation of refrigerant, and in this study estimated based on return temperatures, depends upon operating condition and frost build-up of the coil. Therefore a simple pinching of the distributor lines will not lead to improved performance of the coil for applications where there are changing ambient temperatures or frost build up. Furthermore, to reduce the risk of insufficient capacity due to uneven frost build-up, a system with a TXV controlled evaporator has to be sufficiently oversized, which results in higher capital and operating cost.

2.5 EXV Control Scheme

Figure 23 shows the two parallel stepper motor expansion valves of the EXV control scheme. The two valves were controlled to the same opening degree to reduce possible refrigerant quality maldistribution at the inlet to the distributor. The opening degree of the valves was controlled with a PI control based on evaporation temperature. The set point and parameters of this PI control were adjusted during the test to account for changes in system behavior. The two reasons why the evaporation temperature rather than the superheat was chosen as the controlled variable are

1. evaporator exit superheat behaves nonlinear with respect to coil surface usage, and
2. evaporator exit superheat fluctuates significantly when it is brought to low levels and small amounts of liquid exit some of the circuits.

A combined control based on observed superheat and evaporation temperature therefore leads to better results. This reflects what an advanced and adaptive expansion valve controller will do. The two valves were controlled to have the same opening to avoid maldistribution caused by uneven quality distribution at the inlet to the distributor.



Figure 23: Primary Expansion Valves with (Right) and without Coil (Left) and Junction before Distributor

2.5.1 Steady State Tests, System Behavior

Steady-state tests were conducted at ambient temperatures 2, 12, 22, 35, and 46°C. Figure 24 shows the evaporation temperature and superheat for the test with 2°C condenser air inlet temperature. The low pressure cut-out switch of the condenser caused cyclic behavior of the system. As a result, the superheat fluctuates in a range of approximately 10 K, while the evaporation temperature fluctuates within a range of about 5 K. It was found, that a faster control of the evaporation temperature leads to periodic flashing at the inlet to the

expansion valve, as shown in Figure 25. This flashing limited the accuracy of the control, since it significantly affected the available valve capacity.

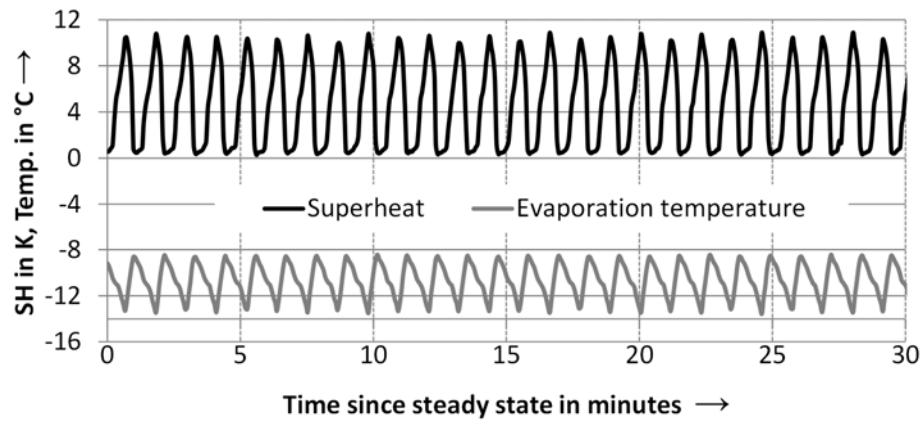


Figure 24: Evaporation Temperature and Evaporator Superheat, Condenser Air Inlet Temperature 2°C, EXV



(a) Subcooled Conditions



(b) Insufficient Subcooling: Flashing

Figure 25: Sight Glass Before Expansion Valve for Sufficient and Insufficient Subcooling

Figure 26 to Figure 29 show that the superheat for the tests with 12, 22, and 35°C ambient temperature was close to 4 K with a similar amount of fluctuation. For the test at 12°C ambient temperature, a higher amount of high frequency noise is noticeable in the superheat signal. Figure 29 shows that the superheat was very stable for the highest tested ambient temperature of 46°C. This made it possible to run a very low superheat of less than 2°C. Such a low superheat might not be possible to achieve in field installations due to limited measurement inaccuracy: A manual check at the sight glass was done to ensure that superheated refrigerant left the evaporator. In the first 15 minutes a barely noticeable amount of mist was noticed in the sight glass and carefully fine-tuning the evaporation temperature (not noticeable in the graph and performance) led to an entirely clear sight glass.

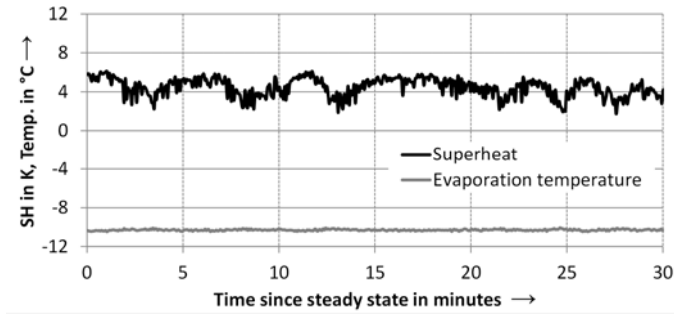


Figure 26: Evaporation Temperature and Evaporator Superheat, Condenser Air Inlet Temperature 12°C, EXV

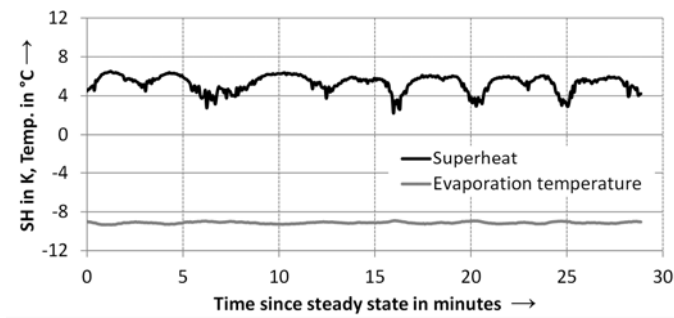


Figure 27: Evaporation Temperature and Evaporator Superheat, Condenser Air Inlet Temperature 22°C, EXV

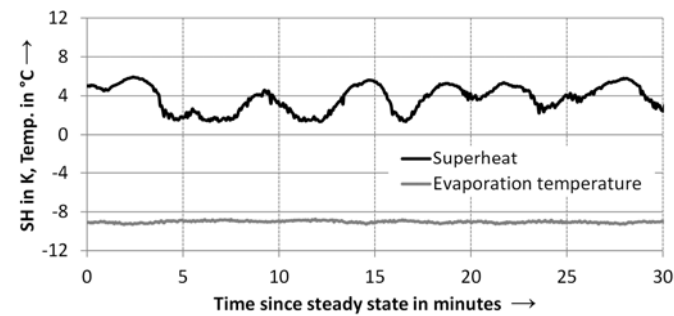


Figure 28: Evaporation Temperature and Evaporator Superheat, Condenser Air Inlet Temperature 35°C, EXV

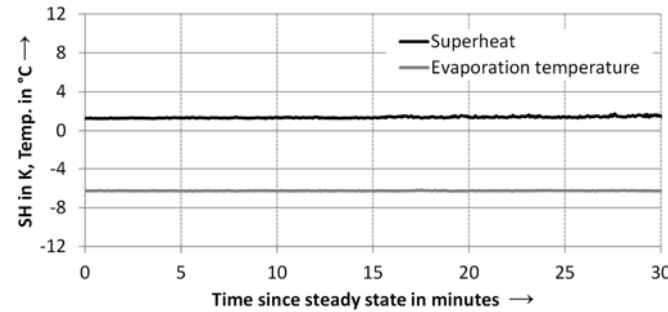
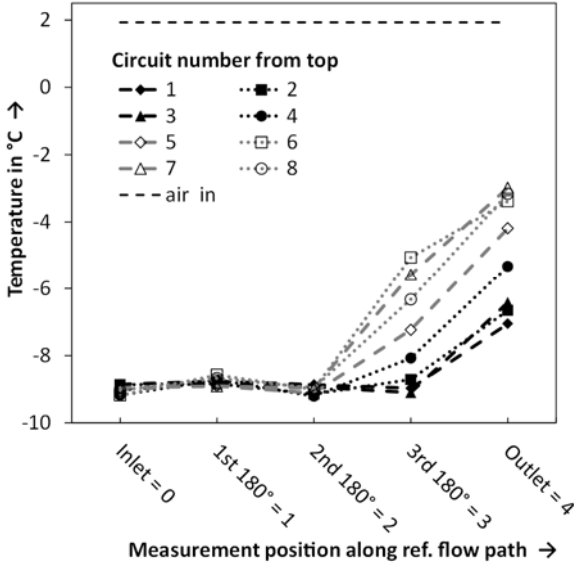
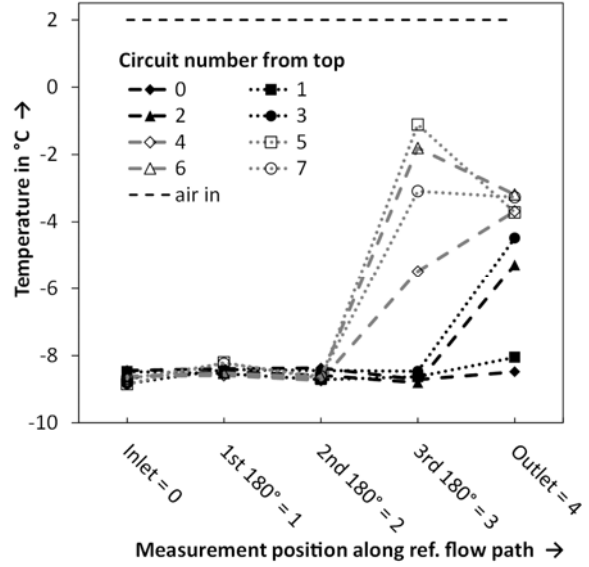


Figure 29: Evaporation Temperature and Evaporator Superheat, Condenser Air Inlet Temperature 46°C, EXV

Figure 30 to Figure 32 show the return-bend temperatures for the steady-state tests with an EXV as the expansion device, conducted at different condenser air inlet temperatures. The shown maldistribution is different than the one observed in the TXV controlled system shown in Figure 14. This is caused by different quality distribution within the tube leading to the refrigerant distributor, slight changes in the bend radii of the distributor tubes and a higher mass flowrate for the same operating conditions. Overall, a better usage of the refrigerant side surface area for evaporation can be noted for the EXV controlled system, resulting in a higher evaporation temperature. In contrast to the TXV controlled system, the maldistribution between the circuits is not a strong function of the condenser air inlet temperature. The order of the return-bend temperatures remains very similar across all tested condenser air inlet temperatures. An increase in condenser air inlet temperature leads to a reduction of cooling capacity. From Figure 30 to Figure 32 it is therefore visible that the evaporation temperature increases with the condenser air inlet temperature. Figure 30(a) shows that for the test with a condenser air inlet temperature of 2°C, the temperature profile for the superheated part of the circuits is linear and does not follow the typical exponential behavior of the superheated section of cross counter flow heat exchangers. This is a result of the previously described hunting caused by the low pressure cut-out switch of the condenser fan. For some tests, the superheat at the exit is apparently lower than at the preceding return-bend, which is a result of conduction from the exit header to the measurement position on the tubes. In the case of the EXV, the top tube feeds liquid through, leading to a “cold” header.

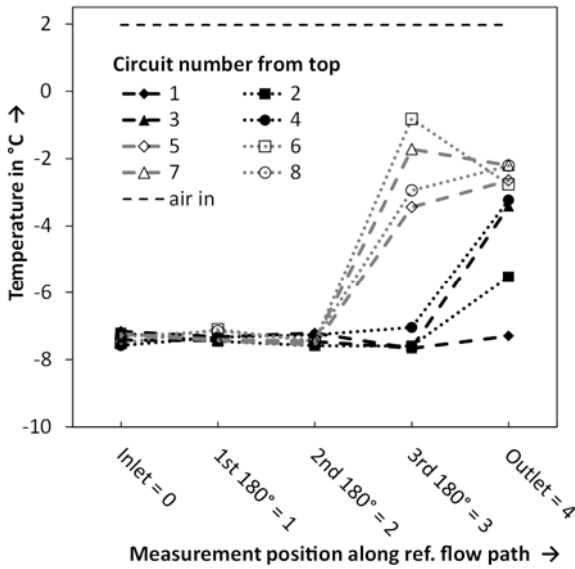


(a) 2°C Condenser Air Inlet Temperature

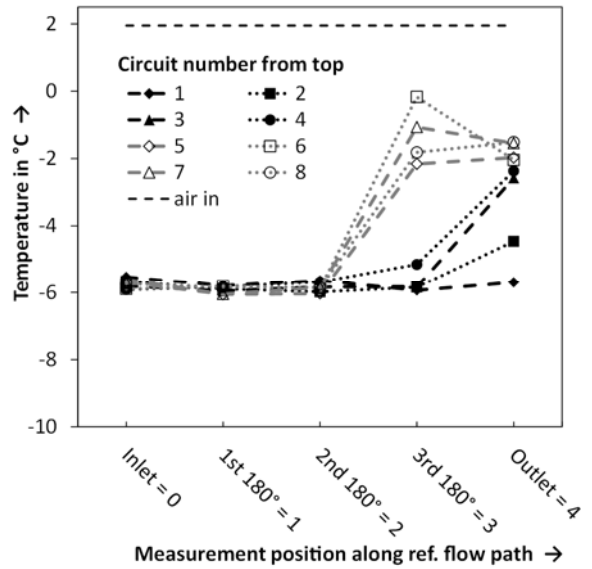


(b) 12°C Condenser Air Inlet Temperature

Figure 30: Measured Return-Bend Temperatures for Steady EXV-Tests At 2°C And 12°C Condenser Air Inlet Temperature, EXV



(a) 22°C Condenser Air Inlet Temperature



(b) 35°C Condenser Air Inlet Temperature

Figure 31: Measured Return-Bend Temperatures for Steady EXV-Tests at 22°C and 35°C Condenser Air Inlet Temperature, EXV

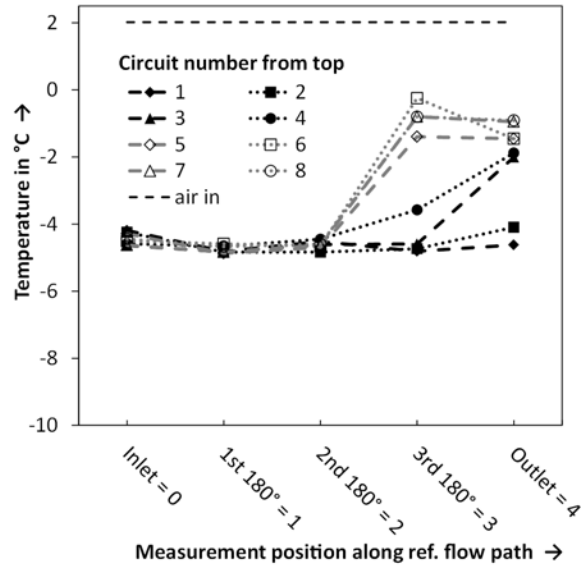


**Figure 32: Measured Return-Bend
Temperatures for Steady EXV-Tests At 46°C
Condenser Air Inlet Temperature, EXV**

2.5.2 Steady State Tests, Performance

Figure 33 shows that COP and capacity decrease linearly with increasing ambient temperature for ambient temperatures larger than 12°C. The measurement at 2°C does not fit this trend: there is a smaller increase in COP while the capacity still increases with a similar trend. The reason for this is that the condenser fan started to cycle for 2°C condenser air inlet temperature as shown in Figure 24, which sets a limit to how far the condensing pressure can be reduced for low condenser air inlet temperatures. For the tests at or above 12°C, as temperature is increased, the relative decrease of the COP is steeper than the downwards slope of the capacity.

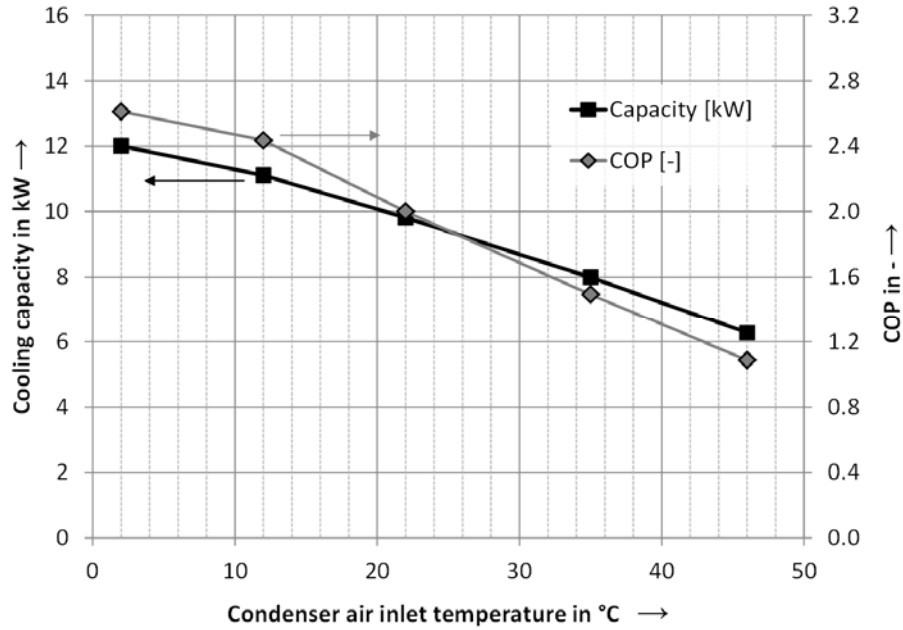


Figure 33: Cooling Capacity and COP for Different Operating Conditions, EXV Control Scheme

2.5.3 Cyclic Test

For the cyclic tests, the same test conditions and cycle duration as for the TXV tests were chosen. It was found that a simple PI control, which is optimized for steady-state operation, does not work very well for the startup of the system. Therefore the expansion valve opening was controlled manually during these tests, which allows for a larger initial valve opening. Figure 34 shows results that demonstrate that an increasingly better (manual) control adaptation during the test led to the lowest possible superheat while protecting the compressor from liquid refrigerant. As can be seen, the first 2 cycles were not very well controlled, while from the 3rd cycle on we were much closer to the optimum. The differences in COP were relatively small; therefore all 10 cycles were used for the determination of the COP. The obtained COP and capacity were within the measurement uncertainty, similar to the steady-state tests. During the cooling period, the COP was slightly higher than for the steady-state case. The reason for this is mainly that, during the off period, the temperature of the condensing coil gets closer to the surrounding temperature which more than compensates for the transient losses, Figure 35(a). While the performance results suggested that there is no significant penalty for cyclic operation, Figure 35(a) also reveals that this is a result of the temperature control of the air inlet temperature by the psychrometric rooms. Figure 35(a) shows that the air inlet temperature of the condenser drops significantly during the off-cycle, which leads to a smaller air-inlet temperature at the beginning of each on-cycle. This in turn leads to a better COP of the compressor and system. Figure 35(b) shows that the air inlet temperature of the evaporator drops slightly at the start of each on-cycle. The COP and capacity results should not be used to get to the conclusion that there is no part load degradation, since both the evaporator air inlet as

well as the condenser air inlet temperature are not constant during the duration of the test and furthermore deviate significantly from their target values.

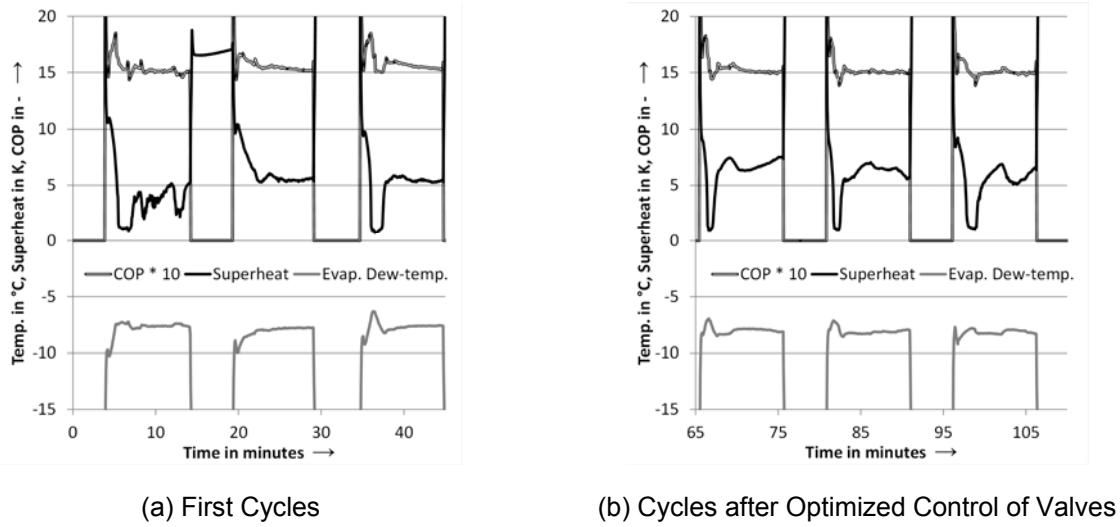


Figure 34: COP, Superheat and Evaporation Dew Point During Cyclic Tests, EXV

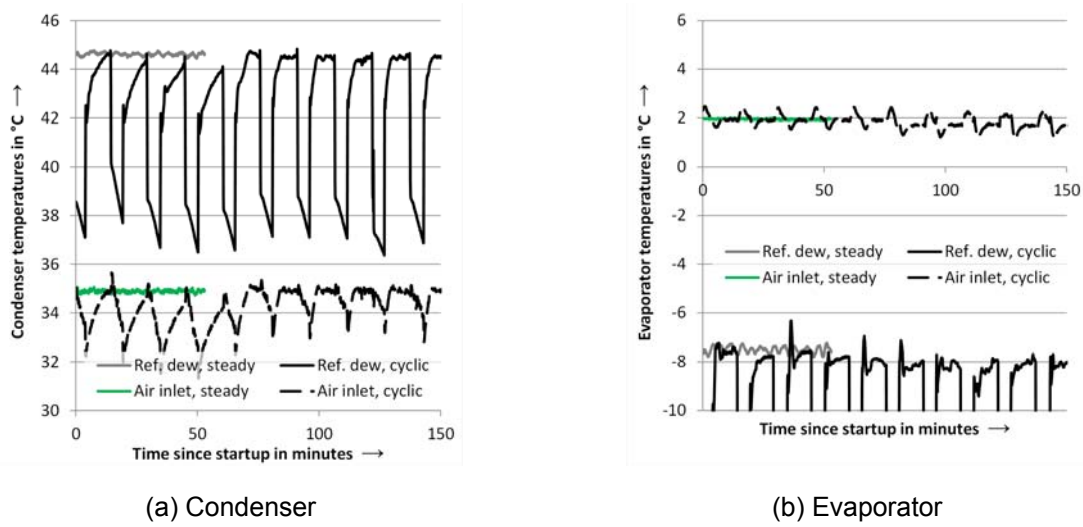


Figure 35: Air Inlet Temperature and Refrigerant Exit Dew Point Temperature, EXV

2.5.4 Frost-Up Test

For the frost-up test, the indoor room was kept at high humidity (average of 78 percent RH) and 2°C while the outdoor room was kept at 35°C. During the testing, the cooling coil of the psychrometric room had to be defrosted, which led to an increase of the room temperature between 5 and 6 hrs and 10 and 11 hrs after the start of the experiment. This increase was on average less than 1 K during those periods, as shown in Figure 36. Figure 36 shows that superheat and evaporation temperature remained very steady until about 5.5 hrs after the start of the experiment. After that, the frost reached a sufficient thickness to noticeably decrease the heat transfer - the evaporation temperature had to be decreased to maintain a sufficient

superheat. At about 8 hrs after startup, the noise in the superheat signal increased. Figure 37(a) shows that, at about 5.5 hrs after the start of the experiments, the superheats of the individual circuits started deviating from each other. Figure 37(b) shows that this also gets visible in the surface usage for the circuits shown in the previous figure. Figure 38 shows that the average circuit surface usage decreased after about 5.5 hrs after the start of the experiment as a result of the increasing maldistribution between the individual circuits. This is also visible in the increasing difference between average superheat (based on the individual circuit exit superheats) and overall superheat (based on insertion measurement at the exit of the evaporator unit). This difference increased after 5.5 hrs from the start of the experiment, which indicates an increased amount of liquid overfeed. Figure 39 shows COP and capacity for the frost-up test. At about 5.5 hrs after start up, capacity and superheat decreased approximately linearly with time. Before that, only a very shallow decrease in COP and capacity is noticeable.

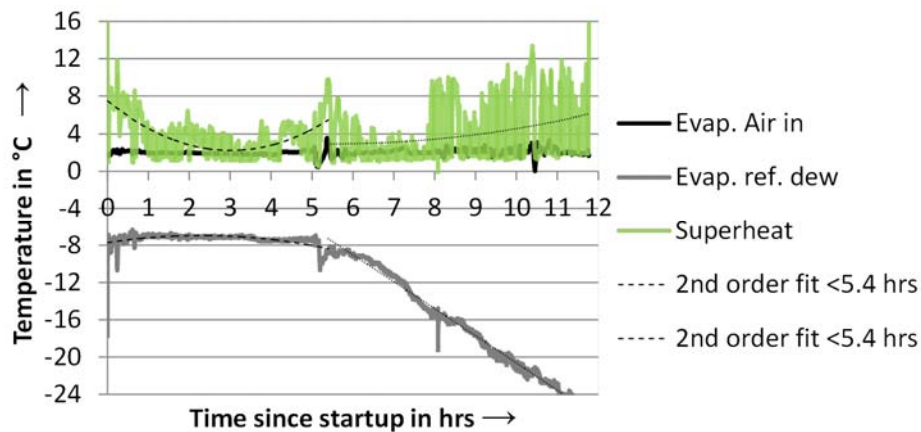
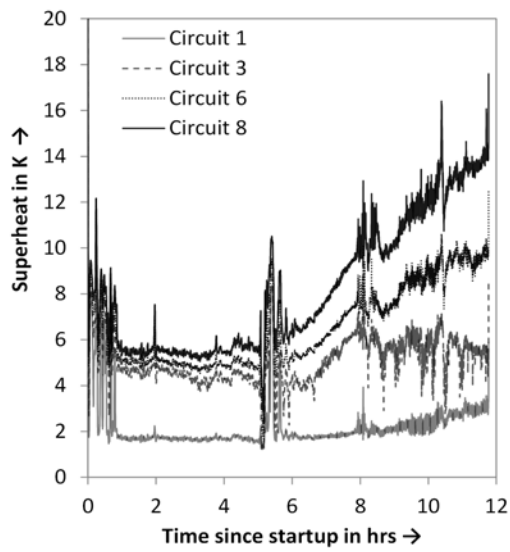
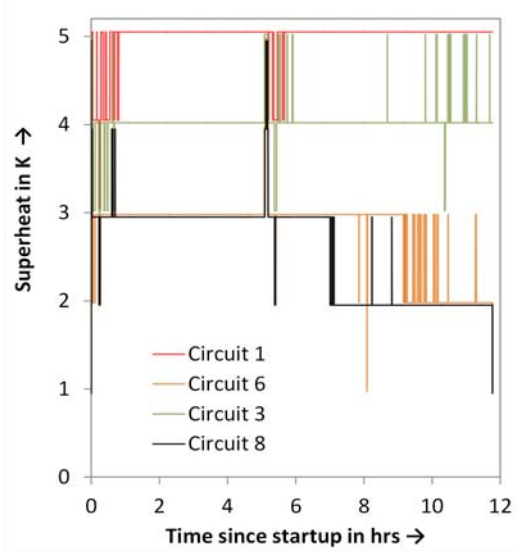


Figure 36: Air Inlet Temperature, Superheat and Evaporation Temperature During Frost-Up Test, EXV



(a) Individual Circuit Exit Superhea



(b) Individual Circuit Surface Usage Based on 1.5 K Threshold for Selected Circuits

Figure 37: Superheat and Surface Usage, EXV

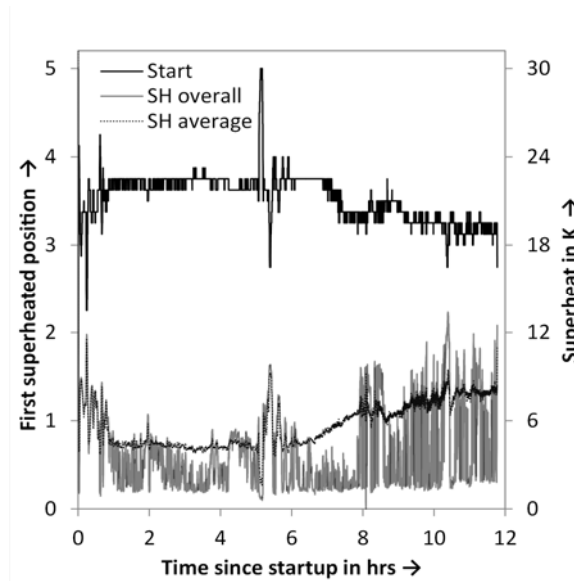


Figure 38: Average Individual Circuit Superheat, Overall Superheat, and First Superheated Position, EXV

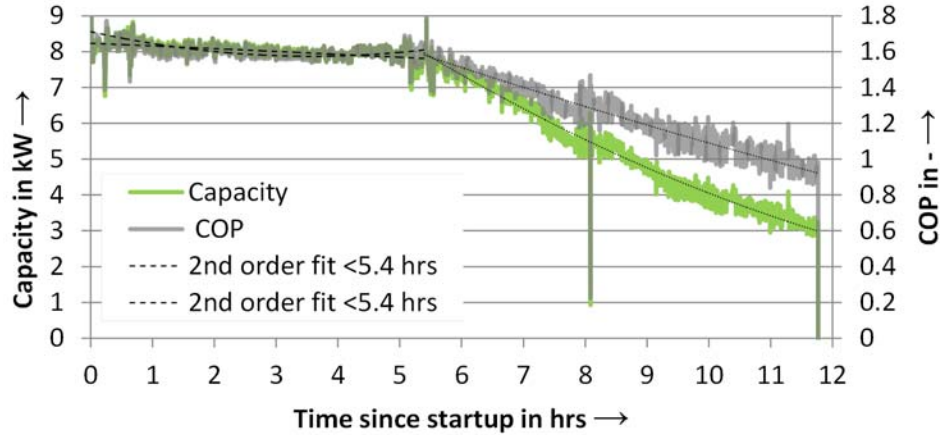


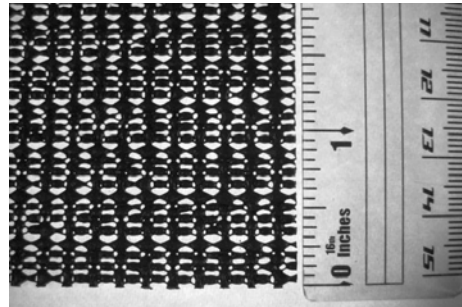
Figure 39: COP and Capacity During Frost-Up Test, EXV

2.5.5 Tests with Different Levels of Coil Blockage

To get more repeatable results than with frost build-up, the inlet to the coil was blocked, Figure 40(a). To block the coil, thin plastic foil was used to simulate severe frosting while porous material, Figure 40(b) was used to simulate very light frosting. Additionally the material was applied in two layers, 90° rotated to achieve a higher pressure drop. If combinations of different materials were used, then the material with higher pressure drop was put on top of the coil to simulate uneven frost build-up. The condenser air inlet temperature for the tests was 35°C (95 F).



(a) Evaporator Coil, Blocked 2/3 from Top

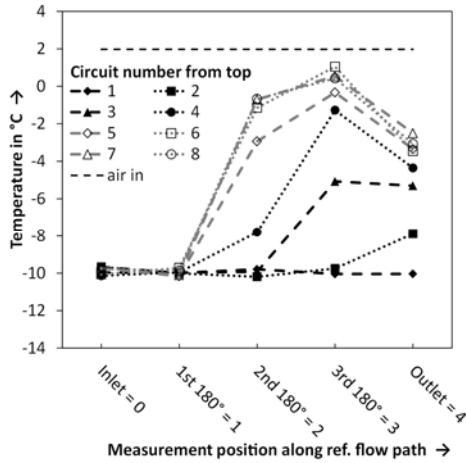


(b) Porous Material for Blockage of Coil

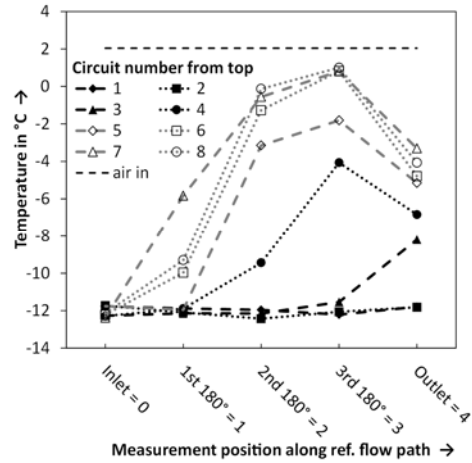
Figure 40: Blockage of Coil, EXV

Figure 41(a) shows the return-bend temperatures for the 1/3 blockage top, 1/3 double porous blockage at the center. Compared to the clean-coil results, Figure 31(b), the points where the bottom and center circuits start to superheat moved towards the refrigerant inlet. This is a result of the reduction of the air flowrate at the top of the evaporator coil, which led to liquid feed-over in circuit 1, which in turn required a significant reduction of evaporation temperature to maintain overall superheat. Figure 41(b) shows that for the case where 2/3 of the coil was blocked with plastic, the bottom circuits started superheating even earlier while circuits 1 and 2 had liquid at their exit. The overall refrigerant side surface usage of the evaporator was

therefore reduced from clean-coil to 2/3 blocked-coil test. Additionally it is visible from the inlet refrigerant temperatures of the 3 aforementioned figures, that increasing airside maldistribution leads to a reduction of the evaporation temperature. As a result it is to be expected that COP and capacity are reduced.



(a) Blockage from Top: 1/3 Plastic,
1/3 Double Layer Porous



(b) Blockage from Top: 2/3 Plastic

Figure 41: Return-Bend Temperatures with Blockage to Coil, EXV

Figure 42 shows the degrading influence of different coil blockage on COP and Capacity. If only porous material is used for the blockage, the COP and capacity drop only slightly. The reason for this is that a) the coil pressure drop is much larger than the pressure drop over the porous material and b) the coil is deep enough, so that the air can flow around the blockage. The large coil depth is the reason that the system, even with 2/3 of the face area of the evaporator completely blocked still performs better than in the frost-up test after 8 hrs. The test with 2/3 blockage was repeated, since minor frost build up on the coil was noticed. This frost build up actually led to a performance improvement. The 1/3 completely blocked case with an additional 1/3 blocked by the porous material leads to similar performance degradation as the frost-up test after 6.5 hrs. The case A and case B blockage which are 2/3 and 1/3 blocked - 1/3 porous blockage respectively were chosen as test cases for the other temperatures and the hybrid control scheme.

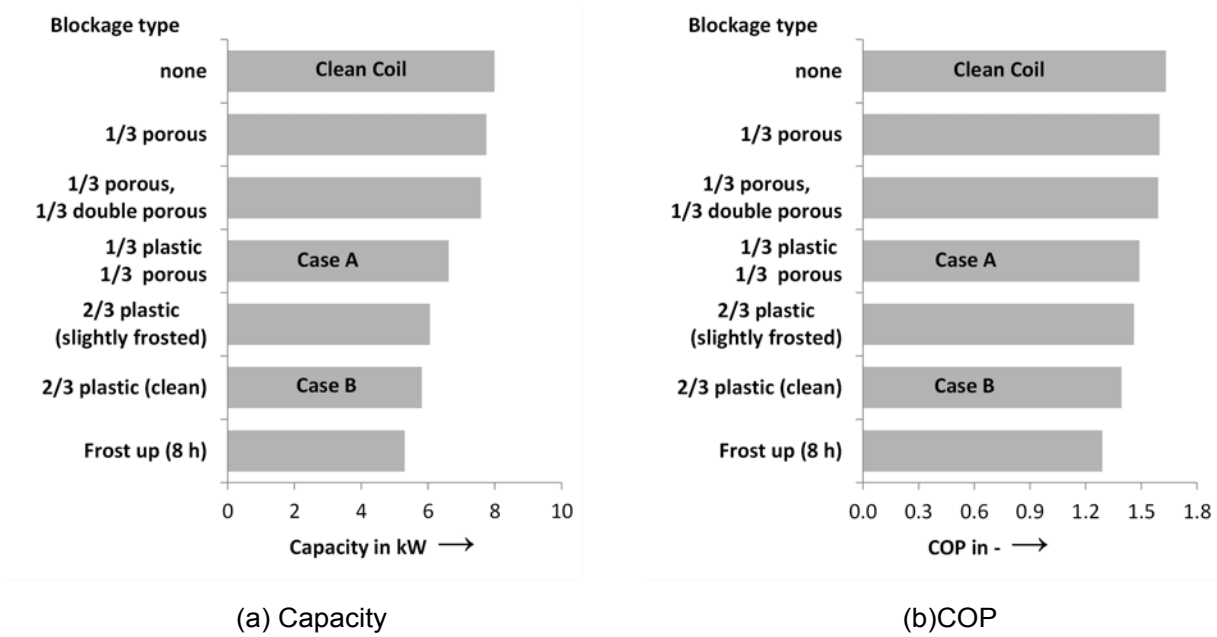


Figure 42: System Performance Indices with Different Levels of Airside Maldistribution, EXV

Figure 43 shows the COP and Capacity of the unit for unblocked and blocked cases. In both there is a trend that the performance degradation due to coil blockage becomes less for increasing ambient temperature. This is caused by a smaller system capacity, which reduces the evaporator air inlet temperature differences for both blocked and unblocked cases. Figure 44 shows COP and capacity change compared to the unblocked base case. COP degrades by a maximum of 15 percent for 1/3 blockage and by a maximum of 29 percent for 2/3 of the coil being blocked. Capacity degrades by a maximum of 19 percent for 1/3 blockage and by a maximum of 31 percent for 2/3 of the coil being blocked.

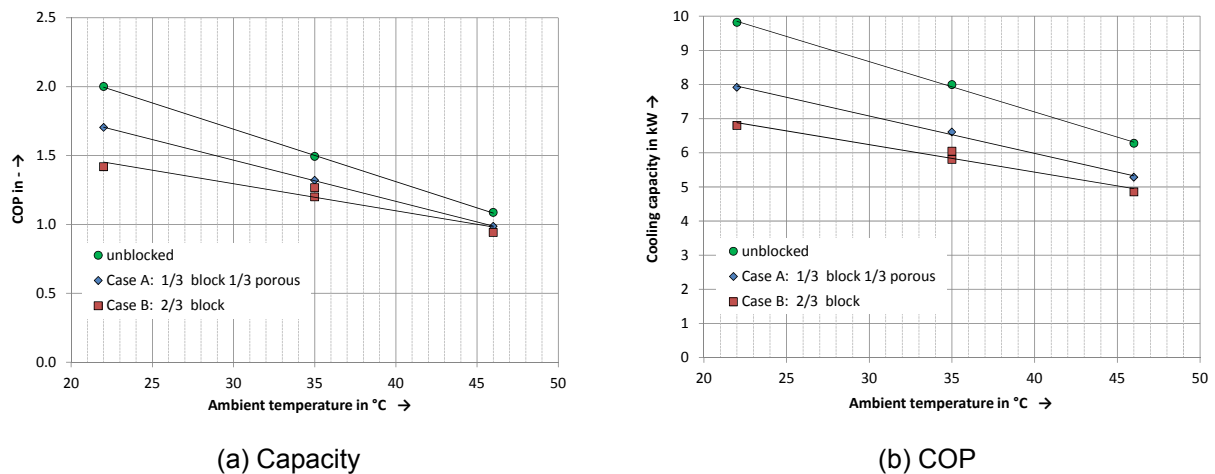


Figure 43: System Performance Indices with Different Levels of Airside Maldistribution, EXV

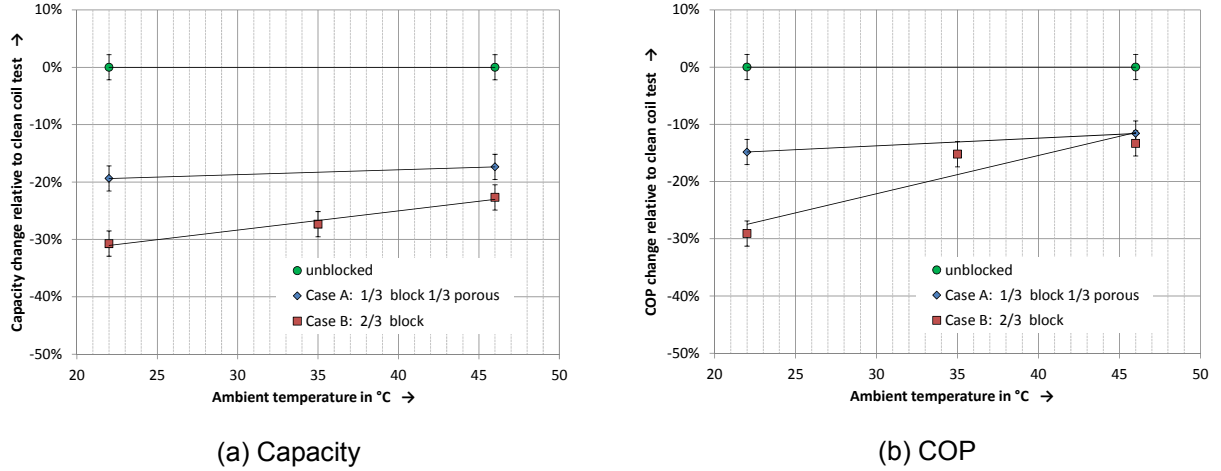


Figure 44: System Performance Indices Change with Different Levels of Airside Maldistribution, EXV

2.5.6 Conclusions, EXV

With an EXV as expansion device, a better control of the superheat than with the TXV and therefore a better usage of the evaporator surface area is possible for steady-state and frost-up tests. For all tests, it was found that for the smallest possible superheat, some circuits have some liquid at their exit. This limits the minimum superheat, since other circuits have to be superheated even more to compensate for this. For low ambient temperatures, e.g. 2°C, the condenser fans start cycling. This leads to a higher required superheat due to flashing in the liquid line. For the frost-up test, the superheat had to be increased towards the end of the experiment due to increasingly unstable behavior. For blocked-coil tests, which were introduced to produce repeatable results for airside maldistribution, it was found that the performance decreases with increasing airside maldistribution, and that this degradation of performance decreases for increasing condenser air inlet temperature.

2.6 Hybrid Control Scheme

For the hybrid control scheme, 8 conventional EXVs were inserted as balancing valves into the distributor lines as shown in Figure 45(a) and (b). The balancing valves were controlled by 4 additional controllers of the same type as used for the primary expansion valves. The opening of the balancing valves and the opening of the primary valves were controlled manually, to achieve uniform individual circuit exit temperatures. The approach was to keep the largest opening among the balancing valves at 450-500 out of 500 steps and adjust the primary valve to achieve the right superheat for that specific circuit. The openings of the other balancing valves were controlled to obtain uniform superheats and were a result of the required mass flow rate and refrigerant quality maldistribution at the distributor.

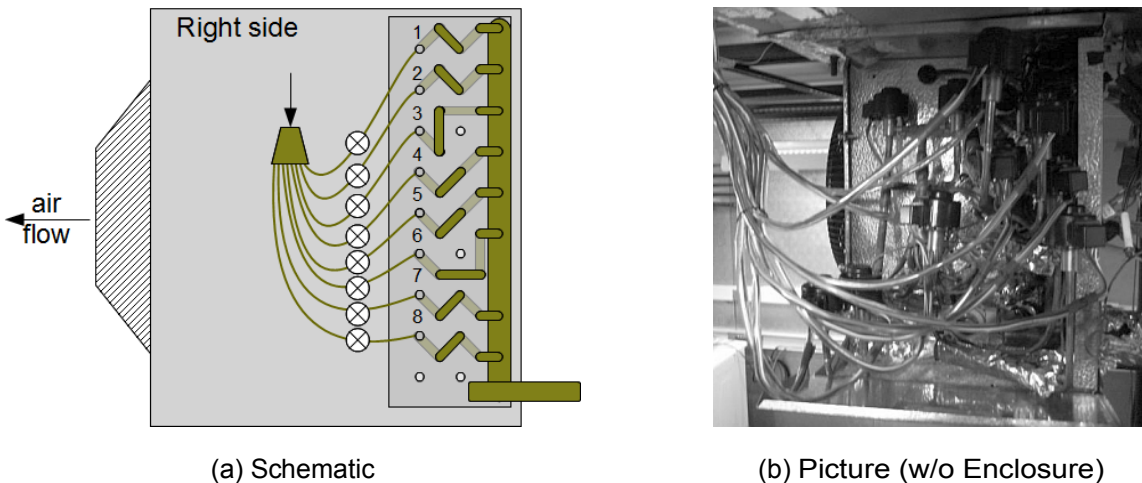
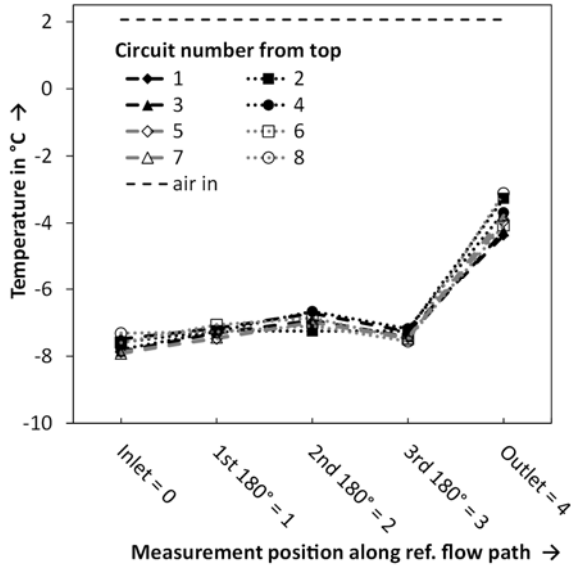


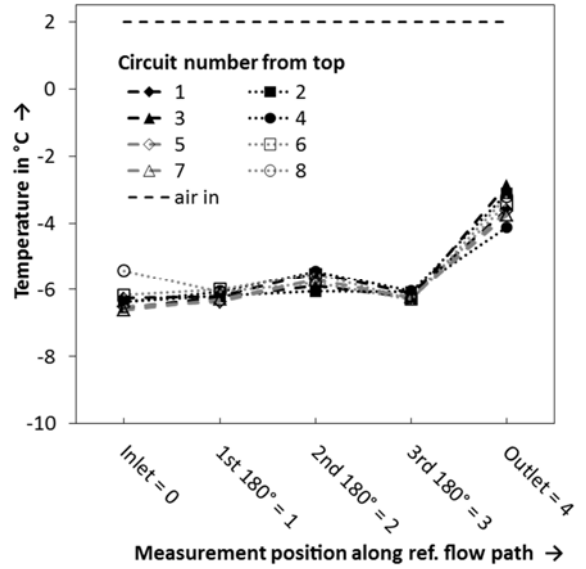
Figure 45: Hybrid Control Scheme, Evaporator

2.6.1 Steady State Tests, System Behavior

With the balancing valves in place, the superheats in each circuit can be controlled individually. The individual circuit exit superheats were within a 1.5 K band, for all tests with the hybrid control scheme, as can be seen from the outlet temperatures shown in Figure 46 and Figure 47. The return-bend temperatures indicate that only the tube between third return-bend and outlet is used for superheating refrigerant. The inlet temperature of the eighth circuit is above the inlet temperature for the other circuits for the tests with a condenser air inlet temperature of 22°C, 35°C, and 46°C. The temperature of the inlet was measured midway between the balancing valve and evaporator coil. The higher temperature of the inlet to circuit 8 therefore indicates quality maldistribution at the distributor: a larger quality at the outlet of the distributor branch leads to a larger velocity in that specific distribution line which leads to pressure drop. If the inlet quality is smaller, as applicable for lower condenser air inlet temperature as shown in Figure 46(a) or if the primary valve is fully open as shown in Figure 48, the pressure drop in the tube section between the distributor and balancing valve is much smaller for all circuits. Therefore the measured circuit inlet temperatures are more uniform. In general, the evaporation temperature, which is approximately the average value of the return-bend temperatures increases as the condenser air inlet temperature increases.

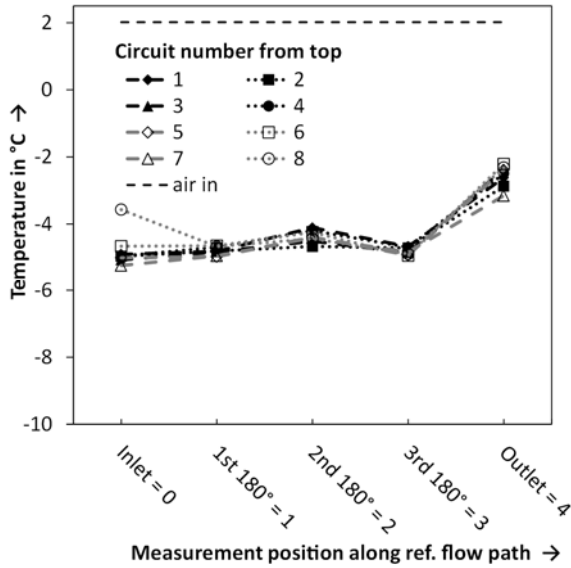


(a) Condenser Air Inlet Temperature 12°C

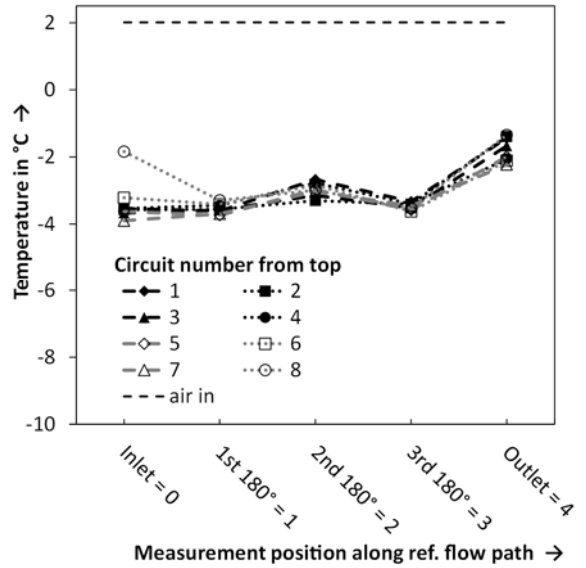


(b) Condenser Air Inlet Temperature 12°C

Figure 46: Measured Return-Bend Temperatures for Steady Hybrid-Tests at 12°C and 22°C Condenser Air Inlet Temperature, Hybrid



(a) Condenser Air Inlet Temperature 35°C



(a) Condenser Air Inlet Temperature 46°C

Figure 47: Measured Return-Bend Temperatures for Steady Hybrid-Tests at 35°C and 46°C Condenser Air Inlet Temperature, Hybrid

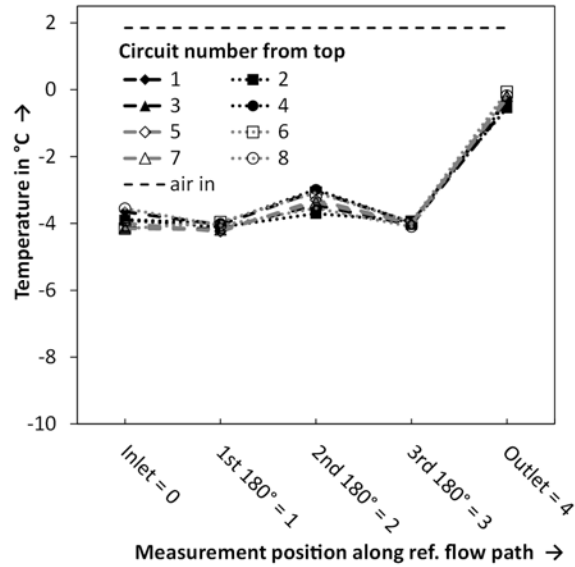


Figure 48: Measured Return-Bend Temperatures for Steady Hybrid-Test with Primary Valve Fully Open at 46°C Condenser Air Inlet Temperature, Hybrid

The hybrid control scheme leads to a better distribution of liquid refrigerant amongst the circuits which leads to a reduction of the occurrence as well as the amount of liquid exiting the individual circuits. As a result of this, the high frequency noise in the superheat signal is reduced. This reduction is most significant for the 12°C test, Figure 49, for the hybrid control scheme as compared to Figure 26 for the EXV control scheme. The reduced occurrence as well as the amount of liquid exiting the individual circuits led to a reduction of the band in which the superheat fluctuated for the hybrid control tests with 12°C, 22°C, 35°C (Figure 49 to Figure 51) as compared to the corresponding EXV (Figure 26 to Figure 28). The superheat for the 46°C ambient case, Figure 52, is smooth but has higher fluctuations than the corresponding EXV-case, Figure 52. The reason for this is mainly that, in the EXV-case, a PI-control was used to stabilize the evaporation temperature, while in the hybrid case, the valve opening was controlled manually - fluctuations in outdoor room temperature therefore lead to fluctuating evaporating temperature and as a result to fluctuating superheat.

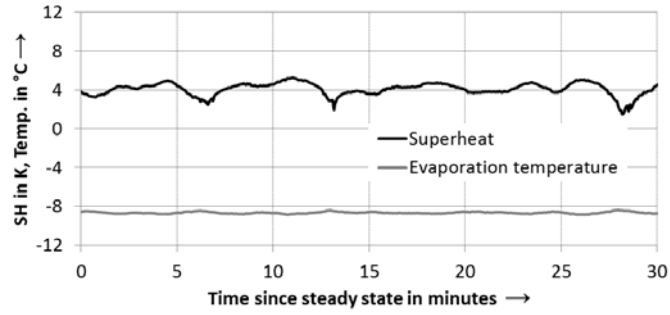


Figure 49: Evaporation Temperature and Evaporator Superheat, Condenser Air Inlet Temperature 12°C, Hybrid

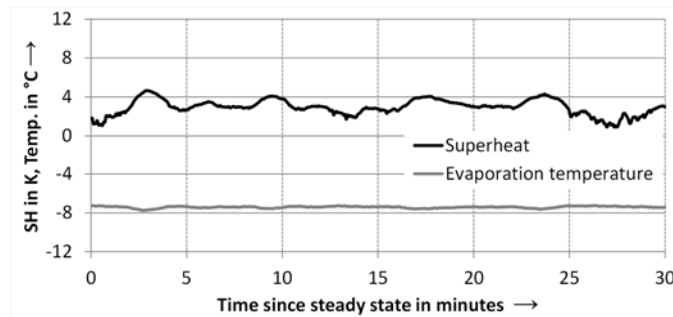


Figure 50: Evaporation Temperature and Evaporator Superheat, Condenser Air Inlet Temperature 22°C, Hybrid

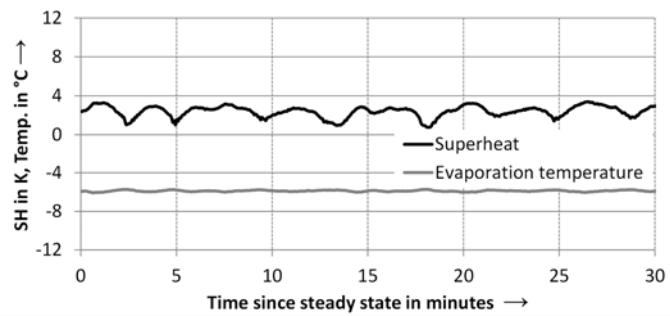


Figure 51: Evaporation Temperature and Evaporator Superheat, Condenser Air Inlet Temperature 35°C, Hybrid

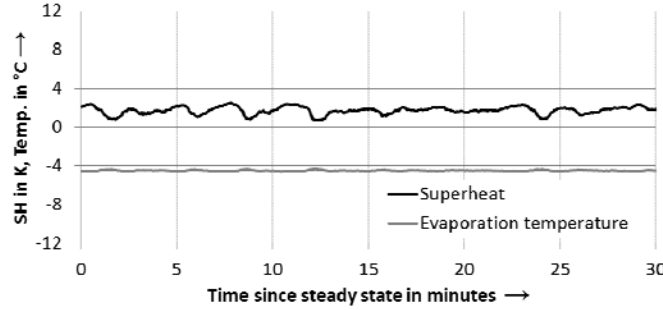


Figure 52: Evaporation Temperature and Evaporator Superheat, Condenser Air Inlet Temperature 46°C, Hybrid

2.6.2 Steady State Tests, Performance

Figure 53 shows that system COP and capacity decrease approximately linearly with increasing condenser air inlet temperature. The relative decrease of the COP with increasing ambient temperature is larger than the relative decrease of the capacity.

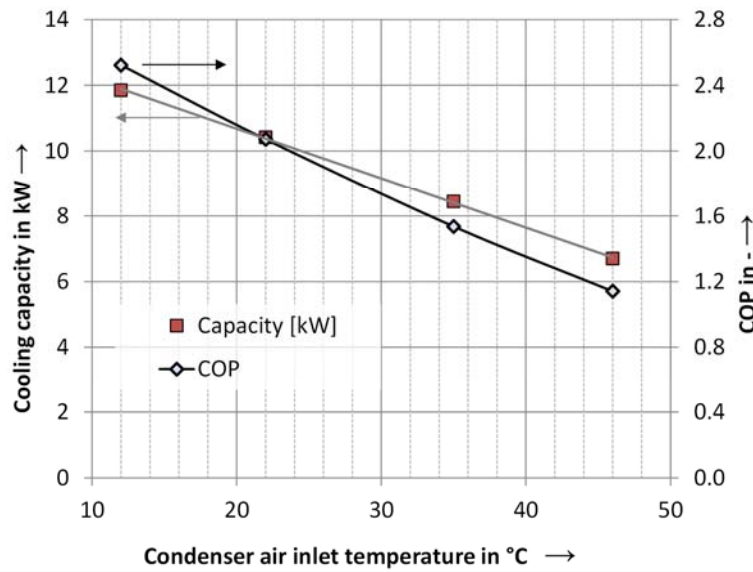


Figure 53: COP and Capacity as Function of Condenser Air Inlet Temperature, Steady State, Hybrid

2.6.3 Frost-Up Test

The frost-up tests were conducted at 35°C condenser air-inlet temperature, and 2°C/75 percentRH indoor condition. Defrost cycles of the psychrometric room coils were conducted between 4 and 5 hrs after the start of the experiment and between 8 and 10 hrs after the start of the experiment. Figure 54 shows that these defrosts led to a slight temporary fluctuation of the evaporator air inlet temperature within $\pm 1.5^\circ\text{C}$ from the setpoint. Superheat decreased and evaporation temperature increased during the first hour of the frost-up test, which is a result of finding the right valve settings as well as slight frost built-up on the evaporator which led to

improved heat transfer. Evaporation temperature starts decreasing with increasing speed about 5 hrs after the start of the experiment.

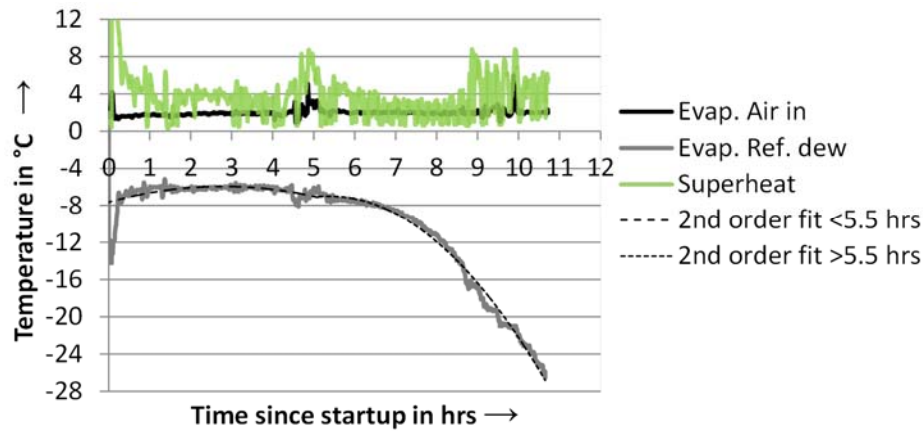


Figure 54: Evaporation Dew Temperature, Room Temperature, and Superheat During Frost-Up Test, Hybrid

Figure 55 shows that this leads to a reduction of COP and capacity. While the initial capacity was reached again 5 hrs after the start of the experiment, an additional 5 hrs later the capacity was lower than 50 percent of the initial capacity. Figure 56(a) shows that even under those conditions, the average superheat at the individual circuit exits, as well as the overall superheat are close to each other. This is an indication that there is only little or no liquid fed over into the header. The low value of the overall superheat is an indication that the refrigerant side surface area of the evaporator is used very well, which is also suggested by the average start of the first superheated position. Figure 56(b) shows 4 exemplary circuits of the evaporator. The superheat values of the circuits are very close to each other for most of the duration of the experiment. Figure 57(a) shows the frost build-up at the coil exit, 6.95 hrs after the start of the experiment, is very even. At the inlet, Figure 57(b), the frost build-up is not completely uniform, but far more uniform than it was with the TXV control scheme at about half the time after startup, Figure 20. Figure 58 shows the frost build-up of the evaporator at the end of the experiment. The evaporator inlet side is covered entirely with fluffy-type frost.

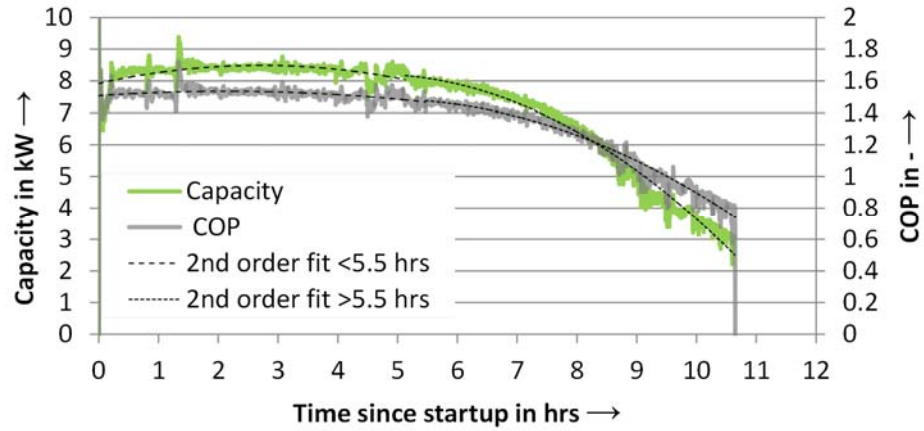
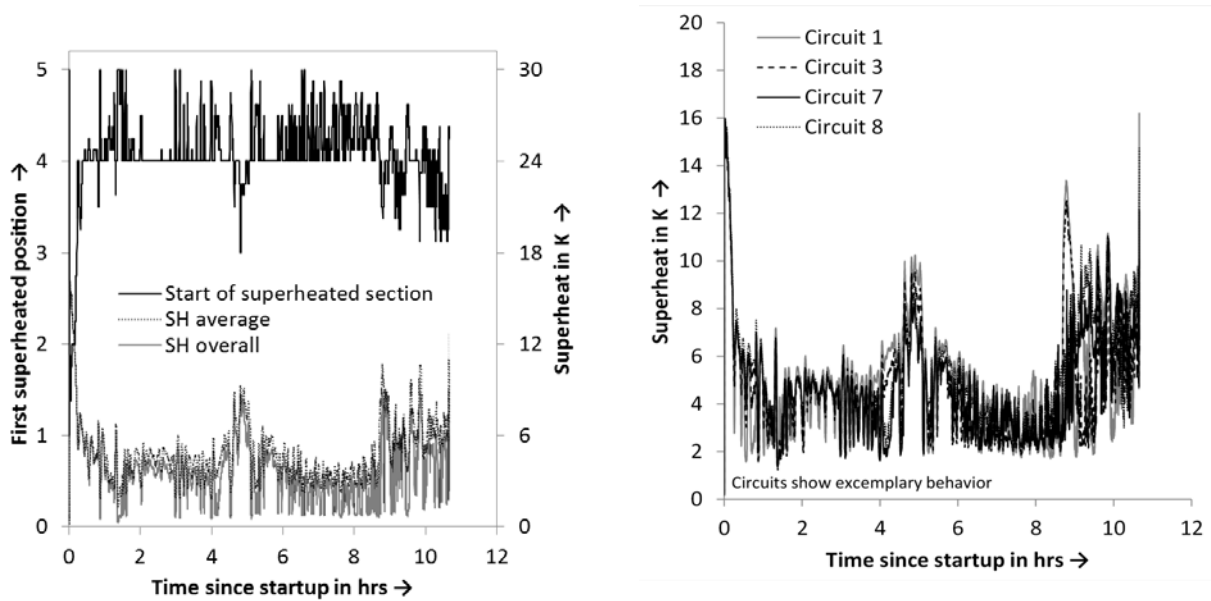


Figure 55: Capacity and COP as Function Of Time During Frost-Up Test, Hybrid



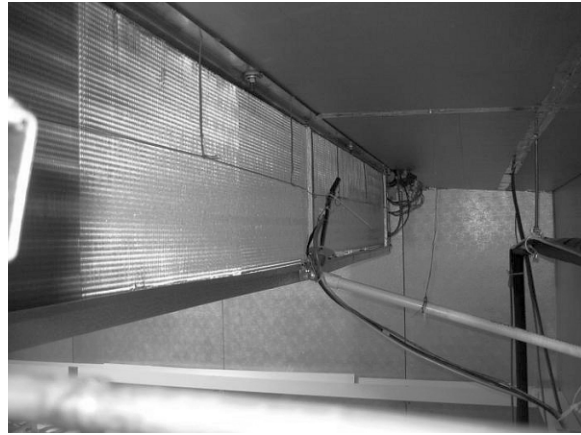
(a) Average Circuit Surface Usage Based on 1.5 K Threshold for Selected Circuits, Average and Individual Superheat

(b) Individual Circuit Exit Superheat

Figure 56: Superheat and Surface Usage During Frost-Up Test, Hybrid



(a) Exit



(b) Inlet

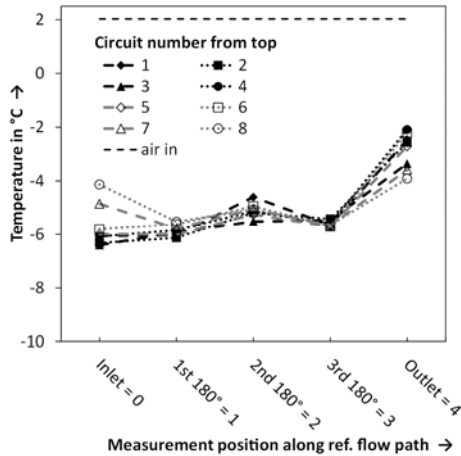
Figure 57: Frost Build-Up 6.95 hrs after Startup



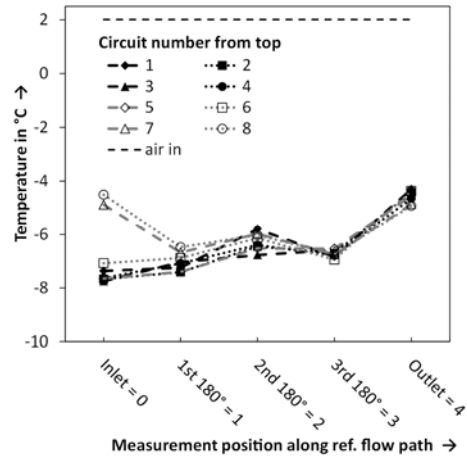
Figure 58: Frost Build-Up 10.6 hrs After Startup

2.6.4 Tests with Coil Blockage

Figure 59 shows the measured return-bend temperatures for the hybrid control tests at 35°C condenser air-inlet temperature with different types of coil blockage. The individual circuit exit temperatures are within a band of 2 K. In both blockage cases, the inlet temperatures of circuit 7 and 8 are higher than for the other circuits. The reasons for this were previously explained for Figure 46, page 43 and are in this case additionally caused by the required higher refrigerant flowrate for the bottom circuits of the coil.



(a) Case A-Blockage (1/3 block, 1/3 porous)



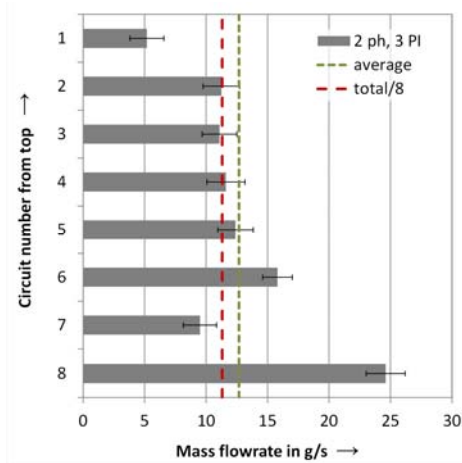
(b) Case B-Blockage (2/3 block)

Figure 59: Measured Return-Bend Temperatures for Tests with Coil Blockage, 35°C Condenser Air-Inlet Temperature, Hybrid

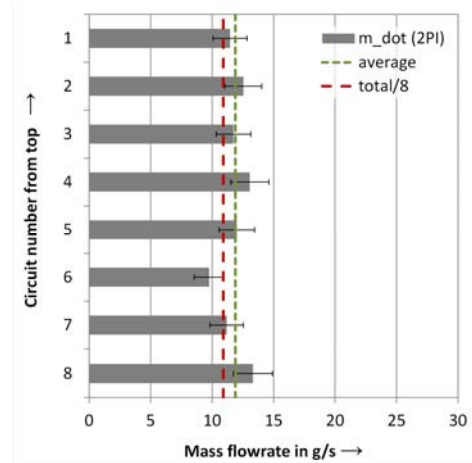
2.6.5 Determination of Maldistribution Using Balancing Valves as Virtual Flow Sensors

Due to cost constraints, it was not possible to equip the individual circuits with accurate mass flow meters. Furthermore it is not possible to determine the effective airside maldistribution directly since the air flow equalizes to some extent after the applied blockage in the depth of the coil. Therefore the balancing valves were used as virtual flow sensors to determine the mass flow rates of the individual circuits at equal exit superheats. The result can be used as an estimate for the effective air-side maldistribution. This airside maldistribution will later be used for the simulation. Figure 60(a) shows the mass flow rates as measured with the expansion valve opening and a 3 PI group correlation for clean-coil condition without additional airside maldistribution. Circuits 1 and 7 seem to have a much smaller, and circuits 6 and 8 a much larger mass flow rate than the average measured value based on the EXVs. Additionally, the average circuit mass flow rate based on the total flowrate measurement using a Coriolis mass flow meter measurement is smaller than the average circuit flowrate determined using the EXV virtual sensors. The reason for the apparent flow maldistribution shown in the Figure 60(a) is quality maldistribution: In circuits with lower inlet quality to the balancing valve, e.g. circuits 1 and 7, a smaller valve opening is sufficient in order to fully utilize the circuit and produce the desired exit superheat. A smaller inlet quality means that a smaller valve opening is required to obtain the same (liquid) mass flowrate. In circuits with larger inlet quality (6, 8), a larger valve opening is required to obtain a sufficient mass flow to produce the target superheat. To summarize the issue: the quality distribution after the distributor is unknown, so that the inlet quality to each valve is unknown, which means that the flowrate of a specific circuit will be either over or under predicted when using the overall quality. To support this reasoning, the primary valve was fully opened, so that there is none or negligible inlet quality at the inlet to the balancing valves. Figure 60(b) shows that in this case, the flow rates through the valves are nearly uniform within the accuracy of the measurement. The accuracy of the average virtual sensor flow rate as compared to the Coriolis measurement is also improved.

Figure 61 shows the flow rates in the case of the 2/3 blockage of the coil for the same operating condition as before. Subfigure a) shows that the average flow rate determined using the virtual EXV sensors is much closer to the value determined using the Coriolis mass flow meter measurement. This suggests less quality maldistribution at the distributor, which means that the quality distribution is influenced by the flowrate exiting each of the feeder tubes. With the primary valve fully open, as shown in subfigure (b), the relative deviations in individual circuit mass flow rates between subfigure (a) and (b) are also smaller than described for the experiments with a clean-coil. This supports the theory that quality maldistribution is influenced by outlet flowrate.

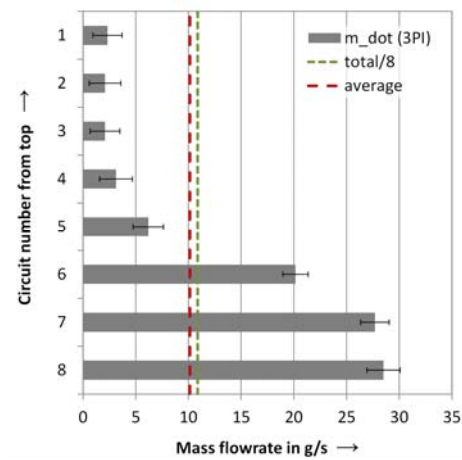


(a) Hybrid Control Approach

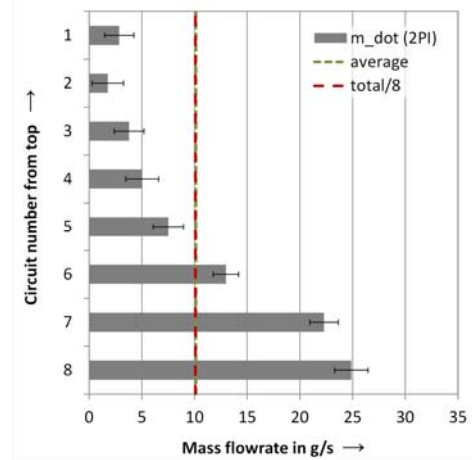


(b) Fully Open Primary Valve

Figure 60: Individual Circuit Mass Flow Rates for Clean-Coil, 46°C



(a) Hybrid Control Approach



(b) Fully Open Primary Valve

Figure 61: Individual Circuit Mass Flow Rates for Type B Blocked-Coil (2/3 blockage), 46°C

2.6.6 Performance

Figure 62 shows COP and capacity for different blockages as a function of ambient temperature. As seen for the EXV control scheme, COP and Capacity degrade with increasing ambient temperature and blockage. Figure 63(a) shows that COP degrades by a maximum of 7 percent for 1/3 blockage and by a maximum of 11 percent for 2/3 of the coil being blocked. Figure 63(b) shows that capacity degrades by a maximum of 7 percent for 1/3 blockage and by a maximum of 13 percent for 2/3 of the coil being blocked. The relative degradation with blockage is smaller for the hybrid control scheme than for the EXV control scheme, page 41.

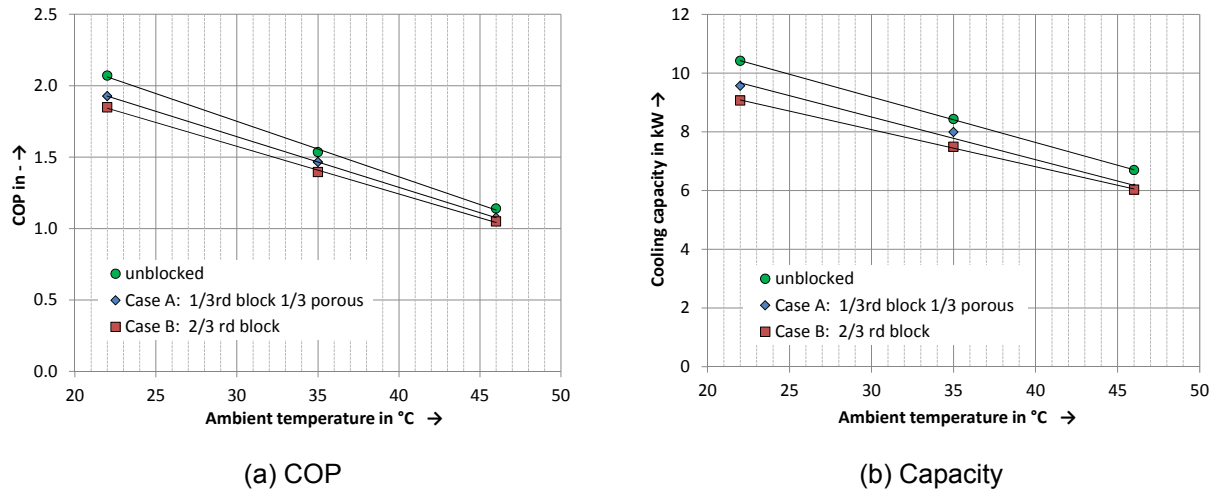


Figure 62: Performance as a Function of Condenser Air Inlet Temperature, Hybrid

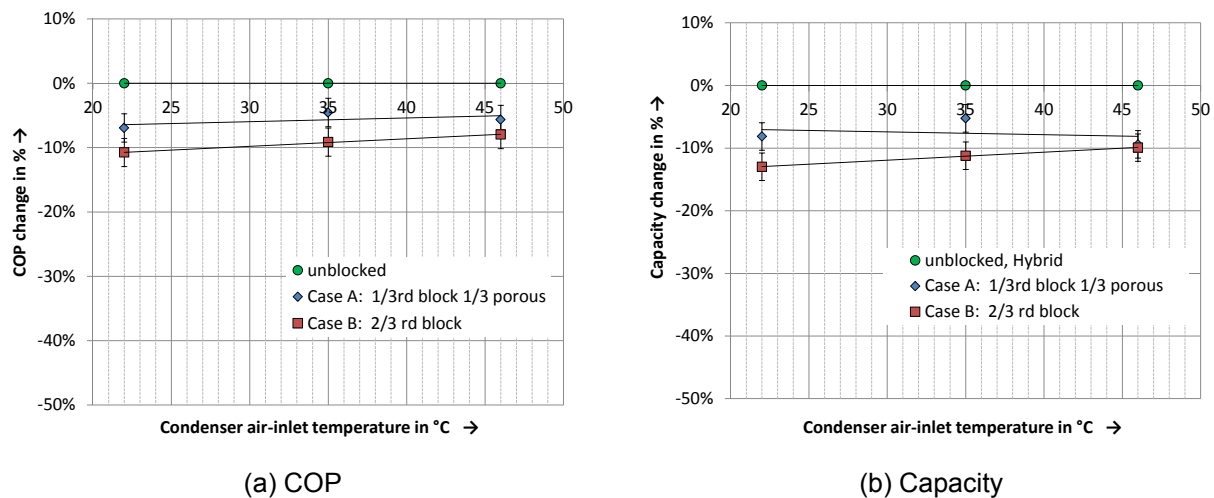
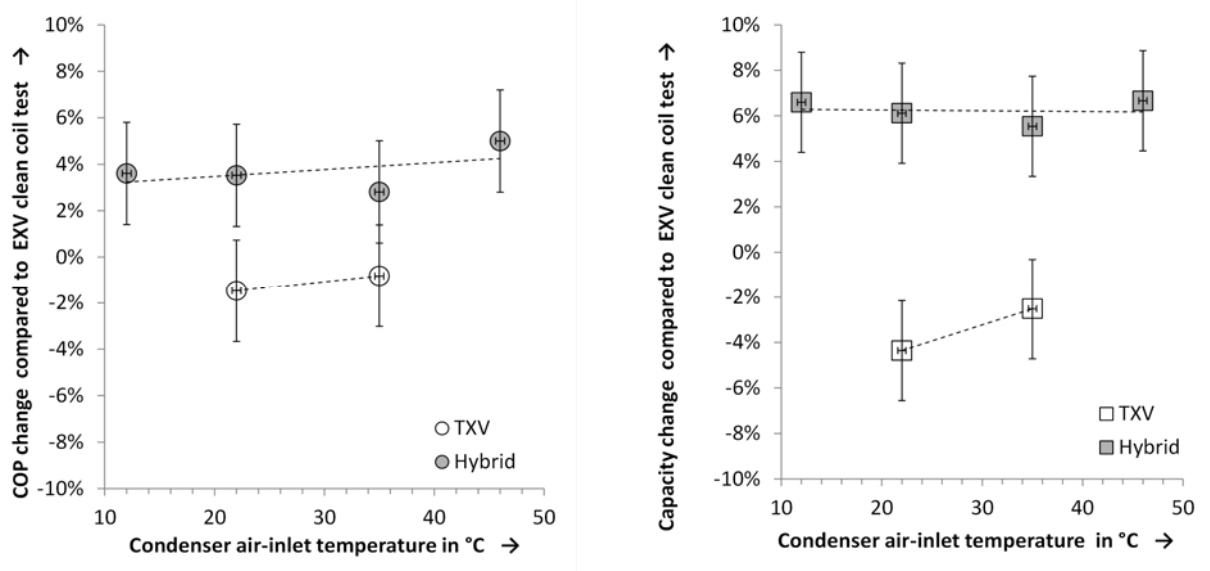


Figure 63: Performance Change as a Function of Condenser Air Inlet Temperature, Hybrid

2.7 Performance Comparison

For the comparison of the different control schemes, the EXV and not the inbuilt TXV was chosen as a base case. The reason for this is that EXVs are considered state of the art and it is likely if not inevitable that they will be the standard expansion device in this application within

a few years. Under clean-coil conditions, as shown in Figure 64, the COP and capacity improve by about 4 percent and 6 percent respectively if the hybrid control is used. There is a slight trend with ambient temperature, which might be caused by experimental accuracy. The TXV decreases COP by less than 2 percent compared to the EXV. The capacity is degraded by more than 4 percent for 22°C condenser air-inlet temperature. Figure 65(a) shows the influence of coil blockage and condenser air-inlet temperature compared to the unblocked EXV base case. With the EXV control scheme, the performance dropped with decreasing ambient temperature and increasing blockage. The degradation in COP was more than 11 percent with the light, 1/3 blocked, 1/3 porous blockage and nearly 20 percent with 2/3 of the coil blocked for 22°C condenser air-inlet temperature. The EXV 2/3 blocked test is a repetition of the EXV 2/3 blocked 35°C ambient test, since minor frost build-up occurred during the latter one. This led to an enhanced heat transfer which, in turn, led to reduced performance degradation. With the hybrid control scheme, the COP dropped by 2.2 percent for 22°C condenser air-inlet temperature at 2/3 blockage while for the lighter blockage, the COP dropped by 1.9 percent compared to the EXV clean-coil COP. For the larger blockage, 57 percent of the lost performance was recovered, while for the slighter blockage, 84 percent of the lost performance was recovered if the hybrid control scheme was used instead of the EXV control scheme. For all tests, the maximum COP reduction recovery was 90 percent, while the minimum was 57 percent.



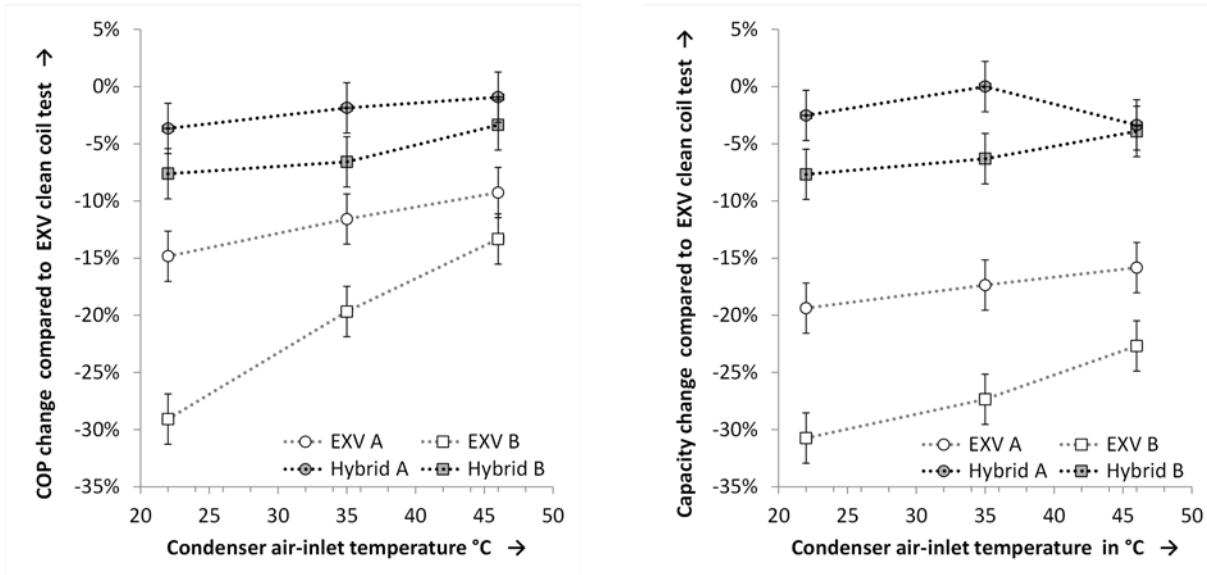
(a) COP Compared to EXV Base Case, Clean-Coil

(b) Capacity Compared to EXV Base Case, Clean Coil

Figure 64: Influence of Ambient Temperature and Control Scheme on Performance Indices

Figure 65(b) looks similar in trend but with a larger magnitude than Figure 65(a): For the EXV control scheme it is questionable whether the system would have enough capacity to maintain the room temperature under peak load with the given maldistribution. For the highest ambient temperature, the capacity degradation was 16 percent and 23 percent for light blockage and 2/3 blockage, respectively. For the same high ambient temperature, the hybrid control scheme had a

only 4 percent reduction for both cases, which corresponds to a recovery of 75 percent to more than 80 percent of the losses in capacity. For all tests, the maximum capacity recovery was 100 percent while the minimum was 74 percent. This potentially means that system oversizing can be reduced if the hybrid control scheme is used.



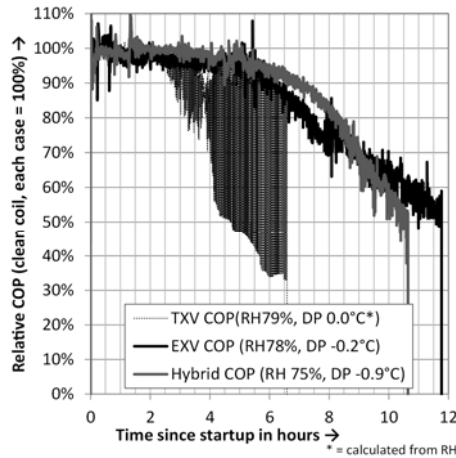
(a) COP Compared to EXV Base Case, Blocked-Coil

(b) Capacity Compared to EXV Base Case, Blocked-Coil

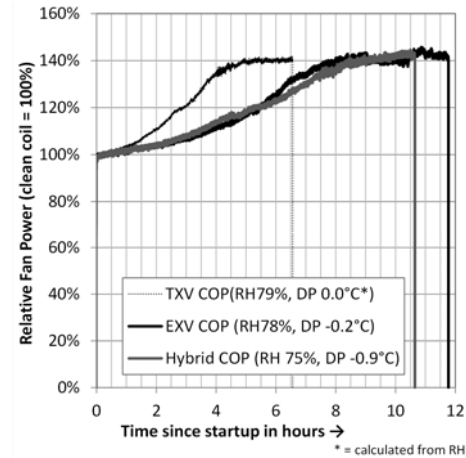
Figure 65: Influence of Coil Blockage onto Capacity for EXV and Hybrid³

The influence of frost build-up was determined using one single frost-up cycle. Frost build up is highly dependent upon operating conditions and therefore the results are not exactly representative since the indoor conditions were not identical. Although comparisons of quantitative behavior are not exact, the qualitative behavior likely is. In Figure 66(a), it is obvious that the TXV controlled system runs into hunting issues. The EXV controlled system has a capacity plateau until about 5.7 hrs and then suddenly follows a downwards trend. The hybrid controlled system follows approximately parabolic profile. Figure 66(b) shows the change in fan power consumption – which is a measure of frost build up. The fan power consumption of the TXV control scheme increases fastest due to fast frost build-up. The limit of all control schemes is about 145 percent of the clean-coil fan power, which is caused by leakage of the air around the evaporator coil.

³ Postfixes are blockage levels: A – Case A blockage: 1/3 block, 1/3 porous; B – Case B blockage: 2/3 block.



(a) Change of Cooling Capacity



(b) Change of Evaporator Power Consumption

Figure 66: Influence of Operating Time on Capacity and Evaporator Fan Power Consumption for Frost Build-up Test

2.8 Analysis

The experimental results showed a range of possible different performance improvements, which were mainly dependent upon condenser air inlet temperature, and (non-) uniformity of the evaporator air flow. In practice, the system will not operate at a single, specified operating point, but rather be subject to varying operating conditions as well as varying maldistribution. These operating conditions, together with the runtime of the system will be dependent on the following variables:

1. condenser air-inlet temperature,
2. cooling load,
3. air-side maldistribution,
4. recirculation of condenser and/or evaporator air,
5. refrigerant-side maldistribution,
6. cyclic losses,
7. transient losses,
8. refrigerant charge.

Condenser air-inlet temperature depends upon the location of the condensing unit. The term “location” is here not only to be read as geographical location, since the micro-climate at the installation position may be significantly different from what weather data (= ambient temperature) suggests. The condenser air-inlet temperature can therefore be significantly higher than the ambient temperature obtained from weather data if the condensing unit is installed on a (dark) roof and/or in vicinity of other heat rejecting equipment. If the condensing unit is installed indoors, the condenser air-inlet temperature may be higher than the ambient temperature during the colder periods of the year. The cooling load, which determines the runtime of the system, is not only dependent on the heat conduction and infiltration into the

(closed) box⁴ but also on the usage of the box. Therefore the cooling load is dependent on the following additional factors:

1. infiltration due to door-opening,
2. sensible/latent heat of brought in warmer products,
3. personnel and fork lifts,
4. lighting,
5. internal heat generation of stored goods,
6. etc..

Air-side flow maldistribution depends upon coil design, fouling and possible coil blockage due to improper storage of goods close to the evaporator air inlet. Improper storage of goods against the ceiling can also lead to air recirculation, which is not only a problem for the quality assurance of the stored goods but also may lead to air-side temperature maldistribution at the evaporator inlet. On the condenser side, recirculation leads to a higher condensing pressure and by that to a lower COP and capacity. The amount of cyclic losses depends upon load and operating conditions, which dictate the number of on/off cycles over a given period of time. Refrigerant-side maldistribution may be caused by unequal oil-logging, leading to different pressure drops in the individual circuits of the evaporator⁵. Cyclic losses depend upon the number of on/off cycles that the system goes through. The number of on/off cycles depends upon the operating conditions as well as the chosen hysteresis and location of the box temperature controller. Transient losses, which include but are not limited to cyclic losses, include the losses caused by non-steady-state operation of the system. In practice, the system will be operated with continuously changing evaporator and condenser air-inlet temperature, leading to transient losses. While great care was taken to ensure a low refrigerant leakage rate of the experimental system, systems in practical application will incur performance degradation caused by refrigerant leakage. A charge loss of 20 percent leads to only minor degradation of COP and capacity for most systems (see Grace et al., 2005 for system without receiver and Kim et al., 2010 for systems without and with receiver), therefore it is likely that the system will run undercharged for an elongated period of time before action is taken.

2.8.1 Bin Analysis

The difficulty of the system performance evaluation lies in the previously outlined number of factors that affect the performance on a daily, yearly as well as a lifetime basis. Most of these factors are very difficult to access, especially if they are dependent on specific field installation and operating practices. Therefore a simpler evaluation method is used in the standards for evaluating performance ratings. For the purpose of the performance comparison between the EXV and hybrid control scheme, the bin- method, as described in the applicable standard for walk-in coolers, AHRI Standard 1251 (2009), is used. Three possible installation configurations are considered:

⁴ AHRI Standard 1251 (2009) uses the term “box” for the cooled storage room. This terminology is adapted in this chapter to make possible reading of the standard easier.

⁵ Wirz (2009) describes oil logging and its causes in general.

1. box and condensing unit indoors,
2. box indoors, condensing unit outdoors, and
3. box and condensing unit outdoors.

If the condensing unit or box, is located indoors, a constant 32°C is used as the ambient temperature. If the condensing unit is located outdoors, the binned ambient temperature is used to determine the condenser ambient temperature. If the box is located outdoors, the box load is calculated as a linear function of the capacity at 35°C ambient temperature and the binned ambient temperature⁶. To capture the effects of different usage of the box throughout the day, the annual walk in energy factor (AWEF) considers a period with high (33 percent) and low box load (67 percent). Idle-time (no cooling demand) power consumption is considered in the calculation of the AWEF and consists for the LRCS of the power consumption of the continuously running indoor fan and the compressor crankcase heater.

For the purpose of the performance evaluation of the EXV and hybrid control scheme, the following modifications were made to the calculation method outlined in AHRI Standard 1251 (2009): (a) use linear interpolation between experimental data points to obtain power consumption and capacity, and (b) use TMY3 data from Sacramento Executive Airport, California, NREL (2012)⁷. Figure 67 shows that the region IV temperature data is significantly different from the Sacramento Executive AP data. In region IV, a much larger proportion of the bin hours is located below 14°C. Therefore it would be inappropriate to use region IV data to estimate achievable energy savings for California. Since systems like the LRCS are typically oversized, it was assumed that the continuously operating evaporator fan will always lead to sufficient defrost of the coil for operating conditions with high ambient temperature. This simplification neglects frost build-up between defrosts and also any other source of maldistribution which would lead to an additional benefit of the hybrid control. Therefore the resulting energy savings are to be interpreted as minimum energy savings. The ambient temperature bin temperatures of region IV cover the range of -19°C to 38°C while the experiments cover the range of 2°C to 46°C. Therefore it was necessary to extrapolate the data for low ambient temperatures. Figure 68(a) shows the experimental data along with the interpolated values for the EXV control scheme. For ambient temperatures below 2°C, COP and capacity were held constant to account for the condensing pressure regulation by the condenser fan cut-out switch. For the hybrid control scheme, the performance was not measured at 2°C ambient temperature. Figure 69 shows the ratio of COP and capacity between the two control schemes, which was linearly extrapolated to 2°C. This linear extrapolation of the ratio of COP and capacity between the two systems was then used to estimate the performance of the hybrid control system at 2°C, Figure 68(b).

⁶ See 6.2 in AHRI Standard 1251 (2009), for further details.

⁷ The Sacramento Executive Airport TMY3 data rather than the Sacramento Metropolitan Airport TMY3 data is used since the first one is of Class 1 and therefore has a lower uncertainty, as described in the database manual by Wilcox and Marion (2008).

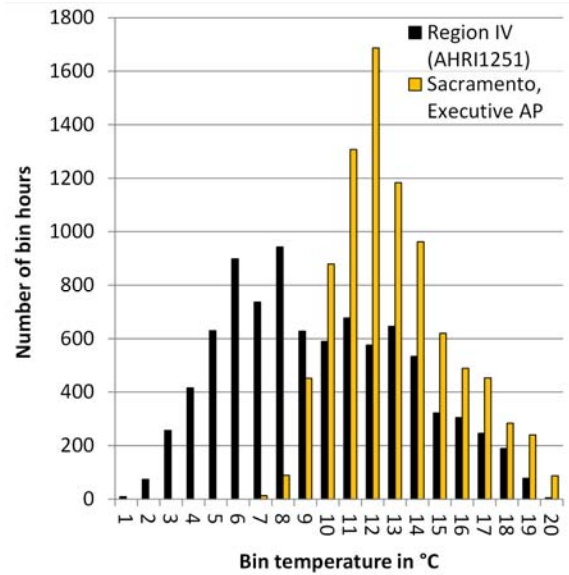


**Figure 67: Bin Temperature Comparison
Region IV Versus Sacramento Municipal
Airport**

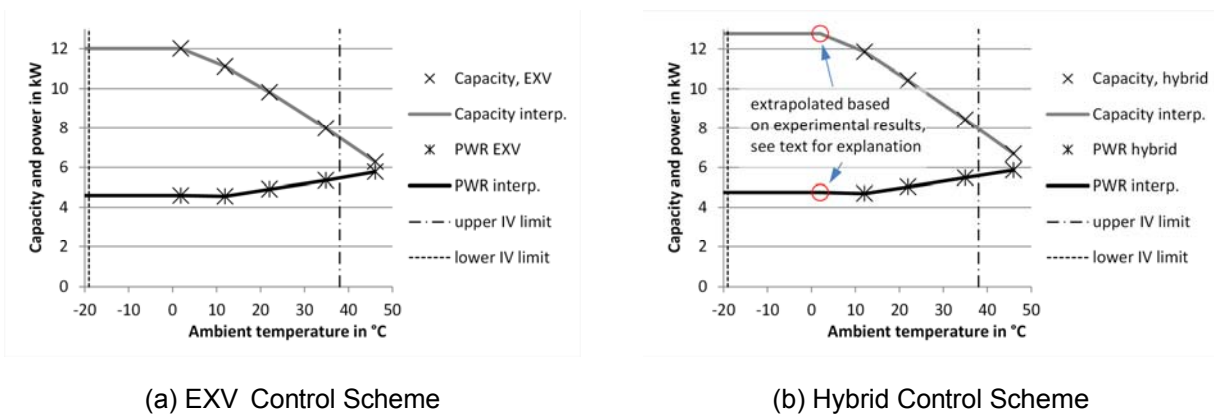


Figure 68: Measured COP and Capacity Data and Inter/Extrapolated Data

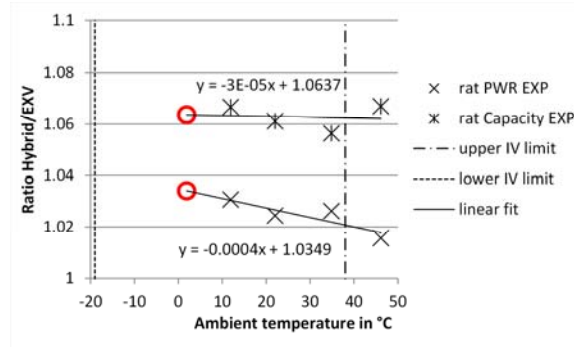
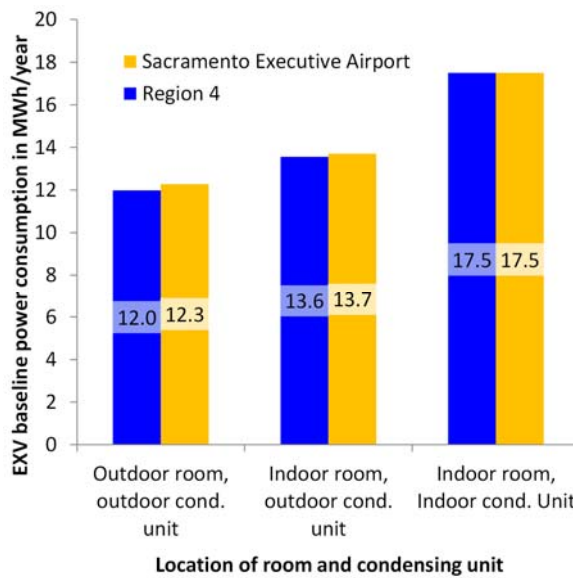


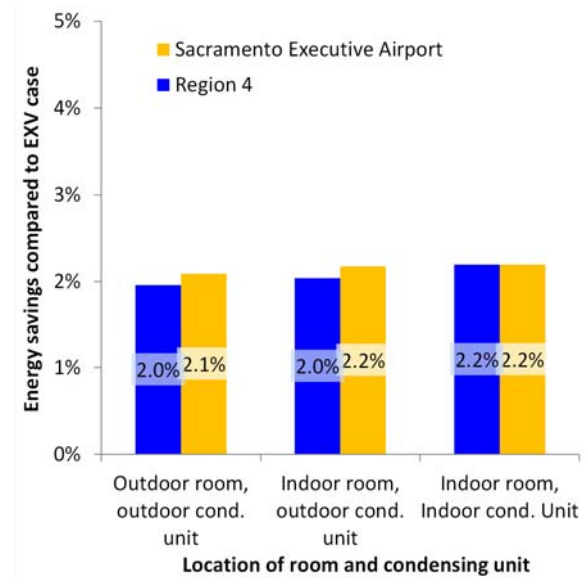
Figure 69: . COP and Capacity Ratios for Hybrid Compared to EXV Control

2.8.2 Results

Figure 70(a) shows the calculated annual energy consumption for the three different system configurations when using the EXV baseline system, at the AHRI Standard 1251 (2009), standard region 4 and at Sacramento Executive airport (AP). If both box and condensing unit are located indoors, the ambient climate does not matter. If the condensing unit is installed outdoors, then the Sacramento Executive climate leads to a slightly higher electrical consumption. Figure 70(b) shows the achievable energy savings when using the hybrid control scheme. The savings are smaller for the region 4 location if the condensing unit is located outdoors, resulting in a 2.0 percent energy saving. For the Sacramento Executive AP location with outdoor condensing units, the achievable energy savings are slightly higher. If both, room and condensing unit are located indoors, the energy savings are 2.2 percent. Figure 71 shows the accumulation of energy savings over the temperature bins. If the condensing unit is located indoors, these savings are independent on the geographical location since a constant indoor temperature is assumed. If the condensing unit is located outdoors, the distribution of the ambient temperatures differs as shown in Figure 67. As a result, the savings are accumulated over a different range of ambient temperatures.



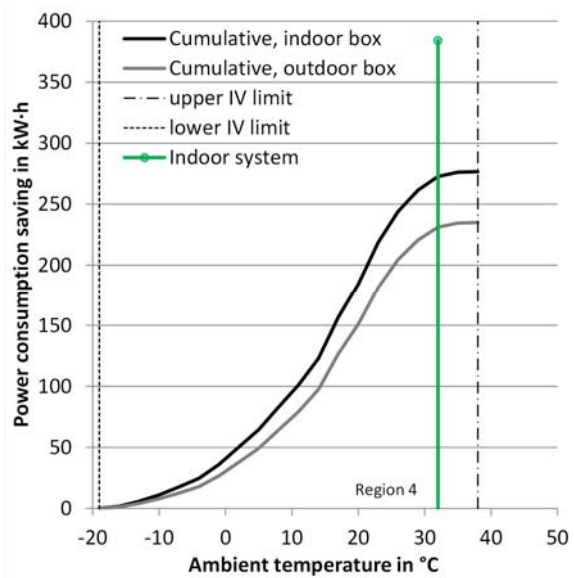
(a) EXV Baseline Power Consumption



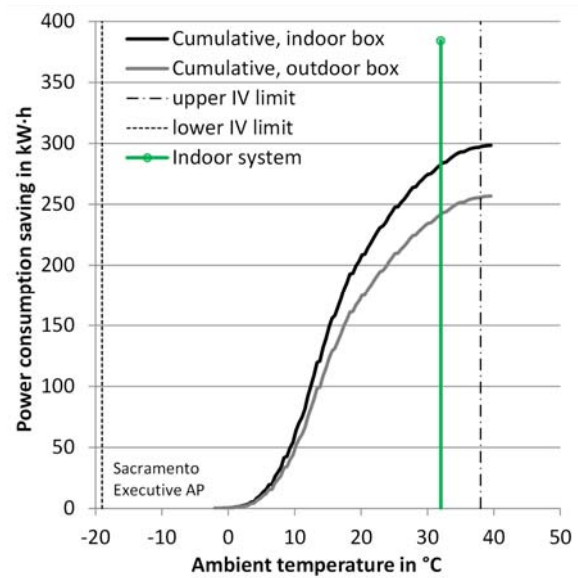
(b) Energy Savings For Hybrid Control Compared to EXV Baseline

Figure 70: Annual Energy Consumption, LRCS

From an end user point of view, the actual monetary savings are more interesting than the percentage savings. Therefore the annual yearly energy savings were calculated. Specific electricity cost for the commercial sector of 13.83 Cents/kWh as YTD to September 2012 was used as given by EIA (2013b). Figure 72(a) shows that the energy savings, for Sacramento Executive AP ambient conditions are in the range of \$36 to \$41 per system and year. For the indoor system, the savings are larger with \$53 per system and year. From a state and environmental point of view, energy savings are more interesting, since they determine the amount of energy imports and CO₂ emissions, respectively. Itron (2006) states that 9014 GWh are used annually for refrigeration in California for the entire commercial sector. Since it was not possible to obtain data on the exact usage of 3-ton large room cooling systems, it was assumed that at least 5 percent of the power consumption is caused by systems with a similar expected performance improvement as the tested 3-ton LRCS. Figure 72(b) shows that the estimated energy savings are in the range of 6.6 to 9.9 GWh/year, which is equivalent to \$0.9 to \$1.4 million of electricity per year at the previously mentioned rate. The exact value will depend on the ratio of the 3 different system configurations and on the total number of units, which was estimated. Due to the large number of unknowns these results are to be seen as an order of magnitude estimate only.

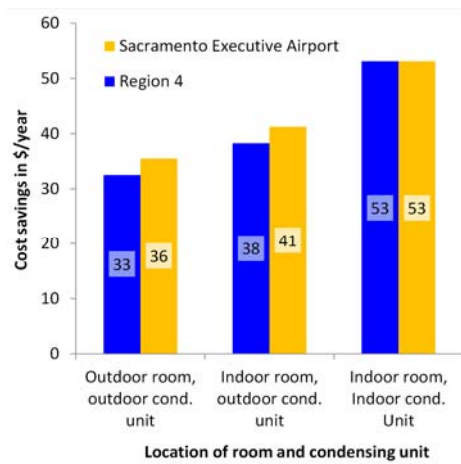


(a) Region 4

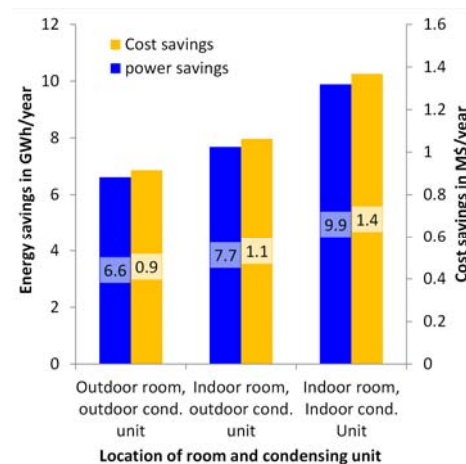


(b) Sacramento Executive Airport

Figure 71: Annual Energy Consumption for Different Ambient Temperature Profiles, LRCS



(A) Energy Cost Savings per System and Year



(A) Estimated Energy Cost and Energy Savings for California (Basis: Sacramento Executive AP) per Year

Figure 72: Estimated Energy and Cost Savings, LRCS

2.9 Refrigerant Maldistribution Effects for Clean-Coil

Airside maldistribution for the clean-coil was found to be insignificant as shown in Appendix A, Figure A 14. However, this is not the case for refrigerant side maldistribution if the EXV or TXV control scheme is employed. Appendix A, from page 188 gives further details on the simulation model and its validation.

Refrigerant side maldistribution is, in practice, often caused by misalignment of the expansion valve and distributor and/or insufficient distance between the valve and distributor. Both can lead to a maldistribution of liquid and vapor, resulting in a loss of performance. In Bach et al. (2012c), several graphs were shown to illustrate this issue that were based on measured temperatures at the inlet, return-bends and exit of the individual circuits. These return-bend temperatures were used to manually estimate the surface area usage for evaporation for each circuit, as shown in Figure 75. For this analysis, it was assumed that the superheated refrigerant exponentially approaches the air inlet temperature. Based on this estimate, in terms of position, the two-phase area fractions as required for the evaporator of the simulation model were calculated. These two-phase area fractions were then used to calculate the individual circuit flowrates with the simulated multi-circuit evaporator. Since one or more circuits in each case fed liquid through in the experiment, an additional residual for the overall exit superheat was used to calculate the overall mass flow rate. This approach assumes that quality maldistribution at the distributor has negligible effect on the two-phase refrigerant side heat transfer coefficient.

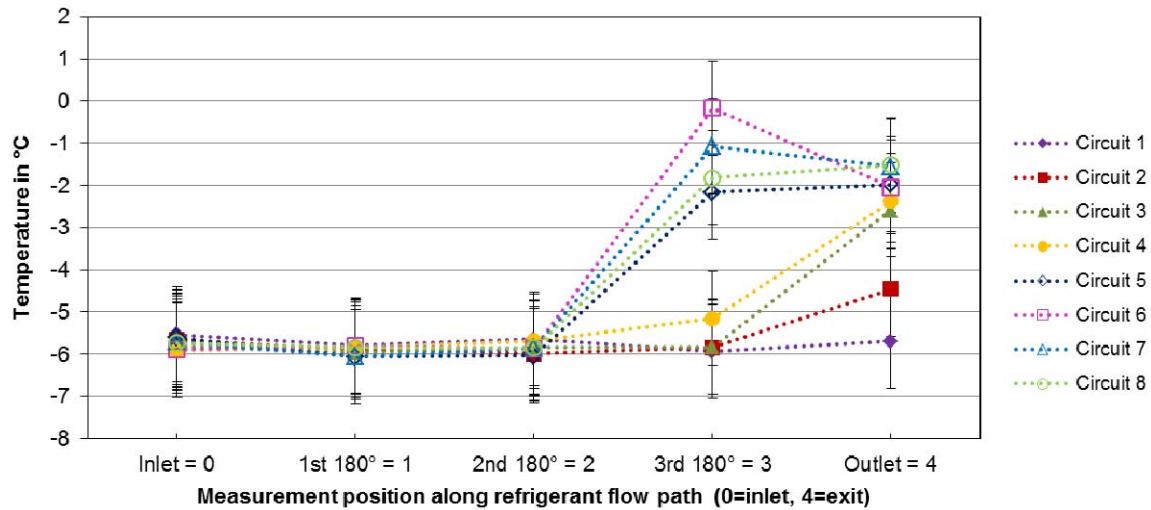


Figure 73: Return-Bend Temperatures, 35°C Ambient Temperature⁸

⁸ Error bars combined uncertainty of thermocouple and data acquisition (=1.12 K).

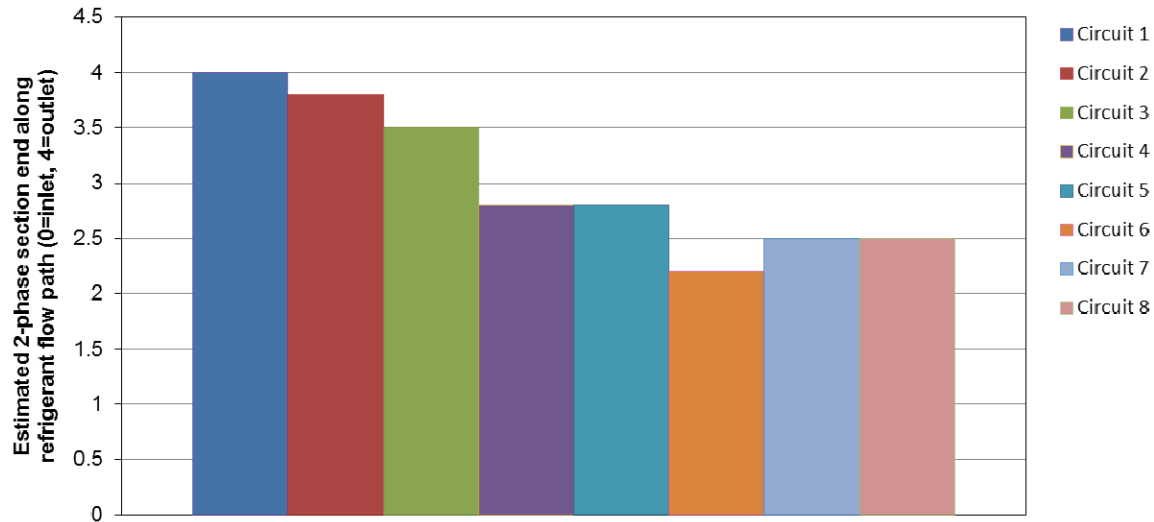


Figure 74: Manually Estimated End of 2-Phase Section for EXV Control Scheme, 35°C Ambient Temperature

Figure 76 shows the result for the two cases with unblocked TXV coil. Individual circuit mass flow rates in the simulations performed using ACHP were obtained by multiplying the total refrigerant mass flowrate of the evaporator by the circuit mass flow distribution factors. Since the large room cooling system has 8 circuits, its average mass flow distribution factor is $1/8=0.125$. It can be seen that the estimated distribution factors deviate significantly from this. For the 22°C ambient temperature case, for example, the maximum distribution factor is more than 0.18 for circuits 3 and 4 and less than 0.6 for circuit 8. Additionally, when the ambient temperature was changed to 35°C, the distribution reversed. The overall mass flowrates differ between experiment and simulation, which is a result of the tuning of the evaporator to the hybrid control case and uncertainty in the estimated circuit usage.

The refrigerant distribution factors used in the simulation model are multipliers to the total mass flowrate. They are used in order to obtain individual circuit mass flow rates, and their sum is therefore identically equal to 1.0, as shown in eqn. (6). Figure 77 shows the results for the refrigerant distribution factors for the EXV control scheme. While there is still significant amount of maldistribution, the change between different operating points is much less than for the TXV control scheme.

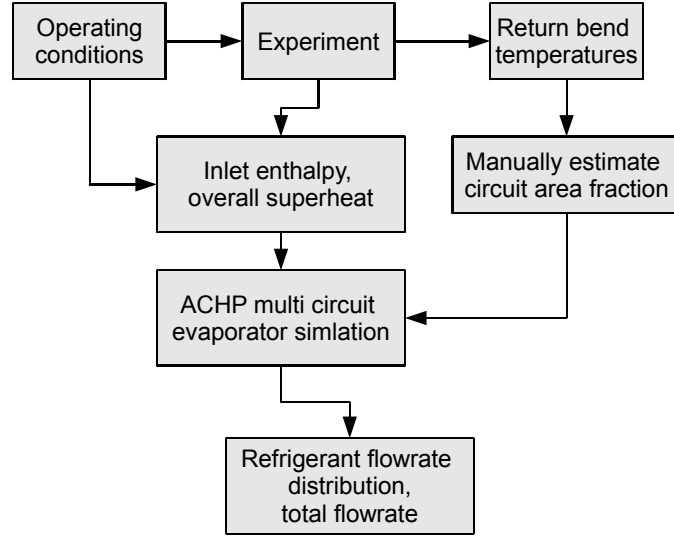


Figure 75: Semi-Empirical Approach to Calculate Flowrate Distribution

$$\dot{m}_{ref} = \sum_{i=1}^N \dot{m}_{ref,i} = \sum_{i=1}^N \gamma_i \cdot \dot{m}_{ref}$$

where

$$\sum_{i=1}^N \gamma_i = 1.0$$

(6)

To illustrate maldistribution results more intuitively, Li et al. (2005)'s mass flow distribution performance index as defined in equation (7) is more appropriate. Since the absolute value of that index increases with increasing maldistribution it is subsequently termed (mass) flow maldistribution index rather than flow distribution performance index.

Figure 78 and Figure 79 show the maldistribution index for the TXV and EXV control case. As previously described there is a significant change in distribution between different tests for the TXV, and from Figure 78 it is straightforward to grasp that the maximum flow rate maldistribution for a specific circuit ranges from 61 percent less than the average at 22°C ambient temperature to 45 percent more than the average at 35°C.

$$\varepsilon_{m,i} = \frac{\dot{m}_i - \bar{\dot{m}}}{\bar{\dot{m}}},$$

where:

$\varepsilon_{m,i}$ = mass flow maldistribution index

\dot{m}_i = individual circuit (or branch) mass flowrate

$\bar{\dot{m}}$ = average circuit (or branch) mass flowrate

(7)

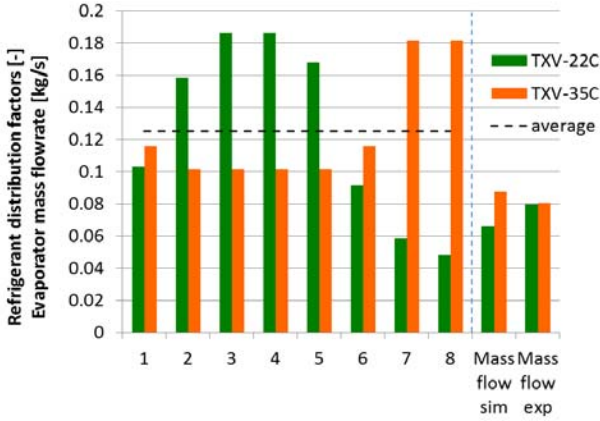


Figure 76: Estimated Refrigerant Distribution Factors, TXV, no Airside Maldistribution

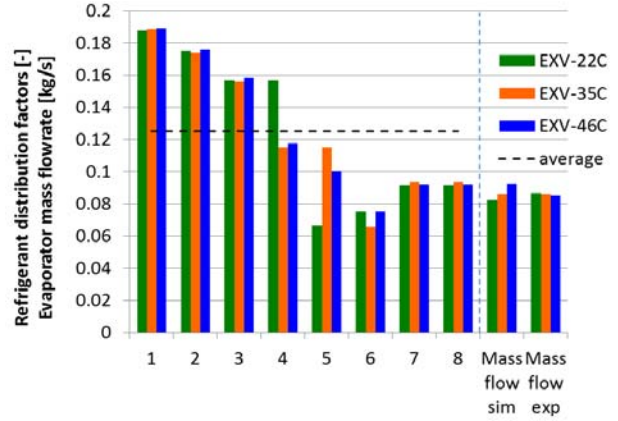


Figure 77: Estimated Refrigerant Distribution Factors, EXV, no Airside Maldistribution

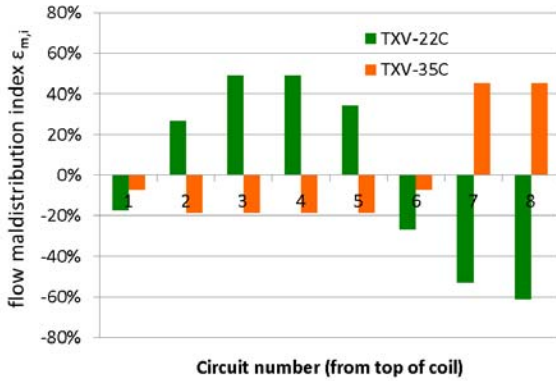


Figure 78: Estimated Refrigerant Mass Flow Maldistribution Performance Index, TXV, no Airside Maldistribution

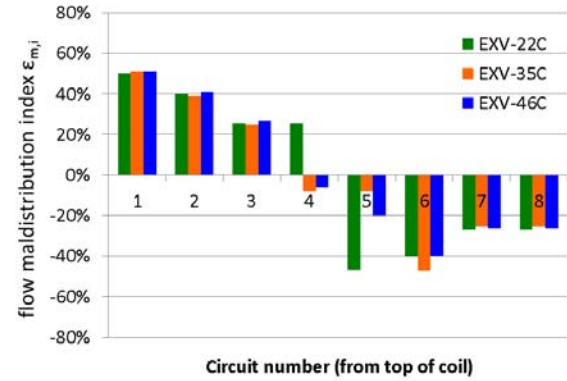


Figure 79: Estimated Refrigerant Mass Flow Maldistribution Performance Index, EXV, no Airside Maldistribution

One possible reason for the change of distribution with operating condition visible for the TXV control scheme is, that the expansion port of the TXV can directly “see” the distributor, as shown in Figure 38. The reason that this might be an issue is that the port of the TXV is off center, Figure 82 a). This eccentricity leads to maldistribution of liquid and vapor phase at the inlet of the distributor, which will likely change the quality maldistribution in the cross-section of the flow leaving the valve and entering the distributor for different operating conditions. It seems that this issue is common. Figure 82 b) shows a valve of a different system that has a similar issue. The gap between port and spring was moved to about the middle of the connection stub for the distributor, which might help to reduce the dependency on operating

condition. For an EXV, Figure 82 c), this is not an issue as long as it is operated in the forward direction⁹, since the port is centric.



Figure 80: Connection Side of Evaporator, TXV Control Scheme

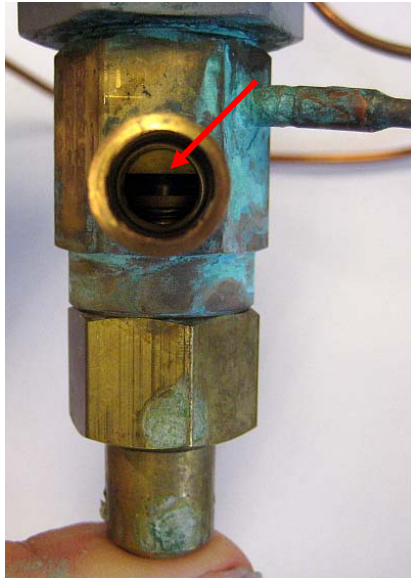


Figure 81: Distributor and Tandem Primary EXV's; Same Setup (Without Balancing Valves) Used for EXV Control Scheme

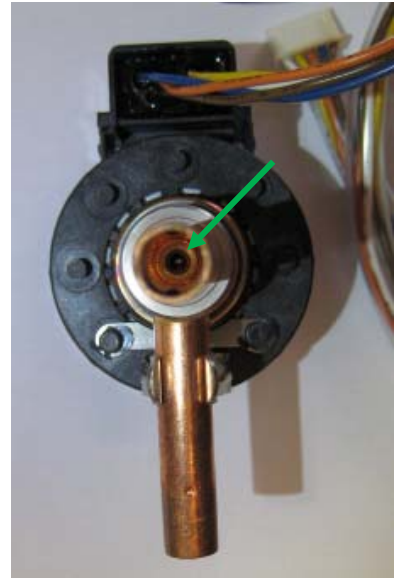
⁹ Most EXV's are bi-flow, meaning they can be operated in forward and reverse.



a) TXV from 3-Ton Large Room Cooling System



b) TXV from 4-Ton R410A Rooftop Unit



c) Standard Direct Drive Stepper Valve

Figure 82: Location of Expansion Port Exits in Different Expansion Valves (Indicated by Arrow).

Optimized Distributor Versus Employed Distributor

Li et al. 2005 numerically investigated two-phase flow through a number of different distributor geometries with 4 outlets in simulation and experiment. The boundary conditions for their simulation are shown in Table 1, along with what can be observed from real conditions in experiments. The experimental results are not considered here, due to the uncertainties in the experiments being of similar order as the measured misdistribution.

Table 1: Boundary Conditions for Distributor in Simulation and Reality

<i>Boundary condition</i>	<i>Li et al. (2005)</i>	<i>Reality</i>
inlet to distributor	velocity and uniform void fraction	non-uniform void fraction and velocity
outlet from distributor	constant and uniform pressure for all outlets	outlet pressure is a function of distribution lines and evaporator circuit, different outlets might have different quality and flowrate, which has interdependence with circuit pressure drop

<i>Boundary condition</i>	<i>Li et al. (2005)</i>	<i>Reality</i>
cause of observed maldistribution	gravity or misalignment of inlet flow by 3.7° relative to distributor centerline	as stated by Li et. al, with varying angles; additionally two points above and varying distance of the orifice inside the distributor

Figure 83 shows results from Li et al. (2005) for horizontally installed, perfect distributors, given in terms of his flow maldistribution index (FMI) as previously defined in equation (7). The maldistribution for these simulations is solely caused by gravity. The best performing distributor, type 5, has a maximum FMI of less than 1 percent. The worst performing distributor has a maximum FMI of more than 14 percent. If the distributors are oriented vertically, but the orifice is misaligned, then the maximum FMI of 35 percent occurs for the type 3 distributor as shown in Figure 102. The type 5 distributor, again, has a maximum FMI of less than 1 percent.

Li et al. (2005)'s type 3 distributor has a cone-shaped base, while the type 5 distributor has a round base. The flow from the valve enters through an orifice, and then impinges on the base. From the base, it is redirected and enters the exit ports to the branches. The orifice is further away from the impinged wall for the type 3 distributor than for the type 5 distributor, which causes the center of the impingement being further from the center of the impingement wall. In an earlier work, Li (2001) simulated the same distributors, along with a commercially available distributor under single phase flow conditions (not 2-phase as in actual working conditions). He found that the commercially available distributor performed significantly worse than the distributors considered here. To quantify this, he used a "mass uneven distribution rate" as defined by equation (8). The mass uneven distribution was 345 percent for the commercially available distributor, while it was 34.3 percent for the type 5 distributor.

$$\mathcal{E} = \frac{\sqrt{\sum_{i=1}^4 (\dot{m}_i - \dot{m}_{average})^2}}{\dot{m}_{average}} \quad (8)$$

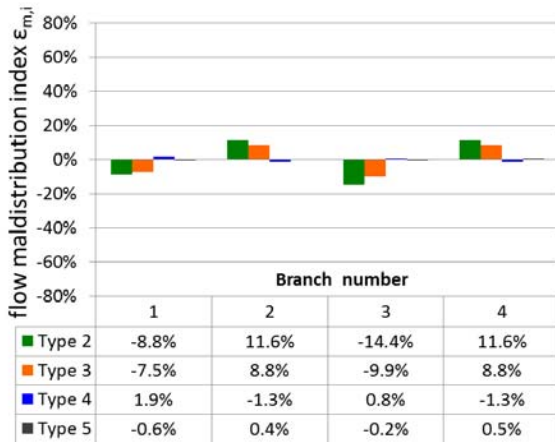


Figure 83: Two-Phase Simulation, Several Distributors, Horizontally Installed, Data Adopted from Graph 7 of Li et al. 2005; Estimated Maximum Uncertainty Caused by Reading from Graph 0.1%

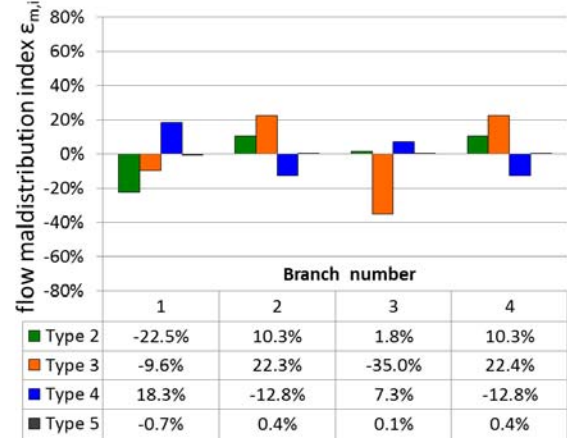


Figure 84: Two-Phase Simulation, Several Distributors, Vertically Installed With Orifice 3.7° Misaligned, Data Adopted from Graph 7 of Li et al. 2005; Estimated Uncertainty Caused by Reading 0.2%

2.9.2 Estimate of Performance Penalty for Distributors

With regard to estimating the performance penalty of distributors, there are two cases of interest:

- A) Using the semi-empirically obtained distribution factors to estimate the resulting performance penalty → validation of model and semi-empirical approach.
- B) Using results from Li et al. (2005) to determine the reduced performance penalty of improved distributors.

For the simulation of the performance degradation caused by the unequal refrigerant distribution between the circuits, the distribution factors from “Refrigerant Maldistribution Effects for Clean-Coil”, page 61 ff. were used. Additionally the superheat for the different cases was adjusted as given in

Table 2. For the simulation of the cases where the performance of the distributors of Li et al. (2005) was used, the superheat was assumed to be the same as for the hybrid control cases. This was done, since the maldistribution as determined for the distributor by Li et al. (2005) is smaller than observed for the TXV and EXV control cases and therefore the superheat will likely be more stable resulting in a lower obtainable value for steady-state tests. Note: For practical applications, superheat values on the order of 3-4 K will be difficult to obtain, since operating conditions will usually not be steady.

Table 2: Overall Superheat Settings for Simulation

Type	Source	Value [K]	Note
Equally distributed flow	Hybrid clean-coil steady tests	3.0	
EXV	EXV clean-coil steady tests	3.9	
TXV	TXV clean-coil steady tests	9.4	
Simulated Li et al. (2005) cases	Hybrid clean-coil steady tests	3.0	only small maldistribution of refrigerant, therefore small superheat

Note: for practical applications, superheat values on the order of 3-4 K will be difficult to obtain, since operating conditions will usually not be steady.

2.9.3 Case A: Semi-Empirically Determined Distribution Factors

Figure 85 shows simulation results for the performance degradation due to refrigerant side maldistribution. Similar to the experiments, shown in Figure 86, the TXV controlled system has a larger COP and capacity degradation compared to the equally distributed flow than the EXV controlled system. COP and Capacity degradation decrease for both control schemes with increasing ambient temperature. The 46°C EXV controlled case of the experiment is an exception to this. The large measurement uncertainty for the comparison of 2.2 percent is part of the reason for this. Another issue is that there was likely small airside maldistribution, which can either reduce the effect of refrigerant side maldistribution (similar flow maldistribution indexes on both sides) or increase it (dissimilar flow maldistribution indexes). This was essentially shown in Figure A 5, where identical flow maldistribution indexes on air and refrigerant side ("Equal flow") lead to a much better performance than dissimilar ones ("uncompensated" – no flow maldistribution on refrigerant side). Since the differences in performance are very small, the small differences in individual coil circuiting as can be seen in Figure A 5, page 192 will have an impact on the results as well. Figure 87 shows the residuals, as defined by equation (9). The residuals are within less than 2 times the previously mentioned experimental uncertainty of 2.2 percent.

$$dif = \text{Value of simulation} - \text{Value of experiment} \quad (9)$$

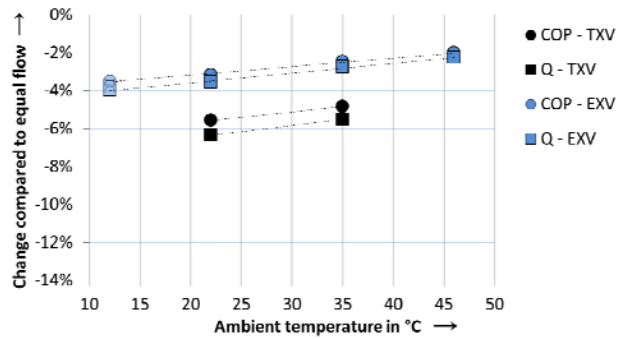


Figure 85: Simulation Results Compared to Equally Distributed Flow¹⁰

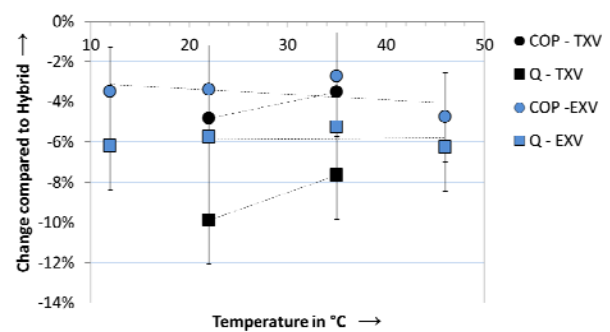


Figure 86: Experimental Results Compared to Hybrid Base Case

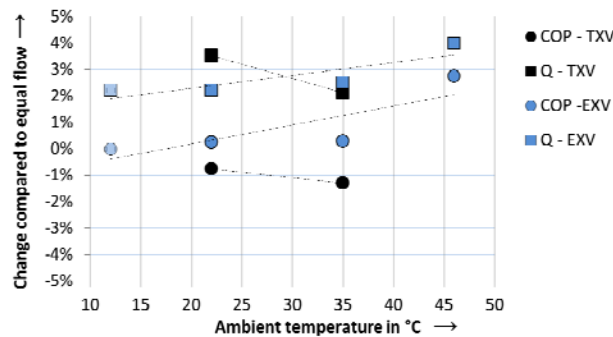


Figure 87: COP And Capacity Change Residual

2.9.4 Case B: Simulated Distribution Factors

Figure 88 through Figure 91 show the effects of the refrigerant maldistribution as simulated by Li et. al (2005). In all the cases, the COP and Capacity degradation are less than what was determined for the EXV. For the Type 5 distributor, the degradations are negligible for both cases. The same is true for the Type 4 distributor in vertical orientation with misaligned orifice. While this suggests that there is not significant room for improvement, one has to be reminded of the assumptions that were made by Li et. al (2005), which do not consider the influence of the expansion valve upstream of the evaporator and potentially different pressure drops through different circuits and distribution lines.

¹⁰ The points at 12°C ambient temperature were calculated using the refrigerant distribution factors from the 22°C EXV case.

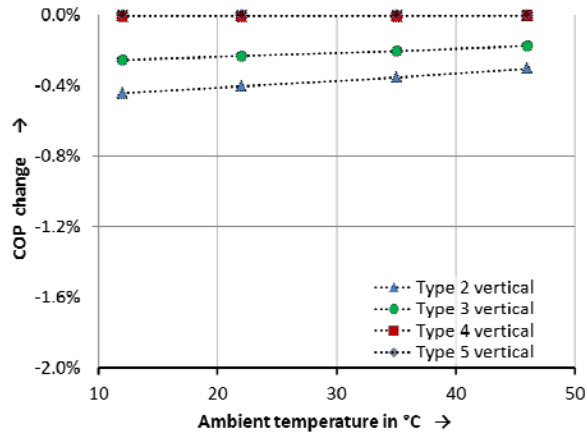


Figure 88: COP Degradation for Vertically Oriented Distributors with Misaligned Orifice

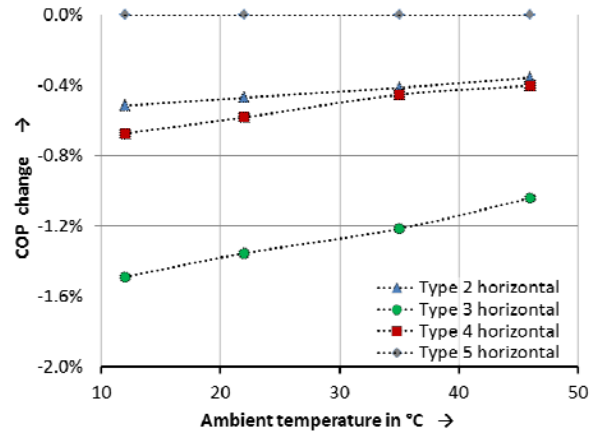


Figure 89: COP Degradation for Horizontally Aligned Distributors with Non-Misaligned Orifice

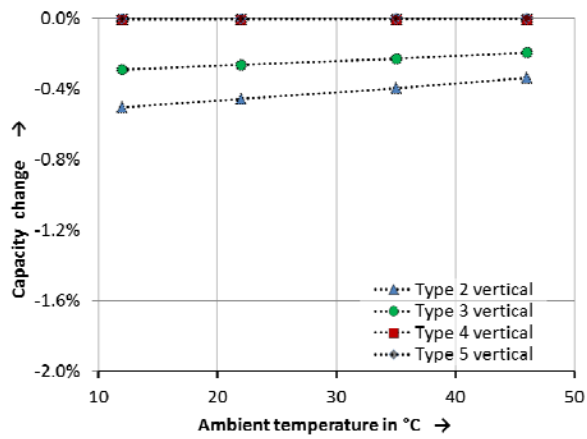


Figure 90: Capacity Degradation for Vertically Oriented Distributors with Misaligned Orifice

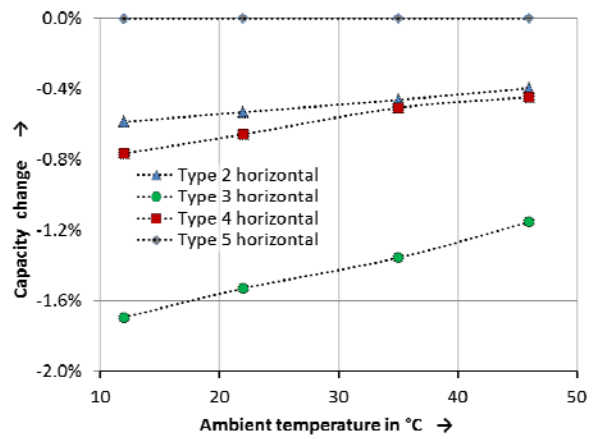


Figure 91: Capacity Degradation for Horizontally Aligned Distributors with Non-Misaligned Orifice

2.10 Conclusions, Future Work and Recommendations

For the 3-ton large room cooling system with clean-coil conditions, the hybrid control led to a 4 percent improvement in COP and a 6 percent improvement in capacity when compared to the EXV controlled baseline system. These performance improvements had negligible dependence on ambient temperature if the hybrid control scheme was applied. A frost-up test showed that the inbuilt TXV led to unacceptable hunting, which was not an issue for the EXV and hybrid control. The hybrid control extended the runtime for the frost-up test by approximately 12 percent compared to the EXV, a result that has to be taken with caution due to slightly different operating parameters which could have influenced the frost build up and led to an advantage for the EXV or hybrid control and non-optimal operation of the balancing valves for the hybrid control that led to a faster than necessary frost build-up test. Therefore, two different levels of a defined coil blockage were used to obtain a more repeatable result. These blockage levels were selected to lead to less performance degradation than observed after 8 hrs of continuous operation in the frost build-up test of the EXV. With blockage, the capacity of the EXV controlled system decreased by between 9 percent and 29 percent, depending on ambient temperature and level of blockage. For the blocked-coil cases, between 57 percent and 90 percent of the lost COP and 74 percent to 100 percent of the capacity were recovered if the hybrid control scheme was used instead. A bin analysis was performed to evaluate the yearly energy savings. Since, no statistically relevant values for a maldistribution as function of operating conditions are available, the clean-coil case was chosen for the bin analysis. The yearly energy consumption reduction was on the order of 2 percent, which is less than one would expect from the 4 percent improvement in COP mentioned earlier. The reason for this is a significant amount of indoor fan power consumption, which runs continuously. However, the 2 percent reduction in total energy consumption is based on pristine coil conditions. Clean coil conditions will not be applicable during the operational lifetime of the system and there would be additional energy savings.

An estimate of the simple payback period for the hybrid control scheme can be found on page 155.

Chapter 3:

Domestic Heat Pump

The 5-ton domestic heat pump was tested in heat pump mode only. Tests were conducted with clean outdoor coil and with partial blockage of the outdoor unit coil air inlet grille. Additionally, frost build up tests were conducted.

3.1 System Description

The 5-ton domestic heat pump consists of an outdoor unit, as shown in Figure 92, and a separate indoor unit, as shown in Figure 93.

The indoor unit contains an HX coil, which is designed as an evaporator. In AC mode, the inbuilt TXV controls the superheat while in HP mode, a check valve in the TXV allows for operation as a condenser. The indoor fan has an electronically commutated (EC) motor that is programmed to deliver a constant flowrate over a wide range of static pressures.

The outdoor unit contains an HX coil, which is designed as a condenser for AC mode. In HP mode, the HX is run in reverse and used as an evaporator. A standard venturi type distributor is used. The HX coil has 9 circuits of which 4 have 10 tubes and 5 have 8 tubes. Two of the circuits that are 10 tubes long are located at the top, while the remaining two are located at the bottom of the HX coil. The number of tubes is approximately proportional to the airside surface area. The HX has two rows, and is operated in cross counter flow in AC mode. In HP mode the HX is operated in cross parallel flow. An orifice-check valve is used as expansion device for HP mode in the original configuration. A four way valve is used to switch the scroll compressors discharge and suction side to be able to run in HP and AC modes. The outdoor unit is equipped with a suction accumulator.



Figure 92: Heat Pump Outdoor Unit

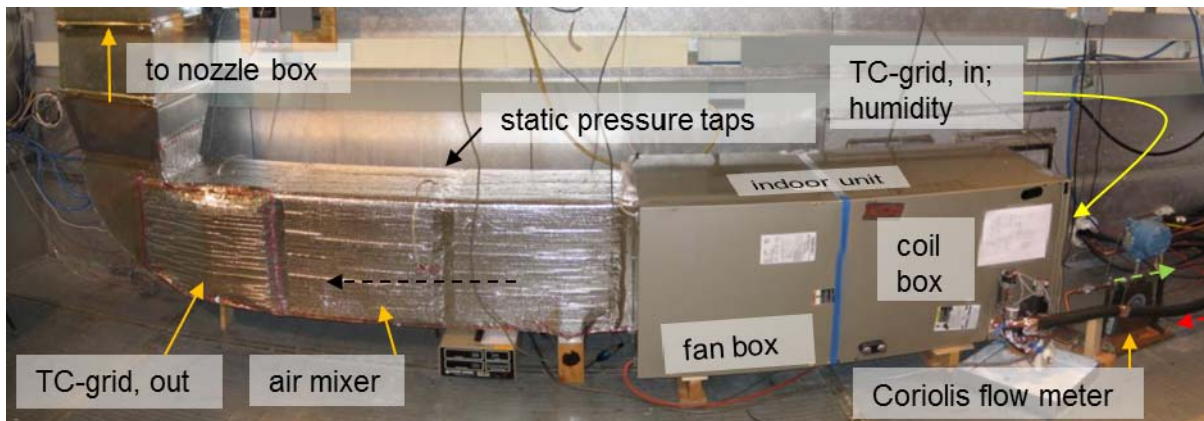


Figure 93: Indoor Unit and Instrumentation

3.1.1 Controls

In standard applications, the system is controlled by a thermostat. The control signals are fan, heating and cooling. For each of the different modes, the indoor fan motor delivers a different volumetric flowrate. For the purpose of testing, it was programmed to run as HP-system in comfort mode. This results in a ≈ 1680 cfm ($\approx 0.8 \text{ m}^3/\text{s}$) flowrate (≈ 336 cfm/nominal ton), which is not the most efficient operation but the commonly preferred one due to reduced indoor noise and draft. In HP mode, no defrost is conducted if the coil temperature is above 0°C , sensed by a bimetallic switch clipped onto one of the circuit inlets of the outdoor HX coil. Once the sensed temperature falls below 0°C , an internal timer starts counting. After passage of a selectable time

of 30, 60, 90 (factory setting) or 120 minutes, a defrost cycle is initiated. For defrost, the HP is switched to AC-mode and heat from the building is used to defrost the outdoor coil. The defrost cycle ends after 10 minutes have passed or after the measured temperature exceeds 0°C.

3.1.2 Instrumentation, Cycle

Refrigerant pressures and temperatures were measured at the state points indicated in Figure 94 to determine the refrigerant state. For the positions indicated in the diagram, immersion thermocouples, type Omega TMQSS with accuracy of 0.5°C, were used. The temperature measurement TO1.2 was relocated in the hybrid control scheme to measure the inlet temperature to the top circuit of the HX. In the EXV configuration, the balancing valves O2.1 to O2.9 were not present to avoid changes of the flow distribution, since the goal here was to test the unit as is without any changes to the existing maldistribution. Pressures were measured with Setra type 207 gauge pressure transducers with an accuracy of 0.13 percentFS. 500 PSIG transducers were used on the high pressure side and 250 PSIG transducers were used on the low pressure side of the system¹¹. Subcooled refrigerant mass flowrate was measured at the condensing unit outlet with a Coriolis mass flow meter of type Micromotion CMF025 with an accuracy of 0.1 percent of the measured flowrate for the applicable range. Compressor and controls power consumption (24V supply for solenoid and HP controls) was measured with an Exceltronic XL5C5A2-8-1 single-phase Watt transducer. Outdoor fan power consumption was measured with an Exceltronic XL5C5A2-1-8 power transducer. Both power transducers have an accuracy of 0.2 percent of reading plus 0.5 watts. Indoor fan power consumption was measured with a Pearson current transformer type 411, where a fixed power factor and voltage was used to obtain real power. Voltage and power factor were obtained initially using the outdoor fan power meter and the measured line voltage using an Extech EX505 multimeter with a base accuracy of 0.5 percent. This was done at a static pressure similar to the one used for the tests to prevent measurement error caused by changes of the power factor for different fan loads.

¹¹ Low and high pressure side as occurring in heat pump operation of the system.

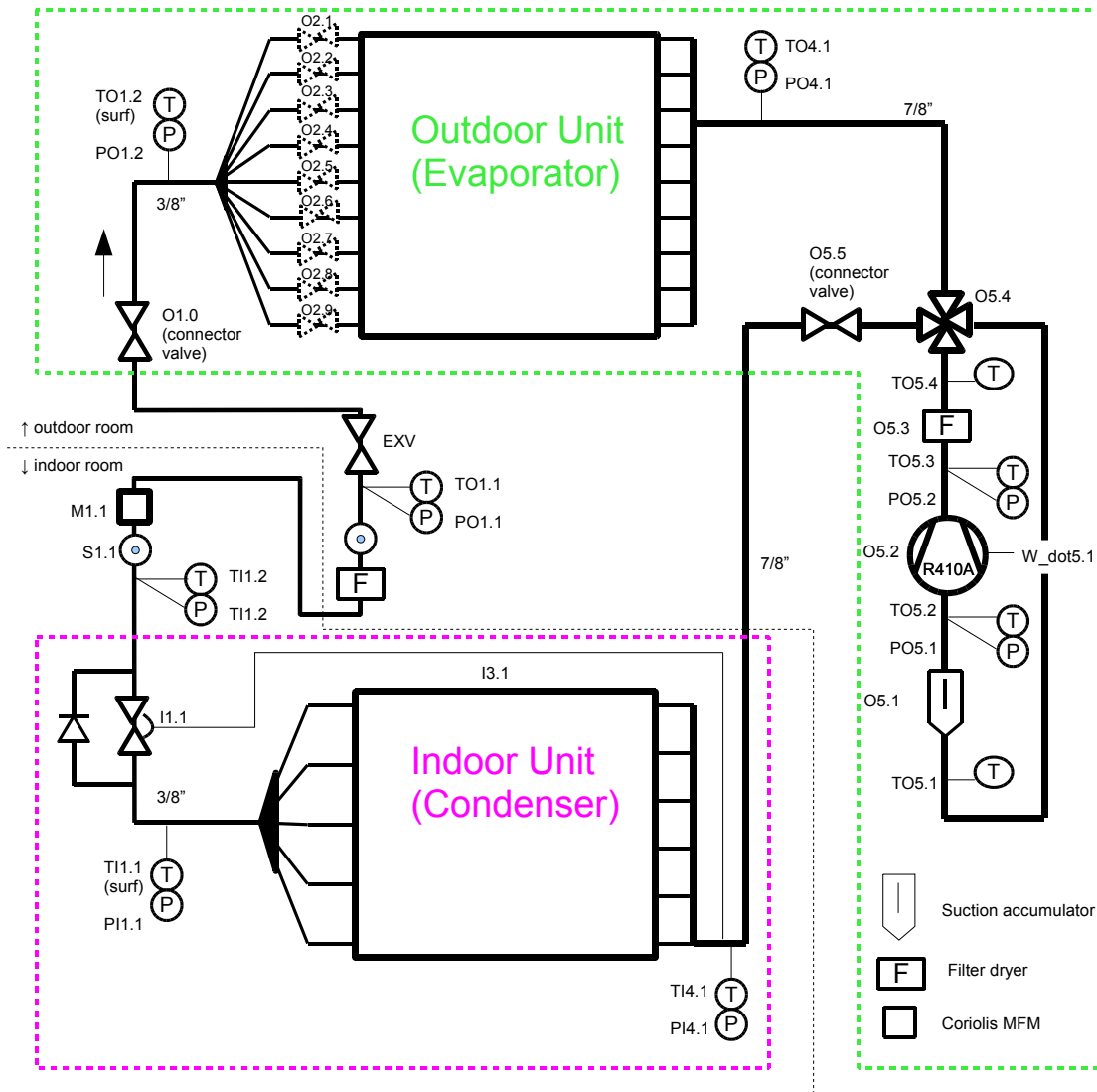


Figure 94: Heat Pump System Schematic with Instrumentation, Cycle Level

3.1.3 Instrumentation, Outdoor Unit

Additionally to the instrumentation shown in Figure 94, the outdoor unit was equipped with return-bend measurements and airside measurements. The return-bend temperatures are measured at each return-bend from the third return-bend on to the exit (for HP-operation) using DS18B20 digital temperature sensors with an accuracy of 0.5°C and a resolution of 0.01°C. Figure 95 shows the coil circuitry schematic with the measurement positions. The coil inlet temperature was measured with an equidistant grid of 3 by 9 thermocouples of 0.5°C accuracy. The unit exit temperature was measured by a 2 by 4 thermocouple (each 0.5°C accuracy) grid that was spaced to cover equally sized sections of the fan exit flow area. Air inlet humidity was measured with a General Eastern dew point monitor model D2 with an accuracy of 0.2°C. The air was sampled from four equidistant points at the middle of the inlet grille of the unit using a tube- and orifice device. Additionally, the relative humidity was measured with a Vaisala HMP233 relative humidity sensor with an accuracy of 1 percentRH at one corner of the inlet grille.

3.1.4 Instrumentation, Indoor Unit

Additionally to the cycle level instrumentation, airside inlet and outlet temperature, static pressure and air flowrate were measured, as shown in Figure 93. The inlet and outlet temperatures to/from the unit were measured by a 3 by 3 grid of equally spaced thermocouples with an accuracy of 0.5°C. At the inlet, the temperature was measured directly before the air filter, at the exit it was measured after a mixing device. The duct section between the mixing device and the temperature measurement was insulated with one layer of R7.5 Foamular 150 insulation foam that was additionally wrapped in two layers of R4.3 (minimum R-value given) Reflectix double reflective bubble insulation. The static pressure was measured before the mixing grid using four ports that are connected with equal total line lengths to a Setra 2601MS1 differential pressure Sensor with an accuracy of ± 0.62 Pa for the selected 0.25" H₂O range which is equal to ≤ 1.3 percent of the measured static pressure. The same type of pressure transducer was used for the measurement of the airflow rate with a nozzle box. At the operating point the accuracy is 2.7 percent. The inlet condition to the nozzle was measured with a RTD grid, the pressure drop between ambient and nozzle inlet pressure at rated air flowrate and static pressure of the heat pump is used to obtain the inlet pressure to the nozzles. Air mixing device, flow measurement nozzle box and static pressure measurements were built in compliance with ASHRAE 37-2009. However, to reduce pressure drop, the baffles after the air mixing device were removed. The individual temperatures of the grid used for measuring the air outlet temperature of the unit were very well within the ± 0.5 K tolerances of the standard, which in part can be attributed to the design of the unit with significant air mixing in the fan and fan box.

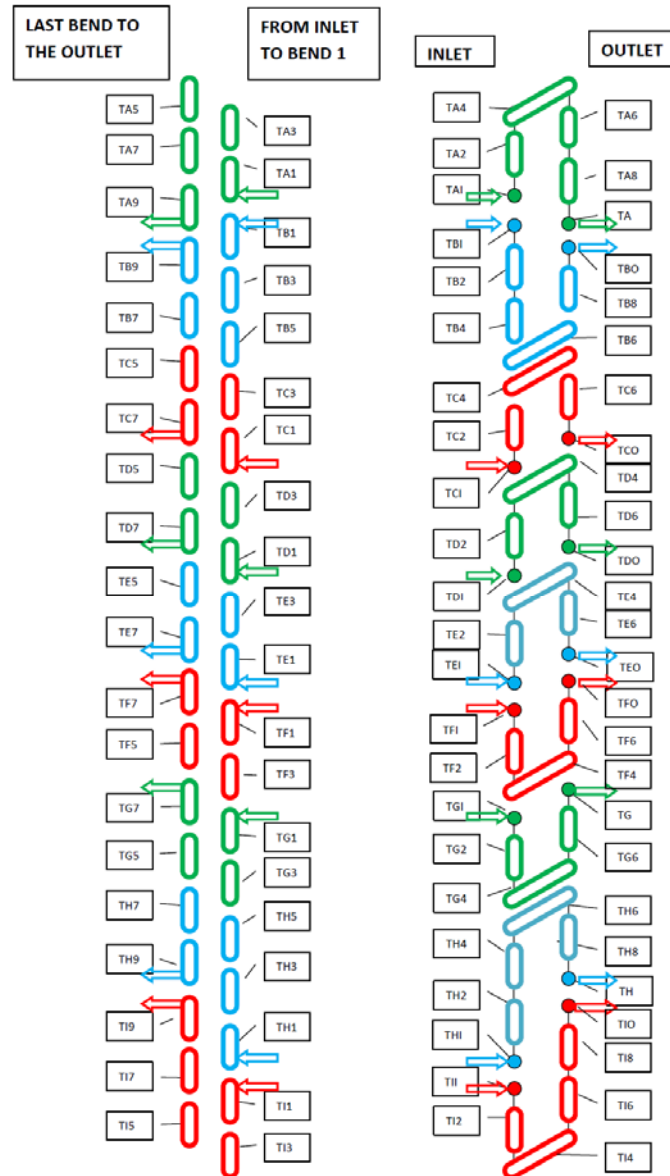


Figure 95: Evaporator Circuitry and Return-Bend Temperature Measurement Points

3.1.5 Performance Indices

Performance indices represent cooling capacity and efficiency. The following performance indices are used: Refrigerant side heating capacity, which is calculated as

$$\dot{q}_{Ref} = \dot{m}_{ref} \cdot (h_{cond,in} - h_{cond,out})$$

where :

$$\dot{m}_{ref} = \text{average refrigerant mass flowrate [kg/s], and}$$

$$h_{cond,in}, h_{cond,out} = \text{average enthalpy of refrigerant entering}$$

respectively leaving the indoor unit [kJ / kg].

(10)

The heating capacity \dot{q}_{ss} is calculated as

$$\dot{q}_{ss} = \dot{q}_{ref} + W_{i-fan}$$

where :

$$W_{i-fan} = \text{average indoor unit fan power consumption [kW]}.$$
(11)

The applicable standard, AHRI 210/240 (2008) specifies that all power consumption of the unit has to be included into the calculation of the coefficient of performance (COP). For the HP, it is therefore defined as

$$COP = \frac{\dot{q}_{ss}}{(W_{comp} + W_{controls} + W_{ccht}) + W_{o-fan} + W_{i-fan}}$$

where :

$$W_{o-fan} = \text{average outdoor unit fan power consumption [kW]}.$$

$$(W_{comp} + W_{controls} + W_{ccht}) = \text{average compressor, controls and}$$

crankcase heater power consumption [kW]

(12)

The crankcase heater consumption during the tests is 0 kW, since it is switched off as soon as the compressor is switched on. In part load operation it will be on during compressor off-times, if the ambient temperature is lower than approximately 85 F(29.4°C). The power consumptions of the EXV and the balancing valves were not included in the controls. This was done, since these, once optimized for low power consumption, will likely be negligible compared to the other power consumers in the system. For the frost-up tests, instantaneous values were calculated for each measurement point according to the previously shown formulas.

3.1.6 Selection of Control Schemes

The inbuilt expansion device for heat pump mode is a fixed opening orifice. The fixed opening orifice is considered to be replaced in all high performance heat pumps by better options within the next few years. Therefore, the inbuilt expansion device was not tested. Instead, an EXV was used as primary expansion device for the baseline, since the two high performing options are EXV and Hybrid control. The orifice type system will continue to

exist for several years in low cost baseline systems, which are not considered a possible applications for the hybrid control approach.

3.2 Steady State Tests

Steady-state tests were conducted to obtain a repeatable performance mapping of the heat pump. These tests were conducted with and without additional airside maldistribution. The purpose of the tests without additional airside maldistribution was to get the performance of a new unit without any refrigerant or airside fouling. This results in the lower limit of possible performance improvement for the Hybrid control scheme, if the different control schemes are compared. Table A 1 in Appendix A shows the test plan, which include extreme ambient temperatures. To get a controlled air-side maldistribution of the coil, the coil inlet was blocked using plastic foil as shown in Figure 96. The plastic foil covers the air inlet grille up to 50 percent of the height of the open part of the grille. Behind the grille, there is an air gap of about 1.3 cm, as shown in Figure 97¹². This air gap, together with the one between the two coils allows for a limited amount of airflow from the unblocked section to the blocked section of the coil. The benefit of the gap is that the amount of airflow passing the coil decreases from the top of the blocked section to the bottom of the blocked section due to pressure drop in the gap. This simulates the uneven distribution of coil blockage caused by frost, where most of the frost is often accumulated at the bottom of the coil where it refreezes after incomplete defrost, or caused by the accumulation of organic material, as shown in Figure 98. In this case though, most of the organic material accumulates at the top where it is protected from rain. Larger organic material, such as leaves during the fall, can also accumulate at the bottom of the coil if the unit is placed in a corner of a building. Figure 98 furthermore illustrates another problem common in AC and HP installations: the coil was hastily cleaned with a pressure washer, resulting in bend-over fins. These fins block the airflow, resulting in permanent airflow maldistribution.

As a result of the 50 percent air-inlet grille blockage, the evaporation temperature decreased and frost build-up was noted for the tests with room temperature below freezing. In between subsequent tests with blockage, complete defrost cycles were conducted, to limit the effects of frost build-up on the result. The same is applicable for the blocked-coil tests with hybrid control scheme.

Some of the tests were done with a different blockage, where the plastic foil only covers the inlet grille up to the humidity sampling tube. In this case, 44 percent of the inlet grille is blocked.

¹² The grille is loose when the top of the unit is taken off. The gap size was therefore calculated from the difference of the inner size of the lid and the size of the coil. For the picture, the gap is adjusted by hand to illustrate the calculated gap width.

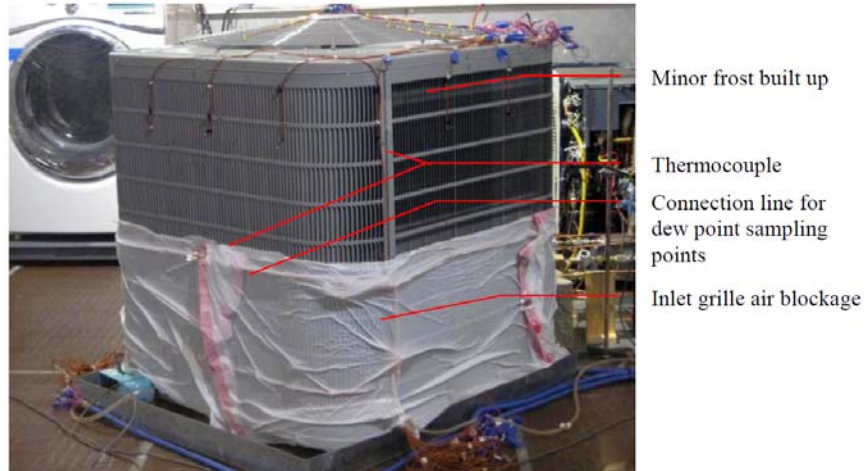


Figure 96: Heat Pump With 50% of Air Inlet Grille Blockage by Plastic Foil

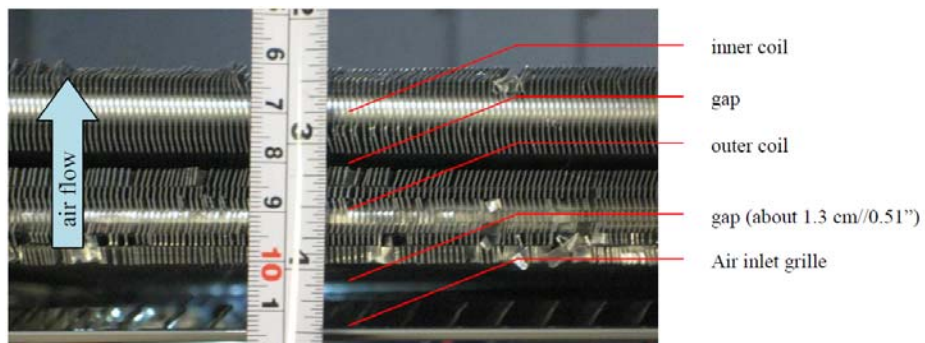


Figure 97: Spacing between Air Inlet Grille and Coil



Figure 98: Coil Blockage on a University maintained AC-Unit

3.3 EXV Control Scheme

For the EXV control scheme, one EXL-B1F valve, was used as primary expansion valve. The valve was controlled using the data acquisition and control software and a low cost open-source microcontroller and motor board combination. In the software, PI-control was used for the evaporation temperature, where the set point was adjusted during the test to account for changed system behavior and to obtain a low, but stable superheat. This reflects what an adaptive expansion valve controller will do in practical applications. To evaluate the best possible performance in heat pump mode, the system was charged up monitoring subcooling in heat pump mode rather than using the rated charging amount of 12.5 lbs. To obtain a subcooling of about 3.5 K, a charging amount of 9.45 lbs was necessary. In practice, higher subcooling is desirable due to faster charging time and longer recharge intervals in case of leaks in the field installation.

3.3.1 Steady State Tests

For the steady-state tests, it was possible to control the superheat to be within a band of 1 K, as shown in Figure 99 to Figure 101. For the -8.3°C test, the superheat slowly increased during the experiment. This change is caused by a minor decrease in evaporation temperature, which is not noticeable in Figure 100. The COP does not vary with time, so that the validity of the test is given. Due to capacity limitations of the psychrometric rooms, it was not possible to reach the lowest required temperature of our initially proposed test plan. Instead of this, we used the lowest achievable temperature, which was -20°C for the blocked and unblocked steady-state tests. The capacity limitation of the psychrometric rooms also resulted in a higher outdoor room humidity than proposed in the initial test plan. Minor frost build up occurred as a result.

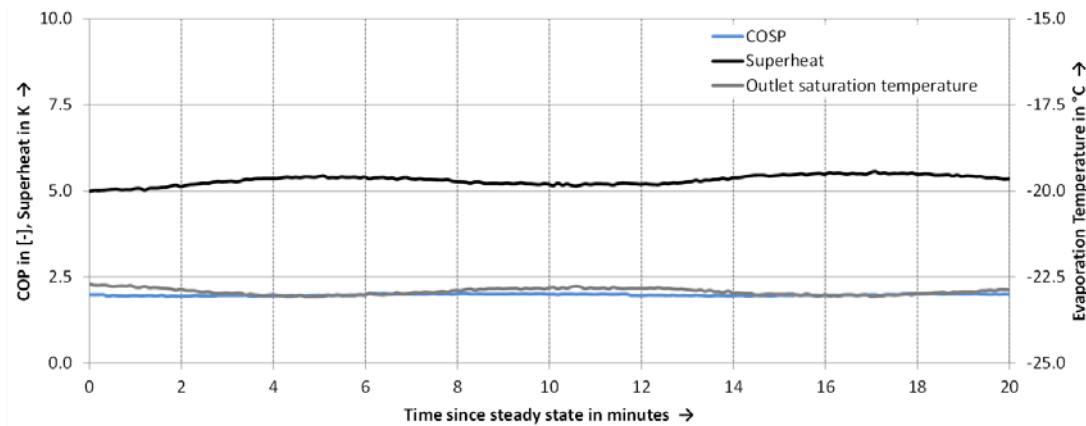


Figure 99: Superheat and Evaporation Temperature, -20°C ambient, EXV

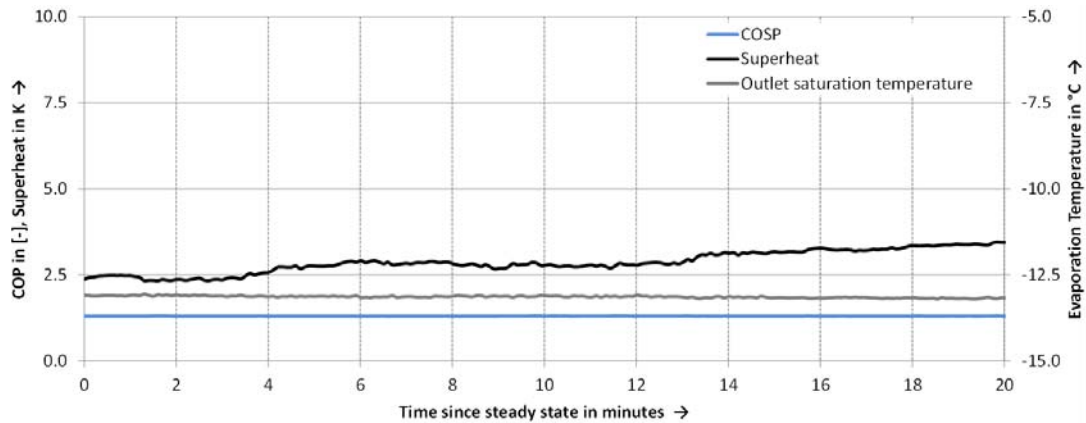


Figure 100: Superheat and Evaporation Temperature, -8.33°C ambient, EXV

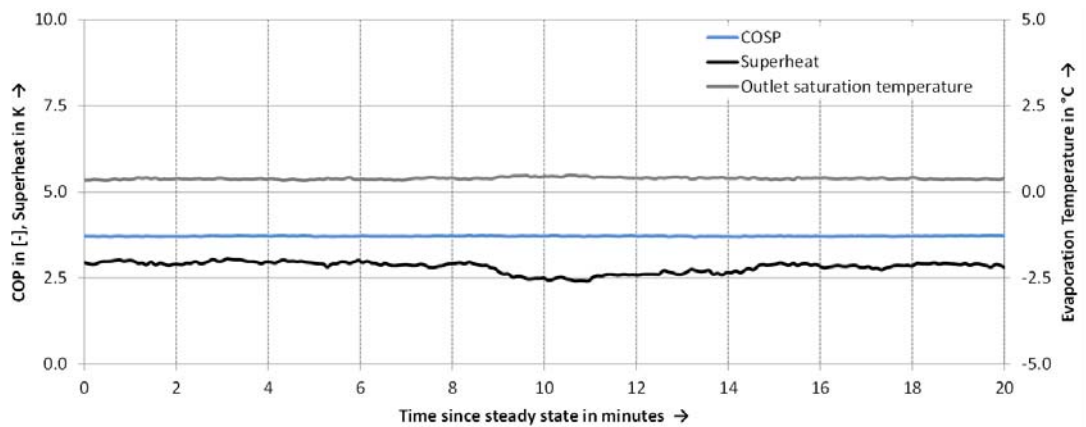


Figure 101: Superheat and Evaporation Temperature, 8.33°C Ambient, EXV

It was found, that the average value of the return-bend temperatures cannot be directly used for the determination of the coil surface usage. Figure 74, as an example, shows the measured return-bend temperatures for the -20°C ambient temperature case. The first point in this graph, at position 0, is the inlet temperature of the distributor. Circuits C, D, F, and G are shorter than circuits A, B, H and I. Their exits are therefore at position 8 and not at position 10. In contrast to the graphs of the LRCS, no plateau for the evaporation temperature is visible. The reason for that is that the outdoor coil is designed as condenser with the tube diameters optimized for condensing mode. This means that the Reynolds number has to be sufficiently high for refrigerant at condensing pressure and the resulting high vapor density. If the outdoor coil is operated in HP mode, the pressure, and therefore the vapor density are much lower. This leads to much faster vapor velocities and by that to higher pressure drop. This explains why the superheated evaporator exit temperature is lower than the saturated inlet temperature to the distributor and similar to the average temperature at the third return-bends. If the refrigerant is

not fully evaporated, it is at the saturation temperature corresponding to the pressure at the return-bend. The temperature along the flow-path, therefore, decreases from elbow to elbow¹³.

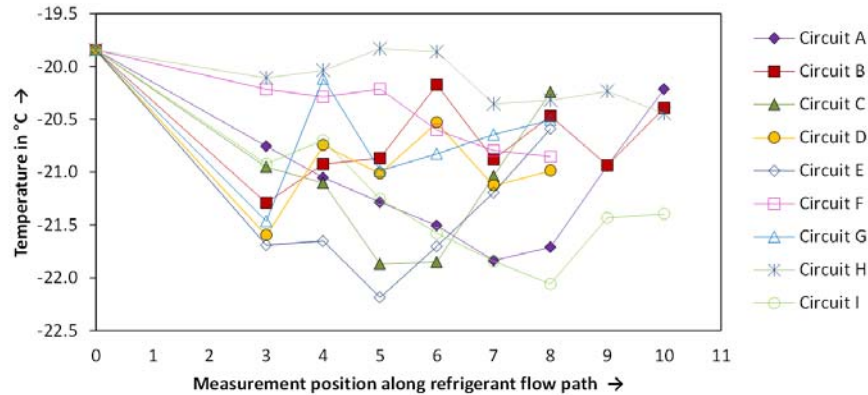


Figure 102: Return-Bend Temperatures, -20°C Outdoor, 21.1°C Indoor Temperature

Once the refrigerant is superheated, heat transfer from and along the tube gets more important. Since the heat transfer coefficient for superheated refrigerant is much smaller than for evaporation, the measurement then deviates more from the temperature of the refrigerant, due to heat conduction along the bend. This means that the temperature of neighboring tubes influences the measured temperature of the return-bend. When considering only the trend in temperatures, then it can be concluded that circuits A and I get superheated between the 8th and 9th return-bend, circuit B between the 3rd and 4th, and circuit F does not get superheated at all. Circuit B has large deviations between the measurement along this path, and a guess is that it superheats between positions 3 and 4.

Obviously it is doubtful if the first superheated position in each refrigerant stream is selected appropriately when only the absolute and average values at the return-bend temperatures shown in Figure 102 are taken into consideration. Figure 103 shows how the temperatures of the 6th return-bend change over the course of the experiment. Circuit C and E show the typical behavior when liquid reaches a return-bend: a flat section (two-phase refrigerant) followed by a bump (superheated refrigerant). The other circuits show a much flatter profile and are therefore either entirely superheated or in two-phase.

To evaluate where superheated section starts, one can therefore search for the largest standard deviation in each of a specific circuits return-bend temperature profiles¹⁴. This method works

¹³ Due to different length of the return bends, as shown in Figure 95, the influence of the coil temperature onto the return bend measurements deviate. This and cross fin conduction leads to the zigzag shape noticeable in Figure 102.

¹⁴ The reason why standard deviation rather than span is chosen is that sometimes the first superheated section moves in between two return bends. The standard deviation captures much better where it is for the majority of the experiment.

well as long as the border between superheated and two-phase section swipes over the return-bend or gets close to it during the experiment.

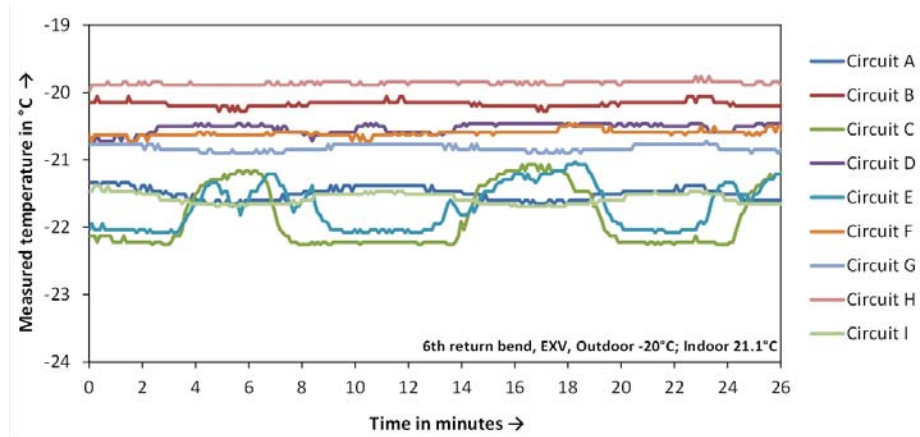


Figure 103: Measured Return-Bend Temperature for 6th Return-Bend, EXV, -20°C Outdoor/21.1°C Indoor Temperature

Figure 104 shows these standard deviations for the same data as shown in Figure 102 and Figure 103. The superheat for all circuits except for circuit H can now be determined simply by using the maximum standard deviation. For circuit H, this does not work: it is neighboring circuit I, which, at that point has a very large standard deviation and, from Figure 103, it is obvious that this tube was superheated before the 3rd return-bend: the temperature stays nearly constant and above the other circuits. If the circuit was entirely flooded, then its pressure drop would be higher and a more significant downwards slope would be noticeable.

Figure 105(a) shows the end of the two-phase section as a result of the evaluation of Figure 102 and Figure 104. Since measurements were only taken at return-bends, and the two-phase section might start in between two return-bends, the uncertainty has a maximum of ± 1 return-bend. Circuits A, I, and F use the available surface very well. Circuit G uses less than 50 percent of the available area for evaporation and circuit H is using approximately 30 percent of its surface area for evaporation. The position for circuit H had to be determined from the course of the temperature, since the standard deviation method failed. Figure 105(b) and Figure 106 show the end of the two-phase sections for the -8.3°C and 8.33°C ambient temperature tests, respectively. Circuit G is now oversupplied with liquid, while circuit H gets more liquid supply with increasing temperature, up to 50 percent of the surface is now used for evaporation. The supply to the other circuits changes less drastically.

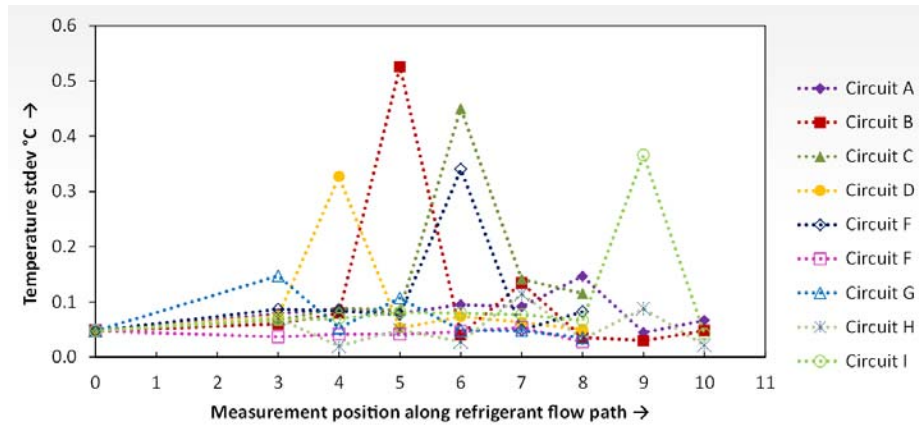
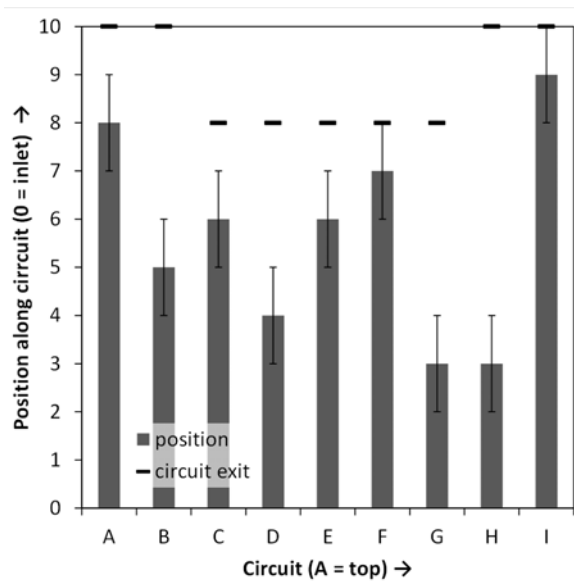
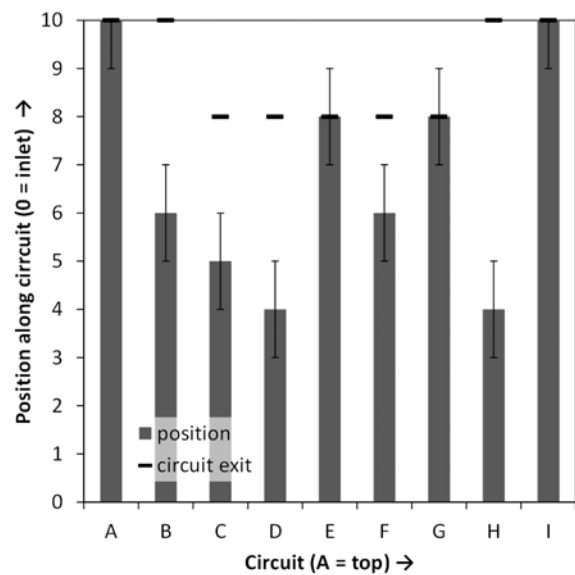


Figure 104: Standard Deviation of Return-Bend Measurements, EXV,



(a) -20°C Outdoor Temperature



(b) -8.33°C Outdoor Temperature

Figure 105: . Circuit Two-Phase Section End, EXV, 21.1°C Indoor Temperature

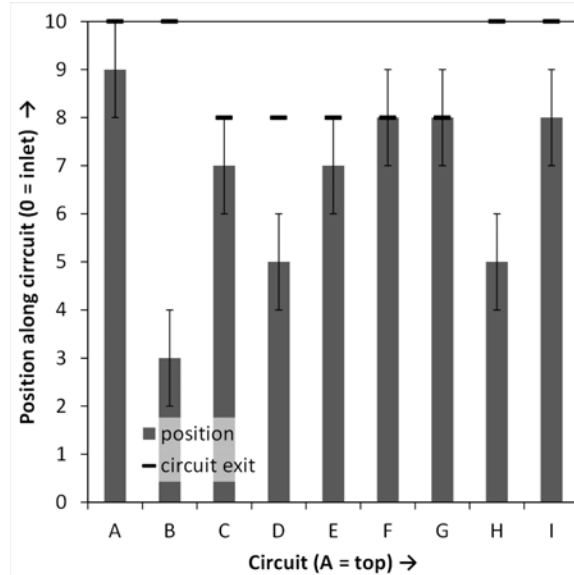


Figure 106: Circuit Two-Phase Section End, EXV, 21.1°C Indoor Temperature, 8.33°C Ambient Temperature

One possible reason for the observed maldistribution with clean and unblocked-coil is that the two-phase connection line between expansion device and distributor is not straight. Li (2001) came to the conclusion that, for a four-branch distributor, depending on the type of distributor and considering a misalignment of 3.7° of the flow into the distributor, the flowrate in each branch can change by as much as +22/-35 percent¹⁵. He found that the largest flowrate does not necessarily coincide with the outwards side of the bend, depending on the type of distributor. The original expansion device of the DHP, an orifice that was mounted in the connector valve to the liquid line, was taken out and replaced by an EXV. The EXV was mounted in the liquid line, with the valve body center line about 4.5" from the nut of the connector valve, using the radial connection of the valve as outlet. The connection between connector valve and distributor is unchanged from the original condition as delivered by the manufacturer. Figure 107 shows the bends in the line leading to the distributor. There is a $\approx 90^\circ$ elbow A that directly follows the connector valve. After that, an 18° bend B is noticeable in the connection between line 1 and line 2. Line 1 has a pressure tap, which, if manufactured inaccurately, penetrates into the flow causing maldistribution. Line 2, which connects to the main body of the distributor, has a misalignment C of about 6° , Figure 108(a). The distribution lines, as shown in Figure 107(b), have the same length, but due to space constraints, they have a different number of bends. Circuits A and B have one 90° bend while all other circuits have an additional bend of about 180° . Note that Kaern et al., 2011 used a generic simulation model and found that different feeder tube bending decreases capacity and COP. They considered the effect to be insignificant compared to liquid/vapor maldistribution at the inlet to the distributor. Figure 108(b) shows a

¹⁵ Determined from the corresponding graphs in Li (2001).

view onto the distributor outlets from the top. The outwards sides of bends B and C are marked. From the results, it looks like circuits A, C, E, F, G, and I are preferred this fits to the outwards side of the two bends marked on the distributor - except for circuit I.

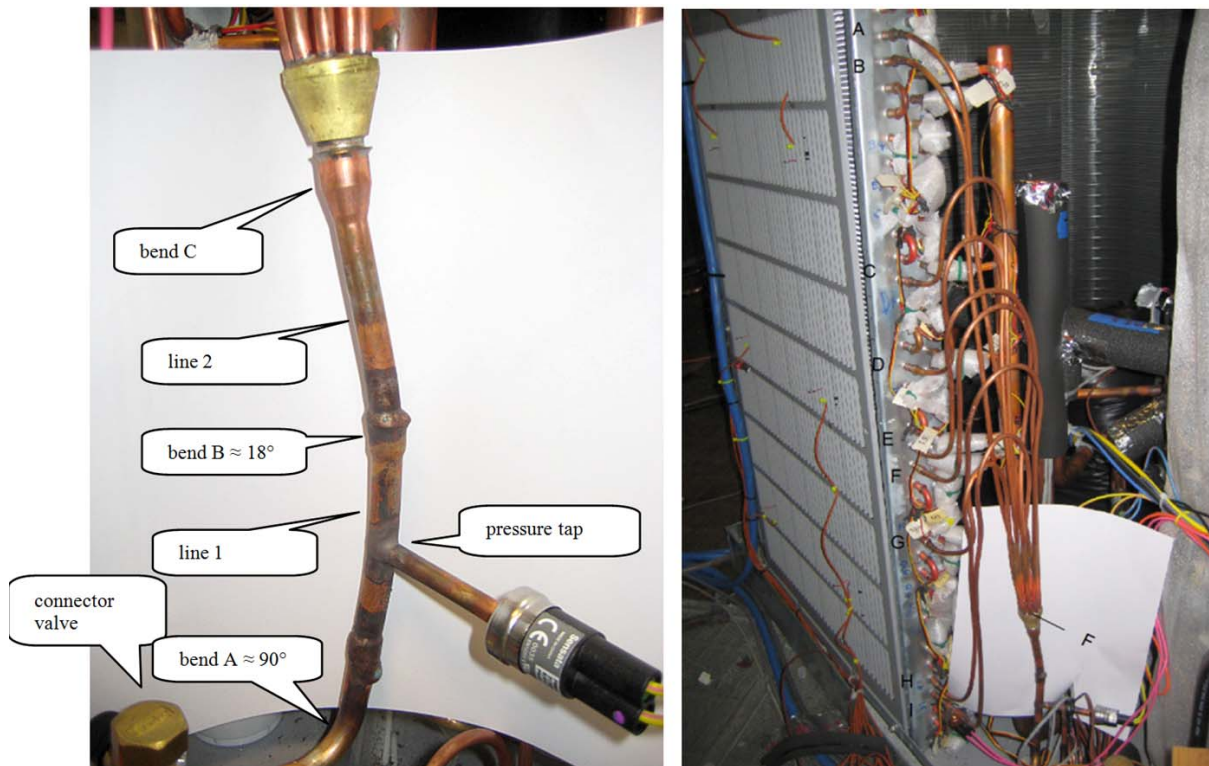


Figure 107: Distributor And Distribution Lines

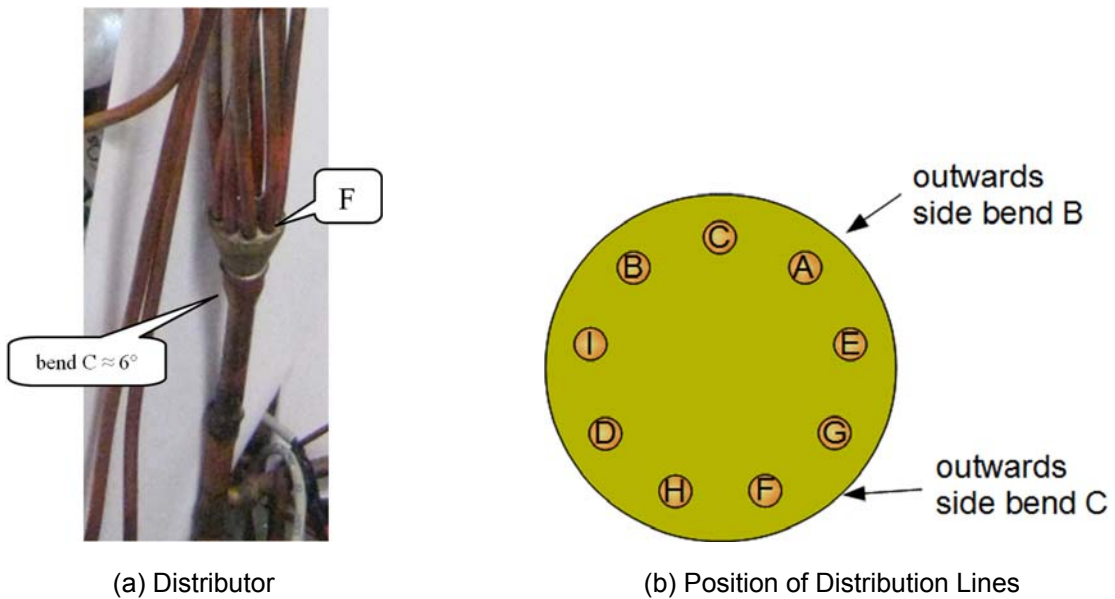


Figure 108: Distributor Details

Li (2001) came to the conclusion that gravity influences the distribution if the distributor is not aligned perpendicular to the flow direction this is also the case in the DHP and an additional source of maldistribution.

Figure 109 shows the individual circuit exit superheats for the three steady-state tests, including one repetition test. For each test, the exit superheats of circuit H and I are the same within the uncertainty of the measurement device. It can be concluded that the exit superheat is not a good measure for the coil surface usage. For the -8.3°C test, as shown in Figure 5.16, only 2/5th of circuit H are used, while circuit I is used entirely.

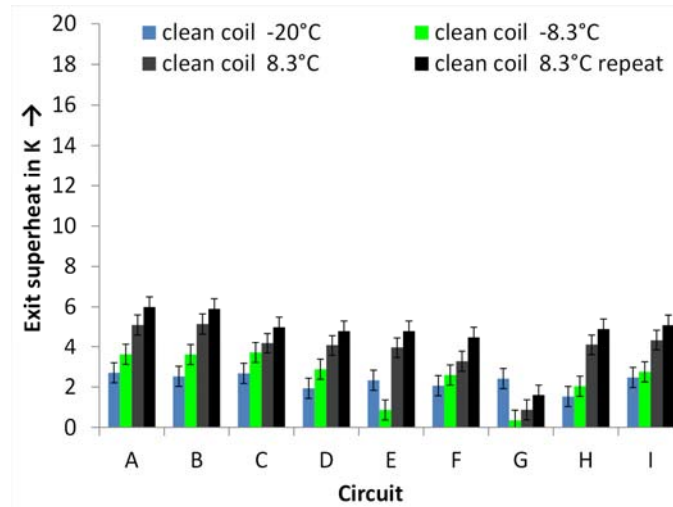


Figure 109: Individual Circuit Exit Superheat for Different ambient Temperatures.

3.3.2 Steady Test, Performance

Figure 110 shows the variation of COP and capacity with ambient temperature for the fixed indoor temperature of 21.1°C . Both, COP and Capacity increase with ambient temperature. COP increases from 2.1 at -20°C ambient temperature to 3.8 at 8.33°C ambient temperature. Capacity increases from 7.4 kW at -20°C to 16.3 kW at 8.33°C ambient temperature.

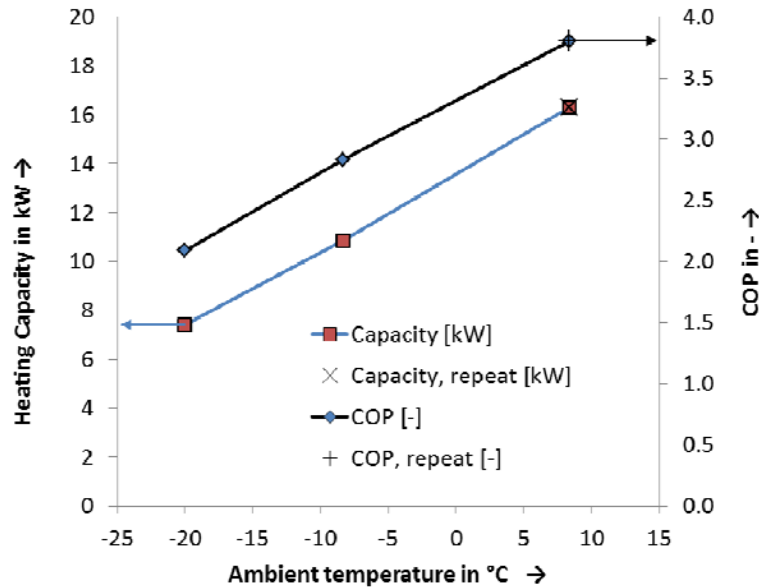


Figure 110: COP and Capacity, Clean-Coil, Steady State, EXV

The test at 8.3°C ambient temperature was repeated and very good repeatability was found. A smaller amount of frost build-up occurred on the coil for the -20°C test, due to the limited cooling and dehumidification capacity of the psychrometric rooms for that temperature.

3.3.3 Tests with Controlled Air Maldistribution

To obtain results with better repeatability, the coil was blocked up to a specified degree as described in the introduction to the heat pump. Figure 111¹⁶ shows that the two-phase section ends sooner for unblocked circuits and later for blocked circuits. The exception is circuit H which shows a similar behavior for clean-coil and frost-up tests. Circuits A, B, C, D, and circuit E in the 44 percent blockage case superheat before the third return-bend. At least one of circuits F, G, and I feed liquid into the suction header in each test. The refrigerant side surface usage of circuit I increases with decreasing ambient temperature. No consistent trend is noticeable for all other circuits. Figure 112 shows the individual circuit exit superheat. A very strong dependency of the superheat on ambient temperature is noticeable for all circuits, with exception of circuit G. Circuit G is the one that likely feeds liquid trough for all tests.

¹⁶ Circuits A, B, C, and D are already superheated at the third return bend, same for circuit E in 9.2C//44% blockage test

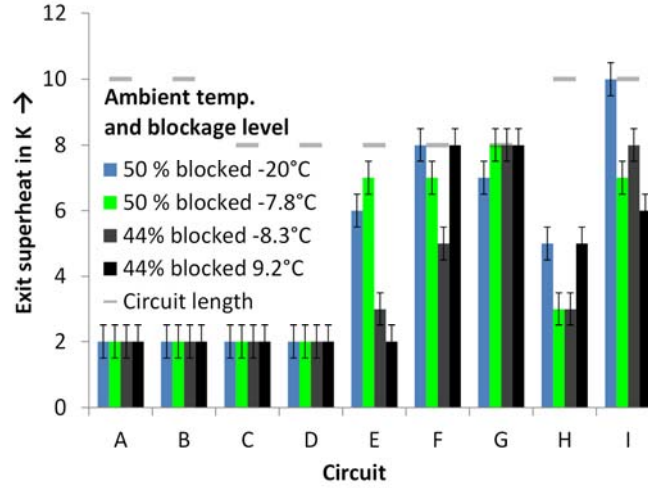


Figure 111: Coil Maldistribution for Blocked-Coil Cases, EXV

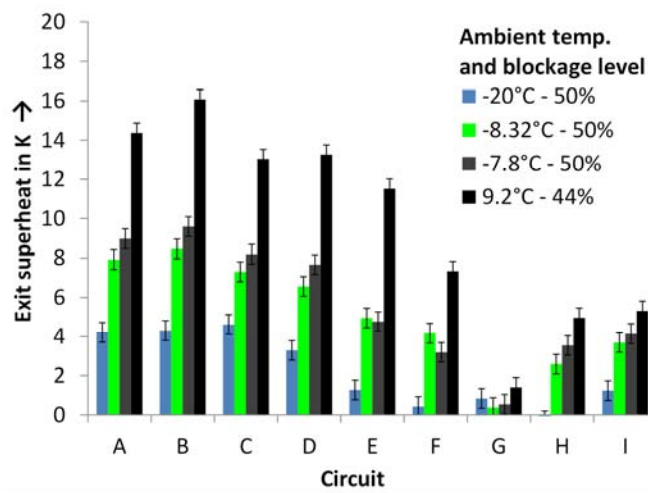


Figure 112: Individual Circuit Exit Superheats for Blocked-Coil Cases, EXV

The reason for the decreasing superheat with decreasing ambient temperature is that the air flowrate through the outdoor coil and the surface area A of the coil that is used for the actual evaporation process is approximately constant, Figure 111, while the transferred heat to the two-phase section decreases due to a lower compressor capacity at low evaporation temperatures. Note that the transferred heat is

$$\dot{Q} = k \cdot A \cdot \Delta T \quad (13)$$

Assuming that the overall heat transfer coefficient k is approximately constant,

$$\Delta T \sim \dot{Q} \quad (14)$$

This means that the temperature difference, which is the difference between air inlet and evaporation temperature decreases for decreasing amounts of transferred heat. For an idealized heat transfer problem (neglecting pressure drop and assuming a constant wall temperature), the superheat develops with exponential behavior as shown in Figure 113. The 100 percent value corresponds to the superheat, if the fluid reaches wall temperature. For the chosen parameters, the outlet superheat varies only little over a wide range of different values for the start of the superheated section. This essentially means that the outlet temperatures are approximately the same and close to the wall temperature. Essentially the same happened for circuits A through D in Figure 112. For the other circuits, different ends of the superheated section also influence the result. Circuit G feeds liquid into the suction header for most tests, which is the reason why the area of the evaporator is fixed in the first place: sufficient superheat needs to be provided by the other circuits to evaporate and superheat the liquid coming from that circuit.

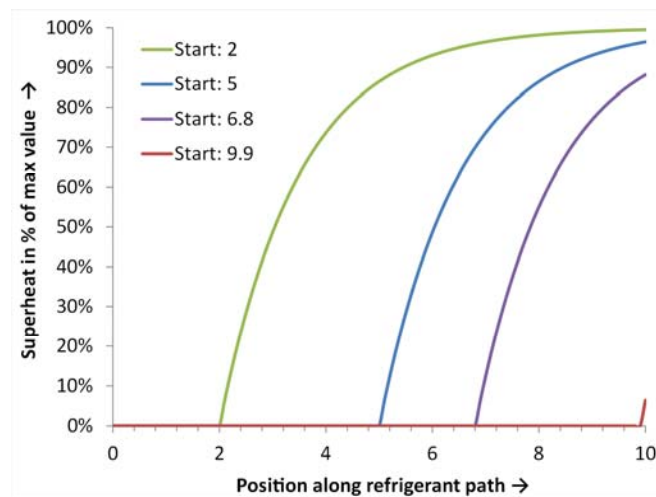


**Figure 113: Idealized Development of Superheat:
Exponential Behavior**

3.3.4 Results of Testing, Performance

The COP and capacity degradation with coil blockage increases with increasing ambient temperature, as it can be seen from the results shown in Figure 114. The reason for this is that the system capacity gets larger while the fraction of the coil that is used for evaporation approximately maintains its size as shown in Figure 111. In the unblocked case, the capacity available at -20°C ambient temperature is only 45 percent of the capacity available at 8.3°C. For the blocked tests, the system capacity is 6.7 kW at -20°C ambient temperature and 12.7 kW at 9.2°C ambient temperature which corresponds to 41 percent and 78 percent of the capacity of the unblocked 8.3°C test.

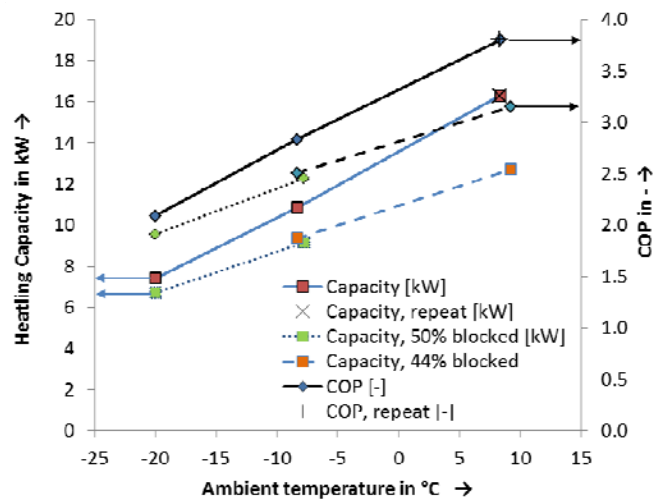


Figure 114: COP and Capacity for Blocked and Unblocked Cases, EXV, Steady State

3.3.5 Frost-up Test

For the frost-up test, the outdoor room target conditions were -8.33°C dry bulb temperature and high humidity. Figure 115 shows the actual room conditions during the experiment. In the first half hour, room temperature and humidity were stabilized. The maximum stable dew point was found to be -11°C .

Figure 116 shows that COP and capacity reached their maximum approximately 1 hour after startup. The main reason for this was that at that point, the superheat was low, while the evaporation temperature was high, as shown in Figure 117. At 1.9 hours after startup, the DAQ and control software crashed. As a result, the software and HP had to be restarted. The restart took about 8 minutes due to the startup delay of the HP. After another 10 minutes, the superheat was on the correct level again. This was also the case for the performance that was back to the trend shown in Figure 116.

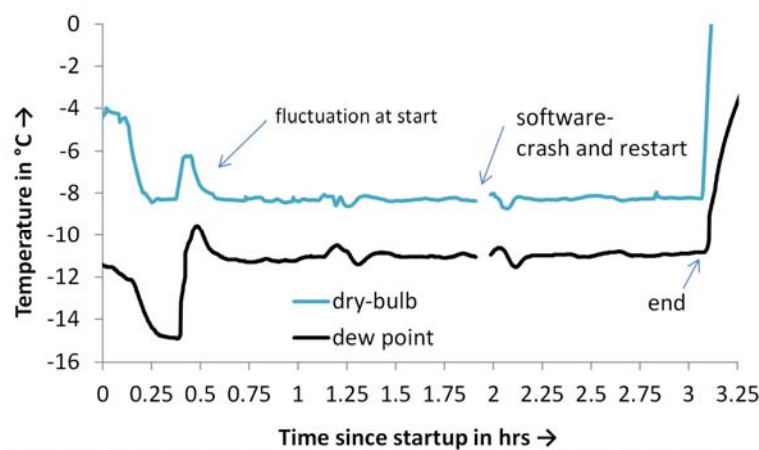


Figure 115: Outdoor Room Conditions, Frost-Up Test, EXV

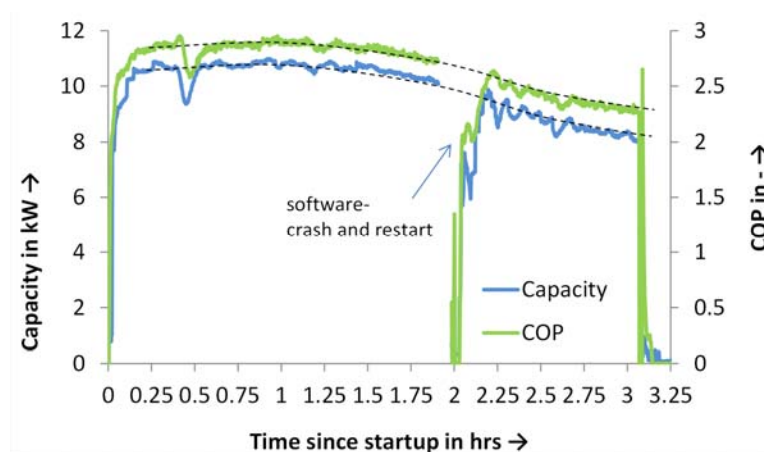


Figure 116: COP and Heating Capacity, Frost-Up Test, EXV

Figure 117 shows superheat and evaporation temperature as a function of time. The evaporator exit superheat at startup and after the software restart exceeded 10 K, while during most of the remaining operation, the evaporator exit superheat was kept between 1 and 8 K. After the start of the heat pump, the superheat at the compressor inlet was nonexistent for approximately 20 minutes. The reason for this was that liquid refrigerant entered the suction accumulator while the heat pump was switched off. This liquid was then metered into the suction gas by a small port in the accumulator, eliminating any suction superheat. The same happened after the software crash at about 1.9 hours since the heat pump was running uncontrolled until the software was back in operation. At 1.5 hours after startup, liquid refrigerant entered the accumulator due to insufficient evaporator superheat, resulting in a dip in compressor suction superheat. The evaporation temperature was subsequently reduced and the amount of liquid evaporating in the accumulator exceeded the amount of liquid fed into it, noticeable in the increasing suction superheat. At approximately 1.75 hours, the evaporator exit was superheated again. Smaller amounts of liquid were injected in the accumulator at 1.3 hours, 2.5 hours and 2.65 hours after the start of the experiment. Between 2.2 and 2.7 hours after the start of the experiment, large fluctuations in evaporator exit superheat occur, while after 2.7 hours to the end of the experiment, smaller but more frequent oscillations in the then lower superheat are noticeable.

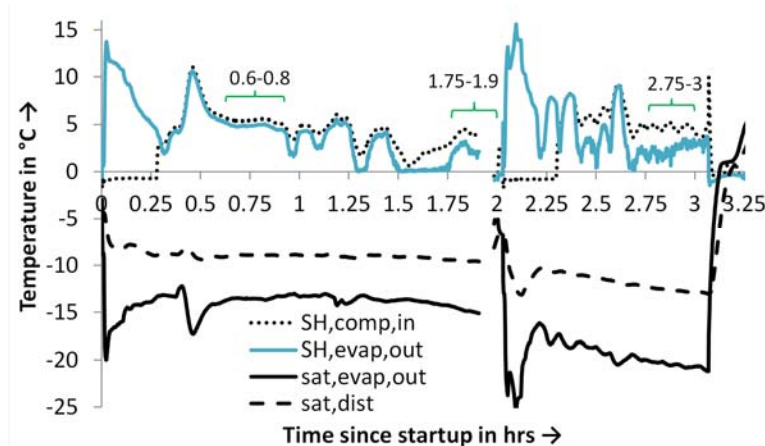


Figure 117: Superheat and Evaporation Temperature, Frost-Up Test, EXV

3.3.6 Coil Maldistribution

Figure 118 shows the end of the two-phase section for three different periods during the frost-up test. The superheat of the first period was approximately 2.5 K higher than for the other two periods, which had comparable superheat. The positions of the end of the two-phase sections are therefore shifted towards the beginning. In all periods, circuit H uses the coil the least.

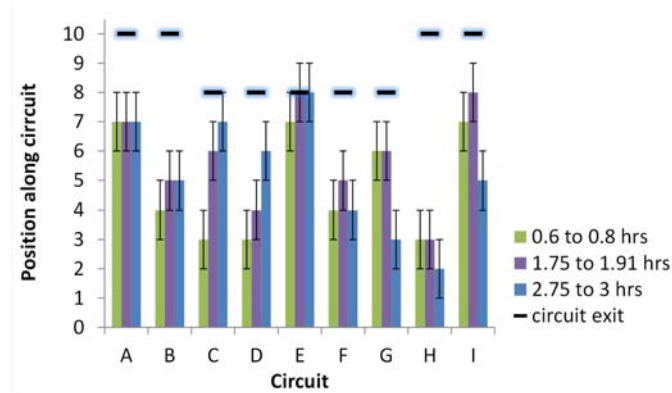


Figure 118: Circuit Two-Phase Section End, Frost-Up Test, EXV

This is also visible in the air inlet pictures shown in Figure 120: circuit H, which is the second circuit from the bottom, is frost free for the entire duration of the experiment. Circuit A has a similar issue, yet not as severe: at the end of the experiment it has a noticeable frost buildup. For all the other circuits, frost buildup is noticeable from 0.47 hours after startup. The pictures for the air inlet are taken from the side. Therefore, even a small amount of frost on the surface leads to a white color. As seen from pictures (e) and (c) in Figure 118, for the air outlet, less frost buildup is noticeable. The reason for that is that the coil operates in cross parallel flow if used in HP mode: the two-phase refrigerant first goes through the outer coil and then through the inner coil before it enters the suction header. Since humidity is removed at a greater rate at the outer coil, less humidity is left for the inner coil, which might not freeze onto the coil if enough superheated circuits are close to two-phase circuits. The very bottom of the inner coil therefore has no visible frost build up, even at the end of the experiment. Figure 119 indicates that circuit E feeds liquid out. This fits, especially for the last period, when checking the evaporator outlet superheat, as shown in Figure 117. This circuit has a much higher high-frequency noise in the last period compared to the first period, which is caused by slightly different amount of liquid that were fed into the suction header. According to the results, the end of the two-phase section does not have any significant sensitivity to the total length of the circuit. The additional lengths of circuits A, B, H, and I are therefore not used to significantly improve the performance of the system in HP mode. The end of the two-phase section for the different circuits changes over the course of the experiment. While it increases for circuits C and D, it decreases for circuits G, H and I.

Figure 119 shows the individual circuit exit superheats over the course of the experiment. Up to approximately 0.9 hours and excluding initial fluctuations caused by the fluctuating room temperature, none of the circuits feeds liquid into the suction header and the individual circuit exit superheats are within a band of less than 1.5 K. Between 0.9 and 1.7 hours, circuit G and circuit E change between feeding liquid through and having superheat, which causes the rapid changes of overall (evaporator outlet) superheat seen in Figure 117. Between 1.7 hours and the software crash, circuit E constantly feeds liquid through, and since the room temperature is relatively steady, the overall superheat in Figure 117 is relatively steady as well. At about 1.75 hours, circuits I and H show a trend of increasing superheat. This is a result of increasing frost

build-up on the remaining circuits that require the evaporation temperature to be lowered to obtain a sufficient overall superheat. Since the frost buildup mainly occurred at the shorter coils, the airflow is throttled on those coils while it increases on circuits H and B.

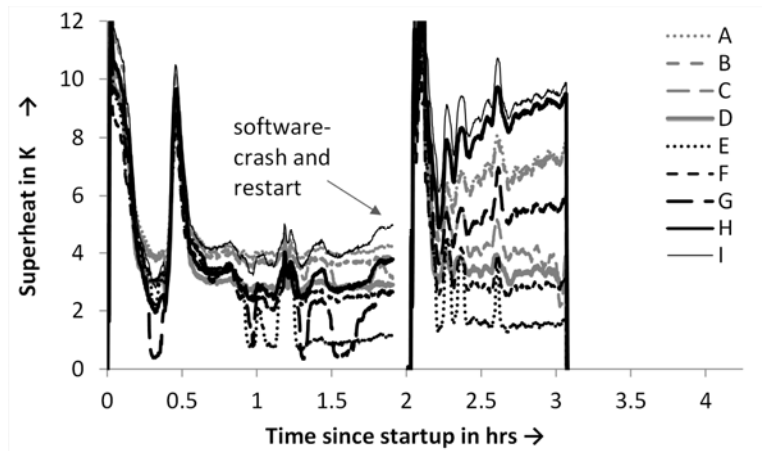
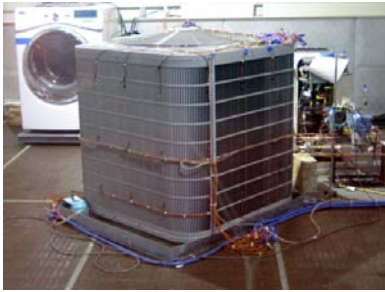


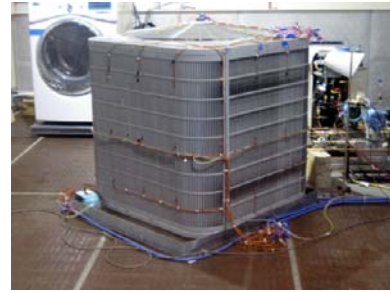
Figure 119: Individual Circuit Exit Superheat During Frost-Up Test, EXV

More airflow means a larger circuit capacity since the air inlet temperature is fixed. Circuits A and I are in direct vicinity of circuits H and B and have no other neighbor. Therefore, it is no surprise that the superheats of circuits A,B and H,I increase further towards the end of the experiment, compensating for the increasing amounts of liquid from circuit E that have to be superheated using sensible heat of the remaining circuits. After 2.7 hours, circuit E constantly feeds liquid out, resulting in a stable yet lower overall superheat, as shown in Figure 117, while a very high temperature difference between saturated evaporator outlet temperature and the air inlet temperature of about 8.3°C exists. The span of individual exit superheats is now approximately 10 K¹⁷. Interestingly, coils that have neighboring exit tubes, as indicated in Figure 5.3, have very close exit superheats even if their surface usage is entirely different. A good example for this is circuits F and E, which at the end of the experiment have approximately 1.5 K different exit superheats while one of them is very well used for evaporation and the other one only by 50 percent. Circuits A and B and H and I have neighboring exit tubes as well and show a similar result. Therefore, it can be concluded that cross fin conduction is not to be neglected for the specific type of coil used in the DHP.

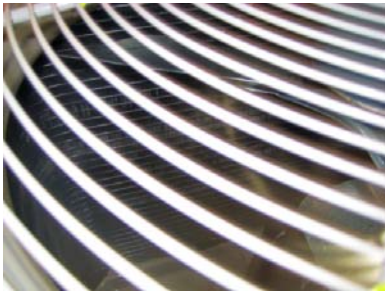
¹⁷ The measurement error for circuit E at the end of the experiment is about 1.5 K. The reason for that are pressure drop in the line to the header and increased measurement error due to the large temperature difference to the surrounding air. This temperature results in noticeable heat conduction along the line to the insulated temperature sensor.



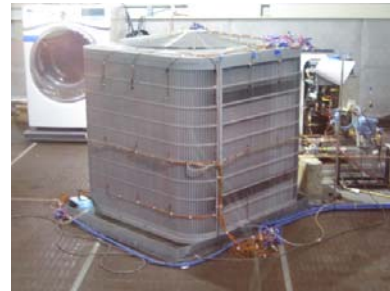
(a) 0.36 hrs, Inlet



(b) 0.47 hrs, Inlet



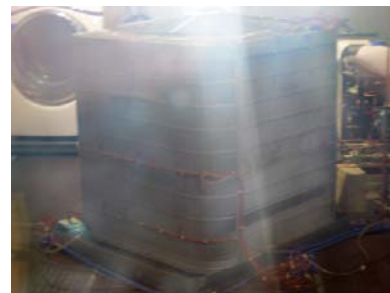
(c) 0.6 hrs, Outlet



(d) 0.6 hrs, Inlet



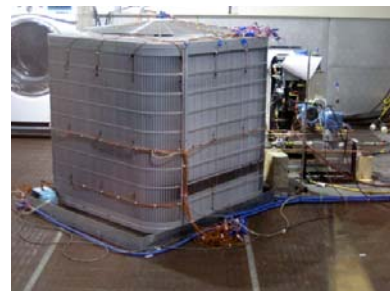
(e) 1 hr, Outlet



(f) 1.9 hrs, Inlet



(g) 2.8 hrs, Outlet



(h) 2.7 hrs, Inlet

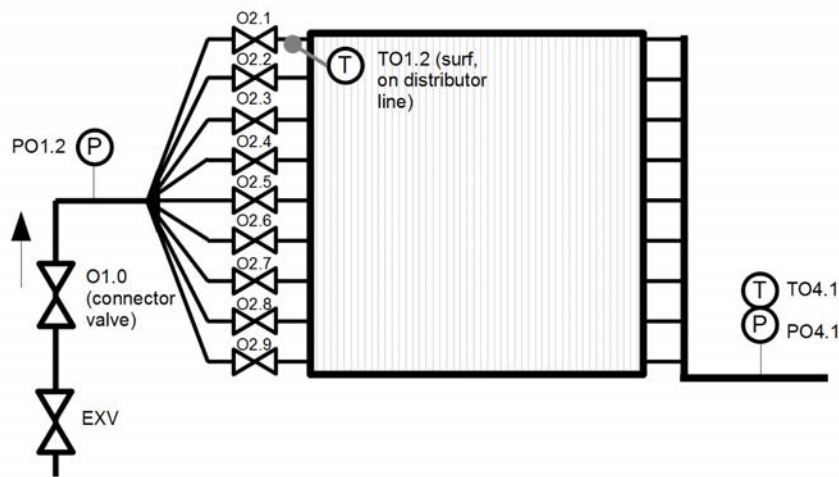
Figure 120: Pictures of Coil Inlet During Frost-Up Test, EXV

3.3.7 Conclusions, EXV

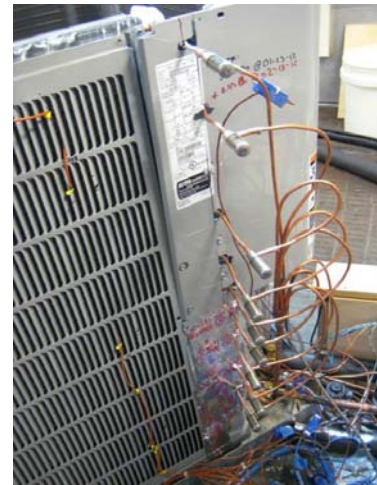
Performance degradation due to airside maldistribution increases with increasing ambient temperature and blockage as shown with the blocked-coil tests. The balance between refrigerant and airside maldistribution is not given. Therefore, the usage of the circuits surface area is different from circuit to circuit. This is noticeable in all, the clean and blocked tests, as well as the frost-up test. For the frost-up tests, this balance additionally shifts due to frost build-up.

3.4 Hybrid Control Scheme and Comparison

For the hybrid control scheme, 9 conventional EXVs were inserted as balancing valves into the distributor lines as shown in Figure 121. The primary valve was controlled using PI control on the inlet temperature TO1.2 to the top circuit of the evaporator. The balancing valves were controlled by additional controllers of the same type as used for the primary expansion valves. The opening of the balancing valves was controlled by hand, to achieve uniform individual circuit exit temperature. The approach was to keep the largest opening among the balancing valves at 450-500 out of 500 steps and adjust the primary valve to get the right superheat on that specific circuit if necessary. The opening of the balancing valves was then a result of the required mass flow rate and refrigerant quality maldistribution at the distributor. The system was charged up to gain an indoor unit subcooling similar to the EXV. The resulting charge amount was 10.25 lbs(4.65 kg), approximately 0.8 lbs(0.36 kg) more than for the EXV control scheme. The reason for this was that more charge resides in the evaporator in the hybrid control scheme, due to the extended overall length of the two-phase section. The condenser subcooling was approximately 1 K lower for the hybrid control scheme than for the EXV control scheme for the clean-coil steady-state tests.



(a) Schematic



(b) Installation (w/o EXV Coils/Insulation)

Figure 121: Modification for Hybrid Control Scheme

3.4.1 Steady State Tests, System Behavior

3.4.1.1 Clean-Coil Tests

Figure 122 to Figure 124 show the evaporation temperature and exit superheat for the hybrid control and the EXV control (dotted) systems. If the hybrid control scheme was used, the superheat was controlled within a band of 0.6°C or less.

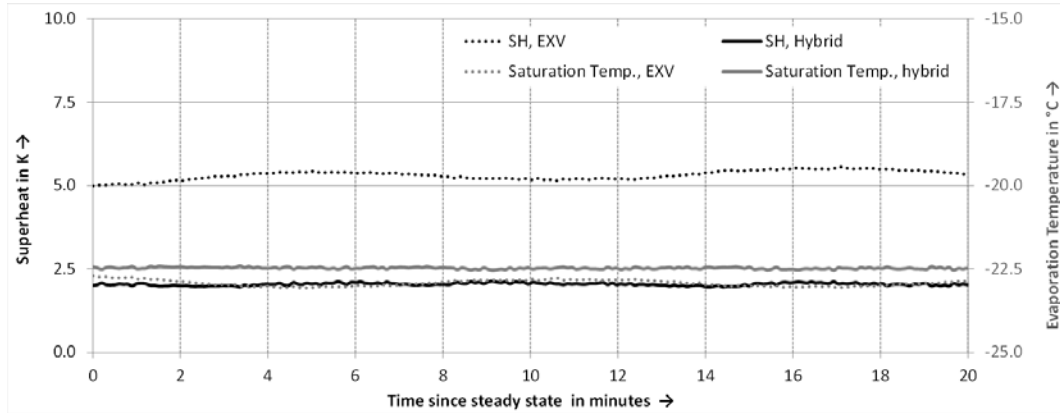


Figure 122: Superheat and Evaporation Temperature, -20°C Ambient, Hybrid

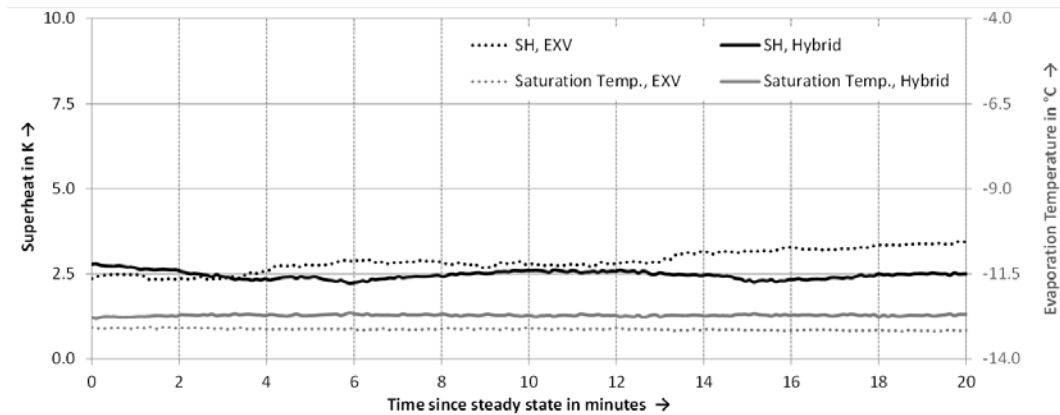


Figure 123: Superheat and Evaporation Temperature, -8.33°C Ambient, Hybrid

The evaporation temperature was as stable as for the EXV system, but higher. The superheat was comparable, except for the -20°C ambient temperature case, where it was higher for the EXV controlled system. Figure 125 shows the exit and overall superheat, for both, the hybrid control and EXV control systems at 8.3°C ambient temperature.

With the hybrid control approach, the individual circuit exit temperatures were controlled within a 0.5 K band. In case of the EXV control, the superheats were within a band of more than 4 K. Circuit G has a superheat of less than 1 K. The overall superheat is much smaller than the average superheat of the individual circuits. This is an indication that circuit G was actually not superheated but rather fed liquid into the suction header. Since the latent heat of vaporization is very large, even small amount of liquid decrease the superheat significantly. If the amount of

liquid that is fed back is reduced, then the superheat goes up quickly while the effect onto coil surface usage is minor the end of the two-phase section in all circuits moves back by only a small amount to cause this effect. The penalty for the EXV control system caused by the superheat being about 3 K higher than for the hybrid control system in the -20°C ambient case is therefore minor.

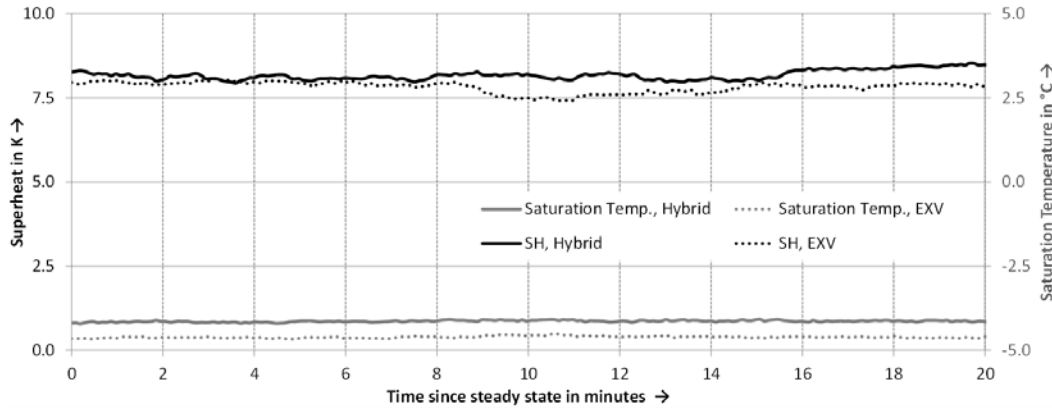


Figure 124: Superheat and Evaporation Temperature, 8.33°C Ambient, Hybrid

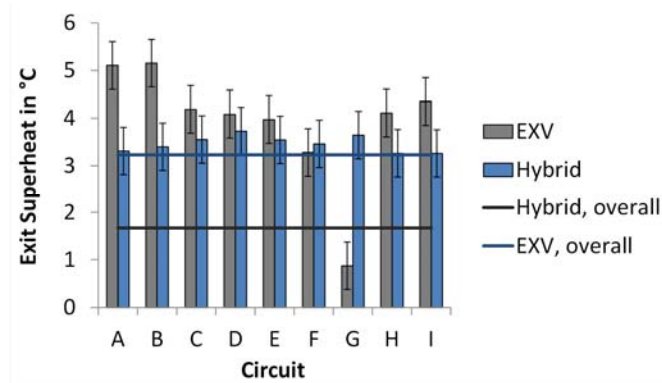


Figure 125: Circuit Exit and Overall Superheat, 8.3°C ambient temperature, Hybrid and EXV

Figure 126 shows that all circuits of the hybrid control system are used well for evaporation for most of the tests; at least 3/4 of the length of each circuit is used for evaporation.

The criteria that was used for the control was circuit exit superheat. Due to measurement error and differences in circuit length, the usage of the circuits differs by up to 2 return-bends. If the hybrid control scheme should be implemented in an actual series system, cheaper temperature measurements will need to be used and even larger measurement error will occur. The control then also has to take the stability of the circuit exit superheat into consideration rather than relying only on the absolute superheat value.

Similar to the tests with the EXV control system, the superheat is not always a very good measure on how the coil is used. While the superheats of the individual circuits are identical

within the measurement accuracy as shown in Figure 127, Figure 126 showed that the two-phase section end for circuit G deviates significantly from the one of the other circuits.

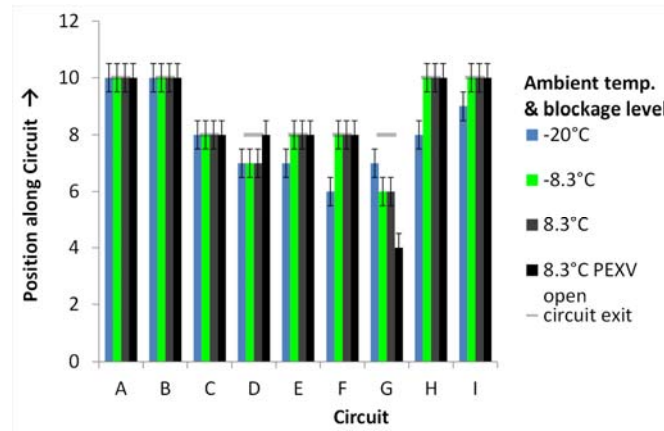


Figure 126: Circuit Two-Phase Section End, Hybrid, Clean-Coil

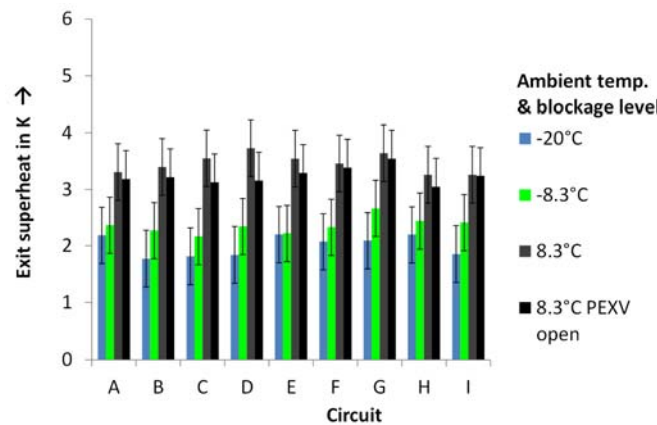


Figure 127: Individual Circuit Exit Superheats, Hybrid, Clean-Coil

3.4.1.2 Blocked-Coil Tests

Figure 128 shows the coil usage for the blocked-coil experiments with the hybrid control system. The 8.4°C PEXV fully open dataset is taken with primary valve fully open. The purpose of this test was to reduce the inlet quality to the distributor and by that to be able to use the balancing EXVs as virtual mass flow sensors. The blockage starts at circuit E, downwards to circuit I. Therefore, the air flow rates are increasingly decreased in the order E, F, G, H, and I. As a result, the capacities of those circuits decrease in the same order. The unblocked circuits A through D, which have more capacity than the remaining circuits, are used very well. The only partial usages of circuits G, H and I are therefore not significantly influencing the result. The superheats, as shown in Figure 129 for the high temperature blocked-coil tests, are very even.

Figure 129 also shows the EXV case, which has approximately the same overall superheat. In this case, the EXV has liquid exiting circuit G, which requires much higher superheat on the remaining circuits. This is only achievable with a lower evaporation temperature, which decreases performance. Figure 130 shows the individual circuit exit superheats for the hybrid control scheme with the blocked-coil. Again, the superheats are the same within the measurement accuracy for most cases, while this is not the case for the previously shown coil usage.

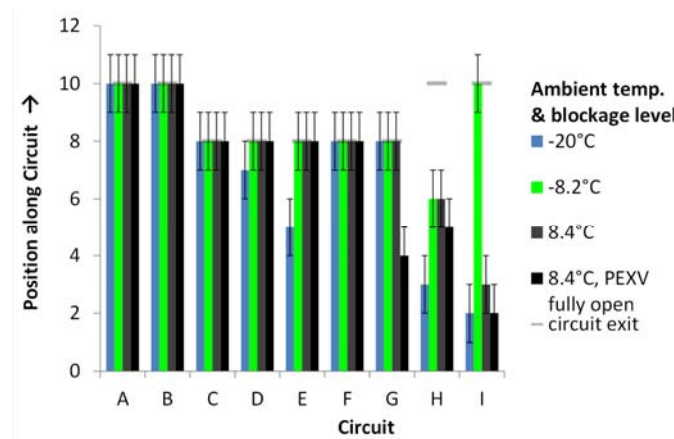


Figure 128: Circuit Two-Phase Section End, Hybrid, Clean-Coil

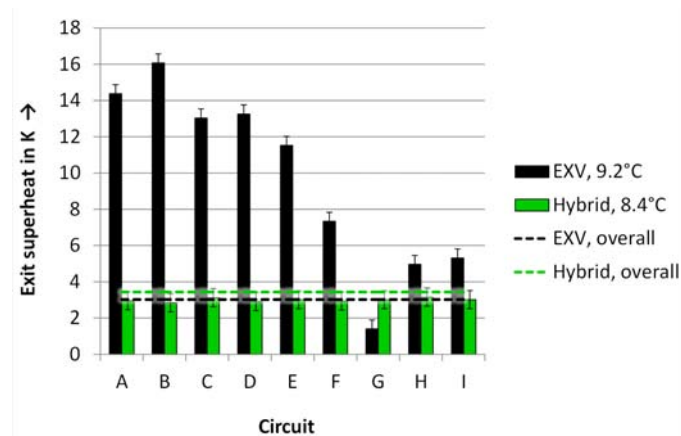


Figure 129: Exit Superheats For High Temperature, Blocked-Coil

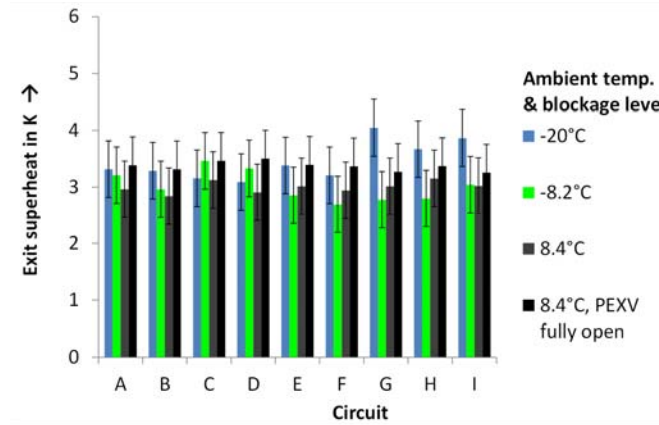


Figure 130: Circuit Exit Superheat, Hybrid, Blocked

3.5 Steady State Tests, Performance and Comparison to EXV

Figure 131 shows the COP and capacity for the hybrid control scheme with clean-coil. The COP and capacity drop by an approximately constant amount of approximately 0.05 and 0.5 kW, respectively, if the coil blockage is applied. A strong temperature dependency on this performance degradation, as was the case for the EXV control scheme, as shown in Figure 5.41, is not given. As a result, the performance of the hybrid control scheme for the blocked-coil cases is better than that for the EXV control scheme.

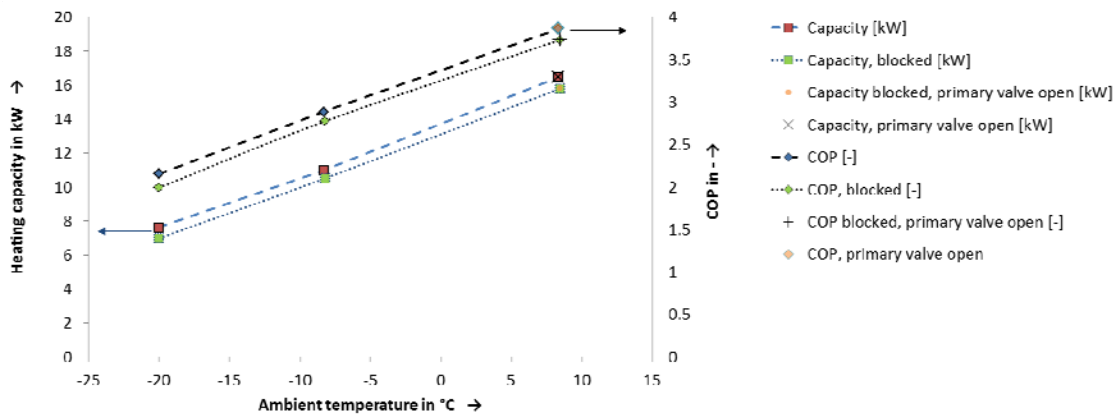


Figure 131: COP and Capacity for Blocked and Unblocked Cases, Hybrid, Steady State

This improvement increases with increasing ambient temperature, as shown in Figure 5.42(a). The performance improvement for the capacity is thereby larger than for the COP. For the clean-coil tests, the COP improved more than the capacity as shown in Figure 5.42(b). The reason for this is not measurement uncertainty - the error bars for the capacity are within the marker size but an approximately 1 K lower subcooling in the condenser than for the EXV. This resulted in a slightly lower condensing pressure since more area was available for condensation. In turn, this results in lower compressor power consumption and by that, in a

better COP of the compressor. The influence of the change in subcooling and change in condensing temperature on capacity is relatively small: the changes due to decreased subcooling and decreased condensing pressure are much less than 1 percent¹⁸ and go into the opposite direction. When the primary valve was fully opened and the system was run with the balancing valves only, more charge was held in the line, distributor and feeder lines to the balancing valves. Figure 133 shows that, as a result, the subcooling decreased by 0.6 K. Figure 132(b) shows that this lead to no change in capacity, while it increased the COP by 0.4 percent points. Therefore, the capacity improvements of 1.2 percent and 1.4 percent for -8.3°C and 8.3°C, respectively, as shown in Figure 5.42(b), are expected to be close to the ones that would be obtained for identical subcooling of EXV and hybrid control. However, the COP improvement needs to be corrected downwards by approximately 0.7 percent points, assuming it behaves linear with subcooling. Figure 134 shows the corrected COP using linear extrapolation based on subcooling. The calculated capacity improvement for -20°C is larger than for the higher ambient temperatures. The reason for the capacity improvement being larger at -20°C is that the psychrometric rooms had not enough excess capacity to decrease the room dew point below the evaporation temperature. Therefore, minor frost build-up on the coil occurred in both -20°C tests, which lead to additional benefits for the hybrid control.

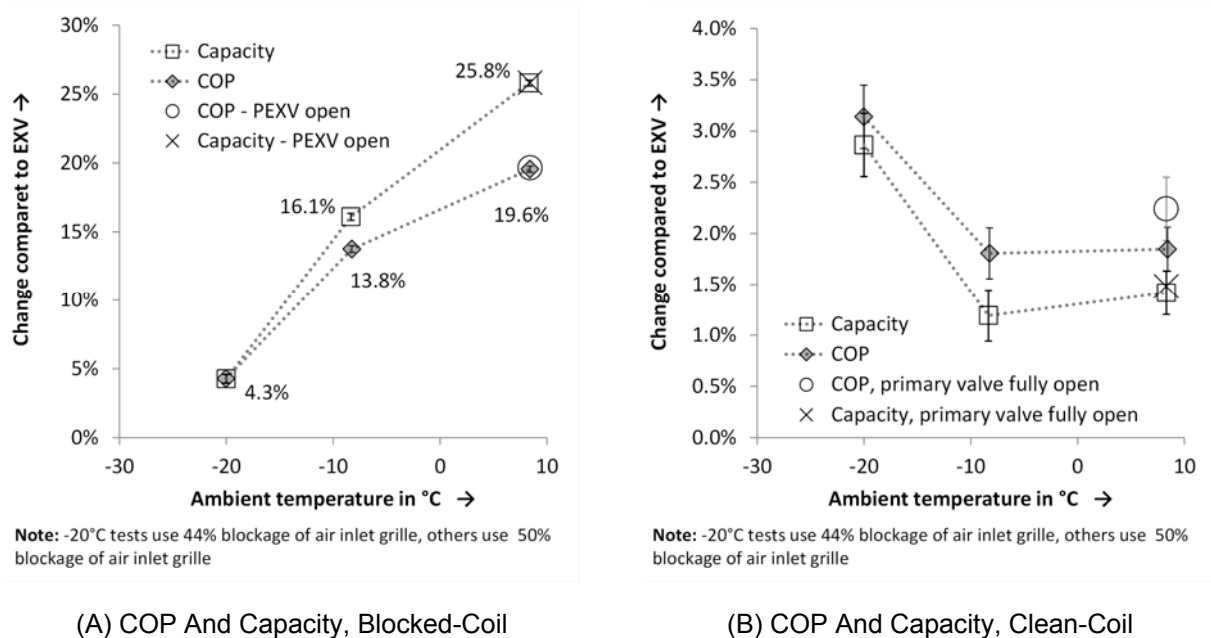


Figure 132: COP and Capacity Change Between EXV and Hybrid Control Scheme¹⁹

¹⁸ Estimated using CoolPack (Skovrup et al., 2012) cycle tool and the manufacturer supplied compressor map.

¹⁹ Linear interpolation was used for COP and capacity for tests that had nonmatching ambient temperatures.

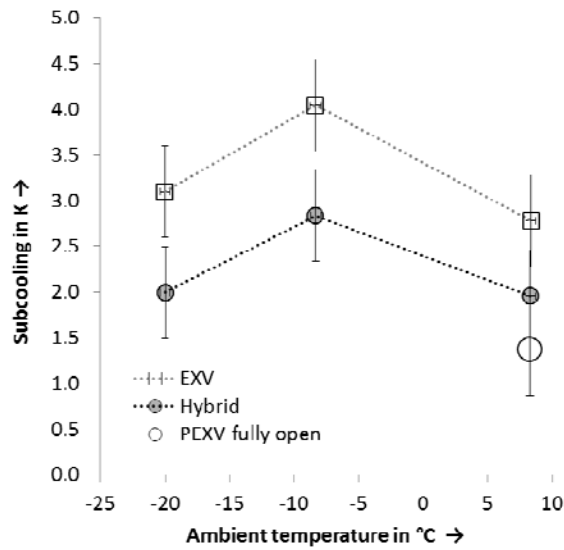


Figure 133: Subcooling for heat pump tests

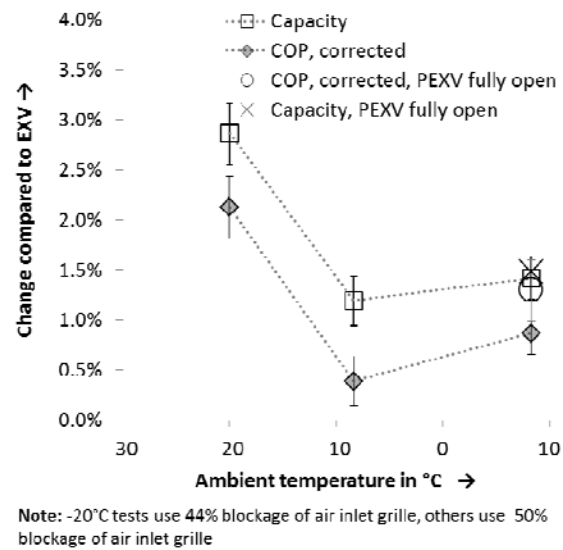


Figure 134: Corrected COP

3.5.1 Frost-up Test

The outdoor room conditions for the frost-up test, as shown in Figure 135, are close to the ones used for the EXV tests, as shown in Figure 115 on page 94. However, the temperature and humidity fluctuations are smaller than in the EXV tests. The target dew point temperature was -11°C, since this was the largest possible steady-state value without causing an increase in room temperature during the EXV tests. The data acquisition software crashed at 2.23 hours after startup. The heat pump was kept running during that time; a valve reset was done after the software was back in operation.

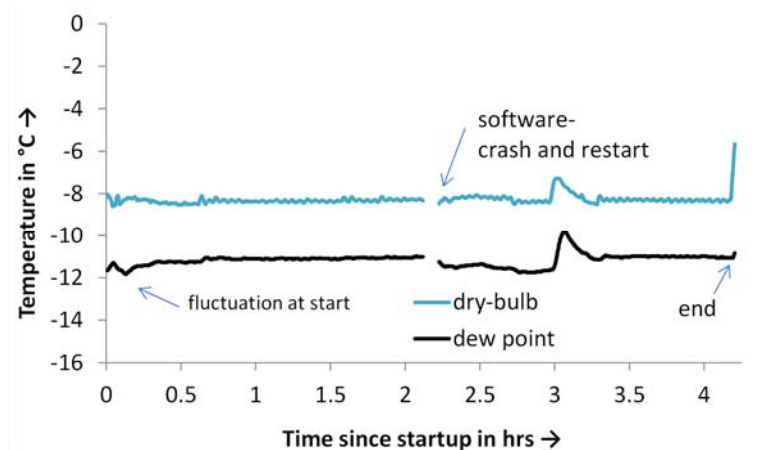


Figure 135: Outdoor Room Conditions, Frost-Up Test, Hybrid

Figure 136 shows the COP and capacity as a function of time. During the first 1.25 hours of operation, the overall superheat was gradually brought down while the valves were controlled

to achieve uniform exit superheats. The maximum capacity and COP with sufficient overall superheat was reached at the end of initial adjustment process. After that, the COP and capacity started dropping with increasing time. After the software crash at 2.23 hours, the COP and capacity stayed at approximately the same value for approximately 45 minutes. The reason for this is, that the superheat was gradually brought down to the lowest stable value while the balancing valve positions were adjusted beginning from the last value before the crash. At about 3 hours after the crash, the COP and capacity follow the downwards trend indicated by the dashed lines again. At 4.13 hours after the start of the experiment, the test was terminated since the performance values dropped below the measured performance of the EXV control scheme. Figure 137 shows the superheat and evaporation temperature over the course of the test. For most of the test, the superheat was held in between 2 and 7 K. The first 0.32 hours after startup were needed to evaporate the liquid refrigerant from the accumulator. Smaller amounts of liquid were fed into the accumulator at 0.92 hours, 1.88 hours, and 2.9 hours. Larger amounts of liquid were fed into the accumulator at 3.1 hours to 3.5 hours. Due to the low evaporator exit superheat of approximately 2 K, it was not possible to evaporate this liquid until the end of the experiment. Figure 137 also shows the pressure drop of circuit A in terms of saturation temperature. This pressure drop is between 5 and 8 K. Due to this large pressure drop, the cross parallel flow across the evaporator is not a disadvantage, but helps transferring the heat across the coil.

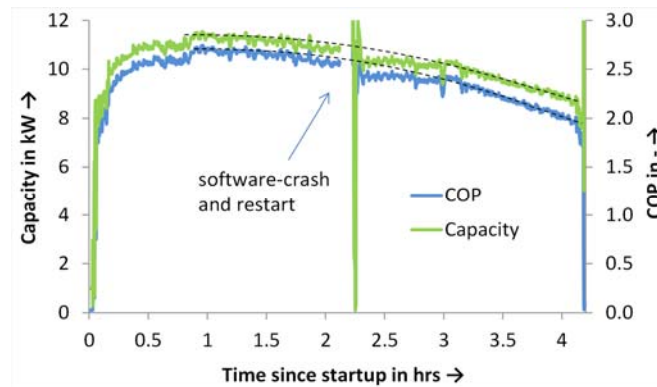


Figure 136: COP and Heating Capacity, Frost-Up Test, Hybrid

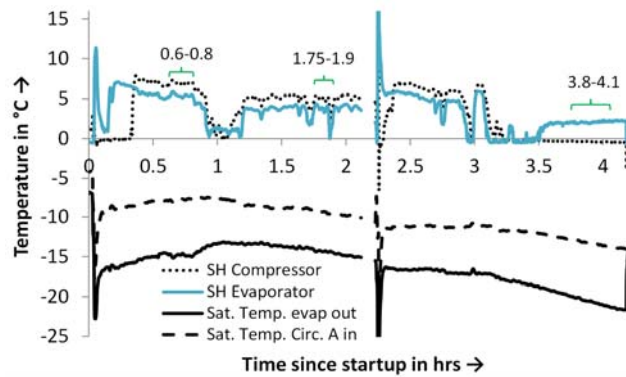


Figure 137: Superheat and Evaporation Temperature, Frost-Up Test, Hybrid

Figure 138 shows the exit superheats for the selected time ranges shown in Figure 137. The control objective was to equalize superheats, since this is the simplest approach and cheaper than equipping the entire evaporator with return-bend sensors (as it was done for this HP). The individual circuit superheats are within a band of 3.2 K or smaller, depending on the time interval. Even though this span is much smaller than for the EXV, the coil surface usage for the hybrid control scheme did not significantly improve, as shown in Figure 139. The coil surface usage for the hybrid control scheme during the first and last time periods is in fact worse than for the EXV control scheme. This results in a reduced performance of the hybrid control system compared to the EXV control system during some, but not all duration of the test. Figure 140 shows the valve openings of the balancing valves. The initial valve openings were the ones found for the clean-coil tests at the same room temperature. The valve openings were subsequently adjusted, e.g. the valve openings for circuits with too large of a superheat were increased. The primary valve opening was controlled by the (saturated) inlet temperature to circuit A using PI-control. It was found, that a change in opening of any of the circuits had a large influence on the exit superheat, especially on the neighboring circuits²⁰. This phenomenon is considered to be a result of the design of the distributor that increases quality maldistribution with a change in throttling of the exiting flow. This problem can be overcome by bypassing the flash gas of the primary expansion around the evaporator into the suction header, which also would reduce the significant coil pressure drop shown in Figure 137 on page 108.

²⁰ If the valve opening of circuit A was adjusted, the set point of the PI controller had to be corrected to compensate for the change in pressure difference across circuit A.

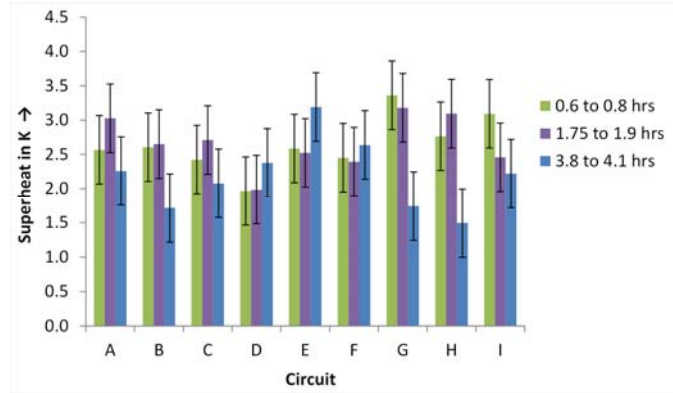


Figure 138: Circuit Exit Superheat During Different Time Ranges, Frost-Up Test, Hybrid

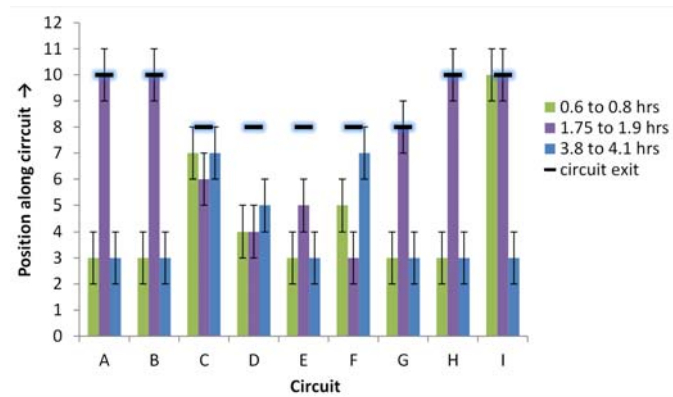


Figure 139: Circuit Two-Phase Section End During Different Time Ranges, Frost-Up Test, Hybrid

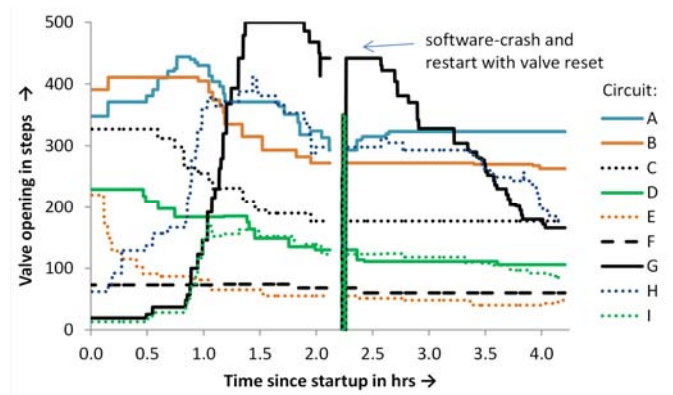


Figure 140: Balancing Valve Opening During Frost-Up Test, Hybrid

Figure 141 shows the individual circuit superheat as a function of time. The most significant difference to the EXV test results, as shown in Figure 119 on page 97, is that they stay within a band of approximately 2.3 K during the entire experiment. The superheats do not increase towards the end of the experiment, which means that there is less need to evaporate liquid refrigerant exiting the circuits. Therefore, the evaporation temperature does not need to be

decreased as rapidly as in the EXV case. Based on the end of the circuit two-phase section, as shown in Figure 139, one would expect more variation in the exit superheat of the frost-up test using the hybrid control scheme.

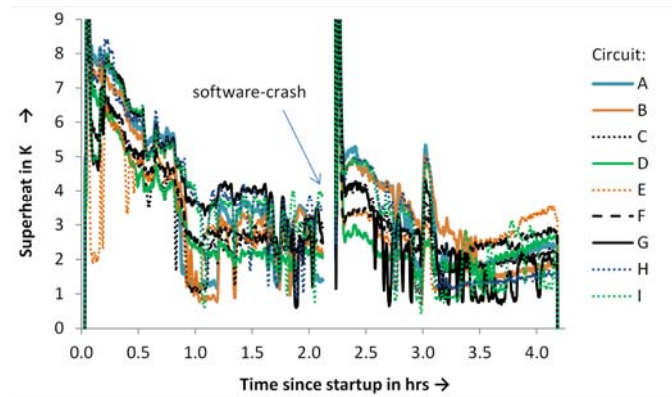
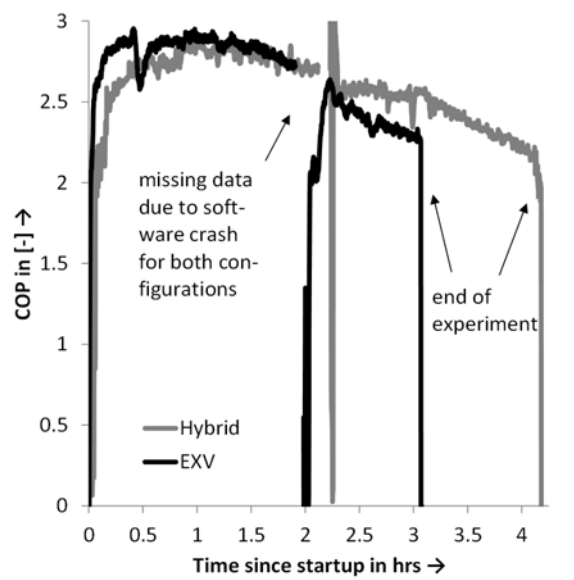
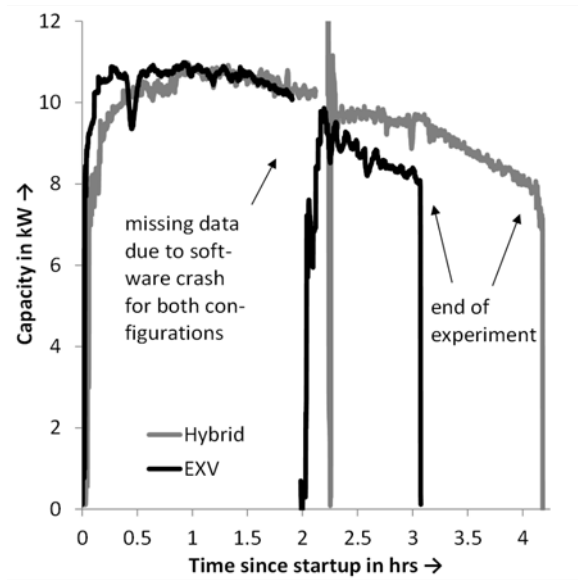


Figure 141: Individual Circuit Exit Superheats During Frost-Up Test, Hybrid

Figure 142 shows the COP and capacity of the frost-up tests with the EXV and hybrid control schemes as a function of time. During the first 1.5 hours of operation, the EXV control scheme performs better than the hybrid control scheme. This is caused by the improper distribution of mass flow due to controlling the distribution based on superheat. The circuits should rather be controlled on a combination of superheat and superheat stability to improve the obtainable performance. If that would have been done, then the performance of the hybrid system would have been better from the beginning. Additionally, the smaller air inlet temperature difference would have resulted in a slower frost build-up, which would have additionally extended the already longer runtime for the hybrid control system. After 1.5 hours of operation, the hybrid control scheme outperforms the EXV control scheme. The reason for this is that liquid carryover is smaller for the hybrid control scheme. This gets increasingly important for increasing frost build-up. As a result it takes nearly an hour longer for the hybrid control scheme to reach the same performance degradation than that of the EXV controlled system when its test was terminated. The hybrid control scheme therefore extended the runtime by more than 30 percent.



(a) COP



(b) Heating Capacity

Figure 142: COP and Capacity, Frost-Up Test, EXV and Hybrid

3.6 Bin Analysis

For the domestic heat pump, ANSI/AHRI standard 210/240 (2008) defines a bin-type method to calculate the heating seasonal performance factor (HSPF). Basis for this is an ambient temperature dependent building load and a mapping of the heat pump system based on linear interpolation between different test data points. The building load and system power consumption are then a result of the binned temperature fractional hours for the regions defined in table 17 of the standard. Figure 143 shows these fractional bin hours – it is obvious that the region will have a significant influence onto the HSPF. Figure 144 additionally shows, that the number of hours in which heat is needed is significantly different in the different regions.

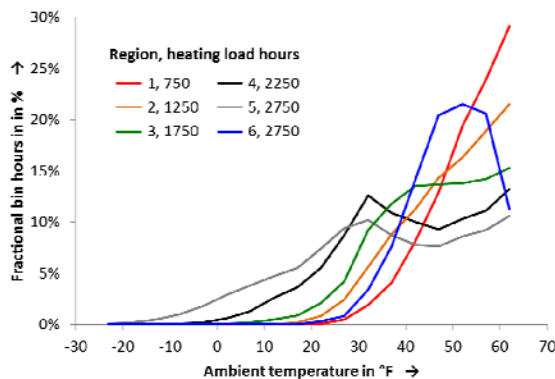


Figure 143: Fractional Bin Hours per Region

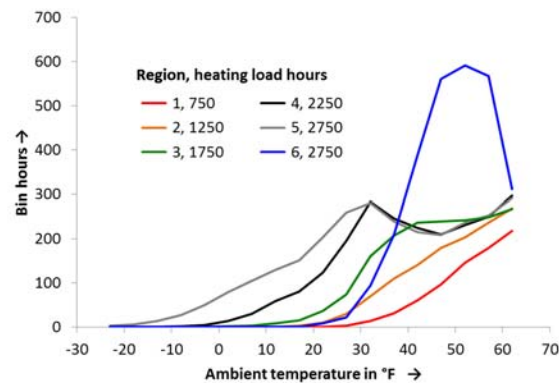


Figure 144: Bin Hours per Region

3.6.1 Modifications Compared to Method Implemented in ANSI/AHRI 210/240

The heating system model was modified to account for the differences between our experimental test matrix and the test matrix implemented in the standard. The heating system model uses linear interpolation between individual data taken during the experiments. In case of repeated tests in the experiment, the average of those tests is taken as input for the model. For temperature bins that lie outside of the data taken, linear extrapolation is used. Note: The frost accumulation test H2₁ of ANSI/AHRI standard 210/240 (2008) was not conducted. Therefore the linear interpolation model does not fully reflect the decreased performance at lower ambient temperatures. This simplification leads to a bias in favor of the EXV controlled system since a potentially reduced number of energetically costly defrost cycles is not considered.

During the experiments, tests with airside maldistribution were conducted. Since these tests added significant maldistribution to the coil, the resulting performance degradation will likely only occur for high ambient humidity and frost build-up or severely fouled coils. These conditions are not expected to be the standard operating conditions. Therefore a weighting between blocked-coil and clean-coil performance was introduced for maldistributed performance as shown Figure 145. Below 35 F(1.67°C), this weighting assumes an increased influence of frost build-up on the coil.

Note: The heating system model does not consider possible additional savings due to a likely smaller number of defrost cycles for the hybrid control scheme.

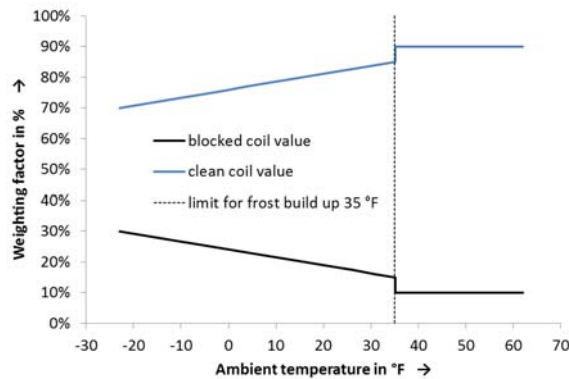


Figure 145: Weighting Factors for Maldistributed Coil Case

ANSI/AHRI 210/240 (2008) specifies a minimum and maximum design heating requirement. From the standard, it is unclear, if the minimum or maximum design heating requirement should be used for calculations other than region 4. For the calculations in this report, the minimum design heating requirement was used for all regions. The design heating requirement

is used in the standard for calculating the building heat load. The majority of California is based in regions 3, 4, and 5, while smaller parts are based in regions 2 and 6.

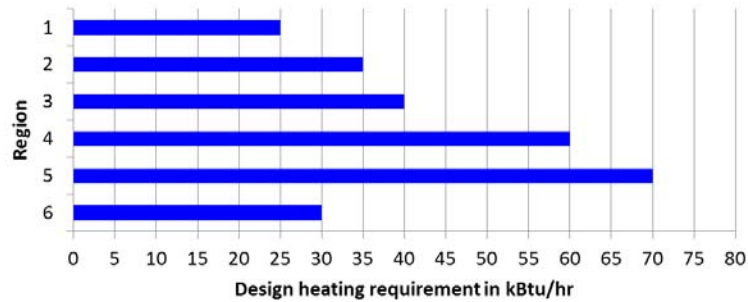


Figure 146: Design Heating Requirement

3.6.2 Results

Figure 147 through Figure 149 show the resulting energy savings for the 5-ton domestic heat pump. Figure 147 shows the clean-coil, the blocked-coil, and the maldistributed coil energy savings of the hybrid control system compared to the EXV controlled system, calculated using equation (15). The clean-coil energy savings range from 1.5 percent to 2.0 percent, while the blocked-coil energy savings range from 12.2 percent to 18 percent. These values present the lower and upper limit of possible energy savings. The maldistributed coil case, using the weighting factors from Figure 145 for each temperature bin, shows energy savings ranging from 2.8 percent to 3.5 percent. The energy savings for the maldistributed coil are considered to be the most realistic ones. Figure 148 shows that the savings per year are in the range of \$2.5 to \$36.9. These savings are largely dependent on the climate region. The hybrid control scheme, or any other method for flow distribution control, will have the shortest return on invest for climate zones 4 and 5.

$$relative\ Savings = 1 - \frac{Energy_{tot,Hybrid}}{Energy_{tot,EXV}} \quad (15)$$

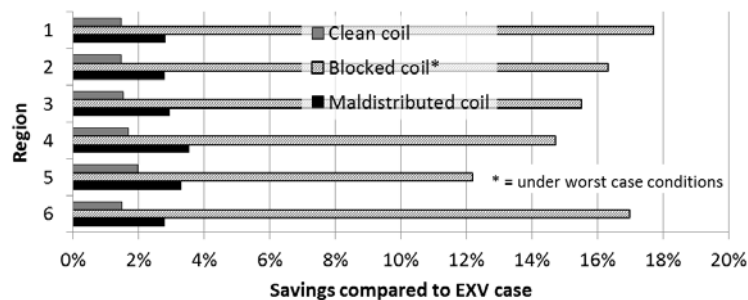


Figure 147: Electricity Savings per Year, Relative Hybrid Compared to EXV

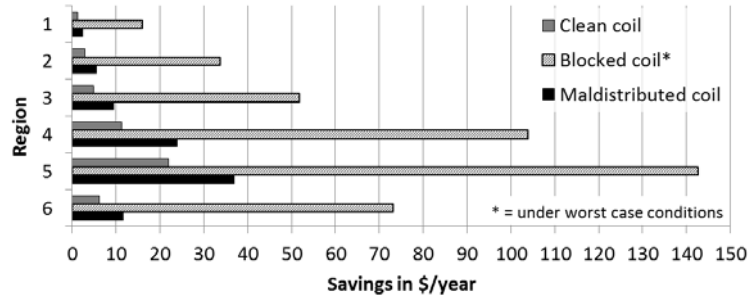


Figure 148: Electricity Cost Savings per Year, Absolute Hybrid Compared to EXV

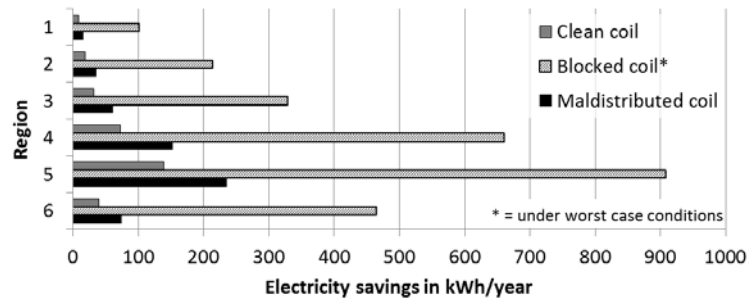


Figure 149: Electricity Savings per Year, Absolute Hybrid Compared to EXV

It is assumed that most of California is located in climate region 3. The estimated savings for that region are smaller than for regions 4 to 6. Assuming that the installed air source heat pump capacity was, on average 3 tons (36 kBtu) and that the US wide unitary HP sales distribute equally across residential units built in US and in California, and that the expected lifetime of the heat pumps was 12 years, the installed air side heat pump capacity for California was estimated to be 80 GBtu/h (more details see Appendix B). Figure 150 shows that, if all of the estimated current heat pump capacity of California was installed in region 3, the yearly energy savings would be \$1.3 Million or, according to Figure 151, 8.0 GWh of electricity. Note that these numbers assume that the maldistributed coil-case is representative of an average effect of maldistribution, since, to the best of the authors knowledge, no detailed statistical data on this topic is currently available.

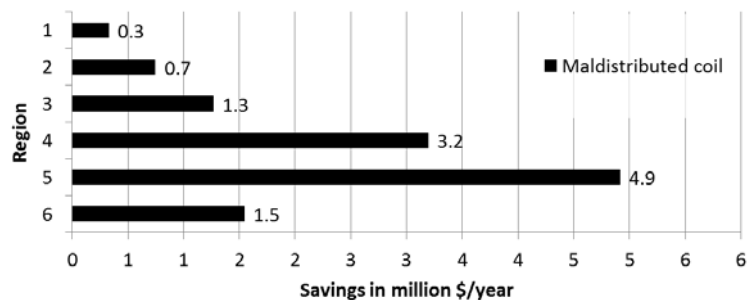


Figure 150: Electricity Savings Potential in M\$/Year, Assuming Entire Estimated Installed Heat Pump Capacity of California is Installed in Each Region

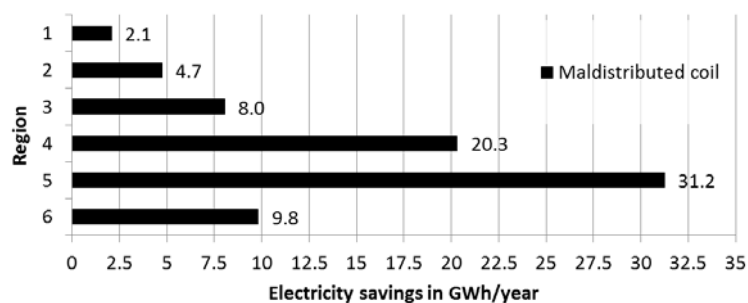


Figure 151: Electricity Savings Potential in Gwh/Year, Assuming Entire Estimated Installed Heat Pump Capacity of California is Installed In Each Region

3.7 Conclusions and Recommendations

The capacity increase for the DHP with clean-coil using the hybrid control scheme is in the order of 1 percent while the corrected COP improvement compared to using the EXV control scheme is approximately 0.6 percent. This suggests that the hybrid control scheme leads to an insignificant improvement of the DHP performance during clean-coil operation. In practice, however, maldistribution due to refrigerant and airside fouling will occur – temporary by frost-up and as a result of often poor maintenance practices over the lifetime of the system. A 4 to 26 percent improvement in capacity along with a 4 to 20 percent improvement of COP can be observed with approximately half the air inlet grille blocked for -20°C to 8.3°C ambient temperature.

The achievable yearly savings were estimated using a bin-type analysis, using uncorrected measurement data. The savings are in the order of 1.5-2 percent for clean-coil operating conditions and 2.8 percent to 3.5 percent for an assumed maldistribution of the coil. For worst-case conditions with severely maldistributed coil, the savings are 12.2 percent to 18 percent. The exact level of maldistribution over the course of a year, specifically in form of a statistically significant correlation is unknown. Therefore future research should focus on the evaluation of a representative level of maldistribution.

One measure of maldistribution, the surface usage of the refrigerant side area of the coil, is difficult to assess for the DHP if only the individual circuit exit superheat is used: cross fin conduction limits the increase of temperature after the end of evaporation, especially if directly neighboring circuits have a low exit superheat. A better way to control the system in hybrid configuration would be to use a combination of absolute superheat value and superheat stability to determine the necessary opening for each balancing valve. It was found that when controlling the flowrates based on exit temperature, significant cross dependence between the circuits exists; changing the flowrate of one circuit alters the superheat of the neighboring circuits. It is unclear whether this is a result of cross fin conduction or actual changed flowrates to the individual circuits due to changes in the distribution of liquid and vapor to the different ports. Future work should include this aspect. If it turns out to be a result of the flow in the distributor, then further system changes might be worthwhile.

For the hybrid control scheme, the COP and Capacity during the first part of the frost-up test were smaller than for the EXV control scheme. An analysis of the return-bend temperatures revealed that this was caused by insufficient coil usage due to the control of the balancing valves to yield close exit superheats. Later on, the hybrid control system reached and exceeded the performance of the EXV control system. In that case, one of the circuits in the EXV test started feeding out liquid, which required a lower evaporation temperature to gain sufficient overall superheat. In the hybrid control system, the flow rate of the circuit that started feeding out liquid was reduced, and the evaporation temperature did not need to be lowered as much, resulting in better COP and larger capacity. The hybrid control system extended the runtime of the frost-up test by more than 30 percent. With better control of the balancing valves, performance improvement and runtime extension would have been even greater.

An estimate of the return of invest for the hybrid control scheme can be found on page 155.

Chapter 4:

Rooftop Air-Conditioning Unit

Rooftop units (RTUs) contain the entire cooling system within a package, similar to window units. This has several advantages compared to split systems. Rooftop units are entirely manufactured under controlled conditions, which reduces the risk for refrigerant leakage due to difficulties at the site installation or poor installation practices. Since, when compared to a central AC system, this also means that no liquid lines are necessary in the building, it can reduce the cost of installation. A rooftop unit is conveniently placed on top of the roof, as shown in Figure 152, and only connection of air ducts, electricity and control signals is required. The dimensions of the RTU for a certain size were kept constant over decades by some manufacturers. This means that a rooftop unit, if it reached the end of its lifetime, can just simply be replaced with a new one in a relatively short amount of time. However, rooftop units do not only have advantages. One issue is, that in contrast to split type systems, heat conduction between the ambient air and return/supply air occurs through the walls of the unit that enclose the indoor fan and evaporator.

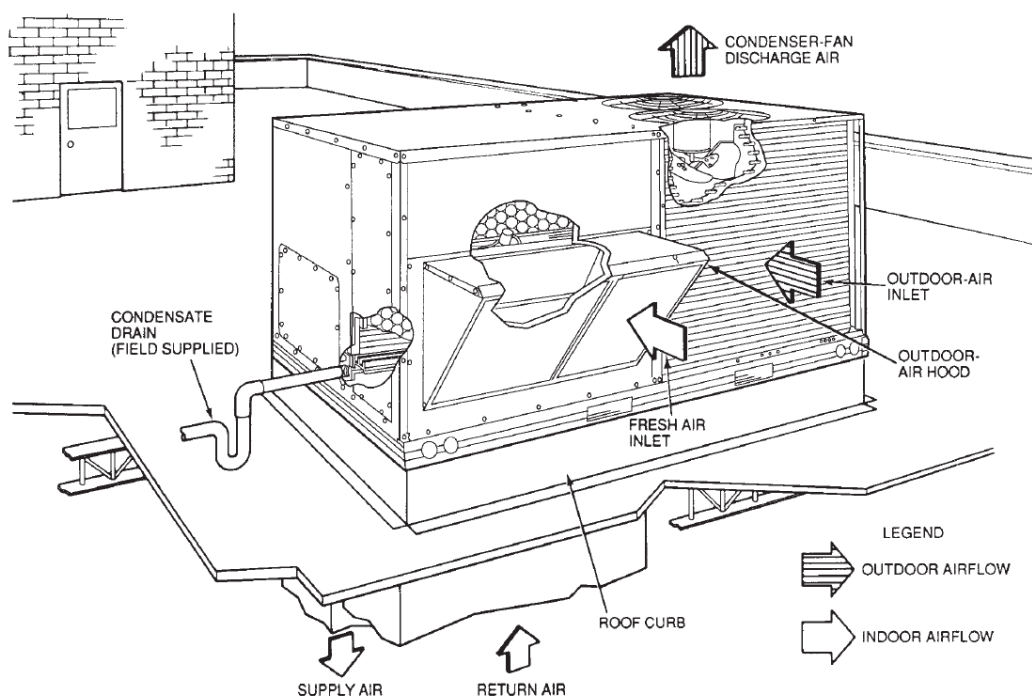


Figure 152: Schematic of a Rooftop Unit, Carrier Corporation (2006)

To increase the cooling efficiency, a high insulation value panel type construction with thermal breaks for the walls of this part of the rooftop unit, is used in some high efficiency units. In the tested 4-ton RTU, the refrigerant connection side of the evaporator is subject to the air in the condenser which leads to a loss of available cooling capacity. However, the most significant

issue arises due to the usage of an airside economizer: since space is limited, mixing fresh air and return air leads to significant maldistribution of the inlet temperature, velocity and humidity to the evaporator, especially at partially open economizer damper. Furthermore, a faulty economizer that got stuck in open position can lead to significant performance degradation if the unit is operated under high ambient temperature conditions.

4.1 System Schematics and Instrumentation

Figure 153 shows the refrigerant side schematic of the 4-ton rooftop unit. The system employs a very basic vapor compression system without any accumulators or receivers. The balancing valves of the hybrid control scheme are shown as dotted outline – they were not in the system for the TXV and EXV tests. The line length between evaporator and compressor is less than 1.2 m (4ft), and the line length between compressor and condenser is less than 1.5 m (5ft). Therefore only the suction and discharge conditions at the compressor were measured.

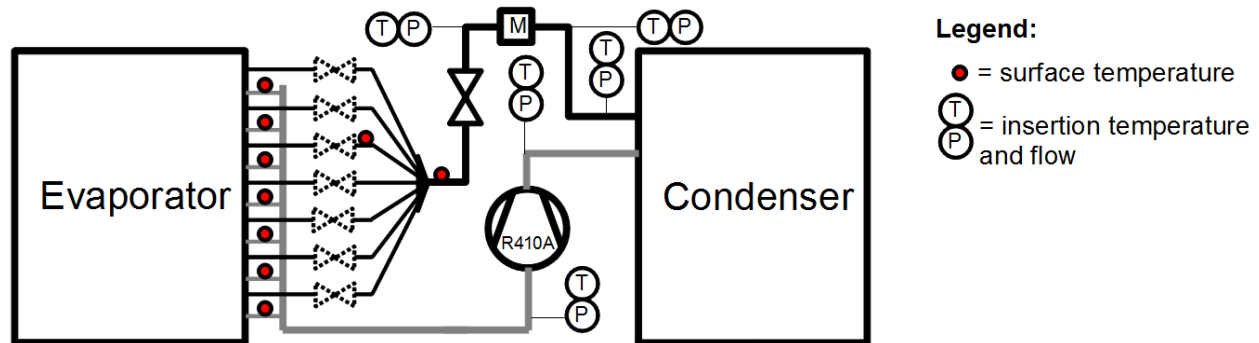


Figure 153: Refrigerant Side Schematic of RTU

Figure 154 shows the airside instrumentation of the rooftop unit. Mixed air temperature was measured within the filter in an equally spaced 4x4 grid. Most temperatures were measured with at least 3x3 grids, with exception of the temperature measurement in the flow measurement nozzle box, which uses 3 sensors that are spaced according to the expected flow distribution.

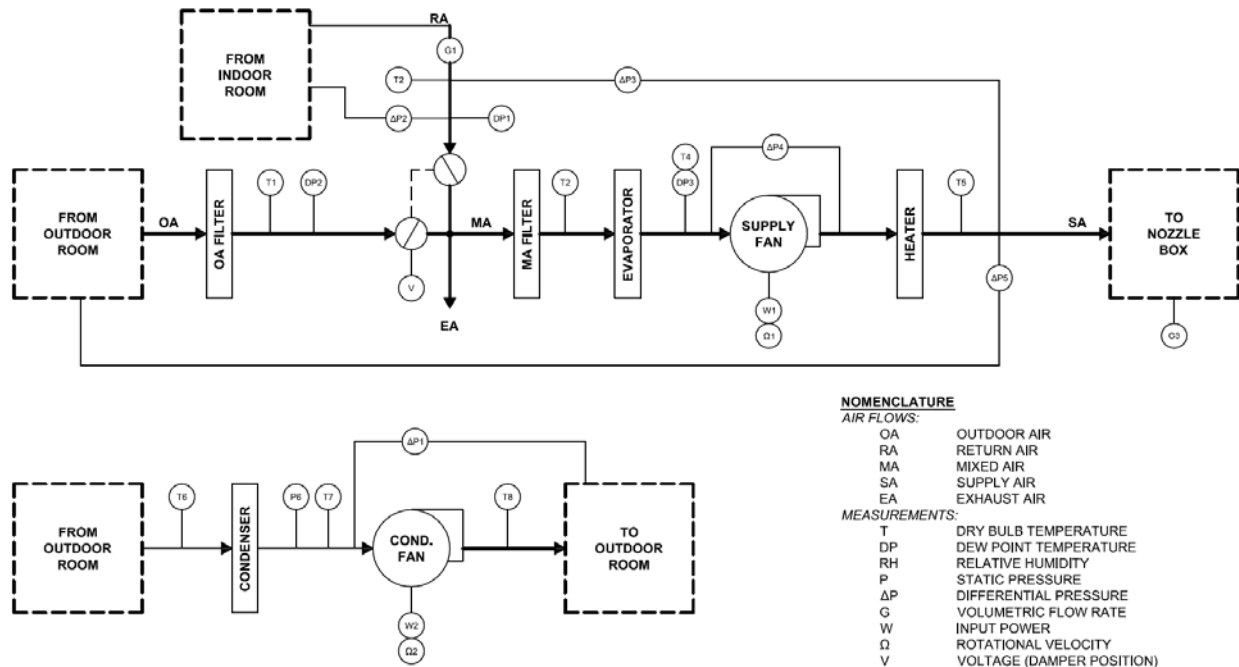


Figure 154: Air Side Instrumentation of Rooftop Unit

Table 3 shows the summary of all measurement points, their rated accuracy and the number of sensors.

Table 3: Measurements and Accuracy

Property	Number of sensors	Individual sensor accuracy, mounting type*	Note
T = Temperature			
P = Pressure			
PD = Pressure difference			
Outdoor air T (inlet to economizer)	9	0.5 K, IF	used as average (without weight)
Return air T	9	0.5 K, IF	used as average (without weight)
Mixed air T	16	0.5 K, IF	used as average and row-wise average (both without weight)
Supply fan air T (inlet to fan)	6	0.5 K, IF	used as average (without weight)
Supply air T (directly after exit terminal)	9	0.5 K, IF	used as average (without weight)
Condenser air T (inlet)	20	0.5 K, IF	used as average (without weight)
Condenser fan air T (exit)	12	0.5 K, IF	used as average (without weight)

Property	Number of sensors	Individual sensor accuracy, mounting type*	Note
T = Temperature			
P = Pressure			
PD = Pressure difference			
Air inlet temperature to flow measurement nozzles	3	0.5 K	RTD
Pressure difference, supply air fan	1	0.01"WC	
Pressure difference, supply-return air	1	0.01"WC	
Pressure supply air relative to ambient	1	0.005"WC	
Pressure return air to indoor	1	0.005"WC	
Pressure difference across condenser fan	1	0.0025"WC	
Flow measurement nozzles pressure difference	1	0.025"WC	
Dew point outdoor air	1	0.2 K	Inlet to economizer
Dew point return air	1	0.2 K	Return air duct inlet
Dew point supply air	1	0.2 K	
Refrigerant T, P at comp. suction	1	0.5 K, IF	suction state and superheat
Refrigerant T, P at comp. discharge	1	0.5 K, IF	discharge state and superheat
Refrigerant T, P at condenser outlet	1	0.5 K, IF	condenser outlet state and superheat
Refrigerant T, P at mass flow meter inlet	1	0.5 K, IF	check state at mass flow meter inlet
Refrigerant T, P at TXV/EXV/PEXV inlet	1	0.5 K, IF	EXV inlet state and superheat
Refrigerant T at inlet to distributor	1	0.5 K, SF	check saturated pressure drop across distributor
Refrigerant T at inlet to balancing valve 3		0.5 K, SF	check saturated pressure drop across distributor (hybrid control only)
Refrigerant T at individual circuit inlet	7	0.5 K, SF	check balancing valve opening offset
Refrigerant T at individual circuit outlet	7	0.5 K, SF	individual circuit exit superheat, together with suction pressure

Property	Number of sensors	Individual sensor accuracy, mounting type*	Note
T = Temperature			
P = Pressure			
PD = Pressure difference			
Refrigerant mass flowrate	1	0.1% of flowrate	Coriolis mass flow meter

* SF = surface, IF=in flow; all temperature measurements T-type thermocouples unless noted otherwise. Accuracy of data acquisition system better than 1.0 K.

4.1.1 Control Schemes

The system was operated with the following configurations of evaporator flow control:

1. Original configuration with thermostatic expansion valve (TXV)
2. Electronic expansion valve (EXV)
3. Hybrid control
4. Primary expansion valve (PEXV) fully open

No changes were applied to the superheat setpoint of the inbuilt thermostatic expansion valve. For the electronic expansion valve, the evaporation temperature was controlled based on the saturated suction temperature using a PI control. The setpoint of the PI control was adjusted manually to reach a target superheat that resulted in a fluctuation of less than 50 percent of its average value. An additional instantaneous limit of 3 K minimum superheat was used to ensure sufficient protection against liquid feed over. This resulted in an average overall superheat of more than 5 K for all cases. For the hybrid control, the overall superheat was controlled in the same manner. However, since the fluctuation were much smaller, the target superheat was set to 5 K since it seems impractical to use smaller superheats in real field applications due to limited sensor accuracy and non-steady system operation. The individual superheats of the hybrid control scheme were controlled with a PI control with the instantaneous average value of the circuits as setpoint. For the PEXV fully open control scheme, the primary expansion valve of the hybrid control scheme was fully open with an additional liquid bypass around the valve. The individual circuits were then solely controlled by the balancing valves, which used the same control as previously. However, the target setpoint was offset manually to control overall superheat.

4.1.2 Limitations of Experimental Setup/Facilities

Due to the limited capacity of the booster fan of the flow measurement nozzle box, it was not possible to operate the unit at a constantly low pressure lift of 0.05 kPa \pm 0.02 kPa as described by AHRI 210/240 (2008). The pressure drop across the system in real applications will depend upon the air flowrate of the unit which in turn depends upon the fan frequency. The duct system that distributes the air from the RTU into the building will have an approximately quadratic behavior of the pressure drop as the function of the flowrate. Therefore, considering the limitations of the booster fan, the building curve (target curve for the experiments) was chosen to intersect at 0.07 kPa pressure drop for 1100 cfm moist air flowrate. Figure 155 shows

the curve together with the pressure drops measured for the EXV control scheme for nominal fan frequency. These points were very closely replicated for the hybrid control.

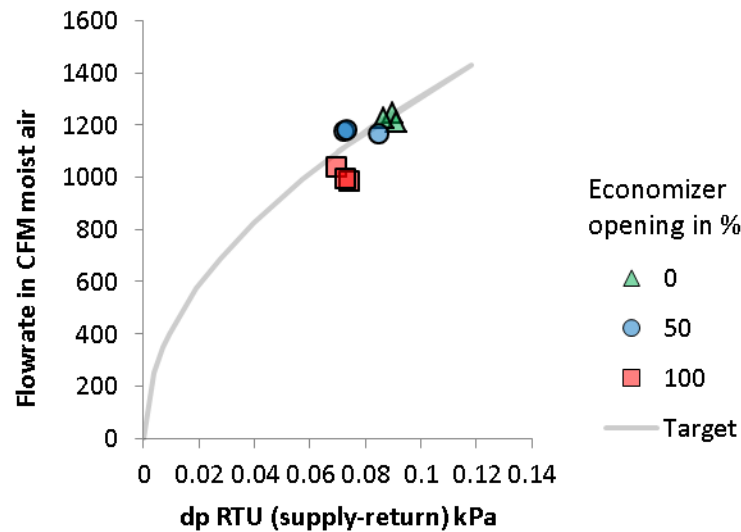


Figure 155: Supply Air Flowrate, RAC, EXV Control Scheme

4.1.3 Effects of Air-Side Economizer onto Maldistribution

The rooftop unit is equipped with an economizer, which exhausts return air and allows fresh air to enter the unit. Due to the compact design of the unit, the air mixing space after the economizer is very small, as shown schematically in Figure 156. This leads to evaporator maldistribution in terms of velocity, and if ambient and indoor temperature and humidity differ, additionally to maldistribution in terms of inlet air enthalpy. Figure 157 shows the 4 numbered measurement positions that were used to measure velocity. The temperature was measured at the indicated 16 points. For analysis purposes, an average of each 4 horizontally neighboring points was taken, since this corresponds to an approximation of the average mixed air temperature of the circuits behind these measurement points.

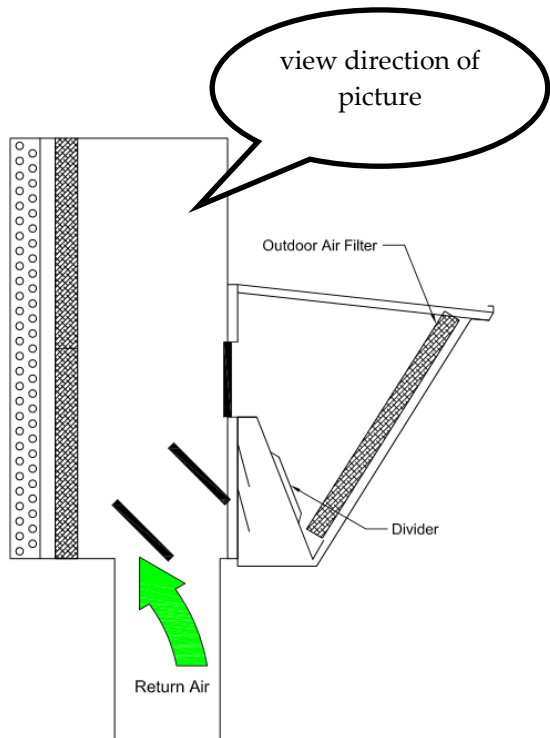


Figure 156: Economizer and Coil Cross Section²¹



Figure 157: Measurement Positions for Temperature (16 grid) and Velocity (Numbered Positions)²²

Figure 169 and Figure 170 show the average mixed air temperature for each temperature measurement position along with the circuit exit superheat for the TXV control with closed damper. The circuit numbers are counted from top (1) to bottom (7). Figure 169 shows that, while the damper is closed, air leakage and heat conduction through the economizer lead to non-uniform mixed air temperature. Where the mixed air temperature is higher, the superheat of the corresponding circuit increases as well. Figure 167 shows, that for approximately uniform air temperature, the circuit in the middle of the coil without any superheat. This is consistent with a much lower superheat observed with the same circuit for higher ambient temperature, as shown in Figure 169.

There are several possible reasons for this:

1. Airside maldistribution caused by:
 - a. Blockage of airflow by filter frame, which is difficult to access, since there is insufficient space for instrumentation after the filter.
 - b. Temperature maldistribution – minimal when compared to neighboring circuits, especially for 28°C ambient temperature with closed damper.
 - c. Turbulence and uneven air flowrate across the circuit caused by economizer.

²¹ Credit: Andrew J. Hortland, 2012, Herrick Labs, unpublished.

²² Cluster image distorted due to view angle of camera – actual size of air filters is identical.

2. Refrigerant side maldistribution.
3. Design limitation for coil design.

Figure 164 shows the coil circuitry; the center circuit is, with 12 circuits, 2 tubes or approximately 14 percent shorter than other circuits. Figure 165 shows the distributor and expansion valve. The valve is directly soldered onto the distributor which likely leads to quality and velocity maldistribution at the distributor inlet, resulting in maldistribution at the outlet of the circuits. The feeder tubes leading from the distributor to the coil have different bend radii, which can lead to unequal pressure drop. This unequal pressure drop may influence the performance of the distributor as well. Figure 170 shows that, with exception of the shorter middle circuit, the superheat values are equal within the measurement tolerance. This suggests that the effects of refrigerant and airside maldistribution either nearly compensate for each other or are relatively small.

Figure 158 shows the economizer section from outside the unit. The exhaust air outlet is in direct vicinity to the air inlet, which leads to recirculation of a part of the exhausted air. Figure 159 through Figure 163 view the economizer for different opening positions. The economizer dampers are linked by plastic gears that are driven by a single servo motor that engages into one of the gears on one side of the economizer. Figure 159 shows the closed economizer position – the outdoor air damper is closed while the return air damper is in a slight angle in order to deflect part of the return air to the lower part of the evaporator coil. Figure 160 and Figure 161 show the 50 percent opening position of the economizer. The outdoor air damper is partially open, while the exhaust and return air damper work together to exhaust a part of the return air. For fully opened economizer, the exhaust and return air damper seal up against each other and the enclosure as shown in Figure 162 and Figure 163, while at the same time, the outdoor air damper is fully open.



Figure 158: Economizer Section of Unit



Figure 159: Closed Economizer



Figure 160: 50% Open Economizer, View Angle 1



Figure 161: 50% Open Economizer, View Angle 2



**Figure 162: Fully Open Economizer,
View Angle 1**



**Figure 163: Fully Open Economizer,
View Angle 2**

The velocity of the coil was measured with a handheld flow meter shown in Figure 168. This flow meter has a threshold of 0.5 m/s as shown in the manufacturer specification in Table 4. It was observed that the flow meter is directionally dependent, e.g. has highest sensitivity if placed in the direction of the airflow. This reduces the influence of air not going horizontally onto the coil if the device is aligned in parallel with the coil. It therefore gives an estimate of the frontal velocity. For the measurement, the flow meter was fixed at a position, then the maintenance opening was closed and the readout from the display was done using a webcam placed outside of the influence range of the flow meter. Figure 166 shows the velocity distribution at the positions indicated in Figure 157 for high fan speed at different damper positions. For closed economizer, the velocity decreases approximately linear from the top of the coil to the bottom of the coil. The measurement at the bottom of the coil is below the rated threshold of the measurement device and has therefore to be taken with caution. For 50 percent economizer opening, the maximum velocity shifts towards the middle of the coil. This is caused by the outdoor air damper opening up below that with air flow direction directly onto the coil in combination with the return air flow from the bottom. For 100 percent damper opening, the maximum flowrate shifts towards the bottom of the coil, which is a result of flow entering from the outdoor air damper and adhering to the exhaust and return air damper in combination with air leakage from the closed return air damper.

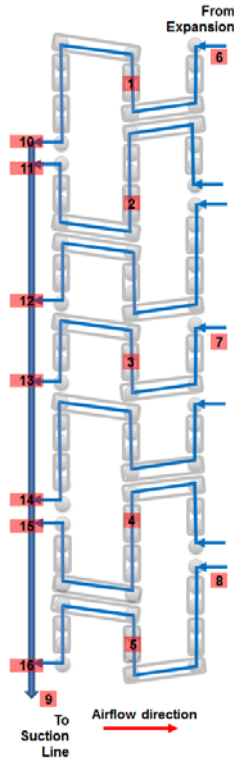


Figure 164: Evaporator Coil Circuitry²³

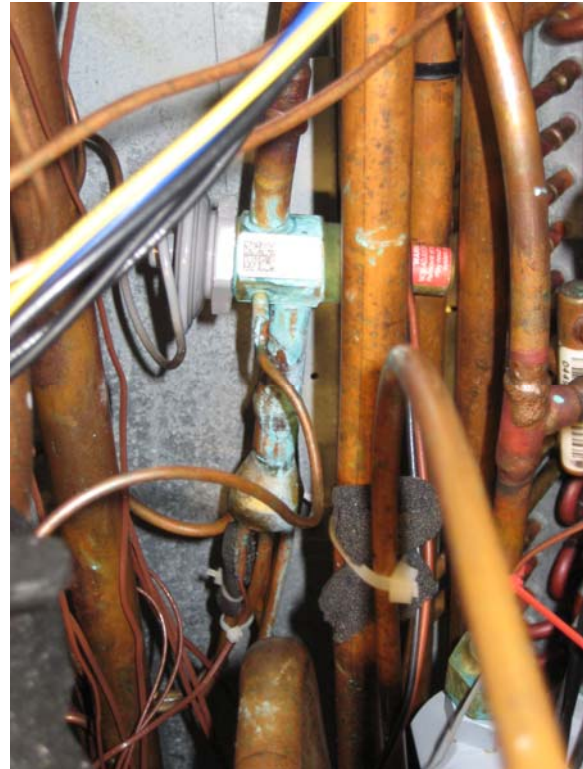


Figure 165: Distributor and Expansion Valve

Figure 167 shows the velocity distribution at the positions indicated in Figure 157 for nominal fan speed at different damper positions. The results look similar to the ones shown for high fan speed in Figure 166 but with reduced magnitude. The handheld anemometer, while being directionally sensitive, does not measure the velocity perpendicular to the coil. Furthermore the measurements were taken in front of the filter rather than directly in front of the coil. Therefore the resulting velocity maldistribution has to be interpreted as “strong suggestion that there exists a maldistribution in frontal velocity” rather than being numerically exact.

²³ Credit: Woohyun Kim, 2012, Herrick Labs, unpublished

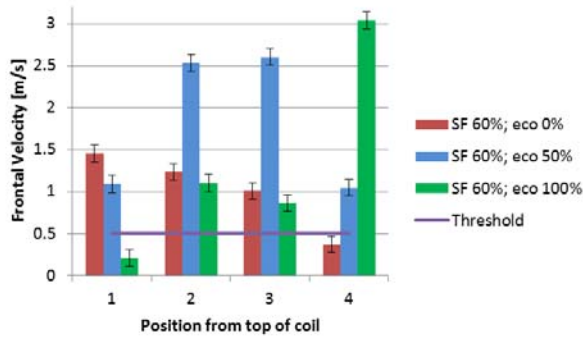


Figure 166: Velocity Distribution along Coil, 60 Hz Supply Fan Frequency, Different Economizer Positions

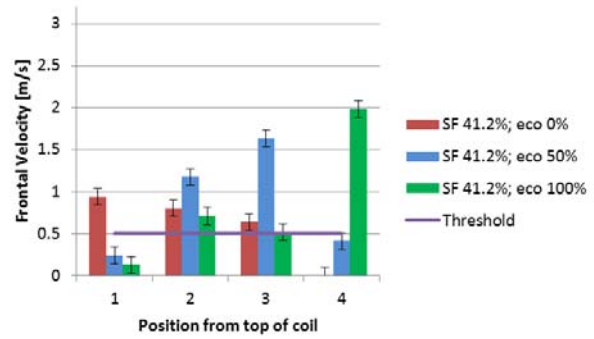


Figure 167: Velocity Distribution along Coil, Nominal Supply Fan Frequency Of 41.2 Hz, Different Economizer Positions

Table 4: Flow Meter Specification

Type	Handheld propeller anemometer
Model	Omega HH-F10
Accuracy	0.1 m/s
Threshold	0.5 m/s



Figure 168: Handheld Anemometer

Besides from the frontal maldistribution of the airflow in terms of temperature and velocity, quality maldistribution exists concurrently.

The result of the combination of air-side and refrigerant side maldistribution caused mainly by changed inlet conditions to the distributor can be seen best by comparing the circuit exit superheats for the same inlet conditions for uniform air temperature distribution. Figure 170 shows that for the TXV, the circuit with missing superheat is in the middle of the coil, while for the EXV, Figure 172, the first circuit at the top of the coil is missing superheat. This means that, by changing from TXV to EXV, the refrigerant flowrate to circuit 1 was increased while the flowrate to circuit 4 was decreased. this also indicates that the refrigerant distribution is depended on the alignment of the distributor.

Changing the ambient temperature to a higher value, for the purpose of the tests 52°C, leads to an uneven temperature distribution on the coil. Figure 169 and Figure 171 show that the top of

the circuit experiences a higher air inlet temperature which leads to higher superheat on those circuits and reduced superheat at the bottom circuits.

Individual circuit exit superheat and average mixed air temperature at nominal fan frequency, TXV

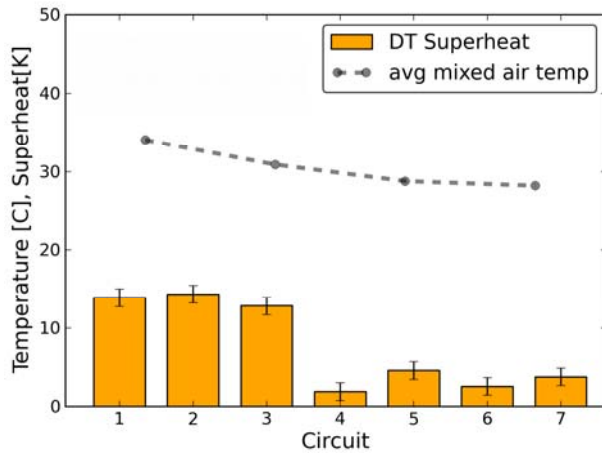


Figure 169: TXV, 52°C Ambient Temperature, Closed Damper

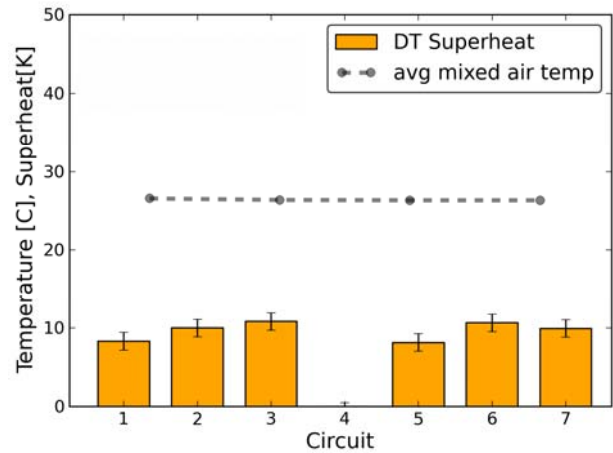


Figure 170: TXV, 28°C Ambient Temperature, Damper Closed

Individual circuit exit superheat and averaged mixed air temperature at nominal fan frequency, EXV

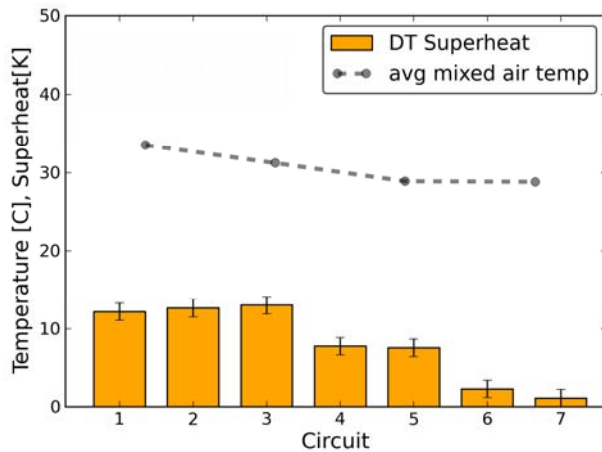


Figure 171: EXV, 52°C Ambient Temperature, Closed Damper

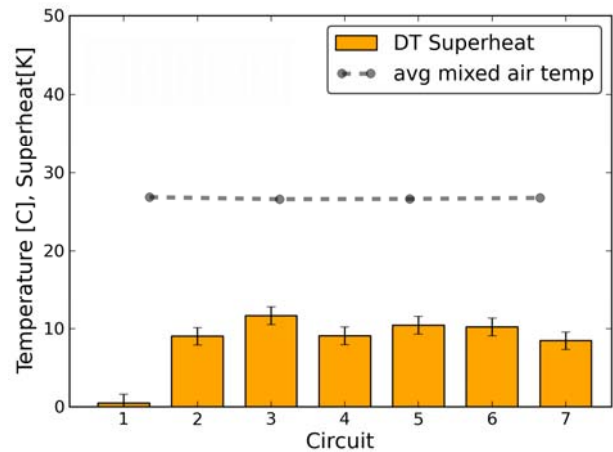


Figure 172: EXV, 28°C Ambient Temperature, Closed Damper

Figure 173 and Figure 174 show the individual circuit exit superheats as well as the overall exit superheat during the high ambient temperature test with closed damper. Figure 173 shows that most individual exit superheats show a wavy, roughly sinusoidal course over time. The exception from this are circuits 6 and 7 which show a bottom limit of approximately 2 K and 0.5 K with occasional spikes. These spikes coincide with an increase in suction superheat, therefore the bottom limit corresponds to liquid overfeed of these circuit. The larger variation of

the suction superheat as compared to the average exit superheat of the individual circuits leads to the same conclusion, since the average exit superheat does not capture the full effects of liquid feed over while the suction superheat does. The average exit superheat is higher than the suction superheat due to the evaporation of the fed over liquid and due to measurement error of the on-surface exit superheat measurements. Similarly for the TXV case, Figure 174, circuit 2 exhibits a similar behavior while circuit 4, even so its superheat value is more unstable and lower, does not indicate constant liquid feed over. The difference of the magnitude of the fluctuations in average exit and overall superheat are smaller which suggests smaller liquid feed over.

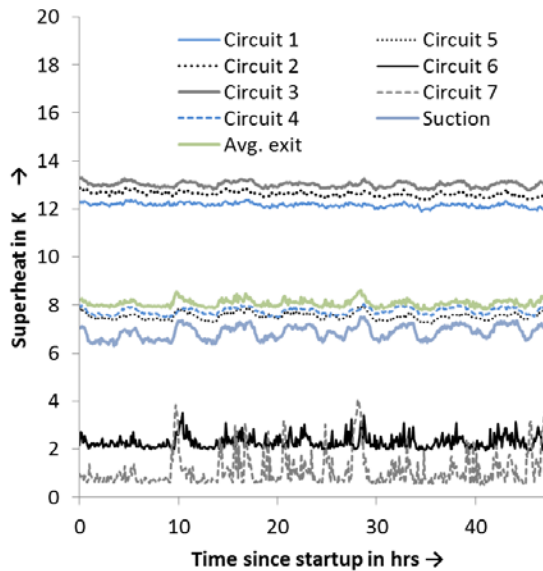


Figure 173: EXV, 52°C Ambient Temperature, Closed Damper, Individual and Overall Exit Superheat

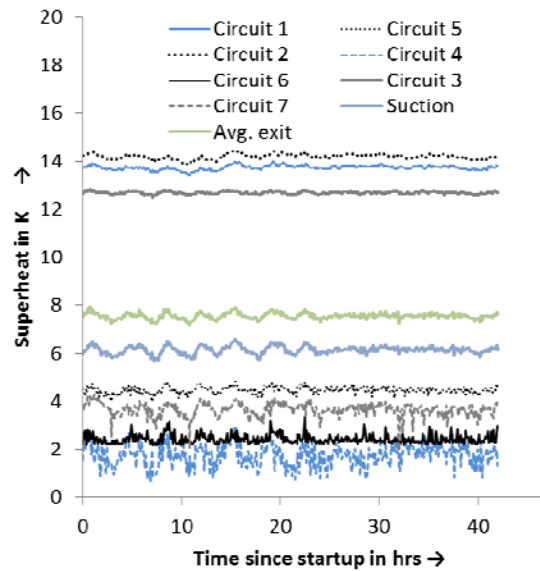


Figure 174: TXV, 52°C Ambient Temperature, Closed Damper, Individual and Overall Exit Superheat

The effects of airside maldistribution are not only depended on ambient temperature but also on economizer damper position. Figure 175, Figure 176, and Figure 177 show the (row-wise) averaged mixed air temperature and individual circuit exit superheats. While there is only a negligible change of the averaged mixed air temperature as the damper is opened up, the exit superheat of circuit 7 increases significantly. This suggests a higher air flowrate for circuit 7. The opposite happens for circuit 1, resulting in increasing liquid feedover. Overall, the sole effects of the air flow velocity maldistribution onto the distribution of superheat appear to be smaller than one would expect from the measured velocity maldistribution shown in Figure 167. The reasons for this are limited directional sensitivity of the used flow meter, flow equalization in and after the air filters and cross fin conduction in the evaporator.

It was noticed that the alignment of the expansion valve relative to the distributor has a significant effect onto the distribution to the individual circuits. It was therefore adjusted several times for the EXV control scheme until relatively even exit superheats were observed. The superheat profile of the original TXV configuration for closed damper position, Figure 170, shows one circuit with lacking superheat. For the same operating condition, the EXV, Figure

175, shows a similar maldistribution but a change in the circuit which feeds liquid over. This suggests that the resulting effect of the initial maldistribution for the EXV control scheme is similar as for the original system.

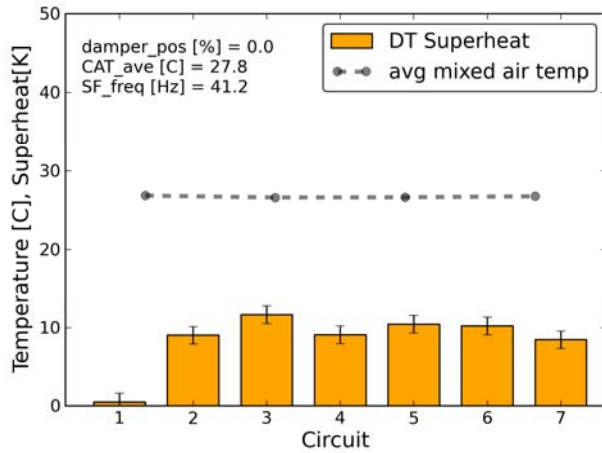


Figure 175 EXV, 27.8°C Ambient Temperature, Closed Damper

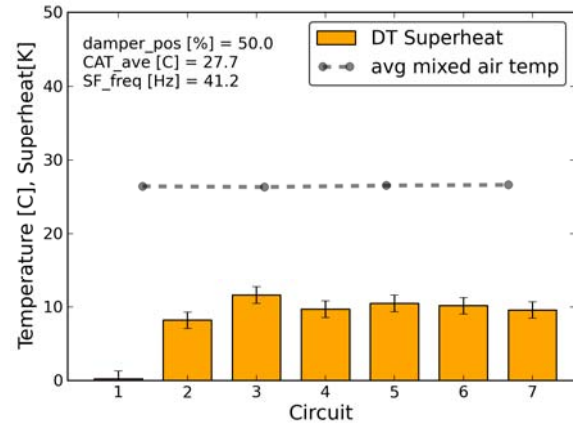


Figure 176: EXV, 27.7°C Ambient Temperature, Half Open Damper

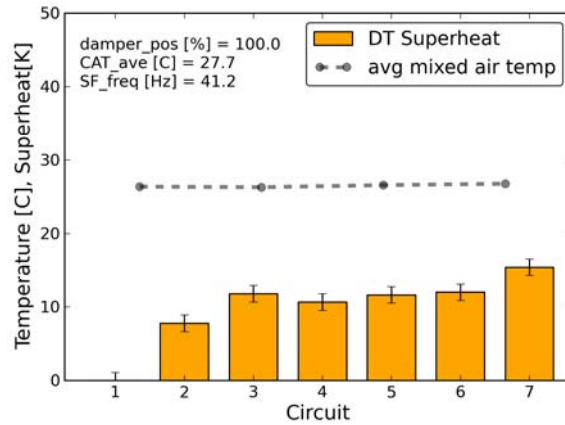


Figure 177: EXV, 27.8°C Ambient Temperature, Fully Open Damper

The effects of airflow maldistribution are exacerbated if the damper is opened when the ambient temperature is significantly lower or higher than the return air temperature. Figure 178 shows that, if the economizer damper is opened 50 percent at high ambient temperature, the air inlet temperature at the top of the evaporator is 18 K higher than at the bottom of the evaporator. This leads to significant liquid overfeed from circuits 1 and 2 and excessive superheat on circuits 4 to 10. While the difference between average and overall superheat was approximately 2 K for the cases with closed damper and small maldistribution, it increased to 8 K due to the large maldistribution between airside and refrigerant side. For the fully opened damper, Figure 179, the differences between maximum and minimum air inlet temperature are much smaller which leads to much smaller differences for the individual superheat as well as to no significant liquid overfeed. This in turn leads to only a small benefit for the hybrid control as

shown later. Notice that under fault-free conditions, the damper should usually not be fully open at high ambient temperatures (except for applications that require 100 percent fresh air).

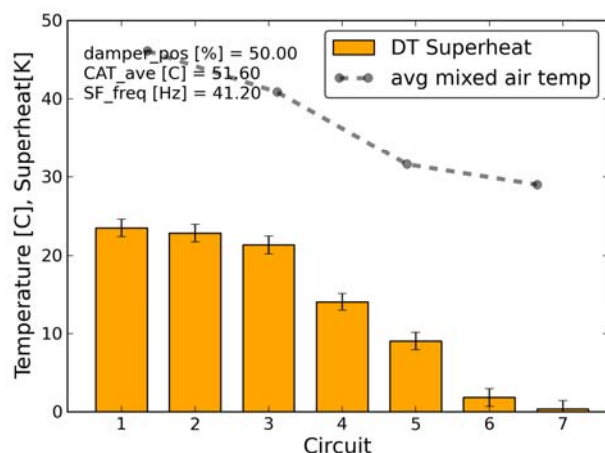


Figure 178: Individual Circuit Exit Superheat and Avg. Mixed Air Temperature at Nominal Fan Frequency, EXV, 52°C Ambient Temperature, Half Open Damper

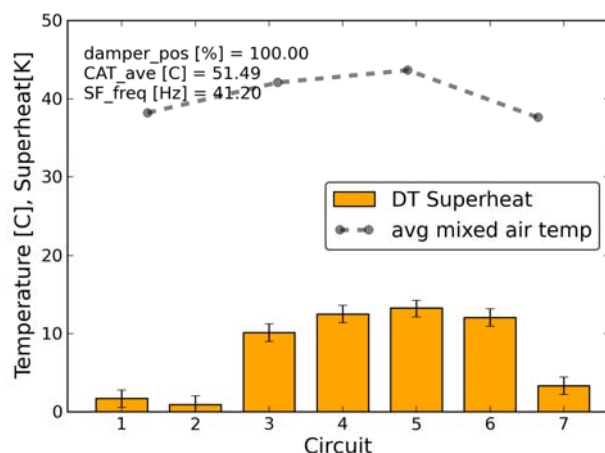


Figure 179: Individual Circuit Exit Superheat and Avg. Mixed Air Temperature at Nominal Fan Frequency, EXV, 52°C Ambient Temperature, Fully Open Damper

For the cases with low ambient temperatures the behavior was similar to the high ambient temperature but with the larger air inlet temperatures as well as larger superheats occurring at the bottom of the coil as shown in Figure 180, Figure 181 and Figure 182 for closed, half open and fully open damper. Notice that for the fully open damper, Figure 182, the ambient temperature had to be increased to prevent automatic shutdown of the compressor by the controls of the RTU. In practice, at these cold ambient temperatures, cooling loads are lower and cooling can be supported by adjusting the damper position in order to reach the zone target temperature, which reduces the demand for the vapor compression system.

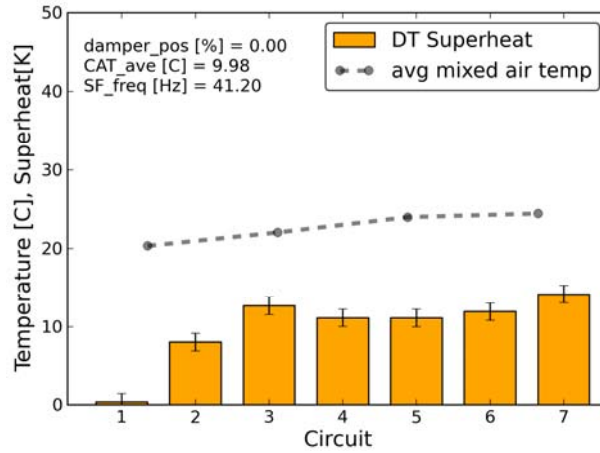


Figure 180: Individual Circuit Exit Superheat and Avg. Mixed Air Temperature at Nominal Fan Frequency, EXV, 10°C Ambient Temperature, Closed Damper

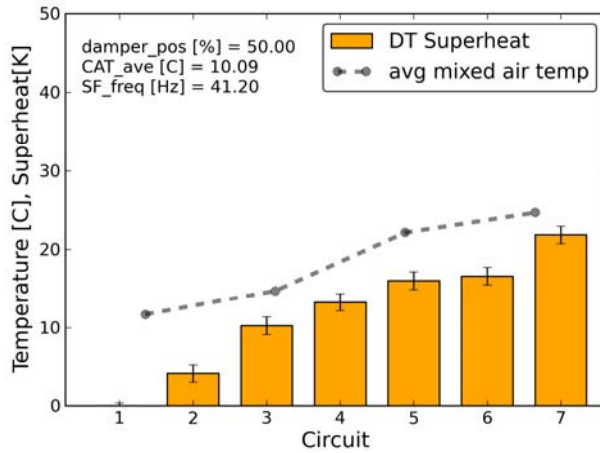


Figure 181: Individual Circuit Exit Superheat and Avg. Mixed Air Temperature at Nominal Fan Frequency, EXV, 10°C Ambient Temperature, Half Open Damper

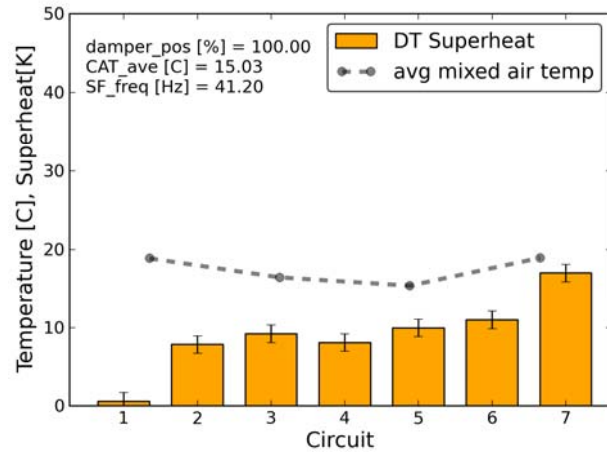


Figure 182: 20 Individual Circuit Exit Superheat and Avg. Mixed Air Temperature at Nominal Fan Frequency, EXV, 15°C Ambient Temperature, Fully Open Damper

For the hybrid control, the exit superheats are essentially identical even for extreme airside maldistribution. This is exemplarily shown in Figure 183, where the difference between individual circuit superheats is essentially not noticeable even though the air inlet temperature is significantly uneven across the coil. The nearly identical exit superheats are caused by the PI control that drives all exit superheats to the same value, as shown in Figure 184. Figure 184 also shows a difference of approximately 1.5 K between the individual circuit exit superheats and the suction superheat. This difference is caused by the non-invasive individual circuit exit temperature measurement²⁴: conduction along the copper tube from the warm fins as well as

²⁴ The less accurate non-invasive measurement needed to be used in order to not change the pressure drop in the individual circuits which could affect the refrigerant flow distribution for the EXV and TXV control scheme.

convection to the individual circuit exit superheat measurement position as shown in Figure 185 leads to measurement error. For the overall superheat measurement, in-flow measurement is used, which is more accurate.

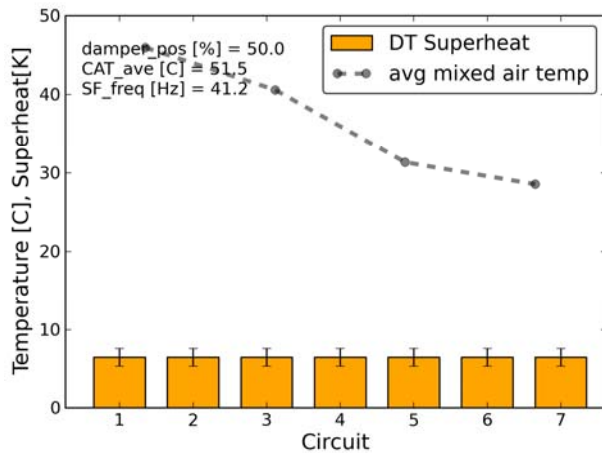


Figure 183: Individual Circuit Exit Superheat and Avg. Mixed Air Temperature at Nominal Fan Frequency, Hybrid, 52°C Ambient Temperature, Half Open Damper

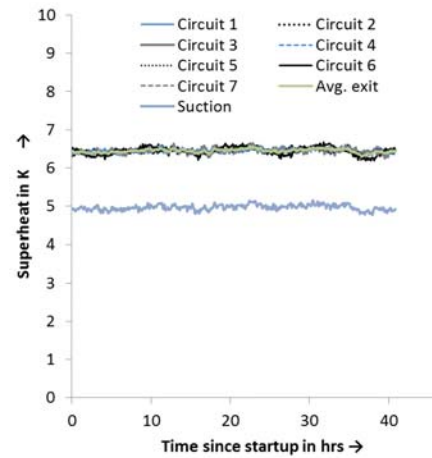


Figure 184: Individual Circuit Exit Superheat and Overall Superheat, Hybrid, 52°C Ambient Temperature, Half Open Damper

Since the position of each balancing valve is known during the tests, they can be used as virtual flow sensors in order to calculate the flow distribution to the individual circuits. This flow distribution, since equal superheats on the individual circuits are maintained, is equivalent to a capacity distribution between the circuits. For the calculation of the individual circuit flowrates, the 8-PI general correlation of Bach et al. (2012b), which works for subcooled as well as two-phase inlet conditions, was used. For the calculation of the uncertainties, the rated accuracy of the measurements was used. The valve zero position for each of the valves was determined twice, with a maximum difference of 7 steps. The average of the two zero positions for each valve was used for the calculations along with a conservative ± 5 step accuracy for the uncertainty calculation. Figure 186 shows the calculated mass flowrates of the individual circuits for both, the hybrid control case and the primary valve (PEXV) fully open case. The average measured flowrate is the flowrate measured with the Coriolis flow meter upstream of the primary expansion valve divided by the number of circuits. Since test conditions were replicated within less than 0.1°C dry bulb and 0.2°C dew point, the averaged measured flowrates of hybrid and primary valve fully open case are very close. The average of the virtual flow sensor measurements over-predicts the flowrates, since the valve outlet pressure was taken was estimated using the evaporator outlet pressure. The non-uniformity of the individual circuit mass flowrates is greater than the uncertainty of the mass flow measurement, which suggests that the circuits have different cooling capacity.

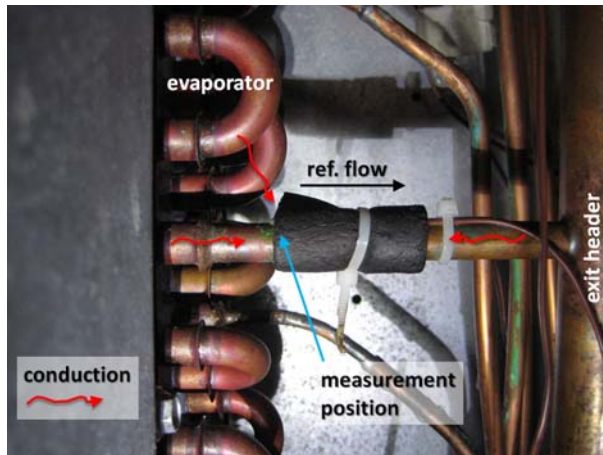


Figure 185: Exit Superheat Measurement Position

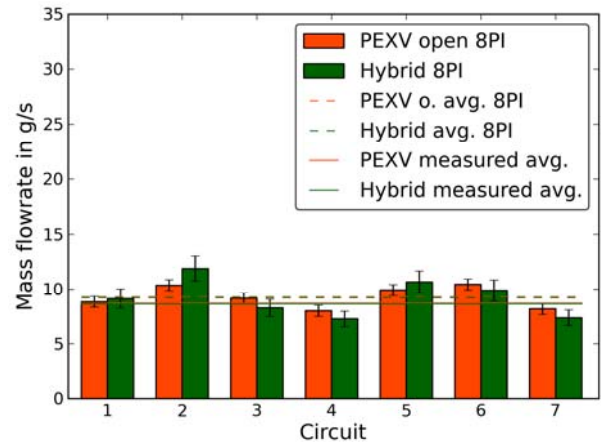


Figure 186: Refrigerant Flow Rates for Closed Damper Position for 28°C Ambient Temperature

To illustrate maldistribution results more intuitively, Li et al. (2005)'s mass flow distribution performance index (FMI) as previously defined in equation (7), page 64 is used. The FMI is the difference between average flowrate and circuit flowrate normalized by the average flowrate. Positive values of the mass flow distribution index indicate more than average flow.

Figure 187 shows the FMI for the 28°C ambient temperature, closed damper case. The differences between hybrid and PEXV fully open case increase for increasing deviation from the average value. This suggests that the quality at the individual circuits increases (decreases) if the circuit flowrate is larger (smaller) than the average flowrate. This tendency is consistent with most of the measurement of the different test points. For the 28°C ambient temperature, closed damper case, the maximum deviation is approximately 12 percent for the PEXV results. Figure 188 shows that if the ambient temperature is increased, the flow distribution changes with more refrigerant flow passing through the top circuits which are subject to a higher air inlet temperature. The maximum deviation from the average increases to approximately 20 percent at the top of the coil.

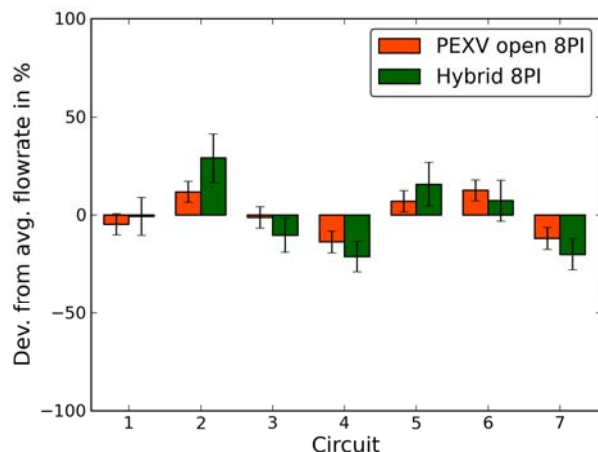


Figure 187: FMI for Closed Damper Position, 28°C Ambient Temperature

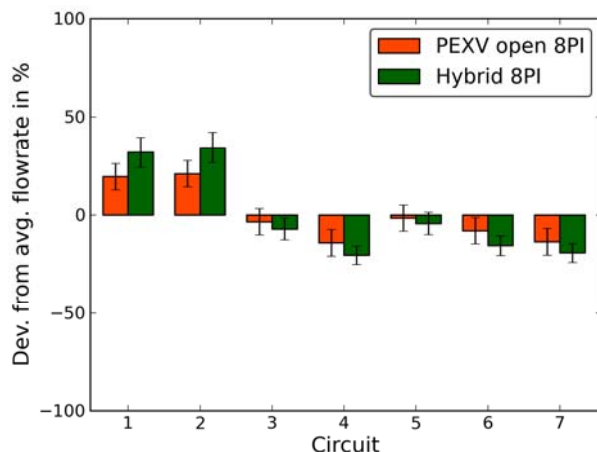


Figure 188: FMI for Closed Damper Position, 52°C Ambient Temperature

Figure 189 shows that, if the damper is half open at 52°C ambient temperature, the necessary refrigerant flow maldistribution to achieve equal exit superheats increases significantly: the maximum deviations are +45 percent at the top of the coil and -56 percent at the bottom of the coil. As to be expected from the temperature distribution for fully open coil, Figure 179, a further increase in opening leads to a reduction in required refrigerant side maldistribution. Figure 190 shows that for this case, the maximum deviation from the average flowrate decreases to -21 percent and +28 percent with inversion of the location of the maxima. The results for low ambient temperature look similar and are not shown here for the purpose of brevity.

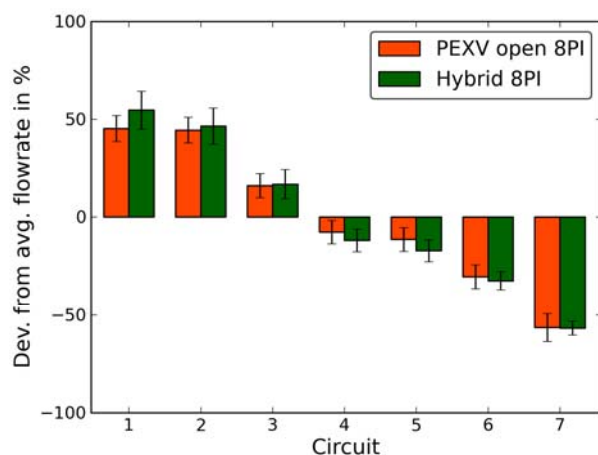


Figure 189: FMI for Half Open Damper Position, 52°C Ambient Temperature

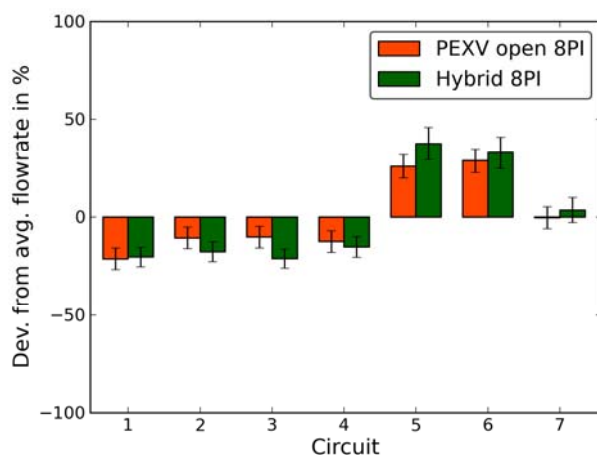


Figure 190: FMI for Fully Open Damper Position, 52°C Ambient Temperature

4.1.4 Overall System behavior - Superheat

Figure 191 shows that the circuit exit superheat of EXV and TXV were very similar with the TXV control leading to a smaller superheat for some conditions. On average, comparing superheats for similar ambient temperatures, the exit superheat of the TXV was less than 0.3 K lower than for the TXV, which means that, on average, there is only a negligible system performance difference between the TXV and the EXV. Since, due to a communication mistake, the operating conditions for the TXV were not matched exactly, and EXV are expected to be standard for this application in a view years, the EXV was chosen as reference for the performance benefits evaluations. Figure 192 shows the superheat for the EXV for different damper positions. For high ambient temperature there seems to be a trend towards lower superheats with increasing economizer opening while lower ambient temperatures generally lead to a higher superheat. Figure 193 shows that there is a trend to lower superheats with increasing mixed air temperature. This might be caused by less boiling based flow instabilities due to smaller difference between liquid and vapor density. For the hybrid control scheme, it was found that the fluctuations of overall superheat are much smaller, which would have lead to a superheat of approximately 3 K according to the control strategy. Since this seems unrealistic for practical applications, where larger measurement tolerances occur and where the operating conditions are less steady, the overall superheat value was fixed to be 5 K, which was achieved within a 0.5 K tolerance as shown in Figure 194.

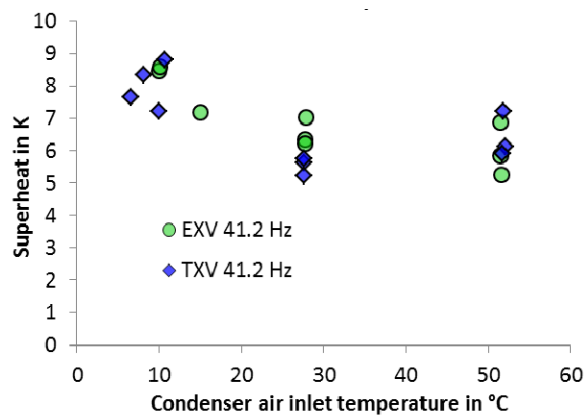


Figure 191: Overall Evaporator Superheat, Nominal Fan Speed

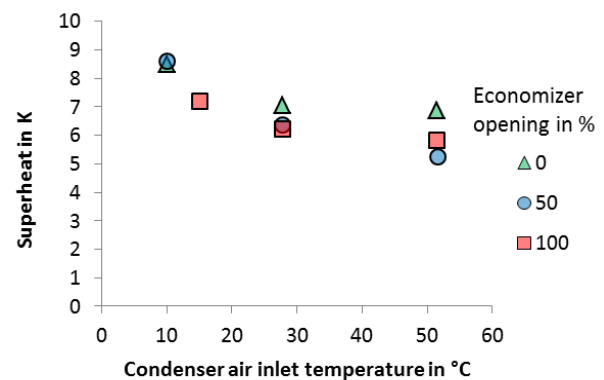


Figure 192: Overall Superheat, EXV, as Function of Air Inlet Temperature with Different Damper Positions

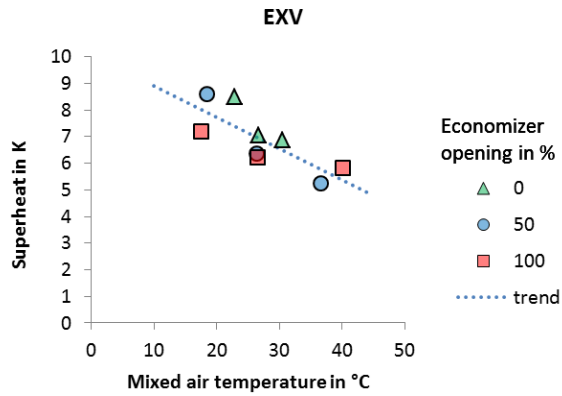


Figure 193: Overall Superheat, EXV, as Function of Mixed Air Temperature with Different Damper Positions

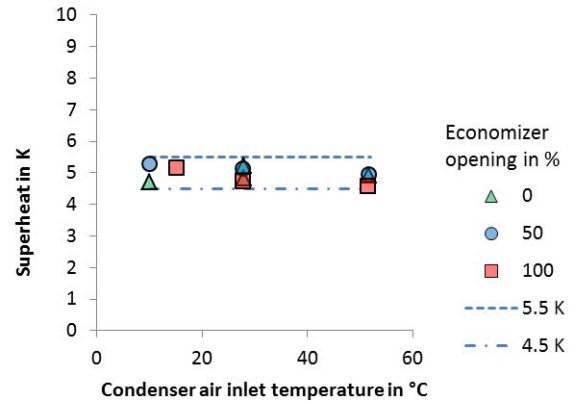


Figure 194: Overall Superheat, Hybrid, as Function of Mixed Air Temperature with Different Damper Positions

Overall System Behavior - Subcooling

Figure 195 shows that the subcooling ranges from 5 to 7 K for the EXV, and Figure 196 shows that the subcooling ranges from 5.5 to 7.0 K. For both control schemes, the trend is a decrease in subcooling with increasing ambient temperature.

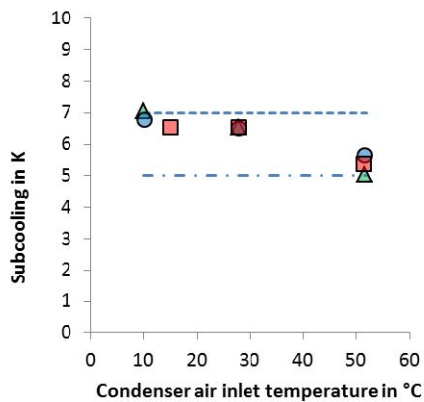


Figure 195: Subcooling for EXV Tests

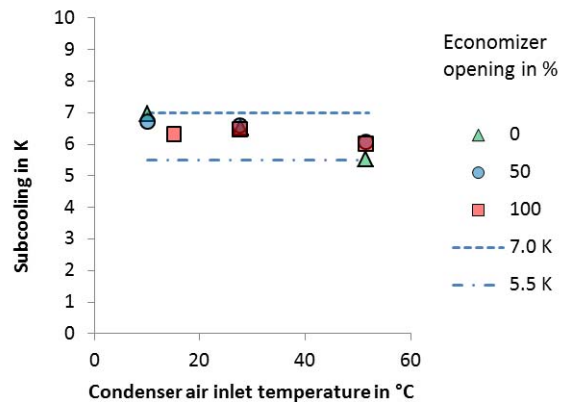


Figure 196: Subcooling for Hybrid Tests

4.1.5 COP and Capacity

4.1.5.1 Definition of Used Terms

Cooling capacity (or short capacity) is defined to be

$$\dot{Q}_{cool} = \dot{Q}_{ref} - \dot{W}_{SF}$$

where:

$$\dot{Q}_{ref} \text{ is the refrigerant side cooling capacity, and}$$
$$\dot{W}_{SF} \text{ is the power consumption of the supply fan, including its variable speed drive.}$$
(16)

The supply fan power meter was found to be broken at the end of the test series. Therefore the supply fan power consumption was mapped using fan only-tests with the power meter that measures the total power consumption. The parasitic load, caused by the controls, was determined to be 30 W and subtracted from the measured values to obtain the fan power.

The coefficient of performance is, analogous to the EER in ANSI/ASHRAE 210/240(2008),

$$COP = \frac{\text{cooling delivered}}{\text{power consumption}} = \frac{\dot{Q}_{cool}}{\dot{W}_{tot}} = \frac{\dot{Q}_{ref} - \dot{W}_{SF}}{\dot{W}_{tot}}$$

where:

(17)

\dot{W}_{tot} is the total power consumption.

The total power consumption was calculated to be

$$\dot{W}_{tot} = \dot{W}_{CF} + \dot{W}_{comp} + \dot{W}_{SF} + \dot{W}_{par},$$

where indexes are:

$CF = \text{Condenser Fan}$

$Comp = \text{Compressor}$

$SF = \text{Supply fan (from mapping)}$

$par = \text{parasitic} = 30 \text{ W}$

(18)

COP and Capacity improvement are calculated as the difference between the two control schemes normalized by the value of the EXV baseline.

4.2 EXV Control Scheme

Figure 197 shows the COP of the RTU as function of ambient temperature and economizer position. For condenser air inlet temperatures below the return air temperature of 26.67°C (80 F), the COP decreases as the economizer opening increases. The opposite happens, if the condenser air inlet temperature is above the return air temperature. Figure 198 shows that the capacity shows a similar behavior as the COP with respect to the dependency of the economizer opening. Figure 199 shows the capacity as a function of the mixed air temperature. An increase in mixed air temperature generally corresponds to an increase in capacity for a given condenser air inlet temperature. An exception of this are the points at 27.78°C (82 F), that do not follow this trend. The reason for this is, as shown in Figure 200 that the air flowrate is significantly smaller for 100 percent damper opening. This is a result of the target pressure drop curve that was used since the nozzle box booster fan was insufficient for the large flowrates used for the TXV tests. The target pressure drop curve emulate that quadratic behavior of pressure drop with flowrate that would occur when the unit is connected to a building. Figure 155 previously showed the target pressure drop as function of flowrate together with the actual flowrate.

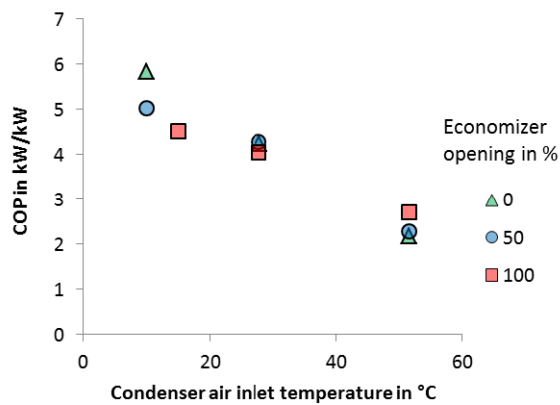


Figure 197: COP for RAC, EXV Control Scheme

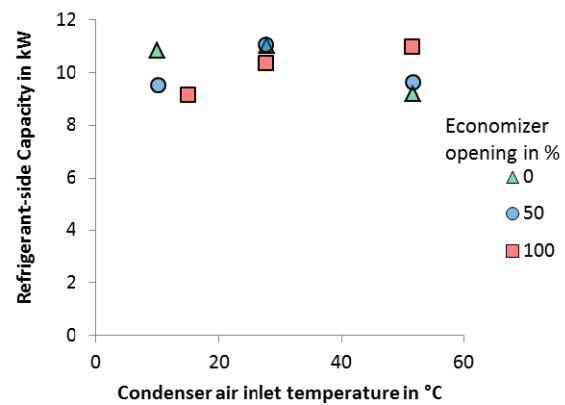


Figure 198: Capacity for RAC, EXV Control Scheme

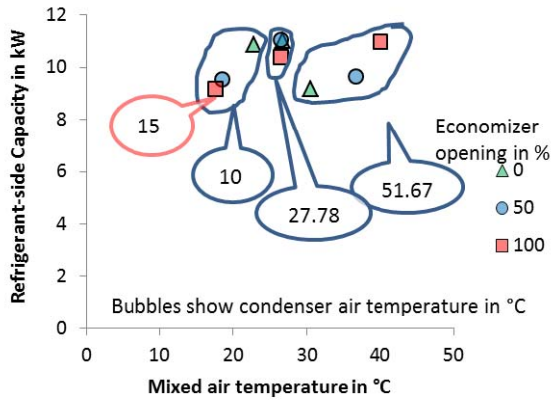


Figure 199: Capacity as Function of Mixed Air Temperature, RAC, EXV Control Scheme

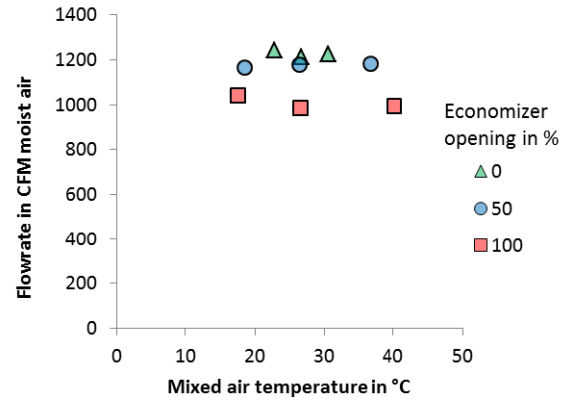


Figure 200: Flowrate of Moist Air as Function of Mixed Air Temperature, RAC, EXV Control Scheme

Figure 201 shows the COP for the hybrid control scheme as a function of ambient temperature. The trends are similar to the EXV control scheme, Figure 197 – the most significant change is, that for 50 percent damper opening, the COP moves closer to the value for 100 percent damper opening. The same is the case for the capacity, Figure 202, where for 52°C, the capacity is nearly identical for 50 percent and 100 percent damper opening. For the low ambient temperature case, the changes between EXV and hybrid control are less significant. Figure 203 shows the refrigerant side capacity as a function of (un-weighted) average mixed air temperature. For the low ambient temperature, the mixed air temperature is lower than the return air temperature which explains why the capacity change between EXV and hybrid control are less significant for that point. For high ambient temperature, the mixed air temperature for 50 percent damper opening is lower than for 100 percent damper opening which intuitively should result in a lower capacity value. However, the air flowrate to the different circuits differs, which invalidates the assumption of averaged flow-un-weighted air inlet difference being roughly proportional to overall capacity. Figure 204 shows the moist air flowrate for the hybrid control tests which is nearly identical to the moist air flowrate for the EXV tests, Figure 200.

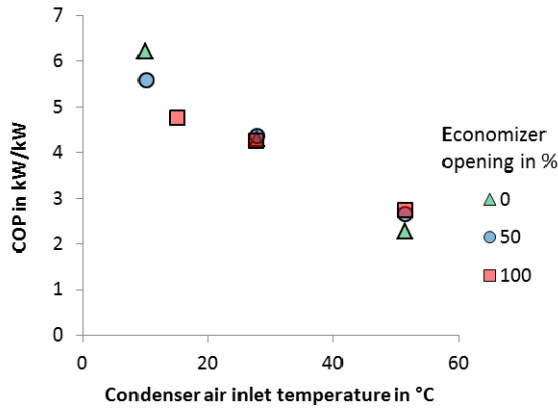


Figure 201: COP for RAC, Hybrid Control Scheme

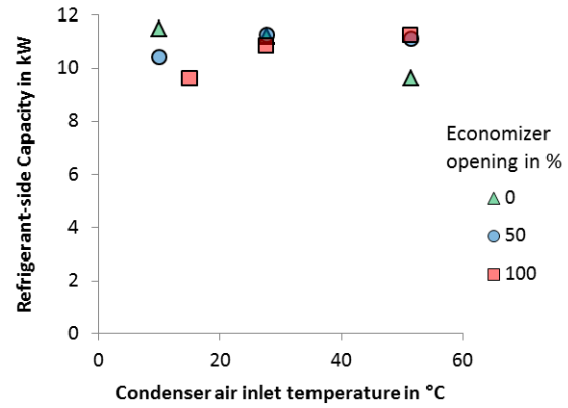


Figure 202: Capacity for RAC, Hybrid Control Scheme

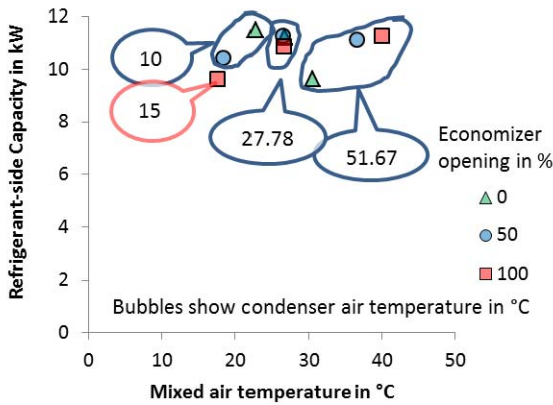


Figure 203: Capacity as Function of Mixed Air Temperature, RAC, Hybrid Control Scheme

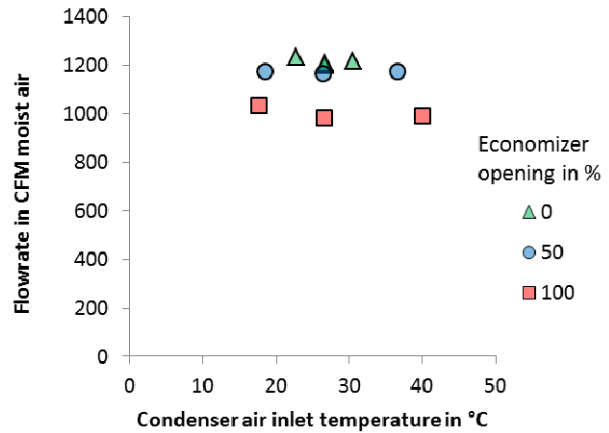


Figure 204: Flowrate Of Moist Air as Function of Mixed Air Temperature, RAC, Hybrid Control Scheme

4.2.1 COP and Capacity improvement

Figure 205 and Figure 206 show the improvement of COP and capacity respectively for the hybrid control scheme.²⁵ The results of COP and capacity improvement are nearly identical. For fully open damper the improvement is about 5 percent for COP and capacity at low and medium ambient temperature while it decreases to approximately 2 percent for high ambient temperature. For closed damper, the maximum improvement is about 6 percent at low ambient

²⁵ The shown uncertainties are calculated using the rated uncertainty for data acquisition, transducers and sensors. Since the hybrid and EXV tests are repetitions of the same operating condition, this leads to an overprediction of the uncertainty – likely by an order of magnitude. However, for the largest source of uncertainty – the temperature measurements – no data for repeatability was available.

temperature, while the minimum improvement is 1.5 percent (COP) and 1.9 (Capacity). For half open damper and 28°C ambient temperature, the COP and Capacity improvement is very similar to the one observed with closed damper. However, if the ambient temperature is low or high, the COP and capacity improvement increases significantly. COP (capacity) increases by 10.8 percent (9.6 percent) at low ambient temperature and 16.6 percent (15.6 percent) at high ambient temperature. All tests of the hybrid control scheme were repeated with PEXV fully open. The average COP (capacity) improvement for the PEXV was found to be 0.2 percent(0.2 percent) higher than for the hybrid control scheme with a maximum difference of 0.9 percent in COP improvement and 0.8 percent in capacity improvement. The only difference between hybrid and PEXV controlled system is the larger amount of charge held in the line between primary valve and balancing valves. For one hybrid test point (27.8°C condenser air temperature, closed damper) a repeatability test in hybrid control mode was performed with a better than 0.01 percent of COP improvement repeatability and a better than 0.26 percent capacity repeatability.

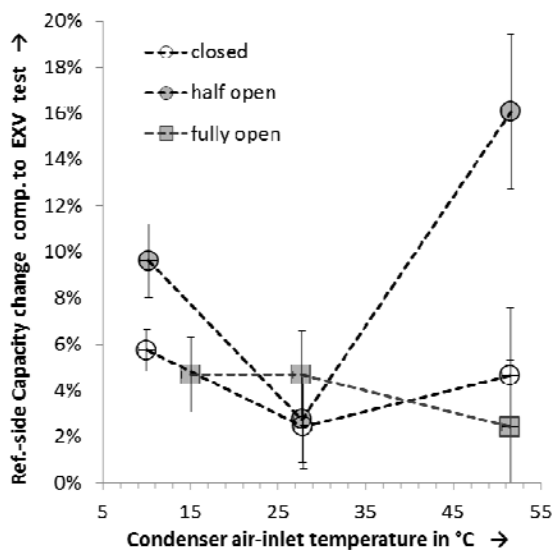


Figure 205: Capacity Improvement for Hybrid Control Scheme

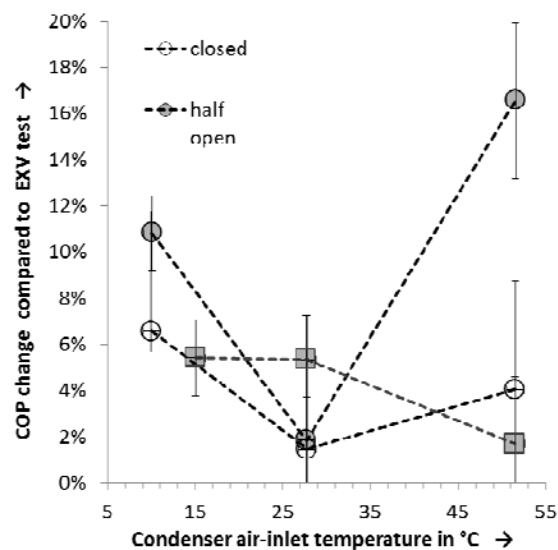


Figure 206: COP Improvement for Hybrid Control Scheme

To obtain a fairer comparison between EXV and hybrid controlled system, the power consumption of the hybrid control (which was not considered in Figure 205 and Figure 206) needs to be considered for the calculation of the COP. Using some assumptions for the type of processing unit used to calculate the necessary valve openings and the valves themselves, the power consumption for the rooftop unit hybrid control was estimated as shown in appendix A, page 226. The entire power consumption (on + off cycle) was added to the on cycle, which resulted in 25.4 W. This resulted, on average, in a reduction of achievable performance improvement of less than 1.1 percent. Figure 207 shows the achievable COP improvement if the control power consumption is considered. It should be noted that the commercially available flow control device is rated at 0.6 W of power consumption, which includes control, Danfoss

A/S (2011b). With a 30 percent duty cycle this corresponds to 2 W power consumption which is an order of magnitude lower than our estimate.

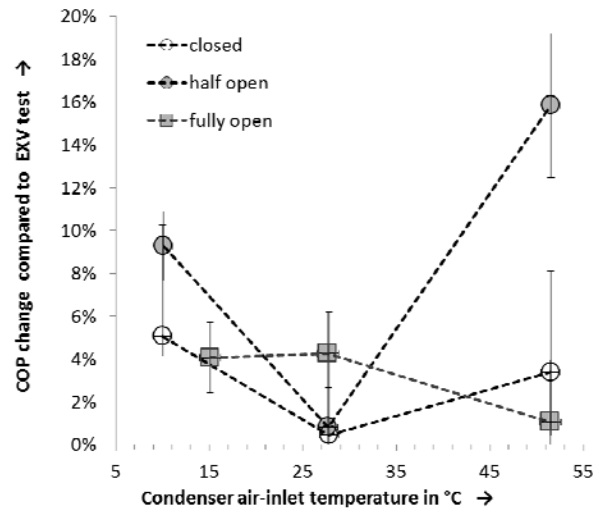


Figure 207: COP Improvement for Hybrid Control Scheme, Considering Additional Power Consumption of Hybrid Control

4.3 Building Capacity and COP

For a split type system, the COP can only be defined in one way, since the only contribution to cooling is achieved by the evaporation of refrigerant in the evaporator. For the rooftop unit, however, COP can also be defined by the amount of cooling delivered to the building. In contrast to a split system, where fresh air needs to be brought in separately, the rooftop unit integrates fresh air delivery. Therefore the suggested alternate definition of COP can have a lower value than the standard definition if ambient temperature is higher than return air temperature. Figure 152 illustrates the air streams of the building and the rooftop unit with economizer. Ambient air is mixed with return air before the air enters the evaporator. Therefore the evaporator air inlet enthalpy is dependent on the ambient temperature. The air is cooled by the evaporator and transported back into the building by the fan. Assuming that the air leakage from the building occurs at the same enthalpy as the return air, and building infiltration due to stack effect and static pressure of wind is negligible, a building COP can be estimated as shown in equation (19). This building COP is a measure of the effectiveness of the actual cooling of the building, in contrast to the COP, which is merely a measure of the effectiveness of the vapor compression system. In particular, this definition of a building COP can also be used for free cooling, where the total power consists merely of the parasitic loads and the supply fan power. For simplification purposes, a sensible heat load ratio of 1 was used for the calculation of the building COP. Note that that the building COP directly reflects the overall performance of the system, which includes how efficient the fresh air is brought to supply condition. Therefore the building COP will increase if air-to-air heat recovery is used for exhaust- and fresh air.

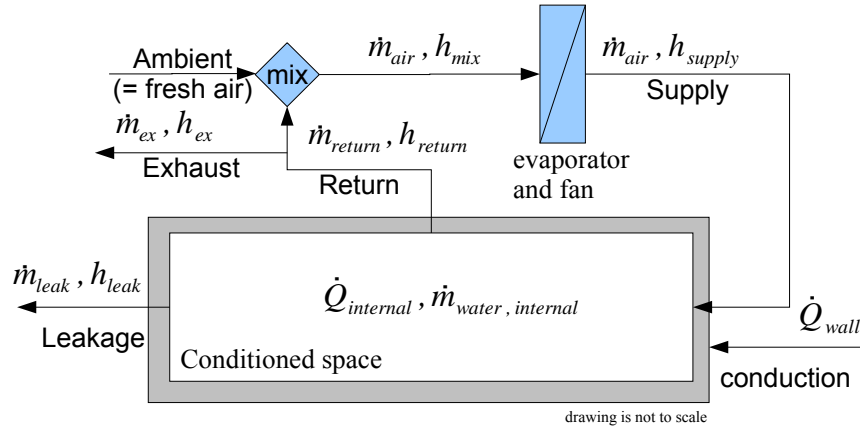


Figure 208: Simplified schematic for rooftop unit and building

$$COP_{Building} = \frac{Capacity_{Building}}{Power\ input} = \frac{\dot{m}_{air, supply} \cdot (h_{return} - h_{supply})}{\dot{W}_{tot}}$$

where :

$\dot{m}_{air, supply}$ = Supply air flowrate

h_{supply}, h_{return} = Supply/return air enthalpy

\dot{W}_{tot} = Total power consumption

(19)

Figure 209 exemplarily shows that the difference between the $\text{Capacity}_{\text{Building}}$ and the capacity defined according to AHRI 210/240 (2008). For low ambient temperatures, the $\text{Capacity}_{\text{Building}}$ is up to 60 percent larger than the AHRI 210/240 (2008) capacity while for high ambient temperatures, the $\text{Capacity}_{\text{Building}}$ is up to 75 percent smaller than the AHRI 210/240 (2008) capacity. If the rooftop unit was equipped with a heat recovery system with bypass, then it could benefit from the lower ambient temperature while reducing the penalty for the required minimum fresh air delivery at high ambient temperatures. The large change of capacity makes it necessary to recalculate the building COP change between hybrid and EXV control scheme based on a linear interpolation for the individual systems building COP for each individual temperature rather than interpolating between the individual measurement point building COP improvements directly. Figure 210 shows that the interpolated COP improvement deviates significantly from a straight line between individual temperature points, especially for half open damper between 27 and 52°C. Using a straight line interpolation of the building COP improvement for a bin type analysis would therefore result in a significant over-prediction of the achievable performance improvement for half open damper.

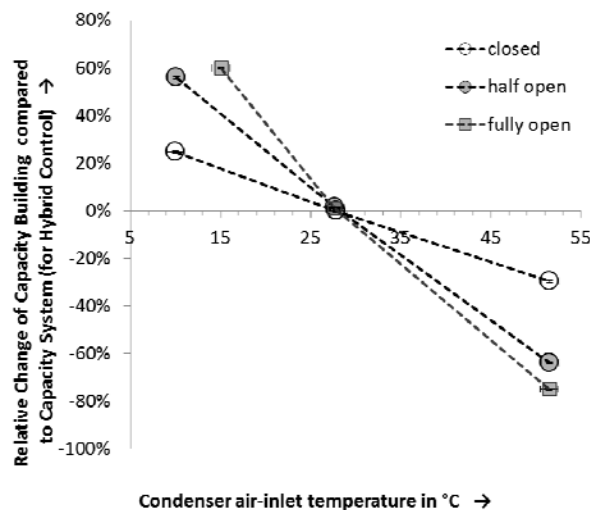


Figure 209: Capacity Difference for Hybrid Capacity if Building Capacity Rather than Vapor Compression System Capacity is Used

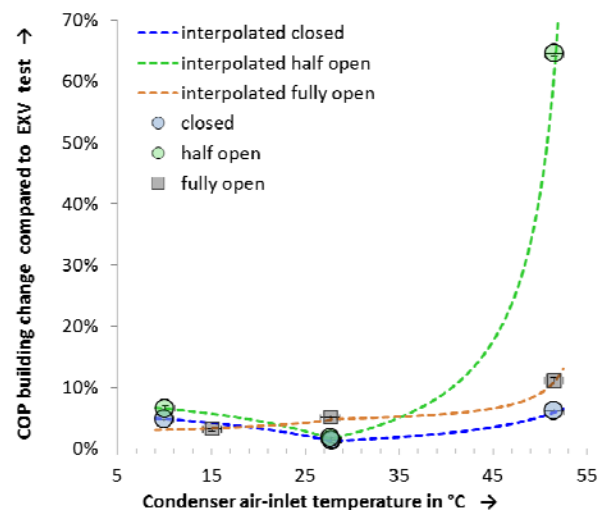


Figure 210: COP Building Change for Hybrid Control Compared to EXV Control Tests

Figure 211 shows that the free cooling building COP, e.g. if the system is operated without compressor, exceeds 10 for half and fully open damper and low ambient temperatures. However, for moderate ambient temperatures of more than approximately 17°C, using the vapor compression system is more efficient. Figure 212 shows the free cooling capacity for different damper positions as a function of the ambient temperature. The free cooling capacity is larger than the building heat load for temperatures less than approximately 23°C. Due to the lower building COP, free cooling only makes sense for temperatures of 17°C or lower. However, commercial buildings are still operated with continuously running supply fan to ensure fresh air supply with low initial cost for the controls. Energy savings could be achieved by using VOC and CO₂ sensors in order to apply demand controlled ventilation with reduced

fan operating time. In order to model effects the effects of demand control ventilation, a detailed analysis of the employed building materials as well as of the building usage is necessary, since VOC and CO₂ levels are highly dependent on these factors. However, this exceeds the scope of this project. Therefore the conventional control scheme, that uses a continuously operating fan was considered for the bin analysis.

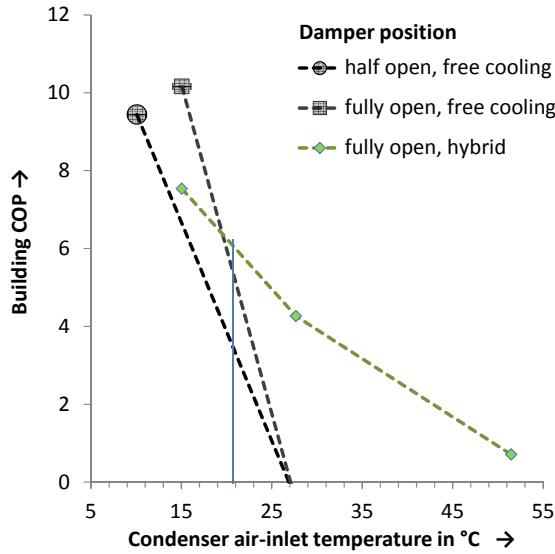


Figure 211: Free Cooling COP

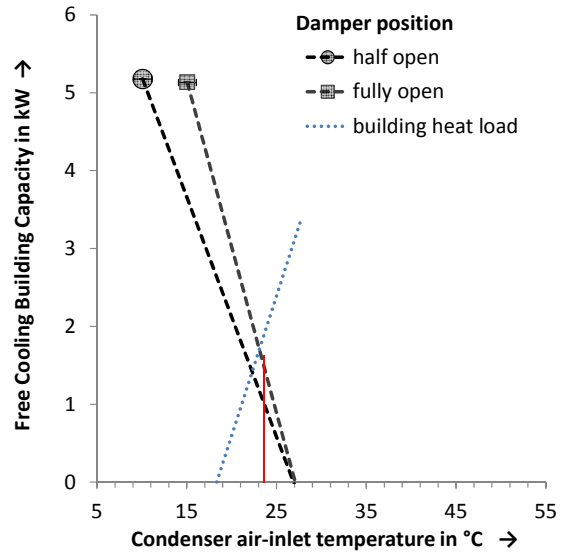


Figure 212: Free Cooling Capacity

4.4 Building Bin Analysis

In order to analyze the achievable performance improvement, a bin analysis for Sacramento Executive AP (Sacramento) and Bakersfield Meadows Field (Bakersfield) were conducted. Bin temperature for these locations was generated using TMY3 data from NREL(2012) and NREL(2013), respectively.

The design cooling requirement was based on a building with a balance point of 18.33°C and the cooling requirement at maximum occurring temperature of both locations matching the capacity for the EXV system. This was done in order to not penalize the Hybrid controlled system for its higher capacity at high ambient temperature. If the 0.4 percent or 1 percent design cooling requirement according to ASHAE Fundamentals (2009), Appendix 14 was used, the EXV controlled system would have had a lower power consumption, due to its smaller capacity and resulting incapability to keep the temperature at setpoint for temperatures above the design point. COP was calculated as an interpolation of the experimental data for each damper position, and for the cases where free cooling is utilized, interpolation in between damper positions. Figure 213 shows a diagram for the bin calculation method. Dependent on the ambient temperature, it is decided, whether free cooling can be utilized or not. If the ambient temperature is not smaller than the return air temperature minus 1 K, the damper is adjusted to the minimum opening according to the fresh air requirement. The work for that bin is then calculated as sum of the continuously running fan and the remaining power consumption of the

unit, both multiplied by the number of bin hours. If the ambient temperature is lower than the return air temperature, the available free cooling capacity with fully open damper is calculated. If it is larger than the cooling requirement (consisting of fan power consumption and building heat load), the damper position required to balance the heat load is calculated. Based on the damper position the required work is calculated as sum of the remaining power consumption and the fan power consumption multiplied by the bin hours.

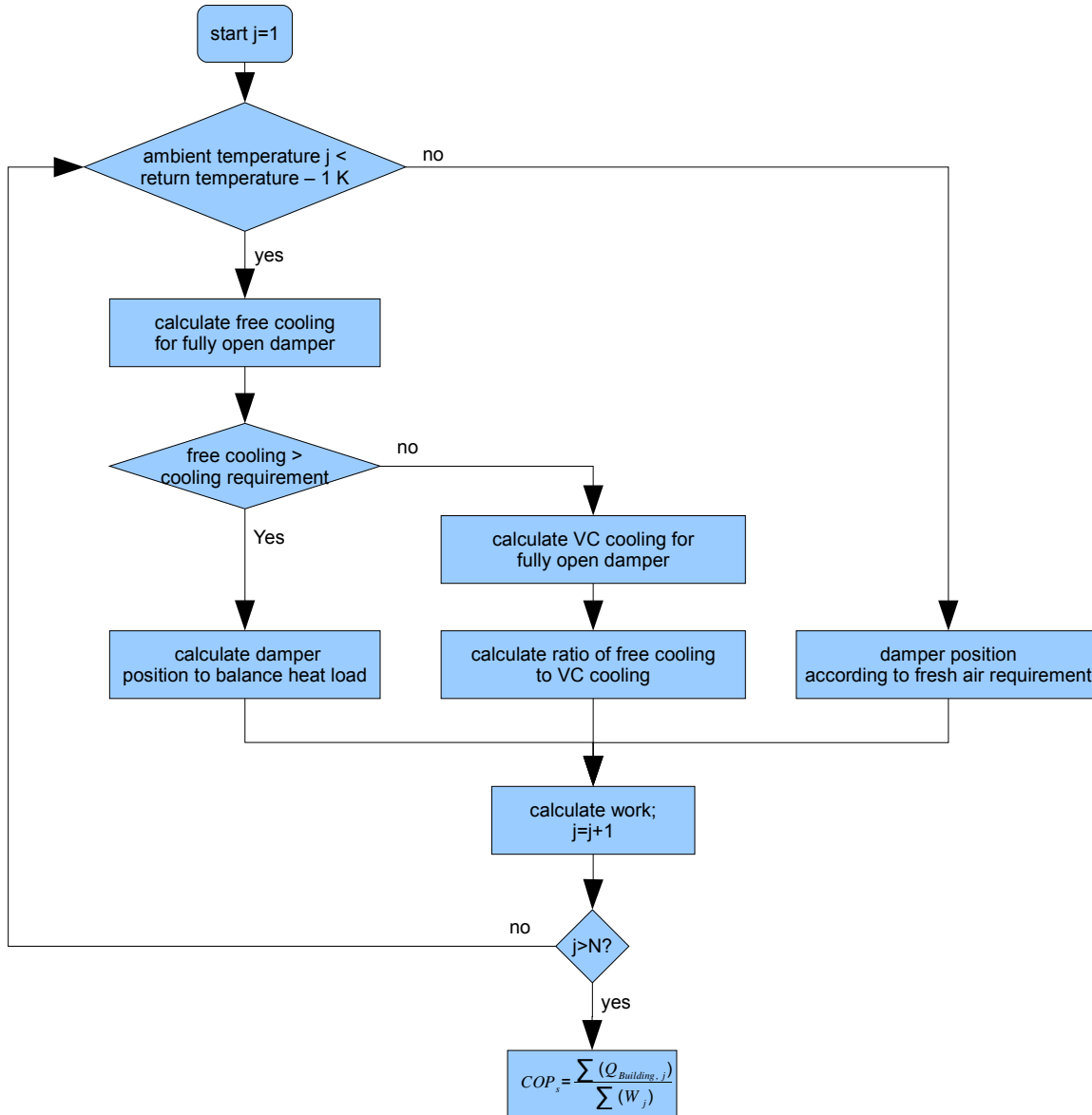


Figure 213: Flowchart for bin calculation model

If the available free cooling capacity is not sufficient to keep the building on temperature, the vapor compression capacity with fully open damper is calculated - with this capacity, the ratio between free cooling and mechanically assisted cooling is calculated, which is then used to calculate the required work for that bin temperature. At the end, the COP is calculated as ratio of the sum of bin-wise building cooling load and the sum of the bin-wise power consumption.

One factor that influences the achievable performance improvement significantly is damper position, as previously shown. For the simulations, a minimum damper position needs to be assumed. The minimum damper position is a result of the fresh air requirement and dependent upon the usage of the building. This fresh air requirement can be given in terms of an outdoor air fraction (OAF),

$$OAF = \dot{m}_{OA} / \dot{m}_{SA}$$

where :

$$\dot{m}_{OA} = \text{mass flow of outdoor air into the unit}$$

$$\dot{m}_{SA} = \text{mass flow of supply air}$$
(20)

Hjortland (2013) did extensive experiments in determining the outdoor air fraction for the the 4-ton rooftop unit, resulting in a third order polynomial for the OAF as function of the ambient temperature. Figure 214 is based on this polynomial function. Note that a fully closed damper does not lead to zero outdoor air fraction due to leakage. Note also that for fully open damper, the outdoor air fraction does not lead to 100 percent outdoor air due to recirculation of exhaust air back into the economizer. Therefore possible outdoor air fractions are in the range of 21 percent to 75 percent.

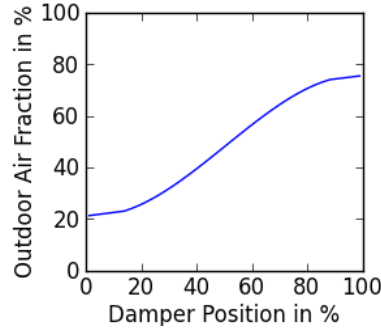


Figure 214: Outdoor Air Fraction as function of damper position

For the analyses, 10 percent damper opening corresponding to 22 percent OAF as a standard case as well as 52 percent damper opening corresponding to 50 percent OAF were selected. The first one is considered representative for most applications while the second one would be for higher required OAF (e.g. kitchens) or for a faulty economizer damper. Faulty economizers are common in practice, Jacobs et al. (2003) states that 62 percent of the tested RTUs had faulty economizers, a result which is comparable to Cowan (2004) which states that 64 percent of the tested RTU's needed economizer service.

4.4.1 Case A: Minimum Damper Position of 10 percent (22 percent OAF)

Figure 215 shows the bin-wise power consumption reduction as absolute and relative value for the rooftop unit operated in Sacramento climate. The relative savings increase significantly with increasing ambient temperature, while the majority of the savings is achieved in the range of 25-40°C. Figure 217 shows that for Bakersfield, higher ambient temperatures are reached, which

leads to higher relative savings at these temperatures. Furthermore the absolute savings are larger, due to the higher number of operating hours at higher temperature.

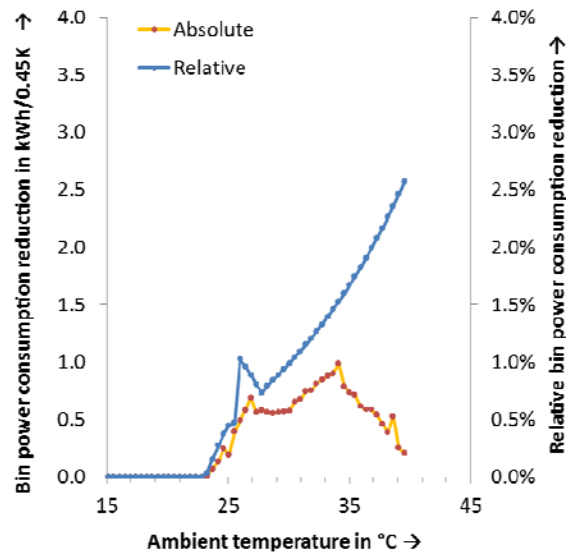


Figure 215: Bin-wise power consumption reduction, Sacramento, 10% minimum damper position

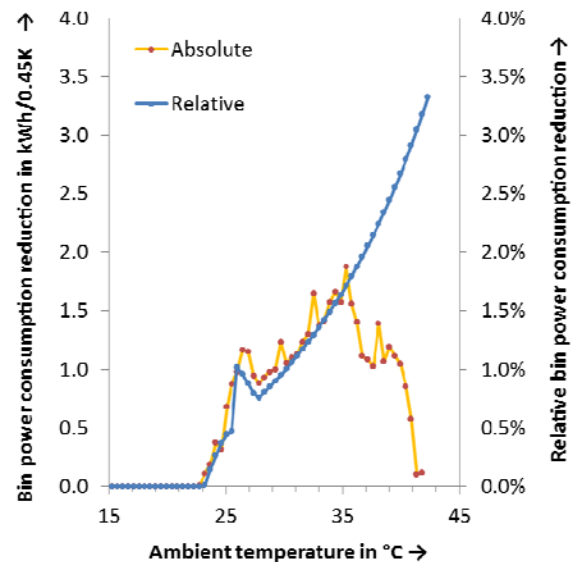


Figure 216: Bin wise power consumption reduction, Bakersfield, 10% minimum damper position

The previous analysis did not include the effect of local microclimate, which can differ significantly from TMY3 data. This is especially the case if the RTU is mounted on a roof with dark surface and if the roof has obstructed airflow flow caused by extended exterior walls as shown in Figure 219. While the obstructed airflow is caused by an architectonic requirement, the roof color can be changed by simply painting it with reflective paint – as it is done traditionally in some regions of the world. The white painting of roofs in USA is also known as “Clinton’s white roofs” since he strongly suggested it for major cities (Escoriaza, 2013). However, it is difficult to exactly assess the effect of this onto the performance of RTUs, since it depends on the time of day, wind, irradiation, water or snow on the surface of the roof and thermal capacity and conductance of the roof. To obtain a general impression how the local microclimate in the roof influences the obtainable savings, a constant roof temperature offset was applied between the ambient temperature (as used for the heat flux into the building) and the operating ambient temperature of the RTU. Figure 217 and Figure 218 show that this significantly affects the achievable relative as well as overall savings. While the relative savings increase more than two-fold for a roof offset of 9 K, the absolute savings are more than three times as large when compared to the 0 K offset case in both locations. Therefore the local heat island effect significantly affects the achievable savings for the hybrid control.

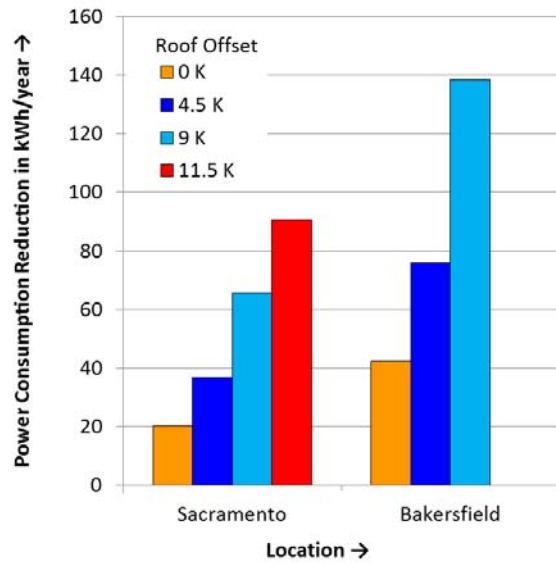


Figure 217: Annual power consumption reduction as function of roof offset, 10% minimum damper position

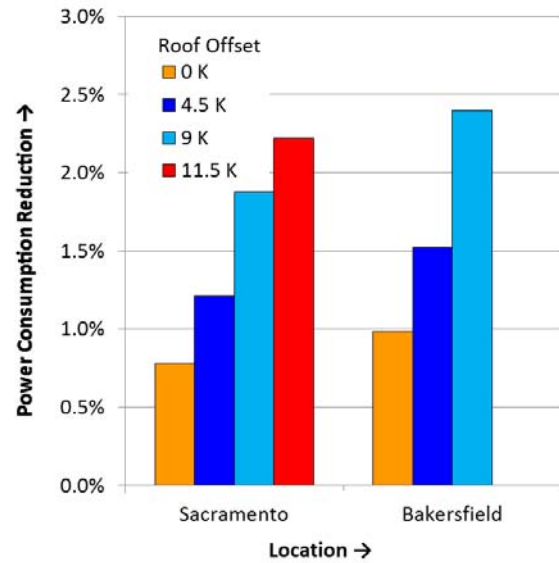


Figure 218: Annual % power consumption reduction as function of roof offset, 52% minimum damper position



Figure 219: Rooftop Units Mounted on Dark-Colored Roof Of a University Owned Building (2012).

4.4.2 Case B: Damper position of 52 percent (50 percent OAF)

Figure 220 shows the bin-wise power consumption reduction as absolute and relative value for the rooftop unit operated in Sacramento climate. The relative savings increase significantly with increasing ambient temperature, while the majority of the savings is achieved in the range of 25-40°C. Figure 221 shows that for Bakersfield, higher ambient temperatures are reached, which leads to higher relative savings at these temperatures. Furthermore the absolute savings are larger, due to the higher heat load of the building. For both locations, the relative as well as the absolute savings are larger than for the case with 10 percent damper opening, which is caused by larger maldistribution.

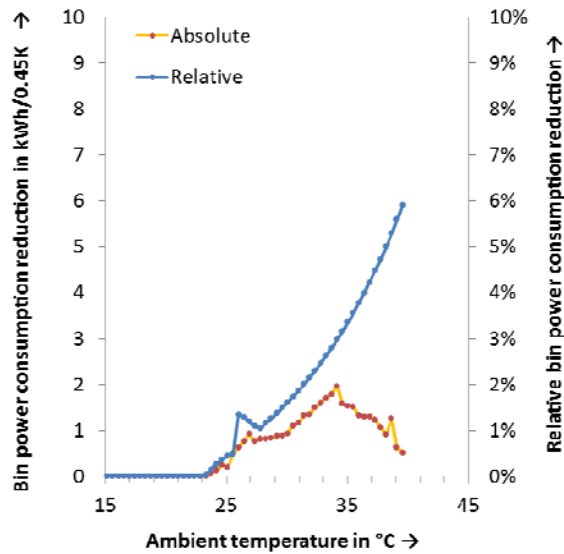


Figure 220: Bin-wise power consumption reduction, Sacramento, 52% minimum damper position

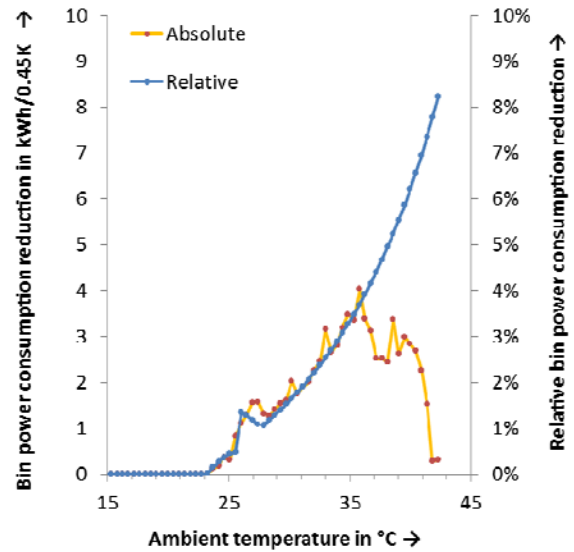


Figure 221: Bin wise power consumption reduction, Bakersfield, 52% minimum damper position

Figure 222 and Figure 223 show that the roof offset significantly affects the achievable relative as well as overall savings. While the relative savings increase more than three-fold for a roof offset of 9 K, the absolute savings are approximately five times as large when compared to the 0 K offset case in both locations. Therefore the local heat island effect significantly affects the achievable savings for the hybrid control and furthermore affects the achievable savings much more than for the 10 percent damper case.

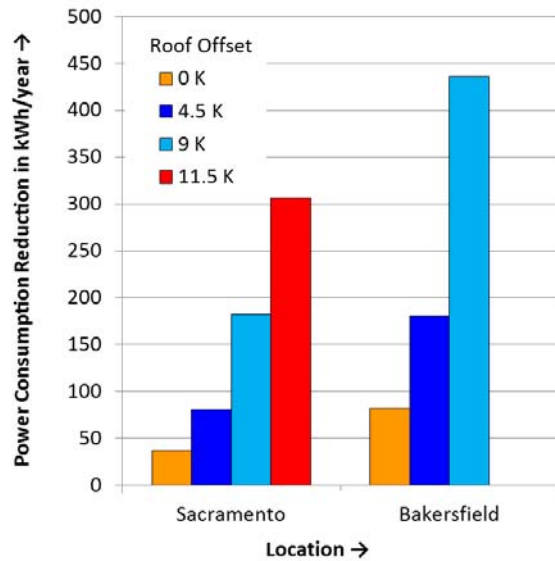


Figure 222: Annual power consumption reduction as function of roof offset, 52% minimum damper position

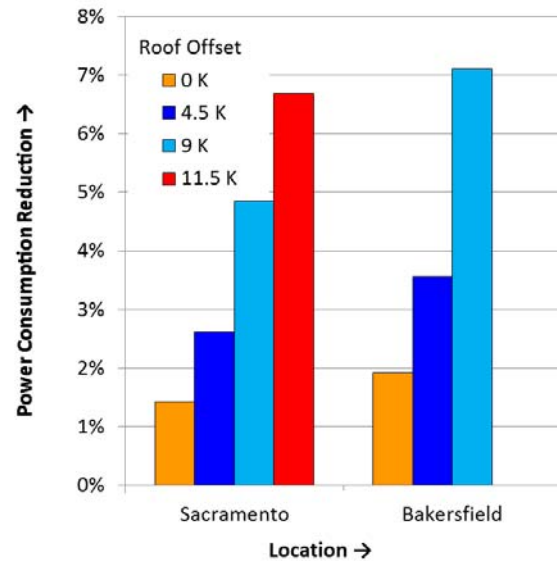


Figure 223: Annual % power consumption reduction as function of roof offset, 52% minimum damper position

4.4.3 Additional Considerations for Free Cooling

As previously mentioned, at cold ambient temperatures, cooling loads are lower and cooling is achieved by adjusting the damper position in order to reach the zone target temperature, which reduces the demand for the vapor compression system. This might be limited by comfort issues. ASHRAE standard 55 (2010) describes the thermal comfort limits, which includes moisture. While the standard does specify an upper limit for humidity of 16.8°C (62.2 F), it does not specify a lower limit for the humidity. However, it is mentioned that low humidity can lead to dry eyes and skin irritation. In the ASHRAE Handbook (1997), further details are given – Liviana et al. (1988) for example are cited to have reported increased complaints about eye discomfort for humidity levels below 36 F (2.2°C). While this is a minor issue from a building operation point of view, Green(1982) is cited to have reported increased absenteeism for low ambient humidity which leads to losses in productivity.

4.5 Conclusions and Recommendation

Significant temperature maldistribution at the inlet to the evaporator coil of the tested rooftop unit was found along with indication of velocity maldistribution. Using the balancing valves in the hybrid control scheme as virtual flow sensors, this resulted in +45 percent refrigerant flow at the top of the coil and -56 percent at the bottom of the coil for the most extreme condition, indicating significant differences in per circuit capacity.

The ability of the hybrid control to balance refrigerant and airside load leads to an improvement in COP and capacity when compared to the currently best option, which is an EXV controlled system. This performance improvement was evaluated. The largest improvement for both, COP as defined in AHRI 210/240 and building COP as defined as ratio of effective building cooling

over total power input was found for ambient temperatures significantly different from the return air temperature. The exception from this is the fully open damper case where the performance improvement is smallest for low ambient temperatures. The achievable improvement in terms of COP as defined in AHRI 210/240 (2008) was in the range of 1.5 percent for closed damper, 28°C(82 F) ambient temperature to 16.6 percent for half open damper at 51.5°C(125 F) ambient temperature. For the building COP, it was found that the achievable performance improvement does not behave linear with temperature – the maximum building COP improvement at extreme ambient temperatures of more than 60 percent for half open damper and 51.4°C(125 F) ambient temperature is therefore misleading.

A bin analysis was conducted in order to obtain a better estimate for the achievable energy savings. Damper positions 10 percent and 52 percent were considered, which correspond to 22 percent and 50 percent outdoor air fraction. For an ideal roof without increased local temperature, energy savings of 0.8 percent (1.0 percent) were predicted for the smaller damper position for Sacramento (Bakersfield). However, if a local temperature increase due to solar irradiation of 9 K was assumed, the savings increased to 1.9 percent (2.3 percent). If the minimum damper position was set to 52 percent, the achievable energy savings increased to 1.4 percent (1.9 percent) for Sacramento (Bakersfield). With a local temperature increase due to solar irradiation of 9 K, the savings increased to 4.8 percent (6.6 percent).

An estimate of the return of invest for the hybrid control can be found in the next chapter.

Chapter 5:

Estimation of Simple Payback Period

The analysis for all three systems showed that the hybrid control can recover the majority of the performance that is lost due to maldistribution. However, based on the conservative bin analysis of each of the systems, it became also clear that the achievable yearly savings are relatively small. In order to estimate the simple payback period (SPP) calculated by neglecting interest rate as

$$SPP = \frac{\text{Yearly Energy Saving in \$}}{\text{Additional Cost to implement Hybrid Control in \$}}, \quad (21)$$

it is necessary to estimate the additional cost for implementing the hybrid control. Since distributor and primary expansion valve as well as its controller can be reused, only the additional components need to be considered. Table 5 shows the undiscounted costs for the necessary individual components along with cost estimates for components where the price was unknown or difficult to evaluate. Some of the components (e.g. the used superheat controller) are assumed to be necessary only once, while other components are needed for each circuit (e.g. balancing valves). Figure 224 shows that, under these assumptions, the estimated additional cost for the hybrid control increases linearly from \$193 to for a system with 5 circuits to \$275 for a system with 10 circuits.

Table 5: Cost Estimates for Components

Type*	Item	Description	Source and part number	Cost
a	Valve driver (1 valve)	Solid State Relais 1.2 Amp	http://digikey.com (#CLA318TR-ND)	1.40 \$
b	Superheat controller	Raspberi Pi model B	http://www.mcmelectronics.com/ (#83-14421)	35.00 \$
b	Power Supply for ontroller	12VDC 600mA	https://www.sparkfun.com/ (#TOL-09442)	5.95 \$
b	Transformer for Valves	24V 40VA	http://www.grainger.com/ (#TR40VA004)	19.43 \$
a	Cost optimized 2-step balancing valve	Estimate for large volume	Estimate	10.00 \$
b	Additional parts, per valve	Elbows, solder, etc	Estimate	5.00 \$
b	Additional parts	Mounting for power supply and controller	Estimate	1.00 \$
a	Overhead	Engineering and assembly	Estimate	50.00 \$

Legend: * a = 1 per circuit necessary, b = assume 1 per system necessary

Note: All prices assessed/estimated April 17/2013, prices from website are not for bulk quantity, which compensates for unaccounted items.

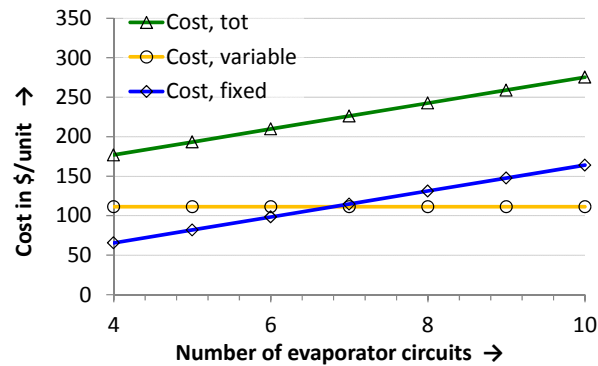


Figure 224: Estimate of Additional Cost for Hybrid Control per System before Markup.

For the additional cost that the consumer has to pay for the hybrid control, a 100 percent markup was considered when compared to the estimates of Figure 224. Table 6 shows the simple payback period for the analyzed systems for different operating conditions and assumptions.

For the large room cooling system, return on investment is reached after 9.2 years for clean coil conditions. Since clean coil conditions are not applicable if frost build up occurs, the actual simple payback period will be smaller. This is especially applicable for humid climate zones, where the humidity infiltration into the room is greater.

For the domestic heat pump, the hybrid control scheme does not seem to be interesting for California, since the simple payback period is longer than the expected system lifetime for the shown climate regions and assumptions. However, if a reduced hybrid control scheme with 5 valves, as illustrated in Figure 6, page 10, is used, the simple payback period of 10.5 years for the maldistributed coil in region 5 is shorter than the equipment lifetime. Recall that these numbers do not include additional savings due to a possible reduction of defrost cycles; a reduction of achievable performance improvement for the reduced hybrid control was not considered.

For the rooftop air conditioning unit, the simple payback period is generally shorter than the equipment lifetime, except for Sacramento without a roof temperature offset. The roof temperature offset accounts for an increase of the local ambient temperature at the RTU due to the roof heating up by solar radiation. For Bakersfield, the SPP is between 10.7 years for 10 percent damper opening and no roof offset and 1 year for 52 percent damper opening and 9 K roof offset.

Table 6: Simple Payback Period for Analyzed Systems for Several Operating Conditions

System	Configuration	Climate region	Savings/year	Electricity rate	Savings/ year	Hybrid Control Cost	SPP (years)
3-ton LRCS	Clean Coil	Sacramento Exec. AP	383 US\$/kWh	0.1383 US\$/kWh	53.0 \$	485.2 \$	9.2
5-ton HP	Clean Coil	2	19 US\$/kWh	0.1572 US\$/kWh	3.0 \$	518.0 \$	175.6
5-ton HP	Clean Coil	5	139 US\$/kWh	0.1572 US\$/kWh	21.9 \$	518.0 \$	23.7
5-ton HP	Maldistributed Coil	2	36 US\$/kWh	0.1572 US\$/kWh	5.6 \$	518.0 \$	92.5
5-ton HP	Maldistributed Coil	5	235 US\$/kWh	0.1572 US\$/kWh	36.9 \$	518.0 \$	14.0
5-ton HP*	Maldistributed Coil	5	235 US\$/kWh	0.1572 US\$/kWh	36.9 \$	386.8 \$	10.5
4-ton RAC	10% damper, 0 K roof offset	Sacramento Exec. AP	148 US\$/kWh	0.1383 US\$/kWh	20.4 \$	452.4 \$	22.2
4-ton RAC	10% damper, 0 K roof offset	Bakersfield	306 US\$/kWh	0.1383 US\$/kWh	42.3 \$	452.4 \$	10.7
4-ton RAC	10% damper, 9 K roof offset	Sacramento Exec. AP	476 US\$/kWh	0.1383 US\$/kWh	65.8 \$	452.4 \$	6.9
4-ton RAC	10% damper, 9 K roof offset	Bakersfield	1001 US\$/kWh	0.1383 US\$/kWh	138.4 \$	452.4 \$	3.3
4-ton RAC	52% damper, 0 K roof offset	Sacramento Exec. AP	267 US\$/kWh	0.1383 US\$/kWh	37.0 \$	452.4 \$	12.2
4-ton RAC	52% damper, 0 K roof offset	Bakersfield	594 US\$/kWh	0.1383 US\$/kWh	82.2 \$	452.4 \$	5.5
4-ton RAC	52% damper, 9 K roof offset	Sacramento Exec. AP	1317 US\$/kWh	0.1383 US\$/kWh	182.2 \$	452.4 \$	2.5
4-ton RAC	52% damper, 9 K roof offset	Bakersfield	3153 US\$/kWh	0.1383 US\$/kWh	436.1 \$	452.4 \$	1.0

* = using reduced hybrid control scheme with five circuits, neglect reduced benefits

Chapter 6: Summary and Conclusions

The achievable benefits for the hybrid control scheme were evaluated for the 3 tested systems, which were a 3-ton large room cooling system, a 5-ton residential heat pump, and a 4-ton rooftop unit. The hybrid control scheme uses a primary expansion valve that provides most of the refrigerant pressure drop and controls the overall superheat, while small balancing valves control the distribution of the refrigerant flow to the individual circuits. The baseline for all three systems was an EXV control scheme, which does not provide individual circuit superheat control but merely control of the overall superheat. For the EXV control system, indication of refrigerant maldistribution at the distributor was found for all systems. This, in conjunction with the design limitations of each system, led to uneven exit superheat as well as liquid overfeed for some circuits and operating conditions. Especially liquid overfeed caused by uneven airside load leads to performance degradation, which can be partially recovered if the hybrid control is employed. The achievable performance improvement increases with applied maldistribution, which was shown by applying a defined airside maldistribution for the large room cooling system and the heat pump as well as by different damper positions for the LRCS. In general, the achievable performance improvement was largest where the most electricity for heating or cooling was needed, leading to a possible reduction of peak energy demand.

For the 3-ton large room cooling system with clean-coil conditions, the hybrid control led to a 4 percent improvement in COP and a 6 percent improvement in capacity when compared to the EXV controlled baseline system. These performance improvements have negligible dependence on ambient temperature if the hybrid control scheme was applied. A frost-up test showed that the inbuilt TXV led to unacceptable hunting, which was not an issue for the EXV and hybrid control. The hybrid control extended the runtime for the frost-up test by approximately 12 percent compared to the EXV, a result that has to be taken with caution due to slightly different operating parameters which could have influenced the frost build up and non-optimal operation of the balancing valves. Therefore, two different levels of a defined coil blockage were used to obtain a more repeatable result. With blockage, the capacity of the EXV controlled system dropped by between 9 percent and 29 percent, depending on ambient temperature and level of blockage. For the blocked-coil cases, between 57 percent and 90 percent of the lost COP and 74 percent to 100 percent of the capacity were recovered if the hybrid control scheme was used. A bin analysis was performed to evaluate the yearly energy savings. Since no statistically relevant values for a maldistribution as function of operating conditions are available, the clean-coil case was chosen for the bin analysis. The yearly energy consumption reduction was on the order of 2 percent, which is less than one would expect from the 4 percent improvement in COP mentioned earlier. The reason for this is a significant amount of indoor fan power consumption, which runs continuously. However, the 2 percent reduction in energy consumption is based on pristine coil conditions, which will not be always the case during the operational lifetime of the system and would lead to additional energy savings. The estimated simple payback period of approximately 9 years will therefore be shorter.

For the 5-ton residential heat pump, the capacity increase with a clean-coil using the hybrid control scheme was on the order of 1 percent while the COP improvement was on the order of 0.6 percent, when compared to the EXV control scheme. This suggests that the hybrid control scheme leads to an insignificant improvement of the HP performance during clean-coil operation. However, in practice, maldistribution due to refrigerant and airside fouling will occur – temporarily with frost-up and as a result of often poor maintenance practices over the lifetime of the system. A 4 to 26 percent improvement in capacity along with a 4 to 20 percent improvement of COP can be observed with approximately half the air inlet grille blocked. The achievable yearly savings were estimated using a bin-type analysis. The savings are on the order of 1.5-2 percent for clean-coil operating conditions and 2.8 percent to 3.5 percent for an assumed maldistribution of the coil. For worst-case conditions with a severely maldistributed coil, the savings are 12.2 percent to 18 percent. The estimated simple payback period exceeded the system lifetime for most operating conditions, except for a maldistributed coil in climate zone 5. The hybrid control currently seems to be not be interesting for California climates. However, note that the SPP estimate does not include additional savings due to a reduced number of defrosts. Therefore the hybrid control should be followed up further for cold climate heat pumps, which should include an in depth evaluation of the assumptions for the maldistributed coil.

For the 4-ton rooftop unit, the achievable performance improvement depends on ambient conditions and economizer damper position. The achievable improvement in terms of COP as defined in AHRI 210/240 (2008) was in the range of 1.5 percent for a closed damper, 28°C(82 F) ambient temperature to 16.6 percent for a half open damper at 51.5°C(125 F) ambient temperature if the hybrid control scheme rather than the EXV control scheme was used. If the actual cooling done to the building was considered in the form of a building COP, the achievable performance improvements were larger. A bin analysis for Sacramento Exec. AP and Bakersfield Meadows Field showed that actual power consumption reduction using the building COP is in the range of 0.8-6.6 percent dependent on climate zone, minimum damper position, and increase of local temperature due to solar irradiation. Solar irradiation was considered in the form of a roof temperature offset. For Bakersfield, the simple payback period was estimated to be 10.7 years with 10 percent minimum damper position and 0 K roof offset; the simple payback period with a minimum damper position of 52 percent and a roof temperature offset of 9 K was only 1 year. For Sacramento, the simple payback period was estimated to exceed the typical equipment lifetime at 22 years with 10 percent minimum damper position and 0 roof offset; the simple payback period with a minimum damper position of 52 percent and a roof temperature offset of 9 K was only 2.5 years. Note that these numbers do not include any additional coil maldistribution caused by uneven fouling over the lifetime of the system.

6.1 Recommendations and Future Work

While the hybrid control can lead to significant performance improvements compared to an EXV controlled system, as shown in the conclusions, there are still a significant number of open questions.

For all systems, an effective, statistically significant maldistribution as a function of operating condition is unknown. This does not only include short term effects, such as frost build-up and fouling, but also long term effects such as uneven corrosion of fins and uneven fin damage due to coil cleaning. Future work should therefore be done to better quantify these issues, such that it is possible to more accurately evaluate the performance improvement of the hybrid control system. For the simple payback period calculations of the RAC, HP and LRCS, the conservative assumption of no additional maldistribution caused by these effects needed to be taken.

For the large room cooling system, it was evident that significant initial refrigerant side maldistribution exists as a result of spatial limitation of the distance between valve and distributor. Previous simulation research by Li et al. (2005) showed that this maldistribution can potentially be greatly reduced, resulting in insignificant levels of performance degradation compared to equal flow distribution as shown for the large room cooling system (page 66 ff.). However, it seems that this approach is not followed up in practice, which potentially is caused by cost constraints. A further potential for improvement was found in the continuous operation of the evaporator fan, with either the fan off during periods of time where no cooling is needed or a reduced fan speed. However, the fan control will need to ensure that product temperature in the room does not increase.

For the tested heat pump, the outdoor coil is designed as a condenser, leading to significant pressure drop and frost build up effects in heat pump mode. While for climate zones with mainly heat pump operation, the outdoor coil should be optimized for evaporator operation, the conclusion for warmer zones is less clear. If frost build up can occur, a compromise of the fin spacing should be found in order to reduce the energy necessary for defrost cycles, while maintaining sufficient AC mode efficiency, leading to a seasonal performance optimized heat pump for a specific climate zone. In addition to the fin spacing, a compromise for the refrigerant tube size needs to be found. Smaller tubes are preferable for AC operation to maintain good heat transfer coefficients but lead to significant pressure drop in HP operation. The defrost cycles should be initiated based on performance degradation of the heat exchanger rather than on the running time of the unit below 0°C coil temperature, as is currently done. Controllers that do exactly this are commercially available for small commercial refrigeration applications, but even there they are not widely applied due to higher initial cost and customers that do not know about their short payback periods.

For the rooftop air conditioning unit, the limited available space leads to significant airside temperature and flow maldistribution, especially at partially open damper positions. A bin analysis for Sacramento Exec. Ap. and Bakersfield Meadows Field showed that actual power consumption reduction using the building COP is in the range of 0.8-6.6 percent dependent on climate zone, minimum damper position, and increase of local temperature due to solar irradiation. These savings do not include uneven fouling of the coil, air filters or outdoor air filter, which potentially leads to additional benefits for the hybrid control. The calculated savings led to an estimated simple payback period between 22 years and 1 year. Minimum damper position was found to significantly affect the overall power consumption. A CO₂ and VOC based control of the damper was not considered, but will be necessary for high performing buildings to maintain acceptable indoor quality while reducing the damper position

at high ambient temperatures and low occupancy. A more detailed building analysis should be conducted in the future to better understand all these effects.

REFERENCES

- AHRI (2004). ANSI/AHRI Standard 540 (formerly ARI Standard 540)- 2004 Standard For Performance Rating Of Positive Displacement Refrigerant Compressors And Compressor Units. *AHRI Air-Conditioning, Heating, and Refrigeration Institute*, Arlington, Virginia, USA.
- AHRI (2008). ANSI/AHRI Standard 210/240 with Addendum 1 - 2008 Standard for Performance Rating of Unitary Air-Conditioning & Air-Source Heat Pump Equipment. *AHRI Air-Conditioning, Heating, and Refrigeration Institute*, Arlington, Virginia, USA.
- AHRI (2009). 2009 Standard for Performance Rating of Walk-In Coolers and Freezers (AHRI STANDARD 1251 (SI)-2009). *AHRI Air-Conditioning, Heating, and Refrigeration Institute*, Arlington, Virginia, USA.
- Alco controls. (2012). EXM/EXL Stepper Motor Driven Electronic Expansion Valves Technical Data. *EXM/EXL Stepper Motor Driven Electronic Expansion Valves Technical Data*.
- ASHRAE (1997). 1997 ASHRAE Handbook – Fundamentals, IP edition., *American Society of Heating, Refrigerating and Air-Conditioning Engineers, Inc.*, Atlanta, Georgia.
- ASHRAE (2012). ANSI/ASHRAE Standard 55-2010 – Thermal Environmental Conditions for Human Occupancy, *American Society of Heating, Refrigerating and Air-Conditioning Engineers, Inc.*, Atlanta, Georgia.
- Bury, T. (2012). *Heat Exchangers - Basics Design Applications, Chapter 5: Impact of a Medium Flow Maldistribution on a Cross-Flow Heat Exchanger Performance*. (J. Mitrovic, Ed.) Rijeka, Croatia: Intech.
- Bach, C.K., Braun, J., Groll, E.A. (2012a). A virtual EXV mass flow sensor for applications with two-phase flow inlet conditions, *International Refrigeration and Air Conditioning Conference at Purdue*, West Lafayette, Indiana.
- Bach, C.K., Braun, J., Groll, E.A. (2012b). Application of a hybrid control of expansion valves to a 3-ton large room cooling system, *International Refrigeration and Air Conditioning Conference at Purdue*, West Lafayette, Indiana.
- Bach, C.K., Braun, J., Groll, E.A. (2012c). Optimizing Refrigerant distribution in evaporators – Equipment Instrumentation and testing- Part 1: Large room cooling system, *California Energy Commission*, Sacramento, California.
- Bell, I. H. (2011). Air conditioning and heat pump model (ACHP) source code revision 70, *sourceforge SCM Repositories – achp*, downloaded from <https://achp.svn.sourceforge.net/svnroot/achp>.
- Bell, I. H. (2012). ACHP Documentation Release 1.3, June 2012, downloaded from http://achp.sourceforge.net/_static/ACHP.pdf.

- Calm, J. M. (2002). Emissions and environmental impacts from air-conditioning and refrigeration systems. *International Journal of Refrigeration*, 25(3), 293-305.
- Carrier Corporation (2006). Weathermaster® – 48HJ004-028 – 48HE003-006 – Single-Package Rooftop Units – Gas Heating/Electric Cooling, Retrieved 04-Jan-2013. *Weathermaster® – 48HJ004-028 – 48HE003-006 – Single-Package Rooftop Units – Gas Heating/Electric Cooling*, Retrieved 04-Jan-2013. Indiana, USA.
- Cowan, A. (2004). review of recent commercial rooftop unit field studies in the pacific northwest and California. Prepared for Northwest Power and Conservation Council and Regional Technical Forum. *New Buildings Institute*. White Salmon, Washington.
- Skovrup, M., Jakobsen, A., Rasmussen, B. D., Andersen, S.E. (2012). CoolPack Version 1.49. *IPU & Technical University of Denmark*, Lyngby, Denmark.
- Danfoss A/S (2011a). Most valves expand your refrigerant - EcoFlow™ expands your options. Most valves expand your refrigerant - EcoFlow™ expands your options. *Danfoss A/S*, Nordborg, Denmark.
- Danfoss A/S (2011b). Technical brochure EcoFlow™ – Electronic Expansion System Type EES. *Danfoss A/S*, Nordborg ,Denmark.
- DOE. (2012). Annual Energy Review 2012 - Table 2.5 - Household Energy Consumption and Expenditures by End Use and Energy Source, Selected Years, 1978–2005. *Annual Energy Review 2012 - Table 2.5 - Household Energy Consumption and Expenditures by End Use and Energy Source, Selected Years, 1978–2005*. Washington DC.
- Domanski, P. A.; Yashar, D. A. (2007). Application of an Evolution Program for Refirgerant Circuitry Optimization. *Challenges to Sustainability. ACRECONF 2007. Proceedings. December 7-8, 2007*, New Delhi, India, 1-16 pp, 2007.
- Domanski, P. A., Yashar, D., Kaufman, K. A., & Michalski, R. S. (2004). An Optimized Design of Finned-Tube Evaporators Using the Learnable Evolution Model. *HVAC&R Research*, 10(2), 201-211.
- EIA. (2006). Table C13. Total Electricity Consumption and Expenditures, 2003. *Table C13. Total Electricity Consumption and Expenditures, 2003*. Washington DC.
- EIA. (2008, 9). Table E5A. Electricity Consumption (kWh) by End Use for All Buildings, 2003. *Energy Infortmation Administration*. Washington DC.
- EIA. (2013a). Table CE3.5 Household Site End-Use Consumption in the West Region, 2009. *Energy Infortmation Administration*. Washington DC.
- EIA. (2013b). Table 5.6.B. Average Retail Price of Electricity to Ultimate Customers by End-Use Sector, by State, Year-to-Date through September 2012 and 2011 (Cents per Kilowatthour). *Energy Infortmation Administration*. Washington DC.

- Escoriaza, J. C. P. (2013). Painting Bill Clinton's "white roofs" into reality. *Reuters*. blogs.reuters.com/great-debate/2011/07/21/painting-bill-clinton's-white-roofs-into-reality/, accessed 03/20/13.
- Funder-Kristensen, T., Nicolaisen, H., Holst, J., Rasmussen, H.M., Nissen, J.H. (2012), US patent 8191384: B2 Refrigeration System, *Unites States Patent Office*, Alexandria, Virginia.
- Gong, G., Tang, J. , Lv, D. and Wang, H. (2012). Research on frost formation in air source heat pump at cold-moist conditions in central-south China, *Applied Energy*, 102:571-581.
- Grace, I., Datta, D., & Tassou, S. (2005). Sensitivity of refrigeration system performance to charge levels and parameters for on-line leak detection. *Applied Thermal Engineering*, 25(4), 557-566.
- Green, G.H. (1982). The positive and negative effects of building humidification, *ASHRAE Transactions*, 88(1):1049-61
- Gunda Mader, Claus Thybo, Henrik Rasmussen (2010). An electronic expansion valve with automatic refrigerant distribution control in Deutsche Kälte-Klima-Tagung 2010 - Kurzfassungen. *Deutscher Kaelte- und Klimatechnischer Verein e.V.*, Hannover, Germany.
- Hjortland, A., Braun, J., E. (2013). Embedded Statistical Economizer AFDD for Rooftop Air-Conditioners, *Graduate student poster show for the EEB hub*, Philadelphia, Pennsylvania.
- Isaac, M., & van Vuuren, D. P. (2009). Modeling global residential sector energy demand for heating and air conditioning in the context of climate change. *Energy Policy*, 37(2), 507-521.
- Itron, Inc. (2006). California commercial end-use energy survey. Tech. rep., *California Energy Commision*, Sacramento, California.
- Jacobs (2003). Small HVAC Problems and Potential Savings Reports. Tech. rep., *California Energy Commision*, Sacramento, California.
- Janghoo Lee, P. A. (1997). Impact of Refrigerant Maldistributions on the performance of finned tube evaporators with R22 and R407C. Tech. rep., *National Institute for Science and Technology*, Gaithersburg, Maryland.
- Kærn, M. R. Elmegaard, B. (2009). Effect of refrigerant mal-distribution in fin-and-tube evaporators on system performance. *Proceedings of 50th International Conference of Scandinavian Simulation Society : Modeling of Energy Technology*. Fredericia, Denmark.
- Kaern, M. R. (2011). Analysis of flow maldistribution in fin-and-tube evaporators for residential air-conditioning systems. Ph.D. dissertation, *DTU Mechanical Engineering*, Kongens Lyngby, Denmark.
- Kærn, M. R., Brix, W., Elmegaard, B., & Larsen, L. F. (2011a). Performance of residential air-conditioning systems with flow maldistribution in fin-and-tube evaporators. *International Journal of Refrigeration*, 34(3), 696-706.

- Kærn, M. R., Brix, W., Elmegaard, B., & Larsen, L. F. (2011b). Compensation of flow maldistribution in fin-and-tube evaporators for residential air-conditioning. *International Journal of Refrigeration*, 34(5), 1230-1237.
- Kim, J.-H., Braun, J. E., & Groll, E. A. (2008a). Analysis of Refrigerant Flow Distribution in Evaporators. CD: Purdue Conferences 2008: 19th International Compressor Engineering Conference at Purdue, 12th International Refrigeration and Air Conditioning Conference at Purdue. West Lafayette, Indiana.
- Kim, J.-H., Braun, J. E., & Groll, E. A. (2008b). Optimizing refrigerant distribution in evaporators. Final Report, *Air-Conditioning and Refrigeration Technology Institute, Inc.*, Arlington, Virginia.
- Kim, J.-H., Braun, J. E., & Groll, E. (2009a). A hybrid method for refrigerant flow balancing in multi-circuit evaporators: Upstream versus downstream flow control. *International Journal of Refrigeration*, 32, 1271 – 1282.
- Kim, J.-H., Braun, J. E., & Groll, E. A. (2009b). Evaluation of a hybrid method for refrigerant flow balancing in multi-circuit evaporators. *International Journal of Refrigeration*, 32(6), 1283-1292.
- Kim, W., & Braun, J. E. (2010). Impacts of Refrigerant Charge on Air Conditioner and Heat Pump Performance, Paper 1122. *International Refrigeration and Air Conditioning Conference*. West Lafayette, Indiana.
- Kim, W., & Braun, J. E. (2010). Impacts of Refrigerant Charge on Air Conditioner and Heat Pump Performance, Paper 1122. *International Refrigeration and Air Conditioning Conference at Purdue*. West Lafayette, Indiana.
- Klein, S.A. (2012) Engineering Equation Solver, Academic Commercial V9.195-3D, *F-Chart Software*, Madison, Wisconsin.
- Li, G. (2001, December). A Numerical and Experimental Investigation Of Refrigerant Flow Control Devices. Master's thesis, *Purdue University*, West Lafayette, Indiana.
- Li, G., Frankel, S., Braun, J., & Groll, E. (2005). Application of CFD Models to Two-Phase Flow in Refrigerant Distributors. *HVAC&R Research*, 11(1), 45-62.
- Laviana, J.E., Rohles, F.H. & Bullock, A.D. (1988). Humidity, comfort and contact lenses. *ASHRAE Transactions*, 94(1):3-11
- Lstiburek, J. W. (2012a). Don't Do Ugly Things. *ASHRAE Journal August*, 54, 62-67.
- Lstiburek, J. W. (2012b). Slab Happy. *ASHRAE Journal April*, 54, 62-68.
- Nakayama, M. Sumida, Y. Hirakuni, S. Mochizuki A. (2000). Development of a Refrigerant Two-Phase Flow Distributor for a Room Air Conditioner. *International Refrigeration and Air Conditioning Conference at Purdue*. Paper 497. West Lafayette, Indiana.

- NREL. (2012). National Solar Radiation Data Base, 1991- 2005 Update: Typical Meteorological Year 3 Location 724830: Sacramento Executive Airport, CA. *National Renewable Energy Laboratory*, Golden, Colorado.
- NREL. (2013). National Solar Radiation Data Base, 1991- 2005 Update: Typical Meteorological Year 3 Location 723840: Bakersfield Meadows Field, CA. *National Renewable Energy Laboratory*, Golden, Colorado.
- Rabas, T. J. (1987). Effect of Non-Uniform Inlet Flow and Temperature Distributions on the Thermal Performance of Air-Cooled Condensers, Maldistribution of Flow and Its Effect on Heat Exchanger Performance. *24th National Heat Transfer Conference and Exhibition*, (pp. 29–35). Pittsburgh, PA, New York.
- Rice, C. K. and A. E. Dabiri, (1981). A Compressor Simulation Model with Corrections for the Level of Suction Gas Superheat, *ASHRAE Transactions*, 87(2):771-782.
- Shen, B. G. (2005). Improvement and Validation of Unitary Air Conditioner and Heat Pump Simulation Models for R-22 and HFC Alternatives at Off-Design Conditions. Technical report, *ASHRAE*, Atlanta, Georgia.
- Payne, W.V. and Domanski, P. A. (2002). Potential benefits of smart refrigerant distributors. Tech. rep., *National Institute of Standards and Technology, Building Environment Division*, Gaithersburg, Maryland.
- T'Joel, C., De Paepe, M., Vanhee, F. (2006). Heat Exchanger Behavior in Non Uniform Flow. *Experimental Heat Transfer*, 19:4, 281 — 296.
- Wilcox, S., & Marion, W. (2008). *Users Manual for TMY3 Data Sets*. Golden, Colorado.
- Wirz, D. (2009). Commercial refrigeration for air conditioning technicians, second edition. *Cengage Learning*, Clifton Park, New York.

GLOSSARY

Acronym	Definition
\$	United states dollar
"H2O	Inches of water column
AC	Air conditioning
ACHP	Air conditioning and heat pump simulation model
AHRI	Air-Conditioning, Heating, and Refrigeration Institute
A-I	Circuit indexes for HP from top (A) to bottom (I), see also Figure 95, page 78
Ambient temperature	Average air inlet temperature to outdoor unit.
ANSI	American National Standards Institute
AP	Airport
ARI	Air-Conditioning and Refrigeration Institute
ASHP	Air source heat pump
ASHRAE	American Society of Heating, Refrigerating and Air-Conditioning Engineers
AWEF	Annual walk in energy factor
Bakersfield	Bakersfield Meadows Field
Bin analysis	Analysis of system performance using temperature data that is sorted into temperature bins, resulting in a specific number of yearly hours for each temperature bin.
Booster fan	Fan used to compensate for duct pressure loss
Box	Cooled room (LRCS, see AHRI, 2009)
Box-load	Cooling requirement for box
Btu	British thermal unit
Btu/(hr·ft·F)	Btu per hour per foot per Fahrenheit
Btu/hr	British thermal units per hour
Building Capacity	Capacity available for the cooling of the building – considers the reduction of actual cooling capacity due to ventilation. See page 145

Acronym	Definition
Building COP	COP considering the actually available cooling capacity for the building (building capacity/total power consumption). See page 145
C	Celsius
Capacity	Cooling capacity (RAC, LRCS), heating capacity (HP); defined for each system individually. See also <i>building capacity</i> .
Case A/B blockage	See Figure 42, page 40.
CEC	California Energy Commission
Clean, Clean coil	Airside evaporator coil surface without fouling or frost formation
CO ₂	Carbon dioxide
COP	Coefficient of performance (W/W), defined for each system individually
Damper	Economizer damper (RTU)
DAQ	Data acquisition and storage
DHP	Domestic heat pump
Dif	Difference
Distributor	Refrigerant Distributor
EC	Electronically commutated
Economizer	Airside economizer (RTU)
Economizer damper position	Normalized position of economizer damper as function of minimum and maximum control voltage, e.g. 0...100%
Economizer opening	See economizer damper position
EER	Energy efficiency ratio
EIA	Energy Information Administration
Evaporator coil	Block consisting of evaporator fins and refrigerant tubes
Exec.	Executive
Exit superheat	Exit superheat of individual circuits, generally measured on surface of exiting tube.
EXL-B1F	Model name of expansion valve
EXV	Electronic expansion valve

Acronym	Definition
EXV base case	EXV controlled system was taken as base-case for all systems
F	Fahrenheit
Feeder tubes	Refrigerant feeder tubes, connecting distributor and evaporator circuit
Flashing	Transition from liquid to gaseous state due to pressure drop
FMI	See mass flow maldistribution index, equation (7), page 64
Free cooling	Cooling of the building without operation of the vapor compression system
GBtu/hr	GigaBtu per hour
GWh	Gigawatt-hour
H2 ₁	Frost accumulation test, see ANSI/AHRI standard 210/240 (2008)
HP	Heat pump, see also DHP and ASHP
Hrs	Hours
HSPF	Heating Seasonal Performance Factor
HX	Heat exchanger
Hybrid, Hybrid Control	See page 8
Inlet grille	Air inlet grille before heat exchanger of outdoor unit
ISHED	Intelligent system for heat exchanger design
K	Kelvin
kBtu	thousand · British thermal unit
kJ/kg	kilojoule per kilogram
kPa	Kilo Pascal (N/m ²)
kW	Kilowatt
kWh	Kilowatt-hour
LRCS	Large room cooling system
Maldistributed coil case	Weighted combination of clean coil and blocked coil tests to evaluate seasonal performance of HP, see Figure 145, page 113.
Maldistribution index	See mass flow maldistribution index, equation (7), page 64

Acronym	Definition
mass uneven distribution rate	See equation (8), page 67
min	Minutes, minimum
MOP	Maximum operating pressure
NREL	National Renewable Energy Laboratory
OAF	Outdoor air fraction
Orifice type system	System with fixed orifice as refrigerant expansion device
Overall superheat	Superheat after the individual circuits are joined back together. Measured with insertion thermocouple after exit header (HP), close to evaporator unit outlet (LRCS), and at inlet to compressor (RAC, short suction line)
P	Pressure
Pa	Pascal (N/m^2)
PD	Pressure difference
PEXV	Primary expansion valve (in case of the hybrid control scheme)
PI control	Controller using proportional and integral action
PSIG	Gauge measurement in pounds per square inch
Quality maldistribution	Maldistribution of refrigerant and vapor at the distributor, e.g. distributor outlet branches carry refrigerant of different quality
RAC	Rooftop air conditioning unit
Relative savings	savings relative to EXV basecase
Return bend	Return bend, which connects the exit of one refrigerant tube to the inlet of the next refrigerant tube of a circuit in the evaporator.
RH	Relative humidity
RTD	Resistance temperature detector
Sacramento	Sacramento Executive Airport
SEER	Seasonal Energy Efficiency Ratio ($\text{BTU/W}\cdot\text{h}$)
SPP	Simple payback period
Subcooling	Temperature difference between refrigerant at the bubble point corresponding to the given pressure and the actual temperature of the liquid refrigerant

Acronym	Definition
Superheat	Temperature difference between calculated refrigerant dew point and actual temperature of the gaseous refrigerant. See also <i>exit superheat</i> and <i>overall superheat</i>
Surf	Surface; surface mounted
T	Temperature
TMY3	Data for typical meteorological year, revision 3
Tons	Tons of refrigeration (12,000 Btu/hr or 3517 Watts)
TXV	Thermostatic expansion valve
Unblocked	Operation without applied blockage to airside of evaporator coil
US	United States of America
US\$/kWh	United states dollar per kilowatt-hour
VOC	Volatile organic compounds
W	Watt
x	Times; refrigerant quality
YTD	Year to date

APPENDIX A: Large Room Cooling System

Test Plan

Table A 1 shows the original test plan for the LRCS. Additional tests were taken with partial blockage as described in the main part of the report.

Table A 1: Original Test Plan for Large Room Cooling System

Test Description ^o [Number of tests]	Unit Cooler Air Entering		Condenser Air Entering		Compressor Capacity	Test Objective
	<i>Dry-Bulb Temperature</i>	<i>Relative humidity</i>	<i>Dry-Bulb Temperature</i>	<i>Wet-Bulb Temperature</i>		
	°F °C	%	°F °C	°F °C		
Off Cycle Fan Power [1]	35.6 2	<50	- -	- -	Compressor Off	Measure fan input wattage during compressor off cycle
Refrigeration Capacity A [3]	35.6 2	<50	95 35	75.2 24	Compressor On	Determine Net Refrigeration Capacity of Unit Cooler , input power, and COP at Rating Condition
Cyclic A* [3] (optional)	35.6 2	<50	95 35	75.2 24	Cyclic operation	Determine effects of cyclic operation
Refrigeration Capacity A** [3]	35.6 2	90	95 35	75.2 24	Compressor On	Determine effect of ice build up
Refrigeration Capacity C [2]	35.6 2	<50	35.6 2	33.8 1	Compressor On	Determine Net Refrigeration Capacity of Unit Cooler and system input power at cold ambient condition
Refrigeration Capacity D* [2]	35.6 2	<50	125.1 51.7	95 35	Compressor On	Determine Net Refrigeration Capacity of Unit Cooler and system input power at hot ambient condition
Refrigeration Capacity D** [3]	35.6 2	90	125.1 51.7	95 35	Compressor On	Determine effect of ice build up

*,** Not specified in AHRI 1251.

^o Each test is done seperately with EXV only and hybrid control scheme.

Tests A, A*, A** are done additionally with the inbuilt expansion device. All tests are required unless otherwise specified.

Data Tables

System-Level Results

Table A 2: TXV (Clean-Coil) Test Results

Test	bd*	be	be*
Air-side: Temperatures			
Evaporator, in	2.0 °C	2.0 °C	1.9 °C
Evaporator, out	-1.9 °C	-0.7 °C	-0.8 °C
Condenser, in	21.9 °C	35.0 °C	34.6 °C
Condenser, out	28.8 °C	41.6 °C	41.2 °C
Air side: Humidity			
RH, indoor	57 %	65	65
DP, outdoor	14.1 °C	23.8	22.7
Refrigerant side: Cycle			
Compressor in, P	391 kPa	425 kPa	425 kPa
Compressor in, T	-0.4 °C	0.2 °C	0.0 °C
Compressor out, P	1513 kPa	2010 kPa	1994 kPa
Compressor out, T	67.1 °C	78.4 °C	78.1 °C
Mass flowrate, g/s	79.61	80.56	79.67
Condenser out, P	1461 kPa	1975 kPa	1961 kPa
Condenser out, T	31.2 °C	44.0 °C	43.4 °C
Pre Filter Drier, P	1475 kPa	1996 kPa	1979 kPa
Pre Filter Drier, T	30.7 °C	43.3 °C	42.6 °C
TXV in, P	1403 kPa	1919 kPa	1897 kPa
TXV in, T	29.5 °C	42.3 °C	41.3 °C
TXV in, SC			0.1 K
Evaporator out, P	415 kPa	450 kPa	449 kPa
Evaporator out, T	-0.1 °C	0.0 °C	-0.4 °C
Evaporator out, SH	11.0 K	8.8 K	8.5 K
Power Consumption, Capacity, COP			
Evaporator Fan	0.381 kW	0.386 kW	0.388 kW
Condenser Fan	0.447 kW	0.447 kW	0.447 kW
Solenoid	0.011 kW	0.011 kW	0.011 kW
Crankcase Heater	0.019 kW	0.019 kW	0.019 kW
Compressor	3.90 kW	4.40 kW	4.37 kW
Heating (w/o fan)	13.68 kW	12.67 kW	12.75 kW
Cooling (w/o fan)	9.78 kW	8.19 kW	8.27 kW
Cooling (net)	9.39 kW	7.79 kW	7.68 kW
COP	1.97	1.48	1.41

Note: Test be* is a cyclic test, $T_{on}=10\text{min}$, $T_{off}=5\text{min}$. Values are given as average for on-phase; COP for entire duration.

Table A 3: EXV Clean-Coil Test Results

Test	bb	bc	bd*	be	be*	bf
Modification	clean coil					
Air-side: Temperatures						
Evaporator, in	1.9 °C	2.0 °C	2.0 °C	1.9 °C	1.7 °C	2.0 °C
Evaporator, out	-3.0 °C	-3.0 °C	-2.4 °C	-1.7 °C	-1.9 °C	-1.2 °C
Condenser, in	1.89	11.93	22.04	34.89	34.22	46.13
Condenser, out	12.2 °C	19.3 °C	29.2 °C	41.7 °C	40.9 °C	52.5 °C
Air side: Humidity						
RH, indoor	47 %	46 %	49 %	49 %	50 %	57 %
DP, indoor	-7.2 °C	-7.4 °C	-6.9 °C	-6.5 °C	-6.5 °C	-4.6 °C
DP, outdoor	-9.8 °C	-5.6 °C	-2.1 °C	1.9 °C	1.1 °C	3.7 °C
Refrigerant side: Cycle						
Compressor in, P	402 kPa	399 kPa	419 kPa	446 kPa	439 kPa	472 kPa
Compressor in, T	-8.9 °C	-5.6 °C	-3.9 °C	-3.0 °C	-2.1 °C	-3.0 °C
Compressor out, P	1269 kPa	1247 kPa	1556 kPa	2037 kPa	2002 kPa	2553 kPa
Compressor out, T	47.8 °C	52.7 °C	62.6 °C	74.5 °C	75.2 °C	84.8 °C
Mass flowrate, g/s	89.66	87.30	86.57	86.10	83.57	85.21
Condenser out, P	1194 kPa	1159 kPa	1491 kPa	1999 kPa	1965 kPa	2528 kPa
Condenser out, T	20.3 °C	22.3 °C	32.1 °C	44.3 °C	43.3 °C	54.2 °C
Pre Filter Drier, P	1191 kPa	1168 kPa	1509 kPa	2018 kPa	1983 kPa	2553 kPa
Pre Filter Drier, T	16.7 °C	21.7 °C	31.8 °C	43.6 °C	42.5 °C	53.5 °C
EXV in, P	1101 kPa	1081 kPa	1429 kPa	1937 kPa	1891 kPa	2467 kPa
EXV in, T	15.7 °C	19.8 °C	30.1 °C	42.7 °C	41.2 °C	52.5 °C
EXV in, SC	4.3 K				0.1 K	
Evaporator out, P	422 kPa	427 kPa	445 kPa	470 kPa	461 kPa	491 kPa
Evaporator out, T	-6.0 °C	-6.0 °C	-3.8 °C	-3.6 °C	-2.4 °C	-4.9 °C
Evaporator out, SH	4.7 K	4.3 K	5.3 K	3.9 K	5.7 K	1.4 K
Power Consumption, Capacity, COP						
Evaporator Fan	0.381 kW	0.380 kW	0.381 kW	0.377 kW	0.377 kW	0.389 kW
Condenser Fan	0.447 kW	0.447 kW	0.447 kW	0.447 kW	0.447 kW	0.447 kW
Solenoid	0.011 kW	0.011 kW	0.011 kW	0.011 kW	0.011 kW	0.011 kW
Crankcase Heater	0.019 kW	0.019 kW	0.019 kW	0.019 kW	0.019 kW	0.019 kW
Compressor	3.74 kW	3.71 kW	4.05 kW	4.50 kW	4.43 kW	4.91 kW
Total Power	4.60 kW	4.56 kW	4.91 kW	5.35 kW	5.29 kW	5.78 kW
Heating (w/o fan)	15.69 kW	15.25 kW	14.31 kW	13.07 kW	13.08 kW	11.90 kW
Cooling (w/o fan)	12.40 kW	11.50 kW	10.21 kW	8.38 kW	8.51 kW	6.68 kW
Cooling (net)	12.01 kW	11.11 kW	9.82 kW	7.99 kW	7.93 kW	6.28 kW
COP	2.61	2.44	2.00	1.49	1.44	1.09

Note: Test be* is a cyclic test, $T_{on}=10\text{min}$, $T_{off}=5\text{min}$. Values are given as average for on-phase; COP for entire duration.

Test bb had evaporation temperature fluctuations of approx $\pm 2\text{K}$ due to OD fan

Table A 4: EXV Blocked-Coil Results

Test	bd*-A	be-A	bf-A	bd*-B	be-B	bf-B	be-C	be-D	be-B-R
Blockage of evaporator coil inlet face area									
Top 1/3	blocked			blocked			porous, double layer	porous, single layer	blocked
Middle 1/3	porous, single layer			blocked			porous, single layer		blocked
Bottom 1/3	clear								
Note					slightly frosted	slightly frosted			repeat: after defrost
Air-side: Temperatures									
Evaporator, in	2.1 °C	2.0 °C	2.1 °C	2.0 °C	1.7 °C	2.0 °C	1.9 °C	2.0 °C	2.0 °C
Evaporator, out	-2.6 °C	-2.3 °C	-1.3 °C	-0.9 °C	-1.3 °C	-0.3 °C	-2.5 °C	-2.1 °C	-0.9 °C
Condenser, in	22.0 °C	34.9 °C	46.0 °C	21.8 °C	34.9 °C	46.1 °C	35.0 °C	35.0 °C	35.1 °C
Condenser, out	28.2 °C	40.9 °C	51.8 °C	27.3 °C	40.4 °C	51.4 °C	41.6 °C	41.7 °C	40.6 °C
Air side: Humidity									
RH, indoor	50 %	52 %	51 %	47 %	50 %	49 %	52 %	51 %	50 %
DP, indoor	-6.3 °C	-6.0 °C	-6.0 °C	-7.1 °C	-6.4 °C	-6.4 °C	-6.0 °C	-6.1 °C	-6.5 °C
DP, outdoor	-1.3 °C	1.7 °C	4.0 °C	-1.3 °C	2.0 °C	5.7 °C	1.5 °C	1.4 °C	3.4 °C
Refrigerant side: Cycle									
Compressor in, P	359 kPa	388 kPa	418 kPa	318 kPa	355 kPa	393 kPa	433 kPa	443 kPa	360 kPa
Compressor in, T	-8.7 °C	-5.1 °C	-4.6 °C	-14.3 °C	-2.8 °C	-5.0 °C	-3.5 °C	-3.5 °C	-7.2 °C
Compressor out, P	1486 kPa	1968 kPa	2489 kPa	1435 kPa	1925 kPa	2452 kPa	2026 kPa	2036 kPa	1937 kPa
Compressor out, T	62.4 °C	76.7 °C	87.1 °C	60.7 °C	81.1 °C	88.8 °C	75.0 °C	74.4 °C	77.4 °C
Mass flowrate, g/s	73.55	72.04	71.94	64.35	62.63	65.15	82.46	84.87	64.88
Condenser out, P	1438 kPa	1942 kPa	2474 kPa	1398 kPa	1905 kPa	2441 kPa	1992 kPa	2001 kPa	1915 kPa
Condenser out, T	30.5 °C	42.9 °C	52.5 °C	29.3 °C	42.0 °C	52.0 °C	44.1 °C	44.3 °C	42.3 °C
Pre Filter Drier, P	1450 kPa	1963 kPa	2501 kPa	1412 kPa	1927 kPa	2470 kPa	2011 kPa	2022 kPa	1936 kPa
Pre Filter Drier, T	29.9 °C	42.3 °C	51.9 °C	28.8 °C	41.3 °C	51.3 °C	43.4 °C	43.6 °C	41.8 °C
EXV in, P	1380 kPa	1892 kPa	2430 kPa	1349 kPa	1865 kPa	2404 kPa	1931 kPa	1938 kPa	1871 kPa
EXV in, T	29.0 °C	41.2 °C	50.8 °C	27.8 °C	40.1 °C	50.2 °C	42.4 °C	42.6 °C	40.4 °C
EXV in, SC									
Evaporator out, P	375 kPa	406 kPa	433 kPa	328 kPa	370 kPa	406 kPa	454 kPa	465 kPa	374 kPa
Evaporator out, T	-12.2 °C	-7.7 °C	-8.6 °C	-16.1 °C	-3.4 °C	-8.0 °C	-5.0 °C	-5.6 °C	-10.8 °C
Evaporator out, SH	1.8 K	4.1 K	1.4 K	1.5 K	11.0 K	3.8 K	3.5 K	2.3 K	3.3 K
Power Consumption, Capacity, COP									
Evaporator Fan	0.432 kW	0.422 kW	0.425 kW	0.475 kW	0.464 kW	0.466 kW	0.411 kW	0.390 kW	0.466 kW
Condenser Fan	0.447 kW	0.447 kW	0.447 kW	0.447 kW	0.447 kW	0.447 kW	0.447 kW	0.447 kW	0.447 kW
Solenoid	0.011 kW	0.011 kW	0.011 kW	0.011 kW	0.011 kW	0.011 kW	0.011 kW	0.011 kW	0.011 kW
Crankcase Heater	0.019 kW	0.019 kW	0.019 kW	0.019 kW	0.019 kW	0.019 kW	0.019 kW	0.019 kW	0.019 kW
Compressor	3.74 kW	4.10 kW	4.46 kW	3.45 kW	3.83 kW	4.21 kW	4.39 kW	4.46 kW	3.90 kW
Heating (w/o fan)	12.34 kW	11.37 kW	10.54 kW	10.84 kW	10.35 kW	9.78 kW	12.62 kW	12.89 kW	10.40 kW
Cooling (w/o fan)	8.36 kW	7.04 kW	5.72 kW	7.29 kW	6.52 kW	5.33 kW	8.00 kW	8.13 kW	6.29 kW
Cooling (net)	7.92 kW	6.61 kW	5.28 kW	6.80 kW	6.04 kW	4.85 kW	7.58 kW	7.73 kW	5.81 kW
COP	1.70	1.32	0.99	1.55	1.27	0.94	1.43	1.45	1.20

Table A 5: Hybrid and PEXV Fully Open Clean-Coil Test Results

Test	bc	bd*	be	bf	bf°
Air-side: Temperatures					
Evaporator, in	2.1 °C	2.0 °C	2.0 °C	2.0 °C	1.9 °C
Evaporator, out	-2.0 °C	-1.6 °C	-1.0 °C	-0.3 °C	-0.9 °C
Condenser, in	12.1 °C	22.0 °C	35.0 °C	46.0 °C	45.8 °C
Condenser, out	19.6 °C	29.3 °C	41.9 °C	52.5 °C	52.5 °C
Air side: Humidity					
RH, indoor	40 %	46 %	45 %	45 %	46 %
DP, indoor	-9.1 °C	-7.6 °C	-7.6 °C	-7.5 °C	-7.7 °C
DP, outdoor	-9.8 °C	-3.9 °C	-2.4 °C	-1.2 °C	0.5 °C
Refrigerant side: Cycle					
Compressor in, P	421 kPa	443 kPa	469 kPa	497 kPa	484 kPa
Compressor in, T	-5.3 °C	-4.8 °C	-3.5 °C	-2.4 °C	-1.2 °C
Compressor out, P	1299 kPa	1604 kPa	2097 kPa	2603 kPa	2588 kPa
Compressor out, T	52.0 °C	60.4 °C	72.9 °C	83.7 °C	85.5 °C
Mass flowrate, g/s	92.72	92.84	91.48	90.42	87.23
Condenser out, P	1201 kPa	1530 kPa	2046 kPa	2565 kPa	2557 kPa
Condenser out, T	22.7 °C	32.5 °C	44.7 °C	54.9 °C	54.5 °C
Pre Filter Drier, P	1178 kPa	1516 kPa	2034 kPa	2553 kPa	2546 kPa
Pre Filter Drier, T	22.1 °C	31.7 °C	43.9 °C	54.0 °C	53.7 °C
EXV in, P	1117 kPa	2481 kPa	1987 kPa	2481 kPa	2481 kPa
EXV in, T	20.2 °C	30.3 °C	42.9 °C	53.2 °C	52.8 °C
EXV in, SC	0.3 K		0.5 K		
Intermediate T	4.0 °C	11.3 °C	18.4 °C	24.4 °C	50.9 °C
Evaporator out, P	453 kPa	472 kPa	497 kPa	521 kPa	509 kPa
Evaporator out, T	-4.6 °C	-4.5 °C	-3.4 °C	-2.7 °C	-1.3 °C
Evaporator out, SH	4.1 K	3.0 K	2.4 K	1.8 K	3.9 K
Power Consumption, Capacity, COP					
Evaporator Fan	0.383 kW	0.382 kW	0.379 kW	0.378 kW	0.369 kW
Condenser Fan	0.447 kW	0.447 kW	0.447 kW	0.447 kW	0.447 kW
Solenoid	0.011 kW	0.011 kW	0.011 kW	0.011 kW	0.011 kW
Crankcase Heater	0.019 kW	0.019 kW	0.019 kW	0.019 kW	0.019 kW
Compressor	3.84 kW	4.17 kW	4.64 kW	5.01 kW	4.96 kW
Total Power	4.70 kW	5.03 kW	5.49 kW	5.87 kW	5.81 kW
Heating (w/o fan)	16.00 kW	15.03 kW	13.59 kW	12.31 kW	12.16 kW
Cooling (w/o fan)	12.24 kW	10.81 kW	8.83 kW	7.08 kW	7.04 kW
Cooling (net)	11.85 kW	10.42 kW	8.44 kW	6.70 kW	6.66 kW
COP	2.52	2.07	1.54	1.14	1.15

Note: Test bf° is identical to test bf, except that the primary valve is fully open. Condenser fan, Solenoid and Crankcase heater use only initial measurement.

Table A 6: Hybrid and PEXV Fully Open Blocked-Coil Test Results

Test	bd*-A	be-A	bf-A	bd*-B	be-B	bf-B	bf-B°
Blockage of evaporator coil inlet face area							
Top 1/3	blocked			blocked			
Middle 1/3	porous, single layer			blocked			
Bottom 1/3	clear						
Note							repeat
Air-side: Temperatures							
Evaporator, in	2.0 °C	2.0 °C	2.0 °C	2.1 °C	2.0 °C	2.1 °C	1.9 °C
Evaporator, out	-3.1 °C	-2.0 °C	-1.4 °C	-3.5 °C	-2.3 °C	-1.6 °C	-1.8 °C
Condenser, in	22.0 °C	35.0 °C	46.0 °C	22.0 °C	35.0 °C	46.0 °C	45.8 °C
Condenser, out	29.0 °C	41.7 °C	52.4 °C	28.8 °C	41.5 °C	52.1 °C	52.1 °C
Air side: Humidity							
RH, indoor	58 %	44 %	43 %	42 %	43 %	42 %	51 %
DP, indoor	-4.5 °C	-7.9 °C	-8.1 °C	-8.6 °C	-7.9 °C	-8.2 °C	-6.2 °C
DP, outdoor	2.0 °C	-3.9 °C	-1.2 °C	-5.1 °C	-3.4 °C	-1.3 °C	0.1 °C
Refrigerant side: Cycle							
Compressor in, P	419 kPa	453 kPa	481 kPa	401 kPa	433 kPa	464 kPa	454 kPa
Compressor in, T	-7.4 °C	-4.3 °C	-3.1 °C	-8.5 °C	-5.9 °C	-4.6 °C	-2.8 °C
Compressor out, P	1575 kPa	2080 kPa	2588 kPa	1557 kPa	2055 kPa	2568 kPa	2553 kPa
Compressor out, T	59.5 °C	73.2 °C	84.0 °C	59.9 °C	73.0 °C	83.8 °C	85.8 °C
Mass flowrate, g/s	87.45	87.66	87.01	83.25	83.27	83.30	80.69
Condenser out, P	1507 kPa	2032 kPa	2551 kPa	1495 kPa	2012 kPa	2533 kPa	2524 kPa
Condenser out, T	31.9 °C	44.5 °C	54.6 °C	31.6 °C	44.1 °C	54.3 °C	54.0 °C
Pre Filter Drier, P	1496 kPa	2020 kPa	2539 kPa	1485 kPa	2002 kPa	2522 kPa	2512 kPa
Pre Filter Drier, T	31.2 °C	43.7 °C	53.8 °C	30.9 °C	43.3 °C	53.5 °C	53.3 °C
EXV in, P	1443 kPa	1976 kPa	2503 kPa	2481 kPa	1962 kPa	2489 kPa	2481 kPa
EXV in, T	30.0 °C	42.8 °C	52.9 °C	29.7 °C	42.5 °C	52.6 °C	52.3 °C
EXV in, SC							
Intermediate T	15.7 °C	21.1 °C	23.2 °C	18.1 °C	24.1 °C	29.6 °C	50.5 °C
Evaporator out, P	445 kPa	479 kPa	504 kPa	425 kPa	457 kPa	484 kPa	476 kPa
Evaporator out, T	-7.5 °C	-4.4 °C	-3.6 °C	-8.5 °C	-6.1 °C	-5.1 °C	-3.2 °C
Evaporator out, SH	1.6 K	2.6 K	1.9 K	1.9 K	2.2 K	1.6 K	4.0 K
Power Consumption, Capacity, COP							
Evaporator Fan	0.446 kW	0.423 kW	0.425 kW	0.470 kW	0.461 kW	0.472 kW	0.466 kW
Condenser Fan	0.447 kW	0.447 kW	0.447 kW	0.447 kW	0.447 kW	0.447 kW	0.447 kW
Solenoid	0.011 kW	0.011 kW	0.011 kW	0.011 kW	0.011 kW	0.011 kW	0.011 kW
Crankcase Heater	0.019 kW	0.019 kW	0.019 kW	0.019 kW	0.019 kW	0.019 kW	0.019 kW
Compressor	4.04 kW	4.55 kW	4.92 kW	3.96 kW	4.43 kW	4.80 kW	4.73 kW
Heating (w/o fan)	14.14 kW	13.09 kW	11.95 kW	13.56 kW	12.49 kW	11.50 kW	11.39 kW
Cooling (w/o fan)	10.03 kW	8.43 kW	6.83 kW	9.55 kW	7.96 kW	6.51 kW	6.50 kW
Cooling (net)	9.57 kW	7.99 kW	6.39 kW	9.06 kW	7.49 kW	6.03 kW	6.03 kW
COP	1.93	1.47	1.10	1.85	1.40	1.05	1.06

Note: Test bf-B* is identical to test bf-B, except that the primary valve is fully open.

Return-Bend Temperatures

This section shows the return-bend temperatures and the valve opening of the balancing valves for the hybrid control and PEXV fully open cases. Note:

- Inlet temperature was measured on the feeder line. Pressure drop leads to significant measurement error for some Hybrid control cases.
- Exit temperature have some cross-conduction effects through header which leads to measurement error for cases with significantly different individual exit superheats.

Table A 7: TXV (Clean-Coil) Test Return-Bend Temperatures

Return Bend Temperatures, bd*, TXV					
	Inlet = 0	1st 180° =	2nd 180° = 2	3rd 180° = 3	Outlet = 4
Circuit 1	-8.9 °C	-9.0 °C	-8.1 °C	-1.6 °C	0.9 °C
Circuit 2	-8.7 °C	-9.2 °C	-9.3 °C	-3.6 °C	0.3 °C
Circuit 3	-8.8 °C	-9.1 °C	-9.2 °C	-7.6 °C	-0.6 °C
Circuit 4	-9.2 °C	-9.0 °C	-8.6 °C	-7.9 °C	-0.7 °C
Circuit 5	-9.1 °C	-9.2 °C	-9.1 °C	-5.1 °C	-0.5 °C
Circuit 6	-9.4 °C	-8.9 °C	-7.3 °C	-0.1 °C	0.0 °C
Circuit 7	-9.3 °C	-9.4 °C	-4.1 °C	-0.4 °C	0.6 °C
Circuit 8	-9.2 °C	-9.2 °C	-2.8 °C	-0.1 °C	1.0 °C
Average	-9.1 °C	-9.1 °C	-7.3 °C	-3.3 °C	0.1 °C

Return Bend Temperatures, be, TXV					
Circuit No.	Inlet = 0	1st 180° =	2nd 180° = 2	3rd 180° = 3	Outlet = 4
Circuit 1	-6.8 °C	-6.6 °C	-6.6 °C	-2.3 °C	0.4 °C
Circuit 2	-6.6 °C	-6.8 °C	-6.6 °C	-0.1 °C	0.4 °C
Circuit 3	-6.6 °C	-7.0 °C	-6.2 °C	-0.7 °C	0.5 °C
Circuit 4	-7.0 °C	-6.8 °C	-6.3 °C	-0.4 °C	0.6 °C
Circuit 5	-6.8 °C	-7.0 °C	-6.6 °C	-0.5 °C	0.2 °C
Circuit 6	-7.1 °C	-6.6 °C	-6.8 °C	-1.7 °C	0.0 °C
Circuit 7	-7.1 °C	-6.9 °C	-6.9 °C	-6.6 °C	-0.9 °C
Circuit 8	-7.0 °C	-6.8 °C	-6.9 °C	-6.7 °C	-0.3 °C
Average	-6.9 °C	-6.8 °C	-6.6 °C	-2.4 °C	0.1 °C

Return Bend Temperatures, be*, TXV					
Circuit No.	Inlet = 0	1st 180° =	2nd 180° = 2	3rd 180° = 3	Outlet = 4
Circuit 1	-7.0 °C	-6.8 °C	-6.8 °C	-3.1 °C	0.1 °C
Circuit 2	-6.8 °C	-7.0 °C	-6.8 °C	-0.6 °C	0.1 °C
Circuit 3	-6.8 °C	-7.2 °C	-5.9 °C	-1.1 °C	0.2 °C
Circuit 4	-7.1 °C	-6.9 °C	-6.5 °C	-0.8 °C	0.3 °C
Circuit 5	-6.9 °C	-7.1 °C	-7.0 °C	-1.1 °C	0.0 °C
Circuit 6	-7.2 °C	-6.7 °C	-7.0 °C	-2.6 °C	-0.2 °C
Circuit 7	-7.1 °C	-7.0 °C	-7.1 °C	-6.8 °C	-1.3 °C
Circuit 8	-7.0 °C	-6.8 °C	-7.1 °C	-6.8 °C	-0.5 °C
Average	-7.0 °C	-6.9 °C	-6.8 °C	-2.9 °C	-0.1 °C

Note: averages over on-period only

Table A 8: EXV Clean-Coil Return-Bend Temperatures, Part 1

Return Bend Temperatures, bb, EXV					
Circuit No.	Inlet = 0	1st 180° = 1	2nd 180° = 2	3rd 180° = 3	Outlet = 4
Circuit 1	-8.9 °C	-8.8 °C	-8.9 °C	-9.0 °C	-7.1 °C
Circuit 2	-8.9 °C	-8.8 °C	-9.1 °C	-8.7 °C	-6.7 °C
Circuit 3	-9.0 °C	-8.8 °C	-8.9 °C	-9.1 °C	-6.4 °C
Circuit 4	-9.2 °C	-8.7 °C	-9.2 °C	-8.1 °C	-5.3 °C
Circuit 5	-9.0 °C	-8.9 °C	-9.1 °C	-7.2 °C	-4.2 °C
Circuit 6	-9.2 °C	-8.6 °C	-9.0 °C	-5.1 °C	-3.4 °C
Circuit 7	-9.0 °C	-8.9 °C	-9.0 °C	-5.6 °C	-3.0 °C
Circuit 8	-9.0 °C	-8.7 °C	-9.0 °C	-6.3 °C	-3.2 °C
Average	-9.0 °C	-8.8 °C	-9.0 °C	-7.4 °C	-4.9 °C

Return Bend Temperatures, bc, EXV					
Circuit No.	Inlet = 0	1st 180° = 1	2nd 180° = 2	3rd 180° = 3	Outlet = 4
Circuit 1	-8.4 °C	-8.4 °C	-8.4 °C	-8.7 °C	-8.5 °C
Circuit 2	-8.5 °C	-8.5 °C	-8.7 °C	-8.6 °C	-8.1 °C
Circuit 3	-8.7 °C	-8.5 °C	-8.6 °C	-8.8 °C	-5.3 °C
Circuit 4	-8.8 °C	-8.4 °C	-8.4 °C	-8.5 °C	-4.5 °C
Circuit 5	-8.6 °C	-8.6 °C	-8.7 °C	-5.5 °C	-3.7 °C
Circuit 6	-8.8 °C	-8.2 °C	-8.7 °C	-1.1 °C	-3.7 °C
Circuit 7	-8.6 °C	-8.5 °C	-8.6 °C	-1.8 °C	-3.2 °C
Circuit 8	-8.7 °C	-8.2 °C	-8.6 °C	-3.1 °C	-3.3 °C
Average	-8.6 °C	-8.4 °C	-8.6 °C	-5.8 °C	-5.0 °C

Return Bend Temperatures, bd*, EXV					
Circuit No.	Inlet = 0	1st 180° = 1	2nd 180° = 2	3rd 180° = 3	Outlet = 4
Circuit 1	-7.2 °C	-7.3 °C	-7.2 °C	-7.7 °C	-7.3 °C
Circuit 2	-7.2 °C	-7.5 °C	-7.6 °C	-7.6 °C	-5.5 °C
Circuit 3	-7.4 °C	-7.4 °C	-7.5 °C	-7.7 °C	-3.4 °C
Circuit 4	-7.6 °C	-7.3 °C	-7.3 °C	-7.0 °C	-3.2 °C
Circuit 5	-7.3 °C	-7.4 °C	-7.6 °C	-3.4 °C	-2.7 °C
Circuit 6	-7.5 °C	-7.1 °C	-7.5 °C	-0.8 °C	-2.8 °C
Circuit 7	-7.2 °C	-7.4 °C	-7.5 °C	-1.7 °C	-2.2 °C
Circuit 8	-7.3 °C	-7.2 °C	-7.4 °C	-2.9 °C	-2.2 °C
Average	-7.3 °C	-7.3 °C	-7.4 °C	-4.9 °C	-3.7 °C

Return Bend Temperatures, be, EXV					
Circuit No.	Inlet = 0	1st 180° = 1	2nd 180° = 2	3rd 180° = 3	Outlet = 4
Circuit 1	-5.5 °C	-5.8 °C	-5.6 °C	-5.9 °C	-5.7 °C
Circuit 2	-5.7 °C	-5.9 °C	-6.0 °C	-5.8 °C	-4.5 °C
Circuit 3	-5.8 °C	-6.0 °C	-5.8 °C	-5.8 °C	-2.6 °C
Circuit 4	-5.9 °C	-5.8 °C	-5.7 °C	-5.2 °C	-2.4 °C
Circuit 5	-5.6 °C	-6.1 °C	-6.0 °C	-2.2 °C	-2.0 °C
Circuit 6	-5.9 °C	-5.8 °C	-5.9 °C	-0.2 °C	-2.0 °C
Circuit 7	-5.7 °C	-6.1 °C	-5.9 °C	-1.1 °C	-1.5 °C
Circuit 8	-5.7 °C	-5.8 °C	-5.9 °C	-1.8 °C	-1.5 °C
Average	-5.7 °C	-5.9 °C	-5.8 °C	-3.5 °C	-2.8 °C

Table A 9: EXV Clean-Coil Return-Bend Temperatures, Part 2

Return Bend Temperatures, be*, EXV					
Circuit No.	Inlet = 0	1st 180° = 1	2nd 180° = 2	3rd 180° = 3	Outlet = 4
Circuit 1	-6.1 °C	-6.3 °C	-6.1 °C	-6.2 °C	-5.2 °C
Circuit 2	-6.2 °C	-6.4 °C	-6.5 °C	-6.1 °C	-3.8 °C
Circuit 3	-6.3 °C	-6.5 °C	-6.3 °C	-5.9 °C	-2.5 °C
Circuit 4	-6.5 °C	-6.3 °C	-6.1 °C	-4.5 °C	-2.1 °C
Circuit 5	-6.2 °C	-6.6 °C	-6.4 °C	-2.0 °C	-1.8 °C
Circuit 6	-6.5 °C	-6.3 °C	-6.1 °C	-0.2 °C	-1.7 °C
Circuit 7	-6.3 °C	-6.6 °C	-6.2 °C	-0.9 °C	-1.2 °C
Circuit 8	-6.3 °C	-6.3 °C	-6.3 °C	-1.5 °C	-1.0 °C
Average	-6.3 °C	-6.4 °C	-6.2 °C	-3.4 °C	-2.4 °C

Note: averages over on-period only

Return Bend Temperatures, bf, EXV					
Circuit No.	Inlet = 0	1st 180° = 1	2nd 180° = 2	3rd 180° = 3	Outlet = 4
Circuit 1	-4.2 °C	-4.8 °C	-4.5 °C	-4.8 °C	-4.6 °C
Circuit 2	-4.2 °C	-4.8 °C	-4.8 °C	-4.7 °C	-4.1 °C
Circuit 3	-4.6 °C	-4.8 °C	-4.6 °C	-4.6 °C	-2.0 °C
Circuit 4	-4.6 °C	-4.7 °C	-4.5 °C	-3.6 °C	-1.9 °C
Circuit 5	-4.3 °C	-4.9 °C	-4.7 °C	-1.4 °C	-1.5 °C
Circuit 6	-4.5 °C	-4.6 °C	-4.7 °C	-0.2 °C	-1.5 °C
Circuit 7	-4.6 °C	-4.8 °C	-4.6 °C	-0.8 °C	-0.9 °C
Circuit 8	-4.4 °C	-4.7 °C	-4.6 °C	-0.8 °C	-0.9 °C
Average	-4.4 °C	-4.8 °C	-4.6 °C	-2.6 °C	-2.2 °C

Table A 10: EXV Blocked-Coil Return-Bend Temperatures, Part 1

Return Bend Temperatures, bd*-A, EXV					
Circuit No.	Inlet = 0	1st 180° = 1	2nd 180° = 2	3rd 180° = 3	Outlet = 4
Circuit 1	-11.5 °C	-11.8 °C	-11.6 °C	-11.8 °C	-11.9 °C
Circuit 2	-11.4 °C	-11.8 °C	-12.0 °C	-11.7 °C	-10.7 °C
Circuit 3	-12.0 °C	-11.6 °C	-11.8 °C	-6.8 °C	-6.9 °C
Circuit 4	-12.0 °C	-11.5 °C	-10.8 °C	-2.1 °C	-6.0 °C
Circuit 5	-11.7 °C	-11.8 °C	-4.6 °C	-0.7 °C	-4.6 °C
Circuit 6	-12.0 °C	-11.4 °C	-1.9 °C	1.2 °C	-4.5 °C
Circuit 7	-12.2 °C	-11.9 °C	-1.0 °C	0.7 °C	-3.4 °C
Circuit 8	-12.0 °C	-11.6 °C	-1.0 °C	0.7 °C	-4.1 °C
Average	-11.9 °C	-11.7 °C	-6.8 °C	-3.8 °C	-6.5 °C

Table A 11: EXV Blocked-Coil Return-Bend Temperatures, Part 2

Return Bend Temperatures, be-A, EXV					
Circuit No.	Inlet = 0	1st 180° = 1	2nd 180° = 2	3rd 180° = 3	Outlet = 4
Circuit 1	-9.7 °C	-10.0 °C	-9.8 °C	-10.0 °C	-10.0 °C
Circuit 2	-9.7 °C	-10.0 °C	-10.2 °C	-9.8 °C	-7.9 °C
Circuit 3	-10.0 °C	-10.0 °C	-9.9 °C	-5.1 °C	-5.3 °C
Circuit 4	-10.1 °C	-10.0 °C	-7.8 °C	-1.3 °C	-4.4 °C
Circuit 5	-9.7 °C	-10.2 °C	-2.9 °C	-0.3 °C	-3.3 °C
Circuit 6	-10.1 °C	-9.7 °C	-1.1 °C	1.0 °C	-3.5 °C
Circuit 7	-9.7 °C	-10.1 °C	-0.7 °C	0.5 °C	-2.5 °C
Circuit 8	-9.8 °C	-9.9 °C	-0.7 °C	0.4 °C	-3.1 °C
Average	-9.8 °C	-10.0 °C	-5.4 °C	-3.1 °C	-5.0 °C

Return Bend Temperatures, bf-A, EXV					
Circuit No.	Inlet = 0	1st 180° = 1	2nd 180° = 2	3rd 180° = 3	Outlet = 4
Circuit 1	-7.9 °C	-8.4 °C	-8.1 °C	-8.4 °C	-8.4 °C
Circuit 2	-7.9 °C	-8.4 °C	-8.5 °C	-8.1 °C	-7.5 °C
Circuit 3	-8.3 °C	-8.3 °C	-8.1 °C	-4.6 °C	-4.7 °C
Circuit 4	-8.3 °C	-8.2 °C	-6.1 °C	-0.7 °C	-3.5 °C
Circuit 5	-8.0 °C	-8.4 °C	-1.8 °C	0.2 °C	-2.6 °C
Circuit 6	-8.3 °C	-8.0 °C	-0.5 °C	1.5 °C	-2.6 °C
Circuit 7	-8.4 °C	-8.4 °C	-0.2 °C	1.1 °C	-1.7 °C
Circuit 8	-8.2 °C	-8.1 °C	0.0 °C	1.1 °C	-2.2 °C
Average	-8.2 °C	-8.3 °C	-4.2 °C	-2.2 °C	-4.1 °C

Return Bend Temperatures, bd*-B, EXV					
Circuit No.	Inlet = 0	1st 180° = 1	2nd 180° = 2	3rd 180° = 3	Outlet = 4
Circuit 1	-15.1 °C	-15.2 °C	-15.1 °C	-15.2 °C	-15.4 °C
Circuit 2	-15.0 °C	-15.2 °C	-15.6 °C	-15.0 °C	-15.4 °C
Circuit 3	-15.4 °C	-15.3 °C	-15.4 °C	-14.1 °C	-10.7 °C
Circuit 4	-15.5 °C	-15.0 °C	-8.8 °C	-4.9 °C	-9.1 °C
Circuit 5	-15.1 °C	-15.3 °C	-4.2 °C	-2.4 °C	-7.2 °C
Circuit 6	-15.4 °C	-12.1 °C	-1.9 °C	0.8 °C	-6.8 °C
Circuit 7	-15.1 °C	-6.7 °C	-1.0 °C	0.9 °C	-4.9 °C
Circuit 8	-15.1 °C	-6.9 °C	-0.4 °C	1.2 °C	-5.8 °C
Average	-15.2 °C	-12.7 °C	-7.8 °C	-6.1 °C	-9.4 °C

Return Bend Temperatures, be-B, EXV					
Circuit No.	Inlet = 0	1st 180° = 1	2nd 180° = 2	3rd 180° = 3	Outlet = 4
Circuit 1	-12.2 °C	-12.4 °C	-12.2 °C	-12.2 °C	-7.4 °C
Circuit 2	-12.2 °C	-12.5 °C	-12.7 °C	-11.7 °C	-7.8 °C
Circuit 3	-12.5 °C	-12.6 °C	-12.4 °C	-8.5 °C	-6.0 °C
Circuit 4	-12.7 °C	-12.4 °C	-5.6 °C	-3.4 °C	-4.3 °C
Circuit 5	-12.2 °C	-12.6 °C	-2.6 °C	-1.6 °C	-2.9 °C
Circuit 6	-12.6 °C	-11.5 °C	-1.5 °C	0.7 °C	-2.0 °C
Circuit 7	-12.3 °C	-10.7 °C	-1.1 °C	0.5 °C	-0.6 °C
Circuit 8	-12.3 °C	-11.8 °C	-0.7 °C	0.6 °C	-0.5 °C
Average	-12.4 °C	-12.1 °C	-6.1 °C	-4.5 °C	-3.9 °C

Table A 12: EXV Blocked-Coil Return-Bend Temperatures, Part 3

Return Bend Temperatures, bf-B, EXV					
Circuit No.	Inlet = 0	1st 180° = 1	2nd 180° = 2	3rd 180° = 3	Outlet = 4
Circuit 1	-9.7 °C	-10.1 °C	-9.8 °C	-10.1 °C	-9.8 °C
Circuit 2	-9.7 °C	-10.2 °C	-10.3 °C	-9.9 °C	-9.8 °C
Circuit 3	-10.2 °C	-10.2 °C	-10.0 °C	-9.4 °C	-6.9 °C
Circuit 4	-10.2 °C	-10.0 °C	-7.0 °C	-3.1 °C	-5.6 °C
Circuit 5	-9.8 °C	-10.1 °C	-2.3 °C	-1.1 °C	-4.2 °C
Circuit 6	-10.2 °C	-9.3 °C	-0.8 °C	1.3 °C	-3.8 °C
Circuit 7	-10.3 °C	-7.3 °C	-0.1 °C	1.2 °C	-2.4 °C
Circuit 8	-10.0 °C	-8.5 °C	0.3 °C	1.4 °C	-3.0 °C
Average	-10.0 °C	-9.5 °C	-5.0 °C	-3.7 °C	-5.7 °C

Return Bend Temperatures, be-C, EXV					
Circuit No.	Inlet = 0	1st 180° = 1	2nd 180° = 2	3rd 180° = 3	Outlet = 4
Circuit 1	-6.5 °C	-6.9 °C	-6.7 °C	-7.0 °C	-6.8 °C
Circuit 2	-6.6 °C	-7.1 °C	-7.1 °C	-6.9 °C	-6.2 °C
Circuit 3	-6.8 °C	-7.0 °C	-6.9 °C	-6.9 °C	-3.4 °C
Circuit 4	-7.0 °C	-6.9 °C	-6.7 °C	-4.9 °C	-2.9 °C
Circuit 5	-6.7 °C	-7.1 °C	-7.0 °C	-1.8 °C	-2.4 °C
Circuit 6	-6.9 °C	-6.8 °C	-6.2 °C	0.3 °C	-2.5 °C
Circuit 7	-6.7 °C	-7.1 °C	-6.0 °C	-0.3 °C	-1.7 °C
Circuit 8	-6.7 °C	-6.9 °C	-6.7 °C	-0.5 °C	-1.8 °C
Average	-6.7 °C	-7.0 °C	-6.7 °C	-3.5 °C	-3.5 °C

Return Bend Temperatures, be-D, EXV					
Circuit No.	Inlet = 0	1st 180° = 1	2nd 180° = 2	3rd 180° = 3	Outlet = 4
Circuit 1	-5.9 °C	-6.3 °C	-6.1 °C	-6.4 °C	-6.2 °C
Circuit 2	-6.0 °C	-6.4 °C	-6.4 °C	-6.3 °C	-5.5 °C
Circuit 3	-6.2 °C	-6.3 °C	-6.2 °C	-6.3 °C	-2.7 °C
Circuit 4	-6.3 °C	-6.3 °C	-6.1 °C	-2.7 °C	-2.3 °C
Circuit 5	-6.0 °C	-6.5 °C	-6.4 °C	-1.3 °C	-2.0 °C
Circuit 6	-6.2 °C	-6.2 °C	-6.2 °C	0.1 °C	-2.1 °C
Circuit 7	-6.0 °C	-6.5 °C	-6.2 °C	-0.6 °C	-1.6 °C
Circuit 8	-6.0 °C	-6.2 °C	-6.3 °C	-1.0 °C	-1.7 °C
Average	-6.1 °C	-6.3 °C	-6.2 °C	-3.1 °C	-3.0 °C

Return Bend Temperatures, be-B-R, EXV					
Circuit No.	Inlet = 0	1st 180° = 1	2nd 180° = 2	3rd 180° = 3	Outlet = 4
Circuit 1	-11.8 °C	-11.9 °C	-12.0 °C	-12.2 °C	-11.8 °C
Circuit 2	-11.7 °C	-12.1 °C	-12.4 °C	-12.1 °C	-11.8 °C
Circuit 3	-12.3 °C	-12.1 °C	-12.1 °C	-11.5 °C	-8.2 °C
Circuit 4	-12.3 °C	-11.9 °C	-9.4 °C	-4.1 °C	-6.8 °C
Circuit 5	-11.8 °C	-12.0 °C	-3.1 °C	-1.8 °C	-5.2 °C
Circuit 6	-12.2 °C	-10.0 °C	-1.3 °C	0.8 °C	-4.8 °C
Circuit 7	-12.4 °C	-5.8 °C	-0.6 °C	0.8 °C	-3.3 °C
Circuit 8	-12.1 °C	-9.3 °C	-0.1 °C	1.0 °C	-4.1 °C
Average	-12.1 °C	-10.6 °C	-6.4 °C	-4.9 °C	-7.0 °C

Table A 13: Hybrid and PEXV Fully Open Clean-Coil Return-Bend Temperatures and Valve Openings, Part 1

Return Bend Temperatures and valve openings, bc, Hybrid						
Circuit No.	Inlet = 0	1st 180° = 1	2nd 180° = 2	3rd 180° = 3	Outlet = 4	Opening
Circuit 1	-7.5 °C	-7.2 °C	-6.7 °C	-7.3 °C	-4.4 °C	90 Steps
Circuit 2	-7.6 °C	-7.2 °C	-7.2 °C	-7.2 °C	-3.3 °C	238 Steps
Circuit 3	-7.9 °C	-7.3 °C	-6.9 °C	-7.4 °C	-4.2 °C	147 Steps
Circuit 4	-7.8 °C	-7.3 °C	-6.7 °C	-7.2 °C	-3.7 °C	139 Steps
Circuit 5	-7.9 °C	-7.5 °C	-7.0 °C	-7.4 °C	-4.0 °C	185 Steps
Circuit 6	-7.6 °C	-7.1 °C	-6.9 °C	-7.5 °C	-4.1 °C	373 Steps
Circuit 7	-7.9 °C	-7.4 °C	-7.0 °C	-7.5 °C	-3.8 °C	235 Steps
Circuit 8	-7.3 °C	-7.3 °C	-7.1 °C	-7.6 °C	-3.1 °C	488 Steps
Average	-7.7 °C	-7.3 °C	-6.9 °C	-7.4 °C	-3.8 °C	

Note: Valve openings using offsets of test bf°, error 20 steps acc. to manufacturer

Return Bend Temperatures and valve openings, bd*, Hybrid						
Circuit No.	Inlet = 0	1st 180° = 1	2nd 180° = 2	3rd 180° = 3	Outlet = 4	Opening
Circuit 1	-6.3 °C	-6.2 °C	-5.5 °C	-6.1 °C	-3.6 °C	48 Steps
Circuit 2	-6.4 °C	-6.2 °C	-6.1 °C	-6.1 °C	-3.1 °C	149 Steps
Circuit 3	-6.6 °C	-6.2 °C	-5.9 °C	-6.2 °C	-2.9 °C	134 Steps
Circuit 4	-6.4 °C	-6.1 °C	-5.4 °C	-6.0 °C	-4.1 °C	146 Steps
Circuit 5	-6.5 °C	-6.4 °C	-5.7 °C	-6.3 °C	-3.6 °C	155 Steps
Circuit 6	-6.2 °C	-6.0 °C	-5.5 °C	-6.3 °C	-3.4 °C	293 Steps
Circuit 7	-6.6 °C	-6.3 °C	-5.7 °C	-6.2 °C	-3.8 °C	158 Steps
Circuit 8	-5.4 °C	-6.1 °C	-5.8 °C	-6.3 °C	-3.2 °C	487 Steps
Average	-6.3 °C	-6.2 °C	-5.7 °C	-6.2 °C	-3.5 °C	

Note: Valve openings using offsets of test bf°, error 20 steps acc. to manufacturer

Return Bend Temperatures and valve openings, be, Hybrid						
Circuit No.	Inlet = 0	1st 180° = 1	2nd 180° = 2	3rd 180° = 3	Outlet = 4	Opening
Circuit 1	-4.9 °C	-4.8 °C	-4.1 °C	-4.7 °C	-2.6 °C	31 Steps
Circuit 2	-5.0 °C	-4.8 °C	-4.7 °C	-4.7 °C	-2.9 °C	136 Steps
Circuit 3	-5.1 °C	-4.8 °C	-4.5 °C	-4.9 °C	-2.4 °C	133 Steps
Circuit 4	-5.0 °C	-4.7 °C	-4.2 °C	-4.7 °C	-2.5 °C	145 Steps
Circuit 5	-5.0 °C	-5.0 °C	-4.4 °C	-4.9 °C	-2.4 °C	161 Steps
Circuit 6	-4.7 °C	-4.6 °C	-4.2 °C	-4.9 °C	-2.2 °C	249 Steps
Circuit 7	-5.2 °C	-4.9 °C	-4.4 °C	-4.8 °C	-3.2 °C	116 Steps
Circuit 8	-3.6 °C	-4.7 °C	-4.4 °C	-4.9 °C	-2.3 °C	488 Steps
Average	-4.8 °C	-4.8 °C	-4.4 °C	-4.8 °C	-2.6 °C	

Note: Valve openings using offsets of test bf°, error 20 steps acc. to manufacturer

Return Bend Temperatures and valve openings, bf, Hybrid						
Circuit No.	Inlet = 0	1st 180° = 1	2nd 180° = 2	3rd 180° = 3	Outlet = 4	Opening
Circuit 1	-3.5 °C	-3.6 °C	-2.7 °C	-3.3 °C	-1.4 °C	34 Steps
Circuit 2	-3.6 °C	-3.6 °C	-3.3 °C	-3.4 °C	-1.4 °C	128 Steps
Circuit 3	-3.7 °C	-3.6 °C	-3.1 °C	-3.5 °C	-1.7 °C	125 Steps
Circuit 4	-3.5 °C	-3.4 °C	-2.8 °C	-3.4 °C	-2.1 °C	135 Steps
Circuit 5	-3.6 °C	-3.7 °C	-3.0 °C	-3.6 °C	-2.0 °C	151 Steps
Circuit 6	-3.2 °C	-3.4 °C	-2.8 °C	-3.6 °C	-2.1 °C	229 Steps
Circuit 7	-3.9 °C	-3.7 °C	-3.0 °C	-3.5 °C	-2.2 °C	96 Steps
Circuit 8	-1.8 °C	-3.3 °C	-3.0 °C	-3.5 °C	-1.3 °C	488 Steps
Average	-3.4 °C	-3.5 °C	-3.0 °C	-3.5 °C	-1.8 °C	

Note: Valve openings using offsets of test bf°, error 20 steps acc. to manufacturer

Table A 14: Hybrid and PEXV Fully Open Clean-Coil Return-Bend Temperatures and Valve Openings, Part 2

Return Bend Temperatures and valve openings, bf°, Hybrid						
Circuit No.	Inlet = 0	1st 180° = 1	2nd 180° = 2	3rd 180° = 3	Outlet = 4	Opening
Circuit 1	-3.7 °C	-4.0 °C	-3.0 °C	-4.0 °C	-0.3 °C	29 Steps
Circuit 2	-3.9 °C	-4.1 °C	-3.7 °C	-3.9 °C	-0.5 °C	33 Steps
Circuit 3	-4.1 °C	-4.2 °C	-3.4 °C	-4.0 °C	-0.5 °C	30 Steps
Circuit 4	-3.9 °C	-4.0 °C	-3.0 °C	-4.0 °C	-0.4 °C	35 Steps
Circuit 5	-4.0 °C	-4.2 °C	-3.3 °C	-4.0 °C	-0.3 °C	31 Steps
Circuit 6	-4.2 °C	-4.0 °C	-3.1 °C	-4.0 °C	-0.1 °C	23 Steps
Circuit 7	-4.1 °C	-4.2 °C	-3.4 °C	-4.0 °C	-0.2 °C	28 Steps
Circuit 8	-3.6 °C	-4.1 °C	-3.5 °C	-4.1 °C	-0.2 °C	36 Steps
Average	-3.9 °C	-4.1 °C	-3.3 °C	-4.0 °C	-0.3 °C	

Note: For this point valve opening offsets were determined after valve reset;
shown value is actual opening (= stepnumber - opening offset) as used for
valve correlation.

Table A 15: Hybrid and PEXV Fully Open Blocked-Coil Return-Bend Temperatures and Valve Openings, Part 1

Return Bend Temperatures and valve openings, bd*-A, Hybrid						
Circuit No.	Inlet = 0	1st 180° = 1	2nd 180° = 2	3rd 180° = 3	Outlet = 4	opening
Circuit 1	-8.0 °C	-8.0 °C	-6.8 °C	-7.7 °C	-6.6 °C	4 Steps
Circuit 2	-8.3 °C	-8.0 °C	-7.4 °C	-7.6 °C	-6.1 °C	14 Steps
Circuit 3	-8.4 °C	-7.9 °C	-7.6 °C	-7.6 °C	-5.5 °C	25 Steps
Circuit 4	-8.1 °C	-7.8 °C	-7.2 °C	-7.6 °C	-6.3 °C	108 Steps
Circuit 5	-8.2 °C	-8.1 °C	-7.3 °C	-7.7 °C	-6.6 °C	101 Steps
Circuit 6	-7.1 °C	-7.5 °C	-7.1 °C	-7.7 °C	-5.7 °C	381 Steps
Circuit 7	-7.7 °C	-7.9 °C	-7.3 °C	-7.8 °C	-6.2 °C	236 Steps
Circuit 8	-7.1 °C	-7.7 °C	-7.3 °C	-7.8 °C	-6.2 °C	284 Steps
Average	-7.9 °C	-7.9 °C	-7.3 °C	-7.7 °C	-6.2 °C	

Note: Valve openings using offsets of test bf°, error 20 steps acc. to manufacturer

Return Bend Temperatures and valve openings, be-A, Hybrid						
Circuit No.	Inlet = 0	1st 180° = 1	2nd 180° = 2	3rd 180° = 3	Outlet = 4	opening
Circuit 1	-6.1 °C	-6.0 °C	-4.6 °C	-5.6 °C	-2.5 °C	3 Steps
Circuit 2	-6.3 °C	-6.1 °C	-5.2 °C	-5.4 °C	-2.6 °C	6 Steps
Circuit 3	-6.4 °C	-5.9 °C	-5.5 °C	-5.5 °C	-3.4 °C	24 Steps
Circuit 4	-6.1 °C	-5.8 °C	-5.1 °C	-5.6 °C	-2.1 °C	112 Steps
Circuit 5	-6.0 °C	-6.0 °C	-5.2 °C	-5.7 °C	-2.7 °C	154 Steps
Circuit 6	-5.8 °C	-5.6 °C	-4.9 °C	-5.7 °C	-2.2 °C	186 Steps
Circuit 7	-4.9 °C	-5.8 °C	-5.1 °C	-5.7 °C	-3.6 °C	364 Steps
Circuit 8	-4.1 °C	-5.5 °C	-5.1 °C	-5.6 °C	-3.9 °C	474 Steps
Average	-5.7 °C	-5.9 °C	-5.1 °C	-5.6 °C	-2.9 °C	

Note: Valve openings using offsets of test bf°, error 20 steps acc. to manufacturer

Table A 16: Hybrid and PEXV Fully Open Blocked-Coil Return-Bend Temperatures and Valve Openings, Part 2

Return Bend Temperatures and valve openings, bf-A, Hybrid						
Circuit No.	Inlet = 0	1st 180° = 1	2nd 180° = 2	3rd 180° = 3	Outlet = 4	opening
Circuit 1	-4.5 °C	-4.6 °C	-3.3 °C	-4.5 °C	-3.2 °C	7 Steps
Circuit 2	-4.8 °C	-4.7 °C	-3.9 °C	-4.3 °C	-3.2 °C	8 Steps
Circuit 3	-4.9 °C	-4.5 °C	-4.2 °C	-4.3 °C	-3.4 °C	21 Steps
Circuit 4	-4.5 °C	-4.4 °C	-3.8 °C	-4.3 °C	-1.8 °C	128 Steps
Circuit 5	-4.6 °C	-4.6 °C	-4.1 °C	-4.5 °C	-1.9 °C	117 Steps
Circuit 6	-3.1 °C	-4.0 °C	-3.6 °C	-4.5 °C	-2.1 °C	452 Steps
Circuit 7	-3.7 °C	-4.4 °C	-3.9 °C	-4.5 °C	-2.6 °C	300 Steps
Circuit 8	-2.6 °C	-4.1 °C	-3.8 °C	-4.4 °C	-1.9 °C	488 Steps
Average	-4.1 °C	-4.4 °C	-3.8 °C	-4.4 °C	-2.5 °C	

Note: Valve openings using offsets of test bf°, error 20 steps acc. to manufacturer

Return Bend Temperatures and valve openings, bd*-B, Hybrid						
Circuit No.	Inlet = 0	1st 180° = 1	2nd 180° = 2	3rd 180° = 3	Outlet = 4	opening
Circuit 1	-9.3 °C	-9.2 °C	-8.1 °C	-9.0 °C	-6.4 °C	3 Steps
Circuit 2	-9.6 °C	-9.4 °C	-8.7 °C	-8.9 °C	-6.6 °C	2 Steps
Circuit 3	-9.7 °C	-9.0 °C	-8.9 °C	-8.7 °C	-7.0 °C	17 Steps
Circuit 4	-9.6 °C	-9.1 °C	-8.4 °C	-8.9 °C	-7.6 °C	18 Steps
Circuit 5	-9.6 °C	-9.3 °C	-8.7 °C	-8.6 °C	-6.8 °C	117 Steps
Circuit 6	-9.0 °C	-8.7 °C	-8.4 °C	-9.1 °C	-7.5 °C	246 Steps
Circuit 7	-7.2 °C	-8.6 °C	-8.2 °C	-8.8 °C	-6.6 °C	585 Steps
Circuit 8	-7.2 °C	-8.5 °C	-8.3 °C	-8.8 °C	-6.9 °C	408 Steps
Average	-8.9 °C	-9.0 °C	-8.4 °C	-8.8 °C	-6.9 °C	

Note: Valve openings using offsets of test bf°, error 20 steps acc. to manufacturer

Return Bend Temperatures and valve openings, be-B, Hybrid						
Circuit No.	Inlet = 0	1st 180° = 1	2nd 180° = 2	3rd 180° = 3	Outlet = 4	opening
Circuit 1	-7.4 °C	-7.2 °C	-5.8 °C	-6.8 °C	-4.3 °C	10 Steps
Circuit 2	-7.7 °C	-7.4 °C	-6.5 °C	-6.7 °C	-4.4 °C	9 Steps
Circuit 3	-7.7 °C	-7.0 °C	-6.8 °C	-6.6 °C	-4.5 °C	39 Steps
Circuit 4	-7.6 °C	-7.1 °C	-6.4 °C	-6.8 °C	-4.6 °C	40 Steps
Circuit 5	-7.6 °C	-7.4 °C	-6.5 °C	-6.5 °C	-4.5 °C	49 Steps
Circuit 6	-7.1 °C	-6.9 °C	-6.1 °C	-6.9 °C	-4.4 °C	156 Steps
Circuit 7	-4.9 °C	-6.7 °C	-6.0 °C	-6.7 °C	-4.9 °C	490 Steps
Circuit 8	-4.5 °C	-6.5 °C	-6.0 °C	-6.7 °C	-4.9 °C	485 Steps
Average	-6.8 °C	-7.0 °C	-6.3 °C	-6.7 °C	-4.6 °C	

Note: Valve openings using offsets of test bf°, error 20 steps acc. to manufacturer

Table A 17: Hybrid and PEXV Fully Open Blocked-Coil Return-Bend Temperatures and Valve Openings, Part 3

Return Bend Temperatures and valve openings, bf-B, Hybrid						
Circuit No.	Inlet = 0	1st 180° = 1	2nd 180° = 2	3rd 180° = 3	Outlet = 4	opening
Circuit 1	-5.6 °C	-5.7 °C	-4.2 °C	-5.5 °C	-4.2 °C	6 Steps
Circuit 2	-5.9 °C	-5.8 °C	-4.7 °C	-5.3 °C	-3.1 °C	5 Steps
Circuit 3	-6.0 °C	-5.4 °C	-5.2 °C	-5.1 °C	-2.9 °C	5 Steps
Circuit 4	-5.9 °C	-5.5 °C	-4.8 °C	-5.4 °C	-3.6 °C	10 Steps
Circuit 5	-6.0 °C	-5.7 °C	-5.1 °C	-5.3 °C	-3.8 °C	32 Steps
Circuit 6	-4.6 °C	-5.2 °C	-4.7 °C	-5.6 °C	-4.3 °C	241 Steps
Circuit 7	-3.2 °C	-5.1 °C	-4.6 °C	-5.4 °C	-3.1 °C	415 Steps
Circuit 8	-2.7 °C	-4.9 °C	-4.6 °C	-5.4 °C	-3.6 °C	436 Steps
Average	-5.0 °C	-5.4 °C	-4.8 °C	-5.4 °C	-3.6 °C	

Note: Valve openings using offsets of test bf°, error 20 steps acc. to manufacturer

Return Bend Temperatures and valve openings, bf-B°, Hybrid						
Circuit No.	Inlet = 0	1st 180° = 1	2nd 180° = 2	3rd 180° = 3	Outlet = 4	opening
Circuit 1	-6.0 °C	-6.1 °C	-4.7 °C	-5.5 °C	-1.1 °C	4 Steps
Circuit 2	-6.3 °C	-6.3 °C	-5.2 °C	-5.5 °C	-1.4 °C	2 Steps
Circuit 3	-6.5 °C	-6.1 °C	-5.5 °C	-5.3 °C	-1.5 °C	6 Steps
Circuit 4	-6.3 °C	-5.9 °C	-5.1 °C	-5.5 °C	-1.5 °C	9 Steps
Circuit 5	-6.1 °C	-6.2 °C	-5.4 °C	-5.6 °C	-2.4 °C	16 Steps
Circuit 6	-5.7 °C	-5.8 °C	-5.0 °C	-6.0 °C	-2.5 °C	35 Steps
Circuit 7	-4.2 °C	-5.7 °C	-5.0 °C	-5.9 °C	-1.6 °C	76 Steps
Circuit 8	-3.2 °C	-5.4 °C	-5.0 °C	-5.8 °C	-1.4 °C	89 Steps
Average	-5.5 °C	-5.9 °C	-5.1 °C	-5.6 °C	-1.7 °C	

Note: Valve openings using offsets of test bf°, error 20 steps acc. to manufacturer

Uncertainty Analysis

Code A 1 shows the EES code which used for uncertainty analysis for the large room cooling system (LRCS). The inbuilt uncertainty calculation method of EES (Klein, 2012), which neglects cross dependency was used. The confidence interval of the measured data was not evaluated. It was found that for the LRCS, the uncertainty is mostly caused by the power meter. To simplify the analysis, the two most extreme operating conditions were considered and the maximum uncertainty was used for graphs, which is shown in Table A 18.

Code A 1: Uncertainty Analysis for Large Room Cooling System

```

"!Setup"
$UnitSystem SI MASS DEG kPa C kJ
"!Conditionals"
$IFNOT PARAMETRICTABLE
"Extreme cases with lowest/highest power consumption considered: 12C ambient and 46C ambient, blocked"
"EXV 12°C"
m_dot=0.0873[kg/s]
W_dot_mess_comp=3.71[kW]
P_EUout=427[kPa]

```

```

P_EUin=1081[kPa]
T_eu_out=-6.0[C]
T_eu_in=19.8[C]
W_dot_mess_fan_evap=0.380[kW]
W_dot_mess_fan_cond=0.447[kW] "same for both tests"
U_fan=115[V] "rated"

```

"Hybrid, 12C"

```

m_dot_H=0.0927[kg/s]
W_dot_mess_comp_H=3.84[kW]
P_EUout_H=453[kPa]
P_EUin_H=1117[kPa]
T_eu_out_H=-4.6[C]
T_eu_in_H=20.2[C]
W_dot_mess_fan_evap_H=0.383[kW]

```

{"EXV 46C, 2/3 blockage"

```

m_dot=0.0652[kg/s]
W_dot_mess_comp=4.21[kW]
P_EUout=406[kPa]
P_EUin=2404[kPa]
T_eu_out=-5.7[C]
T_eu_in=50.2[C]
W_dot_mess_fan_evap=0.380[kW]
W_dot_mess_fan_cond=0.447[kW] "same for both tests"
U_fan=115[V] "rated"

```

"Hybrid, 46C, 2/3rds blockage"

```

m_dot_H=0.0833[kg/s]
W_dot_mess_comp_H=4.80[kW]
P_EUout_H=484[kPa]
P_EUin_H=2489[kPa]
T_eu_out_H=-5.1[C]
T_eu_in_H=52.6[C]
W_dot_mess_fan_evap_H=0.472[kW]}

```

\$ENDIF

R\$='R404a'

"!accuracy"

"Mass flow meter accuracy"

"R:\cec-share\00 Large Room Cooling System\Measurement Instrumentation\Flow Meter"

m_dot_hr=m_dot*convert(h,s)

Z_stability=0.027[kg/h]

Z_Limit=Z_stability/0.0005 "limit, when flowrate smaller than this value, accuracy = ±[(zero stability / flow rate) × 100]%"

m_dot_acc=0.1[%]*convert(%,1) "accuracy for flowrate larger than Z_limit"

"Temperature sensors"

T_acc=0.5[C] "special limit of errors, Omega"

"Pressure transducers"

"neglected temperature dependency "

P_low_acc=250[PSI]*convert(PSI,kPa)*0.13[%]*convert(%,1) "accuracy for 250PSI transducers"

P_high_acc=500[PSI]*convert(PSI,kPa)*0.13[%]*convert(%,1) "accuracy for 250PSI transducers"

"Power Measurements"

"PC5-062-C"

W_dot_acc_comp=40[kW]*(0.5)[%]*convert(%,1)*1/5 "Accuracy, no temperature effects, 5 loops trough current transformer"

W_dot_acc_fan_evap=(0.15/100*W_dot_mess_fan_evap*convert(kW,W)+0.1/100*5[A]*115[V])*convert(W,kW)

"0.15% of reading and 0.1% of rated output"

W_dot_acc_fan_cond=0.14 "relative accuracy, using Extech 505 multimeter w 0.5% accuracy and assumed power factor of 0.7 +/-1"

"!Calculations"

"EXV"

```
T_sat_in=Temperature(R$,P=P_EUin,x=1)
T_sat_out=Temperature(R$,P=P_EUin,x=1)
h_eva_in=min(Enthalpy(R$,T=T_eu_in,P=P_EUin),Enthalpy(R$,X=0,P=P_EUin))
h_eva_out=max(Enthalpy(R$,T=T_eu_out,P=P_EUout),Enthalpy(R$,X=0,P=P_EUout))
Q_dot=m_dot*(h_eva_out-h_eva_in)-W_dot_mess_fan_evap
COP=Q_dot/(W_dot_mess_comp+W_dot_mess_fan_evap+W_dot_mess_fan_cond)
```

"Hybrid"

```
T_sat_in_H=Temperature(R$,P=P_EUin_H,x=1)
T_sat_out_H=Temperature(R$,P=P_EUin_H,x=1)
h_eva_in_H=min(Enthalpy(R$,T=T_eu_in_H,P=P_EUin_H),Enthalpy(R$,X=0,P=P_EUin_H))
h_eva_out_H=max(Enthalpy(R$,T=T_eu_out_H,P=P_EUout_H),Enthalpy(R$,X=0,P=P_EUout_H))
Q_dot_H=m_dot_H*(h_eva_out_H-h_eva_in_H)-W_dot_mess_fan_evap_H
COP_H=Q_dot_H/(W_dot_mess_comp_H+W_dot_mess_fan_evap_H+W_dot_mess_fan_cond)
```

"Comparison between two different system configurations"

Q_dot_diff=(Q_dot_H-Q_dot)/Q_dot

COP_diff=(COP_H-COP)/COP

Table A 18: Uncertainties for Large Room Cooling System

Note	COP	Capacity	COP _{diff}	Capacity _{Diff}
EXV, 46°C, 2/3 blocked	1.9%	1.2%	2.2%	2.2%
Hybrid, 46°C, 2/3 blocked	1.9%	1.3%		
EXV, 12°C, clean	1.7%	0.4%	1.5%	0.8%
Hybrid, 12°C, clean	1.7%	0.7%		
Max	1.9%	1.3%	2.2%	2.2%

Simulation Model Details

The simulation model that was used to simulate the large room cooling system is based on a object oriented programming. This has the benefit, that component models can be reused for different systems. Depended on the system, the cycle model, which is used to interconnect the components and solve them numerically, can be modified. Furthermore, components can be swapped against different ones, if they use the same input/output conventions. This is the case for the two different evaporator models, that were used. Component models are modified versions of ACHP (Bell, 2011).

Cycle Model

The cycle model that was built specifically for the large room cooling system is composed of

- Condenser,
- Evaporator,
- Return line, and
- Compressor.

The reason for using a cycle model that is different from the standard cycle model in ACHP is, that the liquid receiver that buffers charge in the system leads to a negligible subcooling. For tests without severe expansion valve hunting, subcooling at the expansion valve inlet is therefore negligibly small and essentially nonexistent within the measurement tolerance. With an input of close to 0 K subcooling, the standard air conditioning model of ACHP did converge reliably. The objective of the new cycle model is to solve the components to obtain a predetermined superheat and 0 K subcooling, as shown in Figure A 1.

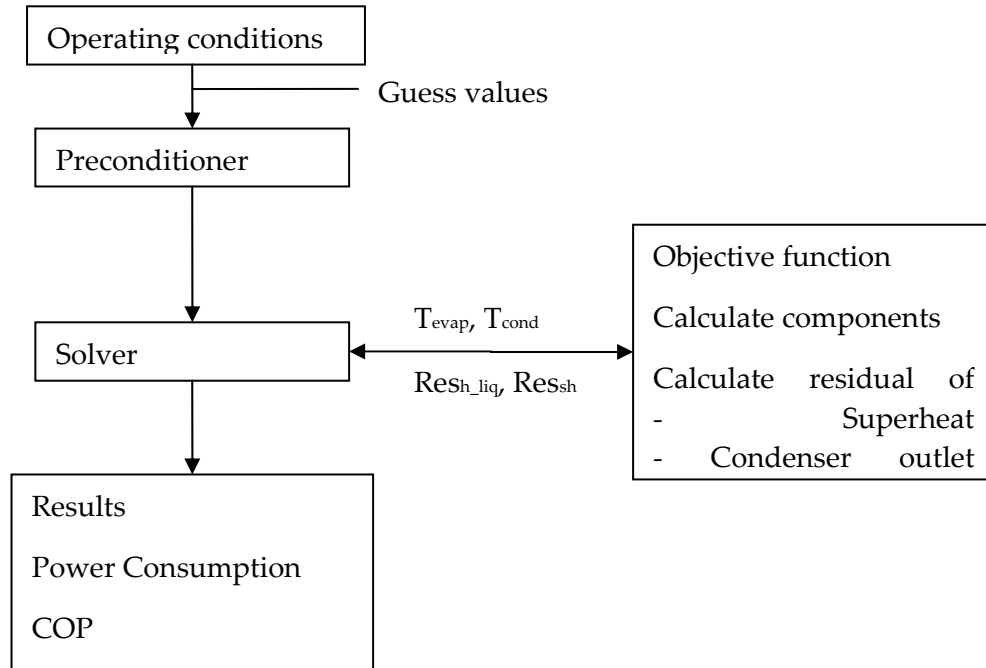


Figure A 1: Cycle Solver

Condenser

The condenser is based on Revision 70 of the ACHP condenser (Bell, 2011). The ACHP condenser splits up the condenser into three sections: desuperheating, condensing, and subcooling as shown in Figure A 2, using a moving boundary method. Given the inlet conditions on air- and refrigerant side, the size of each section is determined starting with the superheated section, followed by the two-phase section. If the condenser is sufficiently large, a subcooled section can exist. Each section is calculated using an ε -NTU method.

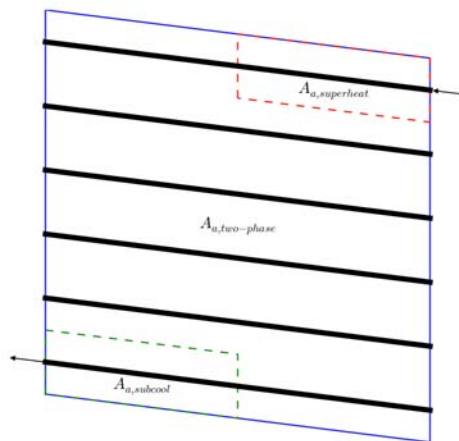


Figure A 2: Sections of Condenser (Bell, 2012)

When the condenser model was initially developed, the case that the two-phase section ends exactly at the outlet of the evaporator with quality 0 was not considered which lead convergence issues during the solving process. Therefore the code was modified to include this case. Additionally, a tuning factor for the two-phase region was included, to be able to obtain a better fit to the experimental data.

Evaporator

Two different evaporator models were used. A single circuit model was used for the cases with no maldistribution while a multi-circuit model was used for the cases with maldistribution.

Single Circuit Evaporator Model

The single-circuit moving boundary evaporator model is based on revision 70 of ACHP (Bell, 2011). The evaporator model consists of a two-phase, and, if it exists, a superheated section on the refrigerant side. In contrast to the condenser model, the possibility of moisture removal from the air has to be considered. Therefore ACHP includes a partially wet/dry analysis.

The evaporator model was modified such that it solves for the specific heat of the refrigerant in an iterative process, since the base version assumed a constant exit superheat of 6 K – which lead to deviations for exit superheats that were significantly higher. The 2-phase refrigerant side heat transfer of the evaporator was tuned as well.

Multi-Circuit Evaporator Model

The multi-circuit evaporator model is based on revision 70 of the multi-circuit evaporator model in ACHP (Bell, 2011). The multi-circuit evaporator model connects multiple single circuit evaporator instances (=circuits) in parallel. It distributes the number of tubes as well as refrigerant and airflow in between these instances. Based on distribution factors, the refrigerant and airside flowrates can be adjusted for the simulation of maldistribution. After the individual circuits are solved, the model calculates overall parameters, such as exit superheat and capacity.

The multi-circuit evaporator model was modified, such that that air inlet temperature, air inlet relative humidity, and number of tubes per bank can be distributed manually. These changes were done for the purpose of simulating the rooftop unit.

Return Line

The return line is modeled using the line set revision 70 of ACHP (Bell, 2011). The ACHP line-set calculates pressure drop and heat gains for gas and liquid lines. The pressure drop is calculated using the Darcy friction factor. The Line set was modified to bound the fluid density, since this previously lead to NaN results during the solving process. The bounds are only effective if the solver uses guess values that are far away from the solution, and therefore does not affect the results. To avoid issues with convergence due to possible flashing in the liquid line during the solving process, the liquid line was not considered in the model.

Compressor

The compressor model in ACHP uses a polynomial compressor map defined in AHRI Standard 540 (2004), of which the coefficients were obtained from the compressor manufacturers product selection software. The results from the compressor map are corrected for suction density and enthalpy based on the methodology described by Rice et al. (1981).

Tuning of model

The model was tuned using component level tuning as described subsequently for each of the components.

Compressor

The compressor model was tuned using the experimental data from all steady-state tests, including the blocked-coil cases. The tuning factors were found using a least squares method. Figure A 3 shows the results for the mass flowrate and Figure A 4 shows the results for the power consumption. The tuning factors are 0.918 for mass flowrate and 1.026 for the power consumption.

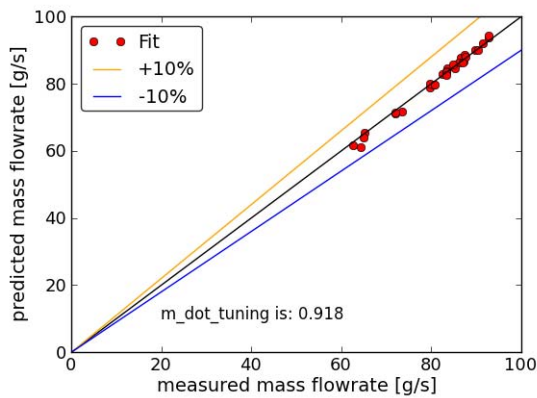


Figure A 3: Predicted and Measured Mass Flow Rate

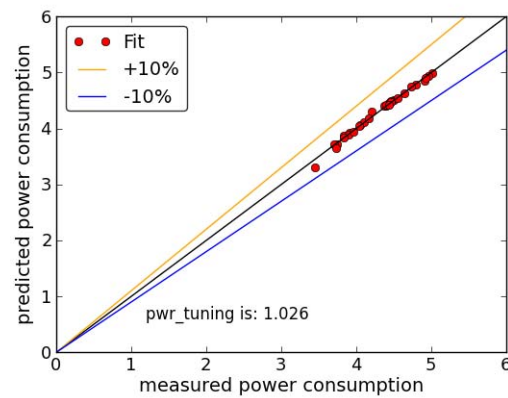


Figure A 4: Predicted and Measured Power Consumption

Evaporator

The evaporator in the experimental setup showed significant maldistribution in the original TXV as well as the EXV configuration. Therefore the resulting data is not suitable for tuning the Evaporator, especially since flowrates in individual circuits were not known. In the hybrid control system, the surface usage of the individual circuits is more uniform, therefore this data was used for the comparison.

One unmeasured variable is the air leakage around the evaporator trough the drain pan, Figure A 5. The air outlet temperature was not measured directly behind the coil, but on the fan grille further downstream. As a result of the occurring mixing of the leakage air and main airflow

through the coil, the outlet temperature of the coil cannot be determined. Therefore it is impossible to determine the tuning factor for the air flowrate numerically. The tuning factor was therefore assumed, and later on varied to determine its effect on the simulated performance improvement. An additional tuning factor was used for the 2-phase section in the evaporator, while the superheated section remained untuned.

For the comparison of measured and predicted capacity, the simulation was fed with the experimental pressure and temperature measurements. The Evaporator model was then wrapped to solve for the mass flowrate that results in identical superheat. Figure A 6 shows the results; the deviation between measured and predicted refrigerant side evaporator capacity is well within 10%.

Figure A 7 shows that the predicted evaporator outlet temperature is lower than the experimentally measured one, which is mainly a result of the influence of the air leakage around the evaporator in the experimental measurement, and therefore an increase is noticeable if evaporator capacity increases. Table A 19 shows the employed tuning constants.

Single circuit and multi-circuit evaporator are based on the same approach, therefore the results should be identical. To ensure that this is actually the case, both evaporators were calculated for the experimental data and compared against each other. Figure A 8 shows, that the resulting error is less than 0.014 mW, and therefore negligible compared to the calculated capacity. The multi-circuit evaporator therefore works properly.

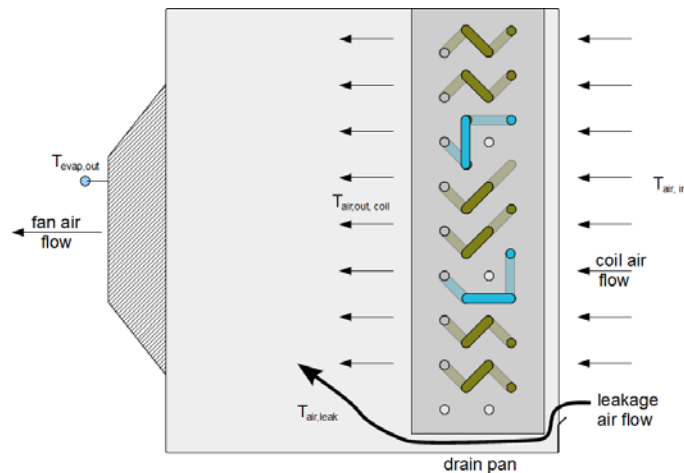


Figure A 5: Evaporator Coil Cross-Section (Cross-Counter Flow)

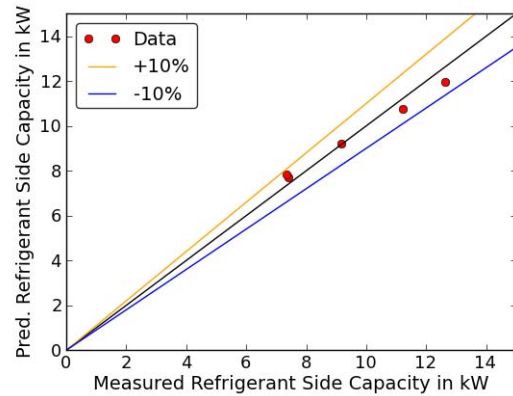


Figure A 6: Predicted Versus Measured Refrigerant Side Capacity

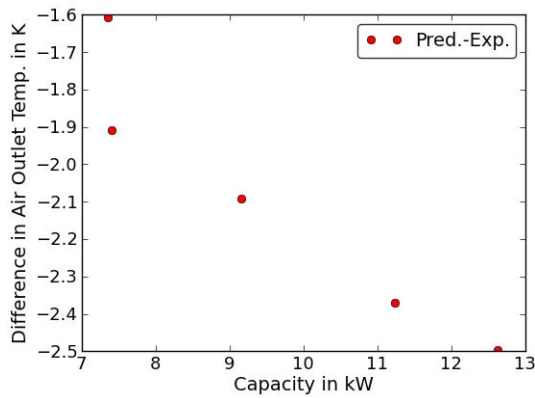


Figure A 7: Error in Air-Outlet Temperature

Table A 19: Tuning Constants for Evaporator

Air flowrate	0.67
2-Phase heat transfer coefficient	0.7

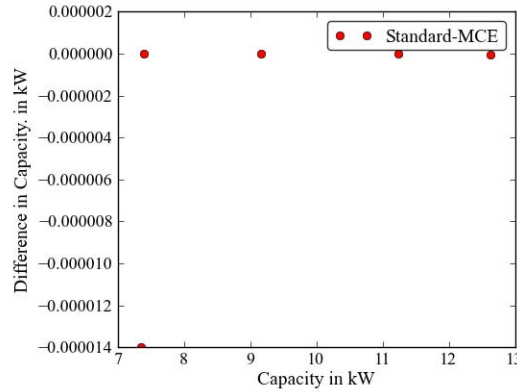


Figure A 8: Capacity Error Between Multi-Circuit Evaporator and Standard Evaporator

Condenser

For the tuning of the condenser, all available experimental data was taken. This was done to obtain better estimates for the tuning factors for the 2-phase and superheated heat transfer rate as well as for the condenser fan volumetric displacement. For the comparison of measured and predicted capacity, the simulation was fed with the experimental pressure and temperature measurements. Figure A 9 and Figure A 10 show the predicted versus measured mass flowrate and capacity, respectively. Most points are within a deviation of 20%. Figure A 11 shows the evaporator air outlet temperature, which is within a range of $\pm 1.6^{\circ}\text{C}$ for most points. The EXV operating point at 2°C ambient temperature was removed from the data, since the condenser fan was not running continuously for that point. The tuning constants for the condenser are shown in Table A 20.

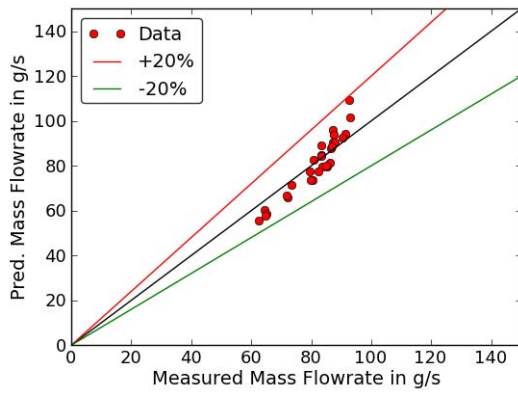


Figure A 9: Predicted Versus Measured Condenser Mass Flowrate

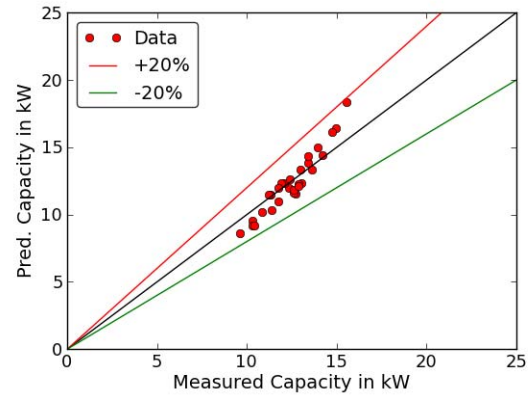


Figure A 10: Predicted Versus Measured Condenser Capacity

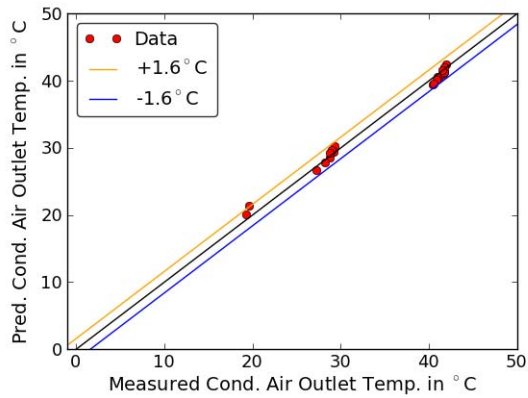


Figure A 11: Predicted Versus Measured Condenser Air Outlet Temperature

Table A 20: Tuning Constants and Empirical Values, Condenser

Air flowrate (m^3/s)	1.625
Air-side heat transfer coefficient	0.65
2-Phase heat transfer coefficient	0.9
Single phase heat transfer coefficient (superheated)	1.4

Return Line

For the tuning of the return line, the heat transfer coefficient to the ambient and the line-length were considered. The entire experimental dataset was considered for the tuning. Table A 21 shows the resulting line length and heat transfer coefficient. Fittings and service valve were not considered as separate pressure drops. Therefore the resulting line length is nearly twice as long as in the experiment.

Table A 21: : Tuned Parameters for Return Line

	simulation (experiment)
Return line length	12 m (6.38m)
Heat transfer coefficient	35 W/m ² K (N/A)

Figure A 12 shows the predicted versus measured pressure drop. Most of the data is within 20% deviation from each other. Figure A 13 shows the predicted versus measured temperature increase in the suction line. Most of the data is within a range of 1.6 K.

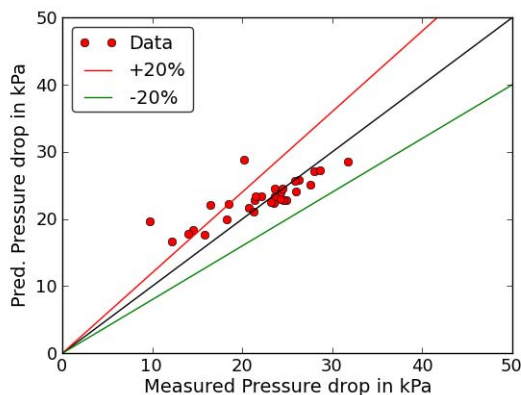


Figure A 12: Predicted Versus Measured Pressure Drop in Return Line²⁶

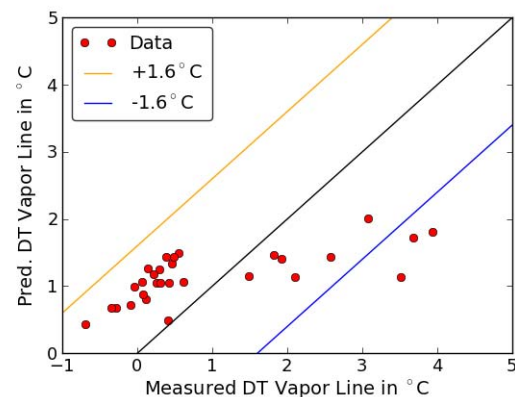


Figure A 13: Predicted Versus Measured Temperature Increase

²⁶ The expected error for the pressure drop is 3.2 kPa for the experimental setup.

Model Validation

From the experimental results, it became obvious that there is no- or negligible airside maldistribution. Figure A 14 shows, as a repetition, the mass flowrates trough each individual circuit using each balancing valve as a virtual mass flow sensor. To obtain the flowrate, a 8 PI group correlation was employed as described in Bach et al. (2012a). For the hybrid control concept, large differences between the predicted mass flowrates were visible. When the primary valve was fully opened to avoid quality maldistribution, the predicted mass flowrates where within 3 times the predicted measurement uncertainty from each other. The large differences are therefore mainly a result of quality maldistribution at the distributor, which lead to different balancing valve inlet qualities in the hybrid control case. As a result, the differences in coil surface usage, as indicated for the EXV control scheme in Figure A 15, are mainly a result of quality maldistribution at the distributor. In the experiments it became also obvious, that this quality maldistribution changes with operating conditions, as indicated in Bach et. al. (2012b). Since this dependence was arbitrary, the EXV case was not chosen as basecase for the simulation studies. Instead, the hybrid control case was chosen as basecase, since the refrigerant side surface usage was equal within the measurement tolerance accross different circuits. The purpose of the experimental study was to show the maximum benefit that is achievable without having to employ individual circuit flow control. In the simulation study we are not limited to the specific type of distributor that was used in the setup. Therefore we employed a distributor having the type 4 characteristic of Li et al. (2005) as a maximum performance EXV case.

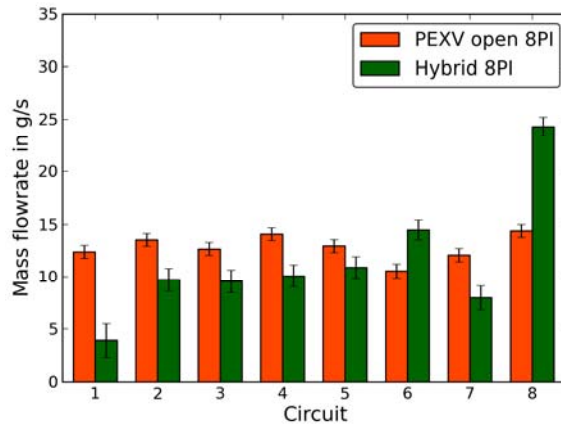


Figure A 14: Mass Flowrates Trough Individual Circuits, 46°C Ambient Temperature (Bach et al. 2012a)

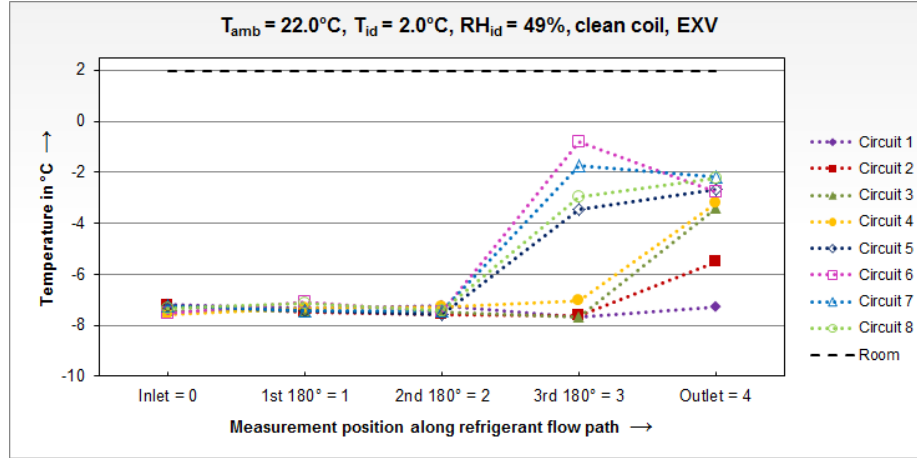


Figure A 15: Return-Bend Temperatures (Bach et al. 2012b)

For the simulation of the hybrid control scheme, it is assumed that refrigerant side and air side have no maldistribution, since no significant maldistribution was found, as described above. Therefore the standard ACHP evaporator was used for the computations, which was validated to result in the same simulation results as the multi-circuit evaporator, as shown in Figure A 8 on page 193. Figure A 16 to Figure A 19 show the relative difference between experimental and simulation results.. The differences are based on equation (22); the numerical values of these are shown in Table A 22 along with the numerical difference as defined by equation (23).

$$rel = \frac{\text{Value of simulation} - \text{Value of experiment}}{\text{Value of Experiment}} \quad (22)$$

$$dif = \text{Value of simulation} - \text{Value of experiment} \quad (23)$$

Figure A 16 shows that COSP is predicted within 2.6% of the experimental data and the capacity is predicted within 1% of the experimental value. Figure A 17 shows that the inlet and outlet pressure are predicted within 0.8% and 5.3% respectively. The compressor power consumption is predicted within 2.4%. Cycle and compressor validation results show only a small trend with temperature. The air-on temperature difference, as defined in equation (24) and the air temperature raise of the condenser, as defined in equation (25) are shown in Figure A 18. The trend and deviation of the air-on temperature difference and the air temperature rise are within 12% and 5% respectively. For the evaporator, the air temperature drop is defined by equation (26) while equation (24) is used for the air-on temperature difference. Figure A 19 shows that the air-on temperature difference is predicted within 8.1%. The air temperature drop is over-predicted by up to nearly 70%. The reason for this over-prediction is, that in the experiment, a mixed air temperature with value between leakage air temperature and coil exit temperature, rather than the coil exit temperature was measured as shown in Figure A 5. To get a better estimate of the actual air temperature drop, it was assumed that the evaporator fan air flowrate is identical with the rated flowrate. Therefore the leakage flowrate is the rated flowrate

multiplied by a tuning factor for the evaporator (from Table A 19). It was assumed that ideal mixing of leaked and actual coil flowrate occurs with constant specific heat of the air. In that case, the simulated air temperature decrease is smaller than the experimental one by a maximum of 21%. This bias is expected, since the air outlet temperature measurement of the evaporator was in the upper part of the fan guard and thus the measurement was biased towards the exit temperature of the coil, see Figure A 5, page 192.

$$TD_{air,on} = abs(T_{dew} - T_{air,in}) \quad (24)$$

$$TD_{air,raise} = T_{cond-air,out} - T_{cond-air,in} \quad (25)$$

$$TD_{air,drop} = T_{evap-air,in} - T_{evap-air,out} \quad (26)$$

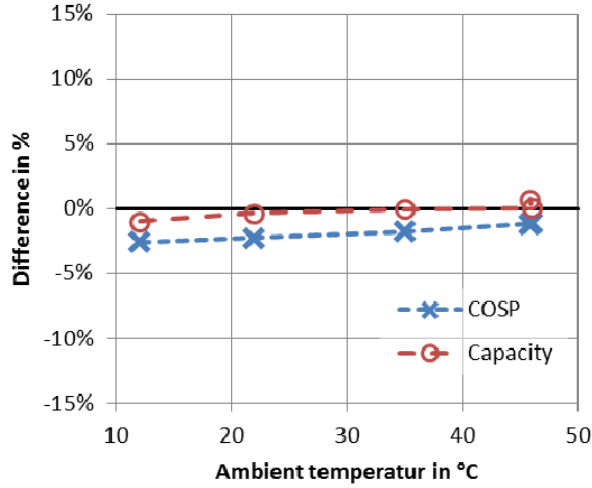


Figure A 16: Cycle Capacity and COSP

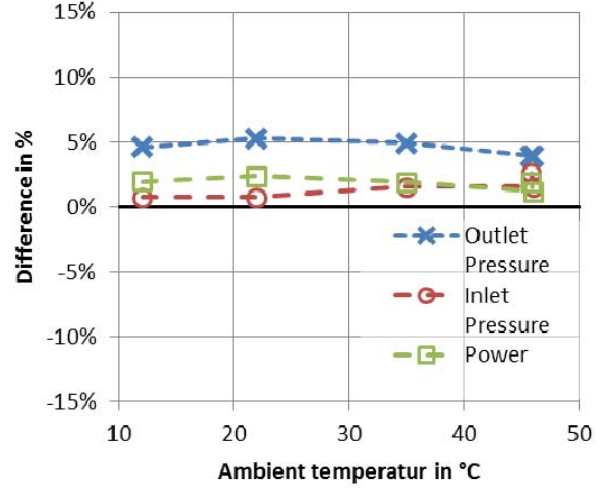


Figure A 17: Compressor Power, Inlet, and Outlet Pressure

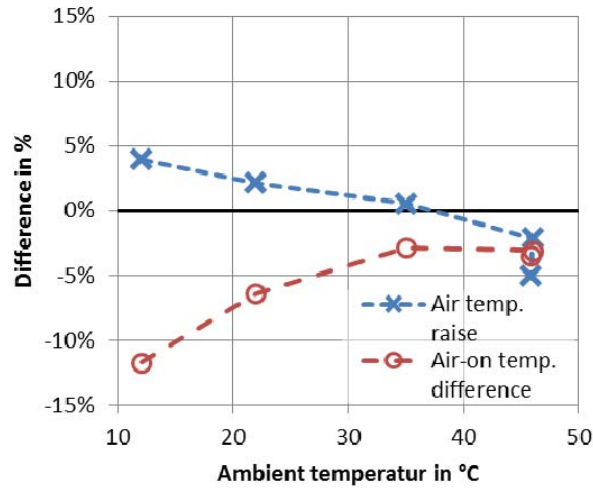


Figure A 18: Condenser Air-on Temperature Difference and Air Temperature Raise

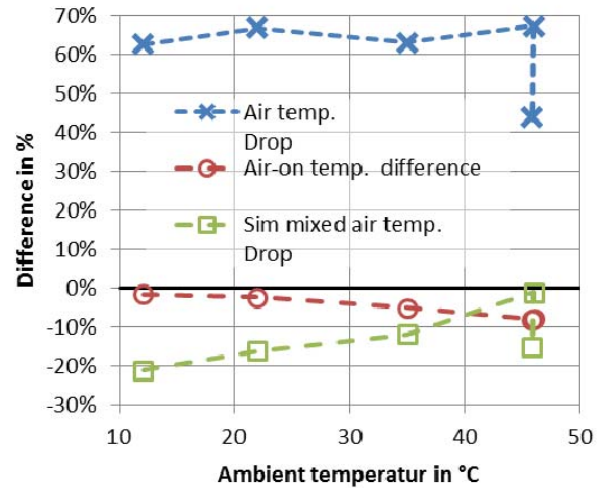


Figure A 19: Evaporator Air-On Temperature Difference and Air Temperature Drop

Table A 22: Deviations Between Experimental and Simulation Values

	Cycle		Compressor					Condenser		Evaporator		
	Capacity	COSP	Power	Outlet Pressure	Inlet Pressure	Outlet Pressure	Inlet Pressure	Air-on temp. difference	Air temp. raise	Air-on temp. difference	Air temp. Drop	Sim mixed air temp. Drop
T_amb/method	rel	rel	rel	dif [kPa]	dif [kPa]	rel	rel	rel	rel	rel	rel	rel
12.1	-1.0%	-2.6%	2.0%	60	3	4.6%	0.7%	-11.7%	4.0%	-1.6%	62.6%	-21.2%
22.0	-0.3%	-2.3%	2.4%	85	3	5.3%	0.7%	-6.4%	2.1%	-2.4%	66.7%	-16.1%
35.0	0.0%	-1.7%	1.9%	103	7	4.9%	1.6%	-2.8%	0.6%	-5.1%	63.0%	-11.8%
46.0	0.1%	-1.1%	1.2%	102	8	3.9%	1.6%	-3.1%	-2.1%	-8.0%	67.3%	-1.1%
45.8	0.7%	-1.2%	1.9%	100	13	3.9%	2.6%	-3.5%	-5.0%	-8.1%	43.9%	-15.0%
min	-1.0%	-2.6%	1.2%	60	3	3.9%	0.7%	-11.7%	-5.0%	-8.1%	43.9%	-21.2%
max	0.7%	-1.1%	2.4%	103	13	5.3%	2.6%	-2.8%	4.0%	-1.6%	67.3%	-1.1%
mean	-0.1%	-1.8%	1.9%	90	7	4.5%	1.4%	-5.5%	-0.1%	-5.0%	60.7%	-13.0%

Simulation of Airside Maldistribution

In the experimental tests, airside maldistribution was created using two different means:

- airflow blockage at the coil inlet, and
- frost build-up.

Airflow blockage was used during the experiments to simulate uneven frost build-up more repeatable and time efficient.

Frost build-up itself is dependent on various parameters, such as fin temperature, dew point of inlet air and air flowrate. Since fin temperature and airflow rate change with increasing frost build-up, frost build-up, once started, often speeds up during the ongoing operation of the system. This was also noticeable during the experiments, where the evaporation temperature decreased quicker towards the end of the experiments. For conciseness, frost build up will not be considered during the system simulation, but it should be pointed out, that frost build-up is subject of in-depth research, as well. Gong et. al (2012), for example, developed a correlation to predict frost accumulation on domestic heat pumps.

Airside Maldistribution Caused by Defined Blockage

Description of Modeling Approach

For clean-coil conditions, most of the air flow passes through the coil itself, while part of the airflow passes through the leakage gap between coil and drain pan, as shown in Figure A 20. According to the previously shown tuning results, the airflow that passes through the coil is about 2/3 of the total airflow. Thus, the leakage is about 1/3 of the airflow. Frost build-up initially does not influence the performance of the system significantly, since increased area due to ice crystals along with increased air velocity due to a reduction in flow area and the insulating effects of frost compensate for each other. At some point, however, frost build-up starts decreasing the performance. In the experiments, one major factor was that frost build-up occurred unevenly, as shown in Figure A 21. This leads to a significant reduction of air flowrate of some parts of the coil, resulting in significant airside maldistribution and a reduction of the overall air flowrate through the coil. The level of blockage for the airside blocked cases in the experiments was determined using experimental results of the EXV system frost build-up experiment. Two different levels of frost build-up were used to simulate these effects, see Bach et al. (2012b). Figure A 22 shows what happens when the case B blockage is applied: a larger part of the flow passes through the lower part of the coil and the drain pan while the flowrate to the upper parts is reduced.

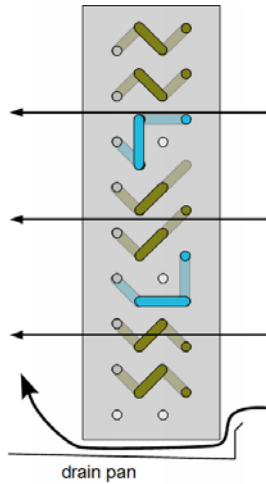


Figure A 20: Clean-Coil Airflow



Figure A 21: Airflow Blockage Due to Frost Built-Up on Coil

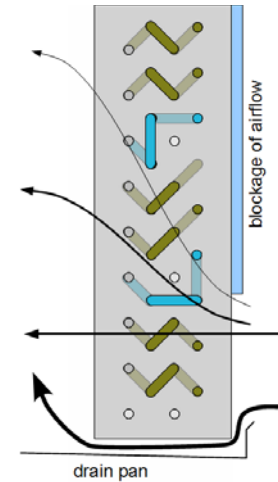


Figure A 22: Case B Blockage of Airflow to Simulate Frost Built-Up

For the simulation of the blocked-coil, the air flowrates through specific circuits of the coil were estimated. This was necessary, since it is practically impossible to measure an effective circuit air flowrate in the evaporator. Therefore the refrigerant side mass flow distribution was used as estimate for the airside flow distribution. The refrigerant side mass flow distribution was obtained by using the EXV-balancing valves as virtual mass flow sensors. Figure A 23 shows the measured circuit mass flowrates. For the hybrid control scheme, quality maldistribution was observed to have the potential to influence the usefulness of the EXV as mass flow sensor. Therefore additional tests were taken with primary expansion valve (PEXV) fully open. Both test results show a similar distribution, where the results agree within the limits of their uncertainties. A un-weighted average of the two measurements was used for the simulation of the blocked-coil cases.

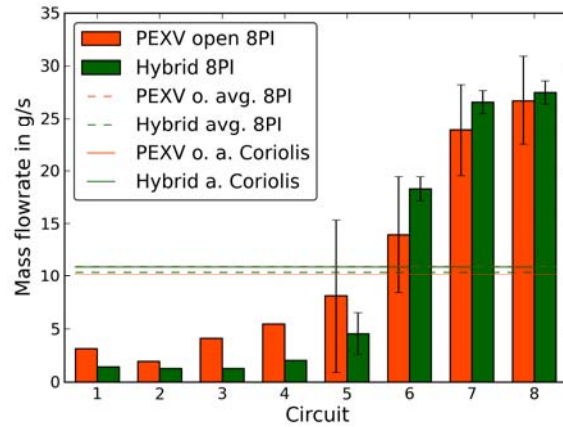


Figure A 23: Measured Average and Predicted Flowrates, Large Room Cooling System for 2°C Room Temperature and 46°C Ambient Temperature²⁷

The evaporator fan power consumption changes with level of blockage, as shown in Figure A 24. In the simulation, the evaporator fan power consumption was therefore updated to the value of the case B blockage.

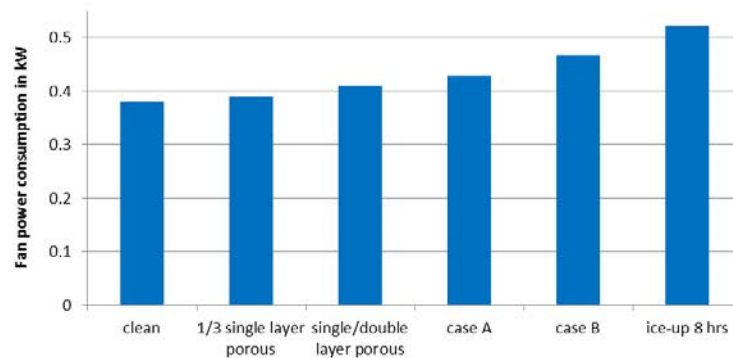


Figure A 24: Fan Power Consumption for Different Levels of Coil Blockage²⁸

During the experiments, the air flowrate through the evaporator coil was not measured. To estimate the air flowrate, simulations were therefore performed at multiple levels of airflow restriction in order to determine the effective air flowrate. An air flowrate of 80% of the one used for the clean-coil conditions lead to results which are comparable to the ones obtained from the experiment. Figure A 25 shows a comparison for the experimental results, with hybrid control as baseline. After the case B-blockage (2/3 of coil blocked) was applied the COP decreased by approximately 10% with a small trend in temperature. For the EXV control case, a

²⁷ Error bars based on measurement accuracy, PI_i RMS of correlation, and valve opening position accuracy of ± 2 steps for PEXV open for unblocked coil, else ± 20 steps accuracy.

²⁸ More detailed description of the different levels of blockage is available in Bach et al. (2012b).

much stronger trend with temperature seems to occur, especially if the 22°C ambient temperature case is considered. Figure A 26 shows the COP a comparison for the simulation results. The “no maldistribution” case is similar to the unblocked hybrid control in the experiment. The “COP optimized” case optimizes the refrigerant flow distribution to obtain the maximum system COP. It was found that, with the model used, the result is nearly identical to using equal circuit exit superheat. While this is disappointing from a simulation point of view, it is encouraging from a practical perspective, since it is essentially impossible to optimize the flow to 8 circuits given the noise in the individual temperature measurements, including power consumption and capacity estimation. The equal flow case assumes equal refrigerant side and airside flow distribution factors. The result is very similar to the COP optimized case, while the computing time is significantly shorter: the refrigerant flow distribution factors do not need to be found. The “uncompensated” case assumes no compensation for the airside maldistribution at all. The result is somewhat similar to the experimental EXV. However, in case of the EXV, refrigerant side maldistribution occurred simultaneously.

Figure A 27 and Figure A 28 show the results for the capacity, which are, with exemption of the point at 22°C ambient temperature, similar to the results for COP.

Figure A 29 and Figure A 30 show the residuals of the change in COP and capacity, respectively. This change residual is defined analogous to equation (23) as the difference of capacity change obtained by the simulation and the one observed in the experiment. For almost all values, simulation and experiment agree within 5%.

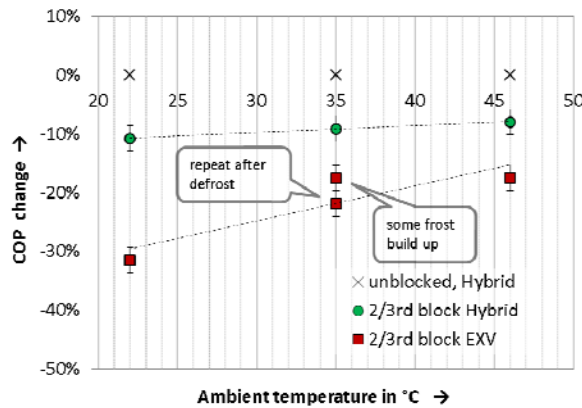


Figure A 25: COP Degradation with Case B Blockage (EXP)

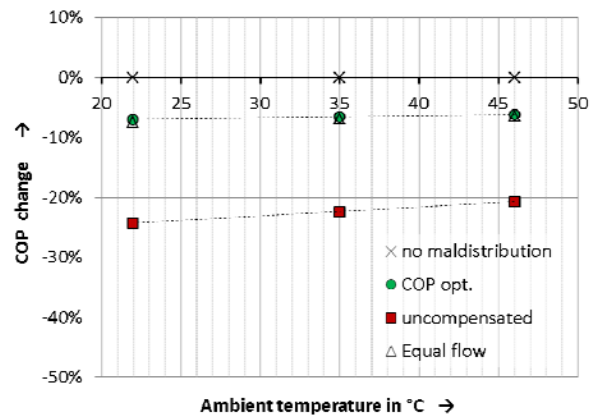


Figure A 26: COP Degradation with Case B Blockage (SIM)

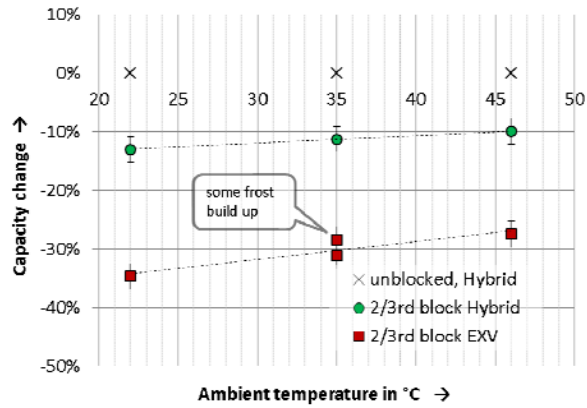


Figure A 27: Capacity Degradation With Blockage (EXP)

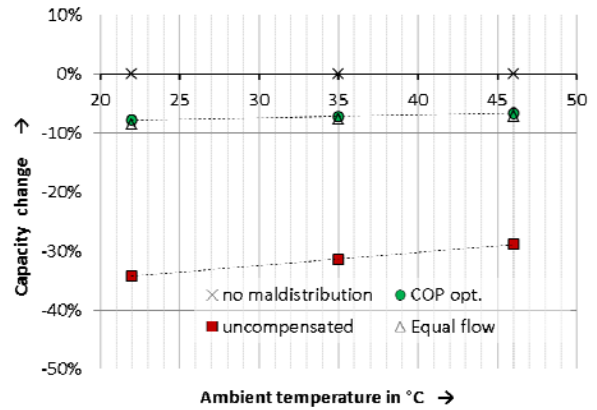


Figure A 28: Capacity Degradation with Blockage (SIM)

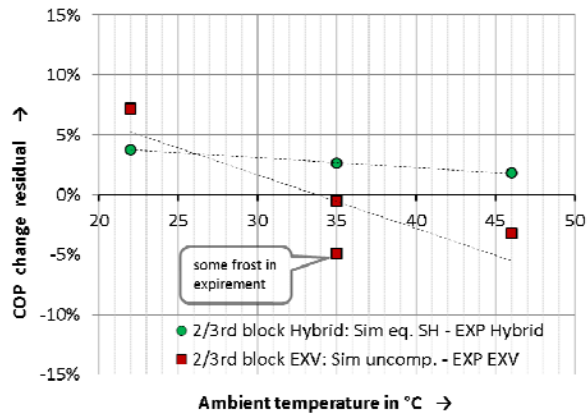


Figure A 29: COP Change Residual

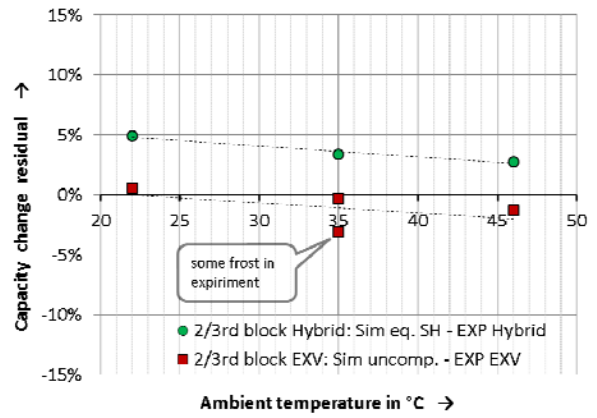


Figure A 30: Capacity Change Residual

APPENDIX B: Domestic Heat Pump

Test Plan

Table B 1 shows the test plan for the domestic heat pump. additional tests were taken with partial air inlet grille blockage as outlined in the report.

Table B 1: Test Plan for Domestic Heat Pump

Test Description** [Number of tests]	Air Entering Indoor Unit Temperature				Air Entering Outdoor Unit Temperature				Test Objective
	Dry-Bulb		Wet-Bulb		Dry-Bulb		Wet-Bulb		
	°F	°C	°F	°C	°F	°C	°F	°C	
H1 Test (required, steady) [3]	70.0	21.1	≤ 60	≤ 15.6	47.0	8.33	43.0	6.11	Determine net heating capacity, input power, and COP at moderate outdoor conditions
H1* Test (required, steady) [3]	70.0	21.1	≤ 60	≤ 15.6	47.0	8.33	45.6(1)	7.5(1)	Determine effect of ice build up
H1C Test (optional, cyclic) [3]	70.0	21.1	≤ 60	≤ 15.6	47.0	8.33	43.0	6.11	Determine cyclic performance of the different control schemes under above conditions
H3 Test (required, steady) [2]	70.0	21.1	≤ 60	≤ 15.6	17.0	-8.33	15.0	-9.44	Determine net heating capacity, input power, and COP at moderately cold outdoor conditions
H4* Test (required, steady) [2]	70.0	21.1	≤ 60	≤ 15.6	-10(2)	-23.33(2)	-11(2)	-23.89(2)	Determine net heating capacity, input power, and COP at cold outdoor conditions

* Not specified in ANSI/AHRI Standard 210/240.

** Each test is done separately with EXV only and hybrid control scheme.

Tests H1*, H1 and H1C additionally with inbuilt expansion device.

(1) Equivalent to 90% relative humidity; for the steady state measurement, the wet bulb temperature is changed to the one of test H1.

(2) Only if unit can operate under those conditions, otherwise minimum possible outdoor temperature.

Data Tables

System-Level Results

Table B 2: EXV System-Level Test Data

Test	H1	H1-repeat	H3	H4*	H1	H3 - a	H3 - b	H4*
Modification	clean coil	clean coil	clean coil	clean coil	blocked 44%	blocked 50%	blocked 44%	blocked 50%
Air-side: Temperatures								
Outdoor Unit, in	8.3 °C	8.3 °C	-8.3 °C	-20.0 °C	9.2 °C	-7.8 °C	-8.3 °C	-20.0 °C
Outdoor Unit, out	3.7 °C	3.7 °C	-11.1 °C	-21.6 °C	5.4 °C	-10.5 °C	-10.9 °C	-21.6 °C
Indoor Unit, in	21.1 °C	21.1 °C	21.2 °C	21.1 °C	21.0 °C	21.1 °C	21.1 °C	21.1 °C
Indoor Unit, out	39.7 °C	39.7 °C	33.4 °C	29.4 °C	35.5 °C	31.3 °C	31.5 °C	28.6 °C
Air side: Humidity								
Outdoor Unit, in, RH	14%	14%	14%	15%	15%	14%	16%	13%
Outdoor Unit, in, DP	-8.2 °C	-7.3 °C	-14.5 °C	-21.7 °C	-3.2 °C	-13.1 °C	-13.4 °C	-21.9 °C
Indoor Unit, in, RH	28%	28%	58%	65%	38%	55%	56%	64%
Indoor Unit, in, DP	1.7 °C	1.8 °C	12.6 °C	14.2 °C	6.2 °C	11.7 °C	11.8 °C	14.1 °C
Air side: Flow Rate								
Indoor, m³/s	0.795 m³/s	0.795 m³/s	0.792 m³/s	0.787 m³/s	0.791 m³/s	0.787 m³/s	0.791 m³/s	0.786 m³/s
Refrigerant side: Cycle								
Compressor in, P	791 kPa	788 kPa	500 kPa	345 kPa	578 kPa	413 kPa	423 kPa	311 kPa
Compressor in, T	2.1 °C	2.1 °C	-12.4 °C	-20.1 °C	-4.0 °C	-15.1 °C	-16.0 °C	-23.6 °C
Compressor out, P	2513 kPa	2515 kPa	2145 kPa	1915 kPa	2282 kPa	2032 kPa	2045 kPa	1860 kPa
Compressor out, T	72.4 °C	73.2 °C	80.6 °C	100.5 °C	79.1 °C	93.1 °C	89.8 °C	108.5 °C
Condenser out, P	2442 kPa	2445 kPa	2095 kPa	1874 kPa	2240 kPa	2000 kPa	2013 kPa	1829 kPa
Condenser out, T	37.5 °C	37.2 °C	30.0 °C	26.6 °C	30.3 °C	26.8 °C	27.0 °C	26.3 °C
After TXV, P	2410 kPa	2413 kPa	2086 kPa	1875 kPa	2224 kPa	1993 kPa	2006 kPa	1827 kPa
After TXV, T	37.3 °C	37.0 °C	29.7 °C	26.6 °C	29.7 °C	26.6 °C	26.7 °C	26.5 °C
EXV in, P	2369 kPa	2372 kPa	2097 kPa	1908 kPa	2208 kPa	2007 kPa	2017 kPa	1855 kPa
EXV in, T	36.4 °C	36.0 °C	27.9 °C	23.0 °C	28.9 °C	24.3 °C	24.6 °C	22.2 °C
EXV average, steps	297.5/500	297.0/500	143.8/500	83.7/500	169.5/500	107.3/500	111.8/500	76.4/500
Evaporator in, T	6.2 °C	6.2 °C	-8.8 °C	-19.8 °C	-0.3 °C	-12.2 °C	-12.2 °C	-21.2 °C
Evaporator out, P	808 kPa	805 kPa	513 kPa	357 kPa	592 kPa	424 kPa	435 kPa	322 kPa
Evaporator out, T	3.2 °C	3.6 °C	-10.2 °C	-17.6 °C	-6.0 °C	-12.1 °C	-13.0 °C	-20.2 °C
Evaporator out, SH	1.7 K	2.5 K	0.7 K	2.8 K	3.0 K	3.3 K	1.7 K	1.9 K
Refrigerant flow	78.8 g/s	78.2 g/s	46.7 g/s	28.8 g/s	55.4 g/s	36.4 g/s	37.8 g/s	25.3 g/s
Power Consumption, Capacity, COP								
Evaporator Fan	0.286 kW	0.287 kW	0.296 kW	0.307 kW	0.308 kW	0.325 kW	0.319 kW	0.340 kW
Condenser Fan	0.384 kW	0.382 kW	0.382 kW	0.377 kW	0.379 kW	0.381 kW	0.383 kW	0.378 kW
Crankcase Heater	0.00 kW	0.00 kW	0.00 kW	0.00 kW	0.00 kW	0.00 kW	0.00 kW	0.00 kW
Compressor + Trafo	3.62 kW	3.62 kW	3.15 kW	2.86 kW	3.34 kW	3.02 kW	3.03 kW	2.79 kW
Heating (w fan)	16.30 kW	16.29 kW	10.85 kW	7.41 kW	12.70 kW	9.15 kW	9.36 kW	6.71 kW
Heating (w fan, airside)	16.48 kW	16.46 kW	11.02 kW	7.53 kW	12.89 kW	9.22 kW	9.44 kW	6.79 kW
COP	3.80	3.80	2.83	2.09	3.15	2.46	2.51	1.91

Note:

- > Condenser and evaporator names given for HP-mode.
- > The TXV in the ID-unit has a bypass valve for HP mode.

Table B 3: Hybrid System-Level Test Data

Test	H1	H1-PEXV	H3	H4	H1	H1-PEXV	H3	H4*
Modification	clean coil	PEXV open	clean coil	clean coil	blocked 44%	blocked 44 %	blocked 50%	blocked 50%
Air-side: Temperatures								
Outdoor Unit, in	8.3 °C	8.3 °C	-8.3 °C	-20.0 °C	8.4 °C	8.4 °C	-8.2 °C	-20.0 °C
Outdoor Unit, out	-2.9 °C	-2.3 °C	-13.4 °C	-21.0 °C	-2.3 °C	-2.4 °C	-13.9 °C	-21.1 °C
Indoor Unit, in	21.1 °C	21.1 °C	21.2 °C	21.1 °C	21.1 °C	21.1 °C	21.1 °C	21.1 °C
Indoor Unit, out	39.7 °C	39.7 °C	33.4 °C	29.5 °C	38.9 °C	38.9 °C	32.8 °C	28.7 °C
Air side: Humidity								
Outdoor Unit, in, RH	23%	24%	25%	35%	24%	24%	23%	37%
Outdoor Unit, in, DP	-2.9 °C	-2.3 °C	-13.4 °C	-21.0 °C	-2.3 °C	-2.4 °C	-13.9 °C	-21.1 °C
Indoor Unit, in, RH	42%	44%	64%	67%	44%	44%	60%	67%
Indoor Unit, in, DP	0.4 °C	1.2 °C	1.6 °C	6.0 °C	1.2 °C	1.0 °C	0.7 °C	6.9 °C
Air side: Flow Rate								
Indoor, m³/s	0.793 m³/s	0.793 m³/s	0.793 m³/s	0.790 m³/s	0.793 m³/s	0.792 m³/s	0.788 m³/s	0.790 m³/s
Refrigerant side: Cycle								
Compressor in, P	806 kPa	811 kPa	508 kPa	352 kPa	760 kPa	758 kPa	479 kPa	322 kPa
Compressor in, T	4.2 °C	4.2 °C	-9.4 °C	-18.0 °C	2.0 °C	2.5 °C	-9.5 °C	-18.0 °C
Compressor out, P	2505 kPa	2504 kPa	2126 kPa	1911 kPa	2453 kPa	2453 kPa	2090 kPa	1864 kPa
Compressor out, T	72.3 °C	71.7 °C	79.5 °C	96.0 °C	72.8 °C	73.4 °C	83.9 °C	105.8 °C
Condenser out, P	2431 kPa	2428 kPa	2075 kPa	1865 kPa	2391 kPa	2392 kPa	2051 kPa	1832 kPa
Condenser out, T	38.1 °C	38.7 °C	30.8 °C	27.5 °C	36.7 °C	36.4 °C	29.5 °C	26.3 °C
After TXV, P	2398 kPa	2394 kPa	2069 kPa	1866 kPa	2362 kPa	2364 kPa	2045 kPa	1834 kPa
After TXV, T	38.1 °C	38.7 °C	30.7 °C	27.5 °C	36.5 °C	36.2 °C	29.2 °C	26.3 °C
EXV in, P	2356 kPa	2350 kPa	2077 kPa	1894 kPa	2326 kPa	2328 kPa	2055 kPa	1862 kPa
EXV in, T	37.2 °C	37.8 °C	28.9 °C	24.4 °C	35.6 °C	35.3 °C	27.4 °C	22.9 °C
EXV average, steps	361.0/500	500.0/500	138.7/500	76.6/500	369.8/500	499.0/500	135.3/500	80.3/500
Evaporator in, T	6.4 °C	6.4 °C	-8.4 °C	-19.5 °C	7.5 °C	7.3 °C	-7.8 °C	-19.3 °C
Evaporator out, P	822 kPa	827 kPa	521 kPa	363 kPa	775 kPa	773 kPa	491 kPa	332 kPa
Evaporator out, T	4.2 °C	4.2 °C	-10.4 °C	-20.5 °C	2.5 °C	3.0 °C	-10.6 °C	-20.5 °C
Evaporator out, SH	3.2 K	3.0 K	2.3 K	2.0 K	3.4 K	4.0 K	4.4 K	4.3 K
Refrigerant flow	80.0 g/s	80.7 g/s	47.6 g/s	30.3 g/s	75.1 g/s	74.7 g/s	44.1 g/s	26.6 g/s
Power Consumption, Capacity, COP								
Evaporator Fan	0.287 kW	0.286 kW	0.299 kW	0.310 kW	0.306 kW	0.306 kW	0.317 kW	0.327 kW
Condenser Fan	0.386 kW	0.384 kW	0.389 kW	0.387 kW	0.387 kW	0.386 kW	0.390 kW	0.385 kW
Crankcase Heater	0.00 kW	0.00 kW	0.00 kW	0.00 kW	0.00 kW	0.00 kW	0.00 kW	0.00 kW
Compressor + Trafo	3.59 kW	3.58 kW	3.12 kW	2.84 kW	3.54 kW	3.54 kW	3.08 kW	2.80 kW
Heating (w fan)	16.47 kW	16.47 kW	10.99 kW	7.62 kW	15.79 kW	15.79 kW	10.51 kW	6.99 kW
Heating (w fan, airside)	16.67 kW	16.68 kW	11.15 kW	7.73 kW	16.04 kW	16.01 kW	10.67 kW	7.00 kW
COP	3.86	3.87	2.88	2.15	3.73	3.73	2.77	1.99

Note:

- > Condenser and evaporator names given for HP-mode.
- > The TXV in the ID-unit has a bypass valve for HP mode.

Return-Bend Temperatures and Balancing Valve Openings

Circuit numbering is in according to main part of report. Circuits C to G have 1 return-bend less, therefore their exit is the 8th return-bend. Note that the pressure drop within the circuits along with conduction leads to significant measurement error for the return-bends, as outlined in main part of the report. Exit temperature sensors are placed farther away from the exit to reduce this problem.

Table B 4: EXV Clean-Coil Test Return-Bend Temperatures

H1, EXV, outdoor T: 8.3°C, indoor T: 21.1°C

	Inlet = 0	3rd 180° = 1	4th 180° = 2	5th 180° = 4	6rd 180° = 4	7rd 180° = 5	8rd 180° = 6	9rd 180° = 7	outlet=8
Circuit A	6.2 °C	4.8 °C	4.5 °C	3.9 °C	3.9 °C	3.1 °C	3.3 °C	4.6 °C	5.5 °C
Circuit B	6.2 °C	4.6 °C	5.0 °C	3.9 °C	4.2 °C	4.2 °C	5.2 °C	5.0 °C	5.5 °C
Circuit C	6.2 °C	4.5 °C	4.2 °C	3.2 °C	2.7 °C	3.8 °C	4.6 °C		
Circuit D	6.2 °C	3.7 °C	3.7 °C	4.3 °C	4.7 °C	4.4 °C	4.5 °C		
Circuit E	6.2 °C	3.9 °C	3.8 °C	2.8 °C	2.8 °C	2.8 °C	4.4 °C		
Circuit F	6.2 °C	4.3 °C	3.9 °C	3.2 °C	2.7 °C	2.0 °C	3.7 °C		
Circuit G	6.2 °C	4.6 °C	4.3 °C	3.2 °C	2.9 °C	2.1 °C	1.3 °C		
Circuit H	6.2 °C	4.4 °C	4.0 °C	4.0 °C	5.8 °C	4.7 °C	5.0 °C	4.7 °C	4.7 °C
Circuit I	6.2 °C	4.7 °C	4.9 °C	3.9 °C	3.6 °C	3.1 °C	3.1 °C	4.5 °C	4.5 °C

H1, EXV, repeat, outdoor T: 8.3°C, indoor T: 21.1°C

	Inlet = 0	3rd 180° = 1	4th 180° = 2	5th 180° = 4	6rd 180° = 4	7rd 180° = 5	8rd 180° = 6	9rd 180° = 7	outlet=8
Circuit A	6.2 °C	4.7 °C	4.4 °C	3.7 °C	3.7 °C	3.0 °C	3.3 °C	4.6 °C	5.7 °C
Circuit B	6.2 °C	4.5 °C	4.9 °C	3.8 °C	4.3 °C	4.2 °C	5.3 °C	4.9 °C	5.6 °C
Circuit C	6.2 °C	4.4 °C	4.1 °C	3.1 °C	2.6 °C	4.1 °C	4.6 °C		
Circuit D	6.2 °C	3.6 °C	3.6 °C	4.4 °C	4.6 °C	4.4 °C	4.4 °C		
Circuit E	6.2 °C	3.8 °C	3.8 °C	2.7 °C	2.8 °C	2.9 °C	4.4 °C		
Circuit F	6.2 °C	4.2 °C	3.8 °C	3.0 °C	2.5 °C	1.9 °C	4.1 °C		
Circuit G	6.2 °C	4.6 °C	4.2 °C	3.1 °C	2.9 °C	2.0 °C	1.2 °C		
Circuit H	6.2 °C	4.3 °C	4.0 °C	5.0 °C	5.8 °C	4.8 °C	5.0 °C	4.9 °C	4.7 °C
Circuit I	6.2 °C	4.6 °C	4.8 °C	3.8 °C	3.5 °C	3.1 °C	3.8 °C	4.5 °C	4.6 °C

H3, EXV, outdoor T: -8.3°C, indoor T: 21.2°C

	Inlet = 0	3rd 180° = 1	4th 180° = 2	5th 180° = 4	6rd 180° = 4	7rd 180° = 5	8rd 180° = 6	9rd 180° = 7	outlet=8
Circuit A	-8.8 °C	-9.9 °C	-10.3 °C	-10.7 °C	-10.8 °C	-11.3 °C	-11.3 °C	-10.2 °C	-9.5 °C
Circuit B	-8.8 °C	-10.3 °C	-10.0 °C	-10.9 °C	-10.4 °C	-10.6 °C	-9.7 °C	-10.1 °C	-9.5 °C
Circuit C	-8.8 °C	-10.5 °C	-10.7 °C	-11.4 °C	-10.4 °C	-10.3 °C	-9.4 °C		
Circuit D	-8.8 °C	-11.1 °C	-9.4 °C	-10.4 °C	-9.6 °C	-10.4 °C	-10.2 °C		
Circuit E	-8.8 °C	-10.6 °C	-10.6 °C	-11.4 °C	-11.4 °C	-12.2 °C	-12.3 °C		
Circuit F	-8.8 °C	-10.8 °C	-11.1 °C	-11.5 °C	-10.4 °C	-10.6 °C	-10.5 °C		
Circuit G	-8.8 °C	-10.1 °C	-10.5 °C	-11.4 °C	-11.6 °C	-12.1 °C	-12.8 °C		
Circuit H	-8.8 °C	-10.7 °C	-10.6 °C	-9.2 °C	-9.2 °C	-9.9 °C	-9.8 °C	-10.2 °C	-10.4 °C
Circuit I	-8.8 °C	-10.0 °C	-9.8 °C	-10.5 °C	-10.8 °C	-11.3 °C	-11.5 °C	-12.2 °C	-11.1 °C

H4*, EXV, outdoor T: -20°C, indoor T: 21.1°C

	Inlet = 0	3rd 180° = 1	4th 180° = 2	5th 180° = 4	6rd 180° = 4	7rd 180° = 5	8rd 180° = 6	9rd 180° = 7	outlet=8
Circuit A	-19.8 °C	-20.8 °C	-21.1 °C	-21.3 °C	-21.5 °C	-21.8 °C	-21.7 °C	-20.9 °C	-20.2 °C
Circuit B	-19.8 °C	-21.3 °C	-20.9 °C	-20.9 °C	-20.2 °C	-20.9 °C	-20.5 °C	-20.9 °C	-20.4 °C
Circuit C	-19.8 °C	-21.0 °C	-21.1 °C	-21.9 °C	-21.9 °C	-21.0 °C	-20.2 °C		
Circuit D	-19.8 °C	-21.6 °C	-20.7 °C	-21.0 °C	-20.5 °C	-21.1 °C	-21.0 °C		
Circuit E	-19.8 °C	-21.7 °C	-21.7 °C	-22.2 °C	-21.7 °C	-21.2 °C	-20.6 °C		
Circuit F	-19.8 °C	-20.2 °C	-20.3 °C	-20.2 °C	-20.6 °C	-20.8 °C	-20.9 °C		
Circuit G	-19.8 °C	-21.5 °C	-20.1 °C	-21.0 °C	-20.8 °C	-20.6 °C	-20.5 °C		
Circuit H	-19.8 °C	-20.1 °C	-20.0 °C	-19.8 °C	-19.9 °C	-20.4 °C	-20.3 °C	-20.2 °C	-20.4 °C
Circuit I	-19.8 °C	-20.9 °C	-20.7 °C	-21.3 °C	-21.6 °C	-21.8 °C	-22.1 °C	-21.4 °C	-21.4 °C

Table B 5: EXV Blocked-Coil Test Return-Bend Temperatures

H1, EXV, Blocked 44%, outdoor T: 9.2°C, indoor T: 21°C

	Inlet = 0	3rd 180° = 1	4th 180° = 2	5th 180° = 4	6rd 180° = 4	7rd 180° = 5	8rd 180° = 6	9rd 180° = 7	outlet=8
Circuit A	-0.3 °C	8.3 °C	8.6 °C	7.7 °C	7.4 °C	6.7 °C	4.8 °C	5.4 °C	5.4 °C
Circuit B	-0.3 °C	8.5 °C	8.4 °C	9.2 °C	7.0 °C	9.0 °C	7.9 °C	8.5 °C	7.0 °C
Circuit C	-0.3 °C	9.3 °C	6.2 °C	9.3 °C	6.5 °C	8.8 °C	4.0 °C		
Circuit D	-0.3 °C	8.8 °C	5.1 °C	8.3 °C	5.5 °C	8.3 °C	4.2 °C		
Circuit E	-0.3 °C	6.3 °C	4.5 °C	7.4 °C	4.6 °C	5.1 °C	2.5 °C		
Circuit F	-0.3 °C	-3.9 °C	-5.2 °C	-5.1 °C	-6.5 °C	-5.9 °C	-1.7 °C		
Circuit G	-0.3 °C	-3.4 °C	-4.5 °C	-5.5 °C	-5.8 °C	-6.2 °C	-7.6 °C		
Circuit H	-0.3 °C	-4.1 °C	-4.9 °C	-3.4 °C	-2.0 °C	-4.0 °C	-2.5 °C	-3.2 °C	-3.7 °C
Circuit I	-0.3 °C	-4.1 °C	-3.3 °C	-4.4 °C	-4.2 °C	-3.3 °C	-3.6 °C	-2.9 °C	-4.1 °C

H3, EXV, Blocked 50%, outdoor T: -7.8°C, indoor T: 21.1°C

	Inlet = 0	3rd 180° = 1	4th 180° = 2	5th 180° = 4	6rd 180° = 4	7rd 180° = 5	8rd 180° = 6	9rd 180° = 7	outlet=8
Circuit A	-12.2 °C	-9.8 °C	-8.1 °C	-9.7 °C	-8.8 °C	-11.0 °C	-10.0 °C	-11.9 °C	-9.4 °C
Circuit B	-12.2 °C	-9.2 °C	-8.1 °C	-7.8 °C	-9.0 °C	-7.9 °C	-8.5 °C	-8.8 °C	-8.8 °C
Circuit C	-12.2 °C	-7.7 °C	-9.4 °C	-7.6 °C	-9.3 °C	-8.3 °C	-10.2 °C		
Circuit D	-12.2 °C	-8.2 °C	-9.9 °C	-8.8 °C	-9.8 °C	-8.6 °C	-10.7 °C		
Circuit E	-12.2 °C	-14.9 °C	-11.7 °C	-10.4 °C	-11.9 °C	-12.4 °C	-13.6 °C		
Circuit F	-12.2 °C	-15.6 °C	-16.3 °C	-16.1 °C	-17.1 °C	-16.3 °C	-15.2 °C		
Circuit G	-12.2 °C	-14.9 °C	-15.7 °C	-16.5 °C	-16.8 °C	-16.8 °C	-17.9 °C		
Circuit H	-12.2 °C	-12.7 °C	-12.5 °C	-11.9 °C	-13.0 °C	-14.6 °C	-13.4 °C	-13.3 °C	-14.3 °C
Circuit I	-12.2 °C	-14.8 °C	-14.6 °C	-15.0 °C	-15.8 °C	-14.8 °C	-14.9 °C	-13.9 °C	-14.9 °C

H3, EXV, Blocked 50%, outdoor T: -8.3°C, indoor T: 21.1°C

	Inlet = 0	3rd 180° = 1	4th 180° = 2	5th 180° = 4	6rd 180° = 4	7rd 180° = 5	8rd 180° = 6	9rd 180° = 7	outlet=8
Circuit A	-12.2 °C	-10.0 °C	-8.4 °C	-10.1 °C	-9.1 °C	-11.4 °C	-10.1 °C	-12.1 °C	-9.8 °C
Circuit B	-12.2 °C	-9.4 °C	-8.3 °C	-8.1 °C	-9.3 °C	-8.3 °C	-8.8 °C	-9.1 °C	-9.2 °C
Circuit C	-12.2 °C	-8.8 °C	-9.8 °C	-8.3 °C	-9.7 °C	-9.9 °C	-10.4 °C		
Circuit D	-12.2 °C	-9.0 °C	-10.2 °C	-10.1 °C	-10.2 °C	-9.2 °C	-11.1 °C		
Circuit E	-12.2 °C	-10.0 °C	-11.4 °C	-9.7 °C	-11.8 °C	-10.2 °C	-12.7 °C		
Circuit F	-12.2 °C	-15.1 °C	-15.8 °C	-15.4 °C	-15.0 °C	-13.4 °C	-13.5 °C		
Circuit G	-12.2 °C	-14.3 °C	-15.1 °C	-15.9 °C	-16.2 °C	-16.2 °C	-17.3 °C		
Circuit H	-12.2 °C	-13.4 °C	-12.2 °C	-12.3 °C	-12.6 °C	-14.4 °C	-13.1 °C	-13.5 °C	-14.0 °C
Circuit I	-12.2 °C	-14.3 °C	-14.2 °C	-14.6 °C	-15.4 °C	-15.1 °C	-15.9 °C	-14.6 °C	-15.1 °C

H4*, EXV, Blocked 50%, outdoor T: -20°C, indoor T: 21.1°C

	Inlet = 0	3rd 180° = 1	4th 180° = 2	5th 180° = 4	6rd 180° = 4	7rd 180° = 5	8rd 180° = 6	9rd 180° = 7	outlet=8
Circuit A	-21.2 °C	-20.4 °C	-20.4 °C	-20.3 °C	-21.3 °C	-20.9 °C	-21.6 °C	-21.4 °C	-21.3 °C
Circuit B	-21.2 °C	-20.2 °C	-19.9 °C	-19.3 °C	-20.0 °C	-19.4 °C	-20.2 °C	-20.0 °C	-21.3 °C
Circuit C	-21.2 °C	-19.7 °C	-20.3 °C	-19.4 °C	-20.6 °C	-20.5 °C	-20.9 °C		
Circuit D	-21.2 °C	-20.5 °C	-20.6 °C	-20.7 °C	-20.9 °C	-21.1 °C	-22.3 °C		
Circuit E	-21.2 °C	-23.9 °C	-24.5 °C	-24.4 °C	-24.8 °C	-24.4 °C	-24.3 °C		
Circuit F	-21.2 °C	-24.2 °C	-24.6 °C	-24.6 °C	-25.1 °C	-25.3 °C	-25.1 °C		
Circuit G	-21.2 °C	-23.9 °C	-24.3 °C	-25.1 °C	-25.1 °C	-24.9 °C	-24.7 °C		
Circuit H	-21.2 °C	-23.7 °C	-24.0 °C	-22.4 °C	-22.6 °C	-23.8 °C	-23.2 °C	-23.6 °C	-24.3 °C
Circuit I	-21.2 °C	-23.4 °C	-22.9 °C	-23.6 °C	-23.9 °C	-24.2 °C	-24.4 °C	-25.0 °C	-25.9 °C

Table B 6: Hybrid and PEXV Fully Open Clean-Coil Test Return-Bend Temperatures

H1, Hybrid, outdoor T: 8.3°C, indoor T: 21.1°C

	EXV pos.	Inlet = 0	3rd 180° = 1	4th 180° = 2	5th 180° = 4	6rd 180° = 4	7rd 180° = 5	8rd 180° = 6	9rd 180° = 7	outlet=8
Circuit A	301	6.4 °C	6.0 °C	5.6 °C	5.0 °C	4.8 °C	4.0 °C	3.8 °C	2.5 °C	4.2 °C
Circuit B	371	6.4 °C	6.1 °C	6.5 °C	5.4 °C	5.6 °C	4.0 °C	4.2 °C	2.5 °C	4.3 °C
Circuit C	285	6.4 °C	5.2 °C	5.2 °C	3.7 °C	3.5 °C	2.8 °C	4.5 °C		
Circuit D	249	6.4 °C	4.6 °C	4.5 °C	3.5 °C	4.2 °C	3.5 °C	4.7 °C		
Circuit E	104	6.4 °C	4.5 °C	4.5 °C	3.2 °C	3.6 °C	2.5 °C	4.5 °C		
Circuit F	111	6.4 °C	4.4 °C	4.4 °C	3.5 °C	3.2 °C	2.4 °C	4.4 °C		
Circuit G	112	6.4 °C	6.4 °C	7.1 °C	5.3 °C	6.1 °C	4.6 °C	4.6 °C		
Circuit H	292	6.4 °C	6.4 °C	6.0 °C	5.4 °C	4.9 °C	4.0 °C	4.5 °C	2.6 °C	4.2 °C
Circuit I	119	6.4 °C	6.3 °C	5.8 °C	5.2 °C	4.9 °C	4.2 °C	3.7 °C	2.8 °C	4.2 °C

H1-repeat, PEXV open, outdoor T: 8.3°C, indoor T: 21.1°C

	EXV pos.	Inlet = 0	3rd 180° = 1	4th 180° = 2	5th 180° = 4	6rd 180° = 4	7rd 180° = 5	8rd 180° = 6	9rd 180° = 7	outlet=8
Circuit A	241	6.4 °C	6.0 °C	5.6 °C	5.0 °C	4.8 °C	4.1 °C	3.8 °C	2.6 °C	4.3 °C
Circuit B	290	6.4 °C	6.1 °C	6.5 °C	5.4 °C	5.6 °C	4.0 °C	4.3 °C	2.7 °C	4.3 °C
Circuit C	241	6.4 °C	5.3 °C	5.3 °C	3.8 °C	3.7 °C	2.9 °C	4.3 °C		
Circuit D	227	6.4 °C	5.0 °C	4.8 °C	3.8 °C	4.2 °C	2.7 °C	4.3 °C		
Circuit E	93	6.4 °C	4.5 °C	4.6 °C	3.4 °C	3.7 °C	2.6 °C	4.4 °C		
Circuit F	102	6.4 °C	4.6 °C	4.5 °C	3.6 °C	3.4 °C	2.6 °C	4.5 °C		
Circuit G	150	6.4 °C	4.9 °C	5.2 °C	4.4 °C	5.0 °C	4.7 °C	4.7 °C		
Circuit H	207	6.4 °C	6.2 °C	5.8 °C	5.2 °C	4.7 °C	3.9 °C	4.4 °C	2.7 °C	4.4 °C
Circuit I	95	6.4 °C	6.1 °C	5.7 °C	5.1 °C	4.9 °C	4.2 °C	3.8 °C	2.9 °C	4.2 °C

H3, Hybrid, outdoor T: -8.3°C, indoor T: 21.2°C

	EXV pos.	Inlet = 0	3rd 180° = 1	4th 180° = 2	5th 180° = 4	6rd 180° = 4	7rd 180° = 5	8rd 180° = 6	9rd 180° = 7	outlet=8
Circuit A	347	-8.4 °C	-8.9 °C	-9.3 °C	-9.7 °C	-9.9 °C	-10.4 °C	-10.7 °C	-11.7 °C	-10.4 °C
Circuit B	402	-8.4 °C	-9.0 °C	-8.8 °C	-9.6 °C	-9.5 °C	-10.7 °C	-10.5 °C	-12.0 °C	-10.5 °C
Circuit C	276	-8.4 °C	-9.7 °C	-9.8 °C	-10.8 °C	-11.2 °C	-11.7 °C	-10.6 °C		
Circuit D	235	-8.4 °C	-10.2 °C	-10.2 °C	-11.1 °C	-10.7 °C	-11.9 °C	-10.4 °C		
Circuit E	91	-8.4 °C	-10.7 °C	-10.5 °C	-11.5 °C	-11.1 °C	-11.9 °C	-10.5 °C		
Circuit F	92	-8.4 °C	-10.4 °C	-10.5 °C	-11.1 °C	-11.3 °C	-11.9 °C	-10.4 °C		
Circuit G	119	-8.4 °C	-8.9 °C	-8.5 °C	-9.9 °C	-8.8 °C	-10.4 °C	-10.1 °C		
Circuit H	308	-8.4 °C	-8.7 °C	-9.0 °C	-9.4 °C	-9.8 °C	-10.6 °C	-10.3 °C	-11.6 °C	-10.3 °C
Circuit I	118	-8.4 °C	-8.8 °C	-9.2 °C	-9.5 °C	-10.0 °C	-10.4 °C	-10.8 °C	-11.5 °C	-10.3 °C

H4*, Hybrid, outdoor T: -20.0°C, indoor T: 21.1°C

	EXV pos.	Inlet = 0	3rd 180° = 1	4th 180° = 2	5th 180° = 4	6rd 180° = 4	7rd 180° = 5	8rd 180° = 6	9rd 180° = 7	outlet=8
Circuit A	377	-19.5 °C	-19.8 °C	-20.1 °C	-20.4 °C	-20.7 °C	-21.1 °C	-21.3 °C	-22.1 °C	-20.3 °C
Circuit B	398	-19.5 °C	-20.1 °C	-19.8 °C	-20.5 °C	-20.4 °C	-21.4 °C	-21.2 °C	-22.5 °C	-20.7 °C
Circuit C	356	-19.5 °C	-20.4 °C	-20.5 °C	-21.3 °C	-21.7 °C	-22.0 °C	-20.7 °C		
Circuit D	308	-19.5 °C	-20.6 °C	-20.8 °C	-21.5 °C	-21.2 °C	-22.2 °C	-20.7 °C		
Circuit E	128	-19.5 °C	-21.2 °C	-21.1 °C	-21.8 °C	-21.6 °C	-22.0 °C	-20.3 °C		
Circuit F	100	-19.5 °C	-20.2 °C	-20.3 °C	-20.2 °C	-20.6 °C	-20.8 °C	-20.4 °C		
Circuit G	120	-19.5 °C	-19.7 °C	-19.8 °C	-20.6 °C	-19.9 °C	-20.1 °C	-20.4 °C		
Circuit H	363	-19.5 °C	-19.8 °C	-20.2 °C	-20.4 °C	-20.7 °C	-21.3 °C	-21.1 °C	-22.1 °C	-20.7 °C
Circuit I	129	-19.5 °C	-19.8 °C	-20.2 °C	-20.4 °C	-20.9 °C	-21.0 °C	-21.4 °C	-21.3 °C	-20.3 °C

Table B 7: Hybrid and PEXV Fully Open Blocked-Coil Test Return-Bend Temperatures

H1, Hybrid, blocked 44%, outdoor T: 8.4°C, indoor T: 21.1°C

	EXV pos.	Inlet = 0	3rd 180° = 1	4th 180° = 2	5th 180° = 4	6rd 180° = 4	7rd 180° = 5	8rd 180° = 6	9rd 180° = 7	outlet=8
Circuit A	413	7.5 °C	6.4 °C	6.0 °C	5.0 °C	4.8 °C	3.8 °C	3.5 °C	1.7 °C	2.0 °C
Circuit B	451	7.5 °C	6.6 °C	6.6 °C	5.6 °C	5.4 °C	4.0 °C	3.6 °C	1.9 °C	1.9 °C
Circuit C	394	7.5 °C	5.6 °C	5.0 °C	3.9 °C	3.0 °C	2.3 °C	2.2 °C		
Circuit D	322	7.5 °C	5.2 °C	4.5 °C	3.6 °C	3.1 °C	1.6 °C	2.0 °C		
Circuit E	123	7.5 °C	4.5 °C	3.7 °C	2.8 °C	2.3 °C	1.3 °C	2.1 °C		
Circuit F	74	7.5 °C	2.0 °C	1.6 °C	1.2 °C	0.7 °C	0.3 °C	2.0 °C		
Circuit G	27	7.5 °C	4.3 °C	5.0 °C	3.3 °C	3.6 °C	2.6 °C	2.1 °C		
Circuit H	57	7.5 °C	1.1 °C	1.1 °C	3.0 °C	4.2 °C	3.5 °C	3.6 °C	2.8 °C	2.1 °C
Circuit I	29	7.5 °C	5.9 °C	6.6 °C	6.4 °C	5.4 °C	5.0 °C	3.7 °C	3.4 °C	2.2 °C

H1, PEXV open, blocked 44%, outdoor T: 8.4°C, indoor T: 21.1°C

	EXV pos.	Inlet = 0	3rd 180° = 1	4th 180° = 2	5th 180° = 4	6rd 180° = 4	7rd 180° = 5	8rd 180° = 6	9rd 180° = 7	outlet=8
Circuit A	290	7.3 °C	6.2 °C	5.9 °C	4.9 °C	4.7 °C	3.7 °C	3.4 °C	1.6 °C	2.4 °C
Circuit B	303	7.3 °C	6.5 °C	6.5 °C	5.5 °C	5.3 °C	3.9 °C	3.6 °C	1.8 °C	2.3 °C
Circuit C	283	7.3 °C	5.6 °C	5.0 °C	3.9 °C	3.0 °C	2.2 °C	2.5 °C		
Circuit D	234	7.3 °C	5.1 °C	4.5 °C	3.6 °C	3.1 °C	1.5 °C	2.5 °C		
Circuit E	103	7.3 °C	4.5 °C	3.7 °C	2.8 °C	2.3 °C	1.3 °C	2.4 °C		
Circuit F	67	7.3 °C	2.1 °C	1.7 °C	1.2 °C	0.7 °C	0.3 °C	2.4 °C		
Circuit G	26	7.3 °C	4.5 °C	5.1 °C	3.4 °C	3.7 °C	2.7 °C	2.3 °C		
Circuit H	54	7.3 °C	1.2 °C	1.1 °C	3.3 °C	4.4 °C	3.8 °C	3.8 °C	3.1 °C	2.3 °C
Circuit I	28	7.3 °C	7.0 °C	6.7 °C	7.2 °C	5.5 °C	5.8 °C	3.7 °C	4.0 °C	2.4 °C

H3, Hybrid, blocked 50%, outdoor T: -8.2°C, indoor T: 21.1°C

	EXV pos.	Inlet = 0	3rd 180° = 1	4th 180° = 2	5th 180° = 4	6rd 180° = 4	7rd 180° = 5	8rd 180° = 6	9rd 180° = 7	outlet=8
Circuit A	347	-7.8 °C	-8.8 °C	-9.2 °C	-9.8 °C	-10.1 °C	-10.8 °C	-11.1 °C	-12.6 °C	-11.2 °C
Circuit B	351	-7.8 °C	-8.8 °C	-8.8 °C	-9.6 °C	-9.8 °C	-10.9 °C	-11.2 °C	-12.7 °C	-11.4 °C
Circuit C	222	-7.8 °C	-9.6 °C	-10.1 °C	-10.9 °C	-11.8 °C	-12.4 °C	-10.9 °C		
Circuit D	229	-7.8 °C	-9.8 °C	-10.3 °C	-11.1 °C	-11.4 °C	-12.8 °C	-11.0 °C		
Circuit E	100	-7.8 °C	-10.4 °C	-10.9 °C	-11.7 °C	-12.1 °C	-12.9 °C	-11.5 °C		
Circuit F	62	-7.8 °C	-12.7 °C	-12.8 °C	-13.2 °C	-13.4 °C	-13.8 °C	-11.7 °C		
Circuit G	26	-7.8 °C	-10.9 °C	-9.9 °C	-11.6 °C	-10.7 °C	-11.8 °C	-11.6 °C		
Circuit H	54	-7.8 °C	-12.7 °C	-13.0 °C	-13.2 °C	-10.6 °C	-11.5 °C	-10.8 °C	-11.7 °C	-11.3 °C
Circuit I	25	-7.8 °C	-7.7 °C	-8.8 °C	-8.2 °C	-9.8 °C	-9.0 °C	-10.7 °C	-10.6 °C	-11.6 °C

H4*, Hybrid, blocked 50%, outdoor T: -20.0°C, indoor T: 21.1°C

	EXV pos.	Inlet = 0	3rd 180° = 1	4th 180° = 2	5th 180° = 4	6rd 180° = 4	7rd 180° = 5	8rd 180° = 6	9rd 180° = 7	outlet=8
Circuit A	126	-19.3 °C	-20.0 °C	-20.2 °C	-20.8 °C	-21.2 °C	-21.8 °C	-22.1 °C	-23.4 °C	-21.5 °C
Circuit B	197	-19.3 °C	-20.1 °C	-20.0 °C	-20.8 °C	-20.8 °C	-21.9 °C	-22.2 °C	-23.6 °C	-21.5 °C
Circuit C	150	-19.3 °C	-20.7 °C	-21.0 °C	-21.9 °C	-22.8 °C	-23.1 °C	-21.6 °C		
Circuit D	119	-19.3 °C	-21.2 °C	-21.4 °C	-22.4 °C	-22.5 °C	-23.3 °C	-21.7 °C		
Circuit E	48	-19.3 °C	-22.6 °C	-22.7 °C	-21.8 °C	-21.6 °C	-21.5 °C	-21.4 °C		
Circuit F	29	-19.3 °C	-20.7 °C	-20.5 °C	-20.8 °C	-21.2 °C	-21.4 °C	-21.6 °C		
Circuit G	19	-19.3 °C	-20.0 °C	-19.8 °C	-20.5 °C	-20.0 °C	-20.4 °C	-20.8 °C		
Circuit H	46	-19.3 °C	-21.4 °C	-20.7 °C	-20.3 °C	-20.0 °C	-20.3 °C	-20.3 °C	-20.8 °C	-20.9 °C
Circuit I	15	-19.3 °C	-18.8 °C	-19.2 °C	-19.3 °C	-19.9 °C	-19.9 °C	-20.4 °C	-20.8 °C	-21.1 °C

Two-Phase Section End

The end of the two-phase section was estimated based on the absolute value of the return-bend temperatures as well as their fluctuations as mentioned in main part of report.

Table B 8: : Estimated Two-Phase Section End, Clean-Coil, EXV

Circuit length	Circuit/Test Name	H1	H3 - a	H3 - b	H4*
10	A	8	9	10	9
10	B	5	3	6	1.5
8	C	6	7	5	7
8	D	4	5	4	5
8	E	6	7	8	7
8	F	7	8	6	8
8	G	3	8	8	8
10	H	3	5	4	5
10	I	9	8	10	8

Table B 9: Estimated Two-Phase Section End, Blocked-Coil, EXV

Circuit length	Circuit/Test Name	H1	H1-repeat	H3	H4*
10	A	2	2	2	2
10	B	2	2	2	2
8	C	2	2	2	2
8	D	2	2	2	2
8	E	6	7	3	2
8	F	8	7	5	8
8	G	7	8	8	8
10	H	5	3	3	5
10	I	10	7	8	6

Table B 10: Estimated Two-Phase Section End, Clean-Coil, Hybrid and PEXV Fully Open

Circuit length	Circuit/Test Name	H1	H1-PEXV	H3	H4
10	A	10	10	10	10
10	B	10	10	10	10
8	C	8	8	8	8
8	D	7	7	7	8
8	E	7	8	8	8
8	F	6	8	8	8
8	G	7	6	6	4
10	H	8	10	10	10
10	I	9	10	10	10

Table B 11: Estimated Two-Phase Section End, Blocked-Coil, Hybrid and PEXV Fully Open

Circuit length	Circuit/Test Name	H1	H1-PEXV	H3	H4*
10	A	10	10	10	10
10	B	10	10	10	10
8	C	8	8	8	8
8	D	7	8	8	8
8	E	5	8	8	8
8	F	8	8	8	8
8	G	8	8	8	4
10	H	3	6	6	5
10	I	2	10	3	2

Savings Estimate

Estimation of Installed Capacity

To estimate the installed heat pump capacity, the following assumptions were made:

1. Estimated heat pump lifetime is 12 Years.
2. For simplification purposes, calculate sum of units in operation as sum of installed units in USA over years 2001-2012. Since data for 2012 was not available at the time when the analysis was done, assume same number of new installations as in 2011.
3. Distribution of heat pump units in US is proportional to number of housing units, independent of climate.
4. Assume installed capacity to be 3-tons on average.
5. Calculate installed capacity in California as:

$$\text{Sum of units in USA} \cdot \frac{\text{Number of Housing units in California}}{\text{number of Housing units in USA}} \cdot 3 \text{ tons.}$$

Used sources for this analysis and their values are:

Item and value	Source
Number of housing units: USA: 132,312,404 California: 13,720,462	United States census Bureau (2012), National and State Housing Unit Estimates: 2010 to 2011, downloaded from http://www.census.gov/popest/data/housing/totals/2011/files/HU-EST2011.CSV

Item and value	Source
Heat pump unit sales data:	Air-Conditioning, Heating, and Refrigeration Institute (2012),
2001 1,442,355	Central Air Conditioners and Air-Source Heat Pumps Historical
2002 1,483,599	Data, downloaded from http://www.ahrinet.org/central+air+
2003 1,626,365	conditioners+and+air_source+heat+pumps+historical+data.aspx
2004 1,886,100	Note: For analysis, data of 2012 was assumed to be same as data of 2011.
2005 2,136,525	
2006 2,118,469	
2007 1,898,905	
2008 1,865,310	
2009 1,642,064	
2010 1,747,920	
2011 1,765,002	

Uncertainty Analysis

Code B 1 shows the EES code which used for uncertainty analysis for the domestic heat pump. The inbuilt uncertainty calculation method of EES (Klein, 2012), which neglects cross dependency was used. The confidence interval of the measured data was not evaluated. For the clean-coil cases, the actual measurement data was used to calculate the uncertainties, since they were in a similar order than the smallest performance improvement for that case. For the blocked-coil cases, the lowest capacity cases (-20°C ambient temperature) were used since this corresponds to the largest expected uncertainty. The resulting uncertainties are shown in Table B 12 and Table B 13.

Code B 1: Uncertainty Analysis for Heat Pump

```

"!Setup"
$UnitSystem SI MASS DEG kPa C kJ
"!Conditionals"
$IFNOT PARAMETRICTABLE
"EXV 21.0/-20C blocked"
m_dot=0.025347[kg/s]
W_dot_mess_comp=2.7924[kW]
W_dot_mess_fan_id=0.3775[kW]
W_dot_mess_fan_od=0.3398[kW]
P_id_in=1845.4[kPa]"PI4.1"
P_id_out=1828.6[kPa] "PI1.1"
T_id_in=84.049[C] "TI4.1"
T_id_out=26.312[C] "PI1.1"

"Hybrid 21.1/-20 C blocked"
m_dot_H=0.026588[kg/s]
W_dot_mess_comp_H=2.7968[kW]
W_dot_mess_fan_id_H=0.3854[kW]
W_dot_mess_fan_od_H=0.3266[kW]
P_id_in_H=1851.6[kPa] "PI4.1"
P_id_out_H=1831.5[kPa] "PI1.1"
T_id_in_H=82.862[C] "TI4.1"
T_id_out_H=26.303[C] "PI1.1"

```


\$ENDIF

R\$='R410a'

"!accuracy"

"Mass flow meter accuracy, Micromotion CMF025"

m_dot_hr=m_dot*convert(h,s)

Z_stability=0.027[kg/h]

Z_Limit=Z_stability/0.0005 "limit, when flowrate smaller than this value, accuracy = ±[(zero stability / flow rate) × 100]%"

"below quoted out/quote lines below out for calculation of table"

m_dot_acc=0.1[%]*convert(%,1) "accuracy for flowrate larger than Z_limit"

"Temperature sensors"

T_acc=0.5[C] "special limit of errors, TMQSS"

"Pressure transducers"

"R:\cec-share\00 Large Room Cooling System\Measurement Instrumentation\Pressure measurement"

"neglected temperature dependency, seemed negligible"

P_low_acc=250[PSI]*convert(PSI,kPa)*0.13[%]*convert(%,1) "accuracy for 250PSI transducers, Setra 207"

P_high_acc=500[PSI]*convert(PSI,kPa)*0.13[%]*convert(%,1) "accuracy for 250PSI transducers, Setra 207"

"Power Measurements, Exceltronic XL5C5A2-8-1 and Exceltronic XL5C5A2-1-8 "

W_dot_acc_comp=max(W_dot_mess_comp,W_dot_mess_comp_H)*0.002+0.0005[kW] "0.2% of reading and 0.01% of rated output"

W_dot_acc_fan_od= max(W_dot_mess_fan_od,W_dot_mess_fan_od_H)*0.002+0.0005[kW] "0.2% of reading and 0.01% of rated output"

W_dot_acc_fan_id=0.00388[kW] "absolute accuracy, determined with values from below"

"for determination of indoor fan power consumption"

U_fan=244.4[V]

I_fan=2.575[A]

PF_fan=W_fan/(U_fan*I_fan)

W_fan=324.3[W] "measured with outdoor fan power meter"

W_fan_later=PF_fan*U_fan_assume*I_fan_later

I_fan_later=3.05[A] "estimate"

U_fan_assume=244.4[V] "for measurements during test"

"with accuracies"

I_fan_acc=0.001 "from reading, assumption"

PF_fan_acc=0.05 "assumption"

U_acc=2[V] "change of line voltage due to different power consumers on grid"

U_Acc_ex505=0.005 "Extech 505 multimeter w 0.5% base accuracy"

I_Acc_ex505=0.005 "Extech 505 multimeter w 0.5% base accuracy"

"!Calculations"

"EXV"

h_id_in=Enthalpy(R\$,T=T_id_in,P=P_id_in)

h_id_out=min(Enthalpy(R\$,T=T_id_out,P=P_id_out),Enthalpy(R\$,X=0,P=P_id_out))

Q_dot=m_dot*(h_id_in-h_id_out)+W_dot_mess_fan_id

COP=Q_dot/(W_dot_mess_comp+W_dot_mess_fan_id+W_dot_mess_fan_od)

"Hybrid"

h_id_in_H=Enthalpy(R\$,T=T_id_in_H,P=P_id_in_H)

h_id_out_H=Enthalpy(R\$,T=T_id_out_H,P=P_id_out_H)

Q_dot_H=m_dot_H*(h_id_in_H-h_id_out_H)+W_dot_mess_fan_id_H

COP_H=Q_dot_H/(W_dot_mess_comp_H+W_dot_mess_fan_id_H+W_dot_mess_fan_od_H)

"Comparison"

"EXV-case is used as baseline for comparisons!"

Q_dot_diff=(Q_dot_H-Q_dot)/Q_dot

COP_diff=(COP_H-COP)/COP

Table B 12: Uncertainties for Clean-Coil Tests

COP	COP_{diff}	COP_H	Q_{dot}	Q_{dot,H}	Q_{dot,diff}	m_{dot}	m_{dot,H}	T_{id,in}
[-]	[-]	[-]	[kW]	[kW]	[-]	[kg/s]	[kg/s]	[kPa]
0.00441	0.00308	0.004505	0.00402	0.00412	0.000794	0.001	0.001	0.006259
0.00493	0.00249	0.004981	0.00455	0.00460	0.000599	0.001	0.001	0.007124
0.00573	0.00215	0.005773	0.00540	0.00544	0.000472	0.001	0.001	0.007415

T_{id,in,H}	T_{id,out}	T_{id,out,H}	W_{dot,mess,c} omp	W_{dot,mess,c} omp,H	W_{dot,mess,fa} n,id	W_{dot,mess,fa} n,i	W_{dot,mess,fa} n,od	W_{dot,mess,fa} n,od,H
[kPa]	[kPa]	[kPa]	[C]	[C]	[C]	[C]	[kW]	[kW]
0.006521	0.018804	0.0181	0.00217	0.00219	0.010286	0.010028	0.003643	0.003614
0.007183	0.016656	0.0162	0.00215	0.0021	0.010157	0.009977	0.003704	0.003674
0.007407	0.013333	0.0131	0.00213	0.0021	0.010094	0.010039	0.003751	0.003741

Table B 13: Uncertainties for Blocked-Coil Cases (Based on -20°C Ambient Temperature Case)

Q_{dot,diff}	COP_{diff}
0.000854	0.003285

APPENDIX C: Rooftop Unit

Test Plan

Table C 1 shows the test plan for the rooftop air conditioning unit.

Table C 1: Test Plan for Rooftop Air Conditioning Unit

Test Description** [Number of tests]	Air Entering Indoor Unit Temperature				Air Entering Outdoor Unit Temperature				Test Objective
	Dry-Bulb		Wet-Bulb		Dry-Bulb		Wet-Bulb		
	°F	°C	°F	°C	°F	°C	°F	°C	
A*-Test (steady, dry coil) [9] (required)	80.0	26.7	(1)	(1)	125(2)	51.67(2)	-	-	Determine influence of damper positions and indoor fan speed at desert outdoor conditions
C-Test (steady, dry coil) [9] (required)	80.0	26.7	(1)	(1)	82.0	27.8	-	-	Determine influence of damper positions and indoor fan speed at moderate outdoor conditions
D-Test (4) (cyclic, dry coil) [3] (optional)	80.0	26.7	(1)	(1)	82.0	27.8	-	-	Determine cyclic performance of the different control schemes under above conditions
E*-Test [9] (required)	80.0	26.7	(1)	(1)	50(3)	10(3)	-	-	Determine influence of damper positions and indoor fan speed at cold outdoor conditions

* Not specified in ANSI/AHRI Standard 210/240.

** Each test is done with damper position fully open, half open and fully closed as well as indoor fan speed low, medium and high. EXV only and hybrid control scheme are evaluated separately.

- (1) Indoor air temperature must be low enough to prevent formation of condensate on the coil, evaluated while using the inbuilt expansion valve.
- (2) Only if unit can operate under those conditions, otherwise maximum possible outdoor temperature.
- (3) Only if unit can operate under those conditions, otherwise minimum possible outdoor temperature.
- (4) Only evaluated at damper half open/indoor fan speed medium, additionally tested using the inbuilt expansion device.

Data Tables

Table C 2 shows the legend for Table C 3 to Table C 10. Further details on where measurements were taken can be found in the main part of the report.

Notes:

- Due an un-weighted average outdoor air measurement, and recirculation at the economizer, the airside capacity deviates from the refrigerant side capacity.
- Primary expansion device for both, hybrid and EXV control scheme is one Emerson EXL B1G valve. Balancing valves are of type Emerson EXM B0B.
- Valve openings are given in terms of virtual step position. To obtain the actual opening divide by 2, and then subtract the opening step number according to manufacturer data (primary valve) or Table C 11 for balancing valves.

Table C 2: Legend for Data Tables

auto	automatic operation using PI control
BXV[i]	Balancing valve [i]
CAT	condenser air (inlet) temperature
CFAT	Condenser fan air temperature (exit)
CFM	air flowrate
Dew	Dewpoint
dP	pressure difference
m	mass
man	manual operation
P_ra	Pressure difference return air to indoor
P_sa	Pressure difference supply air to ambient
PXV	Primary expansion valve
RAT	Return air temperature
SAT	Supply air temperature
Setp	set point
SFAT	Supply fan air temperature (inlet)
T	Temperature
T_pre_dist	Temperature before distributor after PEXV
V	Volume
W	work

Indices

ave	average
cond	condenser
db	drybulb
dis	discharge
dot	time derivative (e.g. flowrate)
evap_out_[i]	surface temperature measured on refrigerant tube of circuit [i] exit
fan	(supply) fan
mass, mf	mass flowmeter
nozzle	flow measurement nozzle box
oa	Outdoor air
pre_BXV3	at inlet of balancing valve 3
ra	Return air
row1...4	row wise average to evaporator, starting from top
rtu	inlet to exit of rooftop unit
sa	supply air
sat	saturated
suc	suction
txv	before expansion valve (=EXV for hybrid control)

Table C 3: Hybrid and PEXV Fully Open Data

Line	Mode 0=Hybrid, 1=PEXV fully open	Description (CAT-RAT-SF[Hz]-Damper)	Duration	CAT_ave	OAT_ave	RAT_ave	MAT_ave	MAT_row1	MAT_row2	MAT_row3	MAT_row4	SFAT_ave	SAT_ave	CFAT_ave	dP_fan	dP_rtu	P_sa	dP_nozzl	dP_cond	P_ra	Dew_sa C
			[min]	C	C	C	C	[C]	[C]	[C]	[C]	C	C	C	kPa	kPa	kPa	e kPa	kPa	kPa	
1		0 50F-80F-41.2SF-0Damp	47.1	10.0	8.8	26.1	22.8	20.5	22.1	24.0	24.6	5.9	6.7	15.9	0.14	0.0853	0.0061	0.0308	0.0305	0.1231	2.0
2		0 82F-80F-41.2SF-0Damp	70.7	27.8	28.2	26.6	26.7	26.8	26.5	26.6	26.8	10.7	11.7	34.1	0.15	0.0904	0.0061	0.0291	0.0299	0.1231	8.3
3		0 82F-80F-41.2SF-0Damp	61.5	27.8	28.2	26.7	26.7	26.8	26.5	26.6	26.7	10.8	11.8	34.1	0.15	0.0902	0.0061	0.0293	0.0300	0.1231	8.1
4		0 125F-80F-41.2SF-0Damp	45.5	51.5	50.2	26.7	30.5	33.8	31.1	29.0	28.3	18.0	19.4	58.1	0.14	0.0855	0.0061	0.0293	0.0290	0.1231	8.8
5		0 50F-80F-41.2SF-50Damp	31.5	10.1	10.0	26.6	18.5	11.4	15.0	22.5	25.1	3.7	4.3	15.5	0.15	0.0765	0.0849	0.0283	0.0306	0.0820	1.9
6		0 82F-80F-41.2SF-50Damp	23.2	27.7	26.5	26.7	26.5	26.3	26.2	26.6	26.8	10.9	11.6	34.0	0.15	0.0730	0.0798	0.0277	0.0298	0.0813	8.7
7		0 125F-80F-41.2SF-50Damp	40.8	51.5	48.3	26.6	36.6	45.9	40.6	31.3	28.5	21.3	22.1	58.9	0.14	0.0707	0.0780	0.0271	0.0288	0.0764	8.6
8		0 59F-80F-41.2SF-100Damp	37.3	15.1	16.0	26.7	17.6	19.0	16.4	15.4	19.7	2.8	3.4	20.1	0.16	0.0658	0.0934	0.0228	0.0305	0.0590	0.8
9		0 82F-80F-41.2SF-100Damp	33.0	27.7	26.8	26.6	26.6	26.4	26.4	26.7	26.8	10.2	10.8	33.8	0.16	0.0666	0.0921	0.0204	0.0296	0.0522	8.1
10		0 125F-80F-41.2SF-100Damp	40.4	51.5	42.9	27.1	40.0	37.3	40.3	42.0	40.4	21.9	22.6	58.8	0.15	0.0644	0.0888	0.0205	0.0288	0.0482	7.3
11		1 50F-80F-41.2SF-0Damp	36.6	10.0	8.8	26.1	22.8	20.5	22.2	24.0	24.6	5.9	6.7	15.9	0.14	0.0852	0.0061	0.0307	0.0305	0.1231	2.1
12		1 82F-80F-41.2SF-0Damp	32.6	27.9	28.1	26.7	26.7	26.8	26.5	26.6	26.7	10.8	11.9	34.2	0.15	0.0904	0.0061	0.0297	0.0300	0.1231	8.0
13		1 125F-80F-41.2SF-0Damp	42.1	51.5	50.1	26.7	30.5	33.7	31.1	29.0	28.3	18.0	19.3	58.1	0.14	0.0857	0.0061	0.0293	0.0290	0.1231	8.7
14		1 50F-80F-41.2SF-50Damp	41.2	10.3	10.1	26.7	18.6	11.5	15.1	22.6	25.1	3.7	4.4	15.7	0.15	0.0763	0.0845	0.0282	0.0305	0.0819	1.9
15		1 82F-80F-41.2SF-50Damp	46.1	27.8	26.8	26.6	26.5	26.6	26.4	26.5	26.7	11.1	11.7	34.1	0.15	0.0733	0.0815	0.0277	0.0297	0.0809	8.7
16		1 125F-80F-41.2SF-50Damp	41.1	51.6	48.4	26.6	36.6	46.0	40.6	31.3	28.5	21.3	22.1	58.9	0.14	0.0707	0.0780	0.0270	0.0287	0.0766	8.8
17		1 59F-80F-41.2SF-100Damp	39.0	15.1	16.1	26.7	17.7	19.0	16.4	15.5	19.7	2.8	3.4	20.1	0.16	0.0659	0.0930	0.0227	0.0305	0.0594	0.7
18		1 82F-80F-41.2SF-100Damp	37.8	27.7	26.8	26.6	26.6	26.4	26.3	26.7	26.8	10.2	10.8	33.9	0.16	0.0666	0.0930	0.0205	0.0296	0.0521	8.2
19		1 125F-80F-41.2SF-100Damp	38.8	51.5	42.7	27.1	39.8	37.1	40.1	41.9	40.2	21.9	22.6	58.8	0.15	0.0647	0.0895	0.0205	0.0288	0.0485	7.4

Table C 4: Hybrid and PEXV Fully Open Data, Continued 1

	Dew_ra		Dew_oa		T_dis		T_txv_in		T_mass_in		T_pre_BXV3		T_evap_		T_evap_		T_evap_		T_evap_		T_evap_		T_evap_		P_mf_in		P_cond_out		P_txv_in		P_suc kPa		P_dis kPa		m_dot_ref		V_dot_nozz		T_db_noz		m_dot_noz	
Line	C	C	T_suc C	C	T_cond in C	C	C	C	out 1 C	out 2 C	out 3 C	out 4 C	out 5 C	out 6 C	out 7 C	kPa (abs)	kPa (abs)	kPa (abs)	kPa (abs)	kPa (abs)	kPa (abs)	kPa (abs)	kPa (abs)	kPa (abs)	kPa (abs)	g/s	le m^3/s	zle C	zle kg/s													
1	2.3	1.9	9.2	35.2	9.0	9.3	9.2	6.6	9.5	9.4	9.4	9.4	9.4	9.4	9.4	1277	1290	1271	918	1350	53.8	0.58	10.5	0.70																		
2	9.0	9.9	13.7	59.3	27.6	27.8	27.7	18.5	14.2	14.4	14.2	14.3	14.2	14.3	14.3	2078	2087	2067	1049	2154	60.6	0.57	14.9	0.67																		
3	9.0	9.7	14.1	59.9	27.6	27.8	27.7	18.0	14.7	14.7	14.7	14.7	14.7	14.7	14.7	2082	2089	2069	1051	2156	60.6	0.57	14.9	0.68																		
4	9.7	9.4	21.0	95.8	52.5	52.6	52.6	35.2	22.0	22.1	22.0	22.0	22.0	22.0	22.0	3652	3664	3638	1293	3732	68.1	0.58	21.4	0.67																		
5	1.7	2.4	7.1	36.8	9.1	9.3	9.3	7.0	7.3	7.3	7.3	7.3	7.3	7.3	7.3	1275	1284	1268	845	1333	48.9	0.56	8.3	0.67																		
6	9.4	10.7	14.1	59.7	27.4	27.6	27.6	18.4	14.7	14.5	14.7	14.7	14.8	14.6	14.7	2074	2086	2066	1053	2153	60.7	0.55	14.6	0.65																		
7	9.4	9.7	24.2	91.1	52.6	52.7	52.8	45.4	25.7	25.7	25.7	25.7	25.7	25.7	25.7	3702	3724	3687	1414	3811	78.7	0.55	23.7	0.64																		
8	0.7	0.6	6.1	44.5	14.0	14.2	14.1	6.9	6.5	6.5	6.5	6.5	6.5	6.5	6.5	1449	1453	1441	822	1499	46.8	0.49	7.7	0.59																		
9	8.6	10.6	12.8	60.1	27.5	27.6	27.6	17.7	13.3	13.3	13.4	13.4	13.6	13.3	13.4	2069	2081	2063	1024	2144	58.8	0.46	14.3	0.55																		
10	7.7	8.1	24.2	90.3	52.6	52.7	52.7	41.6	25.4	25.4	25.4	25.4	25.4	25.4	25.4	3691	3715	3677	1429	3804	79.9	0.47	24.2	0.54																		
11	2.4	1.9	9.9	35.9	9.0	9.3	9.2	9.6	10.1	10.1	10.1	10.1	10.1	10.1	10.1	1280	1292	1274	916	1351	53.5	0.58	10.5	0.70																		
12	8.8	9.8	14.0	59.4	27.7	27.8	27.8	28.2	14.5	14.5	14.5	14.5	14.5	14.5	14.5	2075	2089	2067	1052	2155	61.0	0.57	15.0	0.69																		
13	9.7	9.4	21.3	96.1	52.4	52.5	52.5	52.9	22.3	22.3	22.3	22.3	22.3	22.3	22.3	3647	3660	3633	1294	3727	67.8	0.58	21.4	0.67																		
14	1.9	2.4	7.0	36.9	9.2	9.4	9.3	9.7	7.3	7.2	7.2	7.2	7.2	7.2	7.3	1279	1288	1273	845	1337	49.0	0.55	8.3	0.67																		
15	9.5	10.8	13.8	58.9	27.6	27.7	27.7	28.1	14.3	14.4	14.4	14.4	14.4	14.4	14.4	2073	2087	2064	1056	2154	61.4	0.55	14.8	0.66																		
16	9.5	10.1	23.8	90.5	52.7	52.8	52.8	53.1	25.5	25.5	25.5	25.5	25.5	25.5	25.5	3702	3724	3686	1412	3812	79.3	0.55	23.7	0.64																		
17	0.6	0.5	6.4	44.9	14.0	14.2	14.1	14.5	6.8	6.7	6.8	6.8	6.8	6.7	6.7	1451	1454	1442	822	1501	46.7	0.49	7.7	0.59																		
18	8.5	10.5	13.5	60.7	27.4	27.6	27.6	27.9	14.1	13.9	13.6	13.7	14.1	14.2	13.7	2067	2079	2061	1022	2142	58.4	0.46	14.2	0.55																		
19	7.7	8.3	24.3	90.5	52.7	52.8	52.8	53.1	25.4	25.4	25.4	25.4	25.4	25.4	25.4	3689	3713	3675	1425	3801	79.6	0.47	24.1	0.54																		

Table C 5: Hybrid and PEXV Fully Open Data, Continued 2

	CFM_nozz	CFM_ra		m_dot_ra	W_dot_cf	W_dot_co	W_dot_tot	W_dot_ref	W_dot_air	Nozzle
Line	lb CFM	m³/3/s	T ra C	kg/s	kW	mp kW	kW	kW	kW	box fan Hz
1	1236	1064	26.4	0.53	0.265	0.99	1.80	11.51	11.36	48.4
2	1202	1043	26.7	0.52	0.252	1.73	2.49	11.22	10.85	46.3
3	1208	1042	26.6	0.52	0.253	1.73	2.56	11.25	10.90	46.3
4	1220	1031	26.3	0.52	0.234	3.28	4.02	9.62	8.12	47.0
5	1176	792	26.9	0.40	0.267	1.02	1.85	10.45	9.48	41.0
6	1165	793	26.9	0.41	0.252	1.73	2.49	11.28	10.68	41.0
7	1174	775	26.3	0.40	0.235	3.27	3.99	11.15	9.89	41.0
8	1035	696	26.8	0.36	0.264	1.20	1.96	9.62	8.30	35.1
9	981	662	26.6	0.34	0.251	1.73	2.46	10.88	9.41	32.8
10	991	642	26.6	0.34	0.236	3.25	3.95	11.29	9.75	33.3
11	1236	1062	26.4	0.53	0.265	0.99	1.80	11.48	11.32	48.4
12	1212	1060	26.6	0.54	0.256	1.72	2.49	11.31	10.92	46.8
13	1221	1032	26.3	0.52	0.234	3.26	4.00	9.62	8.14	47.0
14	1173	790	26.9	0.40	0.267	1.02	1.85	10.45	9.51	41.0
15	1164	796	26.7	0.41	0.254	1.72	2.48	11.37	10.78	41.0
16	1171	776	26.3	0.40	0.236	3.27	4.00	11.20	9.93	41.0
17	1034	697	26.8	0.36	0.264	1.20	1.97	9.61	8.32	35.1
18	982	660	26.6	0.34	0.251	1.73	2.46	10.86	9.34	32.8
19	993	644	26.6	0.34	0.236	3.24	3.95	11.25	9.68	33.3

Table C 6: Hybrid and PEXV Fully Open Data, Continued 3

	Setp									PEXV	BXV1	BXV2	BXV3	BXV4	BXV5	BXV6	BXV7				
	PXV1	BXV1	BXV2	BXV3	BXV4	BXV5	BXV6	BXV7	[1=man - 0=auto]	[1=man - 0=auto]	[1=man - 0=auto]	[1=man - 0=auto]	[1=man - 0=auto]	[1=man - 0=auto]	[1=man - 0=auto]	[1=man - 0=auto]	[1=man - 0=auto]	T_pre	T_Comp	T_Comp	Fan+parasitic
Line	[virtual	[steps]	[steps]	[steps]	[steps]	[steps]	[steps]	[steps]										dist C	In Sat	Out Sat	power kW
1	556	477	721	484	482	883	841	554	0.00	0.00	0.00	0.00	0.00	0.00	0.00	0.00	0.00	8.4	4.5	17.6	0.51
2	389	656	802	505	485	785	682	477	0.00	0.00	0.00	0.00	0.00	0.00	0.00	0.00	0.00	20.2	8.9	35.3	0.51
3	397	646	902	545	480	784	712	487	0.00	0.00	0.00	0.00	0.00	0.00	0.00	0.00	0.00	19.7	8.9	35.3	0.51
4	325	890	898	538	460	576	491	466	0.00	0.00	0.00	0.00	0.00	0.00	0.00	0.00	0.00	35.8	16.1	58.8	0.51
5	503	167	224	293	375	792	683	692	0.00	0.00	0.00	0.00	0.00	0.00	0.00	0.00	0.00	8.4	1.8	17.2	0.50
6	393	540	709	494	535	913	677	531	0.00	0.00	0.00	0.00	0.00	0.00	0.00	0.00	0.00	20.0	9.0	35.3	0.50
7	430	843	769	558	407	372	293	183	0.00	0.00	0.00	0.00	0.00	0.00	0.00	0.00	0.00	45.4	19.3	59.7	0.50
8	385	351	641	302	299	661	896	789	0.00	0.00	0.00	0.00	0.00	0.00	0.00	0.00	0.00	9.0	0.9	21.4	0.47
9	380	410	577	442	472	999	854	681	0.00	0.00	0.00	0.00	0.00	0.00	0.00	0.00	0.00	19.3	8.1	35.1	0.47
10	418	438	442	411	474	887	847	610	0.00	0.00	0.00	0.00	0.00	0.00	0.00	0.00	0.00	41.9	19.6	59.6	0.47
11	1000	223	297	236	247	333	347	247	1.00	0.00	0.00	0.00	0.00	0.00	0.00	0.00	0.00	10.9	4.4	17.6	0.51
12	1000	197	217	183	179	216	230	181	1.00	0.00	0.00	0.00	0.00	0.00	0.00	0.00	0.00	28.7	9.0	35.3	0.51
13	1000	220	208	156	160	175	166	159	1.00	0.00	0.00	0.00	0.00	0.00	0.00	0.00	0.00	52.3	16.1	58.7	0.51
14	1000	112	144	172	215	331	315	301	1.00	0.00	0.00	0.00	0.00	0.00	0.00	0.00	0.00	11.0	1.8	17.3	0.50
15	1000	191	209	192	197	244	239	196	1.00	0.00	0.00	0.00	0.00	0.00	0.00	0.00	0.00	28.6	9.1	35.3	0.50
16	1000	310	293	218	190	177	143	103	1.00	0.00	0.00	0.00	0.00	0.00	0.00	0.00	0.00	52.4	19.2	59.7	0.50
17	1000	140	184	139	146	204	258	216	1.00	0.00	0.00	0.00	0.00	0.00	0.00	0.00	0.00	15.7	0.9	21.4	0.47
18	1000	133	171	150	163	220	244	187	1.00	1.00	1.00	1.00	1.00	1.00	1.00	1.00	1.00	28.6	8.0	35.1	0.47
19	1000	177	185	179	196	283	293	222	1.00	0.00	0.00	0.00	0.00	0.00	0.00	0.00	0.00	52.4	19.6	59.6	0.47

Table C 7: EXV Data

Line	Description	Duration [min]	SF_freq Hz	CAT_ave C	OAT_ave C	RAT_ave C	MAT_ave C	MAT_row 1 [C]	MAT_row 2 [C]	MAT_row 3 [C]	MAT_row 4 [C]	SFAT_ave C	SAT_ave C	CFAT_ave C	dP_fan kPa	dP_rtu kPa	P_sa kPa	dP_nozzl e kPa	dP_cond kPa	P_ra kPa	Dew_sa C	Dew_ra C	Dew_oa C
1	50F-80F-41.2SF-0Damp	59	41.2	10.0	8.9	26.5	22.8	20.3	22.0	24.0	24.4	6.7	7.6	15.2	0.1501	0.0901	0.0061	0.0320	0.0309	0.1231	2.5	2.2	2.1
2	82F-80F-41.2SF-0Damp	24	41.2	27.8	28.2	26.7	26.7	26.9	26.6	26.6	26.8	11.4	12.1	33.9	0.1504	0.0912	0.0061	0.0299	0.0299	0.1231	8.5	8.9	9.8
3	125F-80F-41.2SF-0Damp	47	41.2	51.5	49.5	26.7	30.5	33.5	31.2	28.9	28.8	18.5	19.8	57.8	0.1437	0.0867	0.0061	0.0298	0.0291	0.1231	9.4	9.7	9.3
4	50F-80F-41.2SF-50Damp	29	41.2	10.1	10.1	26.6	18.5	11.7	14.7	22.2	24.7	4.6	6.1	14.8	0.1539	0.0846	0.0856	0.0285	0.0308	0.0728	1.6	1.4	2.2
5	82F-80F-41.2SF-50Damp	31	41.2	27.7	26.7	26.7	26.5	26.4	26.3	26.5	26.6	11.4	12.1	33.8	0.1510	0.0722	0.0815	0.0284	0.0298	0.0798	8.8	9.4	10.9
6	125F-80F-41.2SF-50Damp	24	41.2	51.6	49.5	26.7	36.7	46.1	40.9	31.6	29.0	23.2	24.0	58.1	0.1413	0.0731	0.0778	0.0277	0.0290	0.0777	9.3	9.6	9.5
7	59F-80F-41.2SF-100Damp	47	41.2	15.0	16.0	26.7	17.6	18.9	16.5	15.4	19.0	3.2	4.2	19.7	0.1664	0.0693	0.0939	0.0234	0.0306	0.0515	1.6	0.6	0.8
8	82F-80F-41.2SF-100Damp	50	41.2	27.7	26.7	26.8	26.5	26.4	26.3	26.6	26.8	10.8	11.5	33.5	0.1641	0.0741	0.0969	0.0209	0.0299	0.0461	8.3	8.5	10.4
9	125F-80F-41.2SF-100Damp	13	41.2	51.5	42.0	26.7	40.1	38.2	42.1	43.7	37.6	22.3	22.7	58.6	0.1564	0.0727	0.0925	0.0207	0.0287	0.0364	8.7	8.9	8.9

Table C 8: EXV Data, Continued 1

Line	T_sat_suc C	T_dis C	T_cond_i n C	T_tv_in C	T_mass_in C	T_pre_dist	T_evap_ in_1 C	T_evap_ in_2 C	T_evap_ in_3 C	T_evap_ in_4 C	T_evap_ in_5 C	T_evap_ in_6 C	T_evap_ in_7 C	T_evap_ out_1 C	T_evap_ out_2 C	T_evap_ out_3 C	T_evap_ out_4 C	T_evap_ out_5 C	T_evap_ out_6 C	T_evap_ out_7 C	P_mf_in kPa (abs)	P_cond_out kPa (abs)	P_tv_in kPa (abs)	P_suc kPa (abs)
1	3.2	39.0	8.8	8.9	8.9	1.7	1.5	2.9	2.2	2.0	1.7	1.8	2.5	3.5	11.2	15.9	14.3	14.3	15.1	17.4	1279	1282	1257	880
2	8.7	61.9	27.5	27.7	27.6	8.1	7.7	9.9	8.9	8.3	7.7	8.0	9.1	9.1	17.7	20.3	17.7	19.1	18.9	17.1	2083	2086	2058	1039
3	15.8	99.0	52.5	52.6	52.6	16.5	15.8	20.3	18.0	16.7	15.6	15.9	18.1	27.9	28.4	28.8	23.5	23.3	18.0	16.9	3616	3631	3585	1276
4	-0.3	41.3	8.8	9.0	8.9	-1.9	-2.2	-0.5	-1.4	-1.7	-2.0	-1.8	-1.0	-1.0	3.9	10.0	13.0	15.8	16.4	21.6	1273	1274	1253	790
5	8.8	61.4	27.6	27.7	27.7	8.3	7.8	10.0	8.9	8.4	7.9	8.1	9.2	9.0	16.9	20.4	18.4	19.2	18.9	18.3	2085	2088	2060	1042
6	16.8	96.5	52.6	52.7	52.7	17.7	17.0	21.4	19.1	17.9	16.8	17.0	19.1	40.3	39.7	38.2	30.9	25.9	18.7	17.2	3664	3683	3633	1316
7	0.0	47.4	13.8	14.0	13.9	-1.6	-1.9	0.2	-0.9	-1.3	-1.8	-1.5	-0.6	0.6	7.8	9.2	8.1	9.9	11.0	17.0	1457	1456	1435	796
8	7.1	62.8	27.4	27.5	27.5	6.4	6.0	8.5	7.2	6.6	6.0	6.3	7.5	7.1	14.9	18.9	17.7	18.7	19.1	22.5	2079	2080	2054	992
9	19.5	91.7	52.8	52.9	52.9	20.5	19.6	23.4	21.5	20.5	19.7	19.9	21.8	21.2	20.4	29.6	32.0	32.7	31.5	22.8	3651	3677	3619	1417

Table C 9: EXV Data, Continued 2

Line	P_dis kPa (abs)	m_dot_re g/s	V_dot_nozzle m^3/s	T_db_noz zle C	m_dot_nozzle kg/s	CFM_nozz le CFM	CFM_ra m^3/s	T_ra C	m_dot_ra kg/s	W_dot_cf kW	W_dot_comp kW	W_dot_tot kW	W_dot_r ef kW	W_dot_r ef air kW	Nozzle box fan Hz	Setp PXV1 [virtual steps]	T_cond_s ubc [K]	T_sac_co nd_out	T_subc_c ond_out	Evap_SH_ 1	Evap_SH_ 2
1	1333	49.8	0.587	11.1	0.721	1245	1064	26.7	0.544	0.274	0.987	1.83	10.9	10.6	47.5	430	7.0	15.8	7.0	0.3	8.0
2	2149	58.8	0.572	15.0	0.690	1213	1048	26.6	0.534	0.256	1.72	2.51	11.0	10.8	46.3	334	6.5	34.1	6.5	0.5	9.0
3	3685	64.1	0.578	21.9	0.679	1225	1045	26.4	0.531	0.239	3.24	4.01	9.2	9.0	47.0	288	5.0	57.6	5.0	12.2	12.6
4	1314	43.9	0.551	9.8	0.679	1167	759	26.8	0.398	0.274	1.02	1.84	9.5	9.3	39.3	343	6.8	15.6	6.8	-0.8	4.1
5	2151	59.2	0.556	14.9	0.670	1178	792	26.7	0.412	0.256	1.72	2.50	11.1	10.9	41.0	336	6.5	34.1	6.5	0.2	8.2
6	3744	68.0	0.557	25.3	0.647	1181	778	26.4	0.404	0.239	3.27	4.02	9.6	9.4	41.0	299	5.6	58.2	5.6	23.5	22.9
7	1495	44.2	0.491	8.3	0.608	1039	662	26.8	0.352	0.269	1.20	1.99	9.2	9.0	34.3	301	6.5	20.4	6.5	0.6	7.8
8	2135	55.6	0.464	14.6	0.561	984	634	26.7	0.337	0.257	1.74	2.48	10.4	10.2	31.5	307	6.5	33.9	6.5	0.0	7.8
9	3757	77.1	0.469	24.3	0.547	995	573	26.3	0.307	0.236	3.20	3.90	11.0	10.8	31.0	344	5.4	58.1	5.4	1.7	0.9

Table C 10: Hybrid and PEXV Fully Open Data

Line	Evap_SH_ 3	Evap_SH_ 4	Evap_SH_ 5	Evap_SH_ 6	Evap_SH_ 7	T _{suc} C
1	12.7	11.1	11.1	11.9	14.2	11.7
2	11.6	9.1	10.4	10.2	8.4	15.7
3	13.0	7.7	7.5	2.3	1.1	22.6
4	10.2	13.3	16.0	16.6	21.9	8.3
5	11.6	9.7	10.5	10.1	9.6	15.1
6	21.3	14.1	9.0	1.8	0.3	22.1
7	9.2	8.1	10.0	11.0	17.0	7.2
8	11.8	10.6	11.6	12.0	15.4	13.3
9	10.1	12.5	13.2	12.0	3.3	25.3

Table C 11: Zero Opening Position (Actual Steps) of Balancing Valves

BXV1 [steps]	BXV2 [steps]	BXV3 [steps]	BXV4 [steps]	BXV5 [steps]	BXV6 [steps]	BXV7 [steps]
31	23.5	20	31	28	29	30

Note: Values averages from two offset tests. Maximum deviation between the two tests 7 steps, 4.4 steps on average.

Uncertainty Analysis

Code C 1 shows the EES code which used for uncertainty analysis for the rooftop unit. The inbuilt uncertainty calculation method of EES (Klein, 2012), which neglects cross dependency was used. The confidence interval of the measured data was not evaluated. It was found that for the RTU, the uncertainty is mostly caused by the power meter. Uncertainties were calculated for the EXV and PEXV fully open case (very similar values as for the hybrid control) and are shown in Table C 12 to Table C 14. Note that the index “H” refers to the hybrid control scheme values, while the values without index are for the EXV baseline.

Code C 1: Uncertainty Calculation for Rooftop Unit

```
!"Setup"
$UnitSystem SI MASS DEG kPa C kJ
!"Conditionals"
$IFNOT PARAMETRICTABLE
"value for 82-80-0damper, EXV data used for both, EXV and hybrid"
"EXV "
m_dot=0.0588[kg/s]
W_dot_mess_comp=1.72[kW]
W_dot_mess_fan_evap=0.215[kW]
W_dot_mess_fan_cond=0.256[kW]
W_dot_mess_tot=2.511[kW]
P_TXV_in=2058.06[kPa]
P_suc=1039.07[kPa]
T_TXV_in=27.66[C]
T_suc=15.71[C]

"Hybrid"
m_dot_H=0.0588[kg/s]
W_dot_mess_comp_H=1.72[kW]
W_dot_mess_fan_evap_H=0.215[kW]
W_dot_mess_fan_cond_H=0.256[kW]
W_dot_mess_tot_H=2.511[kW]
P_TXV_in_H=2058.06[kPa]
P_suc_H=1039.07[kPa]
T_TXV_in_H=27.66[C]
T_suc_H=15.71[C]
$ENDIF

R$='R410a'

!"accuracy"
"Mass flow meter accuracy, Micromotion CMF025"
m_dot_hr=m_dot*convert(h,s)
Z_stability=0.027[kg/h]
Z_Limit=Z_stability/0.0005 "limit, when flowrate smaller than this value, accuracy = ±[(zero stability / flow rate) × 100]%"
"below quoted out/quote lines below out for calculation of uncertainty table"
m_dot_acc=0.1[% ]*convert(%,1) "accuracy for flowrate larger than Z_limit"
"Temperature sensors"
T_acc=1.12[C] "special limit of errors, TMQSS, combined with uncertainty of DAQ and cold junction"

"Pressure transducers, same as for LRCS"
"neglected temperature dependency "
P_low_acc=250[PSI]*convert(PSI,kPa)*0.13[%]*convert(%,1) "accuracy for 250PSI transducers, Setra 207"
P_high_acc=500[PSI]*convert(PSI,kPa)*0.13[%]*convert(%,1) "accuracy for 250PSI transducers, Setra 207"

"Power Measurement Compressor, Exceltronic, Watt Transducer, XL31K5A2-2-RS"
```

W_dot_acc_comp=W_dot_mess_comp*0.002+4/100*0.0001[kW] "0.2% of reading and 0.01% of rated output"
W_dot_acc_comp_H=W_dot_mess_comp_H*0.002+4/100*0.0001[kW] "0.2% of reading and 0.01% of rated output"

"Fan power measurement using AMETEK PCE"

W_dot_acc_fan_evap= 4/100*0.25[kW] "0.25% FS, PCE 20"

W_dot_acc_fan_cond=2/100*0.25[kW] "0.25% FS, PCE 15"

"Overall power measurement, using XL31K5A4-2-7-SC-RS"

W_dot_acc_tot=W_dot_mess_tot*0.002+15/100*0.0001[kW] "0.2% of reading and 0.01% of rated output"

W_dot_acc_tot_H=W_dot_mess_tot_H*0.002+15/100*0.0001[kW] "0.2% of reading and 0.01% of rated output"

"!Calculations"

"EXV"

h_evap_in=Enthalpy(R\$,T=T_TXV_in,P=P_TXV_in)

h_evap_out=Enthalpy(R\$,T=T_suc,P=P_suc)

T_sat=Temperature(R\$,X=0,P=P_TXV_in)

Q_dot=m_dot*(h_evap_out-h_evap_in)-W_dot_mess_fan_evap

COP=Q_dot/(W_dot_mess_comp+W_dot_mess_fan_evap+W_dot_mess_fan_cond)

COP_tot=Q_dot/W_dot_mess_tot

DT_subc=T_TXV_in-T_sat

"Hybrid"

h_evap_in_H=Enthalpy(R\$,T=T_TXV_in_H,P=P_TXV_in_H)

h_evap_out_H=Enthalpy(R\$,T=T_suc_H,P=P_suc_H)

T_sat_H=Temperature(R\$,X=0,P=P_TXV_in_H)

Q_dot_H=m_dot_H*(h_evap_out_H-h_evap_in_H)-W_dot_mess_fan_evap_H

COP_H=Q_dot_H/(W_dot_mess_comp_H+W_dot_mess_fan_evap_H+W_dot_mess_fan_cond_H)

COP_tot_H=Q_dot_H/W_dot_mess_tot_H

DT_subc_H=T_TXV_in_H-T_sat_H

"Comparison"

"EXV-case is used as baseline for comparisons!"

Q_dot_diff=(Q_dot_H-Q_dot)/Q_dot

COP_diff=(COP_H-COP)/COP

COP_tot_diff=(COP_tot_H-COP_tot)/COP_tot

W_dot_mess_diff=W_dot_mess_tot-W_dot_mess_tot_H

T_suc_diff=T_suc_H-T_suc

DT_subc_diff=DT_subc_H-DT_subc

P_TXV_in_diff=P_TXV_in_H-P_TXV_in

Table C 12: Uncertainties for Rooftop Air Conditioning Unit

Description	m_dot	m_dot_H	W_dot_mess_comp	W_dot_mess_comp_H	W_dot_mess_fan_cond	W_dot_mess_fan_cond_H	W_dot_mess_fan_evap	W_dot_mess_fan_evap_H	W_dot_mess_tot	W_dot_mess_tot_H
	[kg/s]	[kg/s]	[kW]	[kW]	[kW]	[kW]	[kW]	[kW]	[kW]	[kW]
50F-80F-41.25F-0Damp_mech_PEXV.xlsx	0.000050	0.000050	0.001970	0.001990	0.005000	0.005000	0.010000	0.010000	0.003660	0.003610
82F-80F-41.25F-0Damp_mech_cool_PEXV.xlsx	0.000060	0.000060	0.003430	0.003450	0.005000	0.005000	0.010000	0.010000	0.005030	0.004990
125F-80F-41.25F-0Damp_mech_PEXV.xlsx	0.000060	0.000070	0.006480	0.006530	0.005000	0.005000	0.010000	0.010000	0.008030	0.008020
50F-80F-41.25F-50Damp_mech_PEXV.xlsx	0.000040	0.000050	0.002040	0.002040	0.005000	0.005000	0.010000	0.010000	0.003690	0.003710
82F-80F-41.25F-50Damp_mech_cool_PEXV.xlsx	0.000060	0.000060	0.003440	0.003450	0.005000	0.005000	0.010000	0.010000	0.005010	0.004980
125F-80F-41.25F-50Damp_mech_PEXV.xlsx	0.000070	0.000080	0.006540	0.006540	0.005000	0.005000	0.010000	0.010000	0.008050	0.008010
59F-80F-41.25F-100Damp_mech_cool_rerun_PEXV.xlsx	0.000040	0.000050	0.002400	0.002400	0.005000	0.005000	0.010000	0.010000	0.003980	0.003940
82F-80F-41.25F-100Damp_mech_cool_rerun_PEXV.xlsx	0.000060	0.000060	0.003470	0.003470	0.005000	0.005000	0.010000	0.010000	0.004970	0.004930
125F-80F-41.25F-100Damp_mech_PEXV.xlsx	0.000080	0.000080	0.006400	0.006490	0.005000	0.005000	0.010000	0.010000	0.007810	0.007900
maximum value	0.000080	0.000080	0.006540	0.006540	0.005000	0.005000	0.010000	0.010000	0.008050	0.008020

Table C 13: Uncertainties for Rooftop Air Conditioning Unit, Continued 1

P _{suc}	P _{suc_H}	P _{TXV_in}	P _{TXV_in_H}	T _{suc}	T _{suc_H}	T _{TXV_in}	T _{TXV_in_H}	COP	COP _{diff}	COP _H	COP _{tot}	COP _{tot_d} iff	COP _{tot_H}	DT _{subc}
[kPa]	[kPa]	[kPa]	[kPa]	[C]	[C]	[C]	[C]	[-]	[-]	[-]	[-]	[-]	[-]	[C]
2.241000	2.241000	4.482000	4.482000	1.120000	1.120000	1.120000	1.120000	0.095340	0.009150	0.063120	0.060050	0.009130	0.051840	1.127000
2.241000	2.241000	4.482000	4.482000	1.120000	1.120000	1.120000	1.120000	0.068960	0.020110	0.071070	0.054670	0.018660	0.057570	1.123000
2.241000	2.241000	4.482000	4.482000	1.120000	1.120000	1.120000	1.120000	0.049030	0.030010	0.051690	0.044240	0.029740	0.047080	1.121000
2.241000	2.241000	4.482000	4.482000	1.120000	1.120000	1.120000	1.120000	0.080850	0.020650	0.090760	0.052150	0.016060	0.058400	1.127000
2.241000	2.241000	4.482000	4.482000	1.120000	1.120000	1.120000	1.120000	0.069700	0.020280	0.071990	0.055380	0.018740	0.058130	1.123000
2.241000	2.241000	4.482000	4.482000	1.120000	1.120000	1.120000	1.120000	0.051960	0.034090	0.061040	0.047170	0.033700	0.055730	1.121000
2.241000	2.241000	4.482000	4.482000	1.120000	1.120000	1.120000	1.120000	0.070060	0.019900	0.075260	0.049260	0.016410	0.052820	1.126000
2.241000	2.241000	4.482000	4.482000	1.120000	1.120000	1.120000	1.120000	0.065410	0.020840	0.069290	0.052300	0.019020	0.055660	1.123000
2.241000	2.241000	4.482000	4.482000	1.120000	1.120000	1.120000	1.120000	0.060780	0.029560	0.062050	0.055470	0.029130	0.056760	1.121000
2.241000	2.241000	4.482000	4.482000	1.120000	1.120000	1.120000	1.120000	0.095340	0.034090	0.090760	0.060050	0.033700	0.058400	1.127000

Table C 14: Uncertainties for Rooftop Air-Conditioning Unit, Continued 2

DT _{subc_H}	Q _{dot}	Q _{dot_diff}	Q _{dot_H}	W _{dot_me} ss_diff
[C]	[kW]	[-]	[kW]	[kW]
1.127000	0.107500	0.008990	0.093360	0.005140
1.123000	0.135500	0.018280	0.141600	0.007090
1.121000	0.176500	0.029560	0.187600	0.011350
1.127000	0.094260	0.015850	0.106200	0.005240
1.123000	0.136700	0.018390	0.142600	0.007060
1.121000	0.188600	0.033390	0.221900	0.011350
1.126000	0.096180	0.015970	0.102200	0.005600
1.123000	0.127900	0.018630	0.135100	0.006990
1.121000	0.215400	0.029320	0.222900	0.011110
1.127000	0.215400	0.033390	0.222900	0.011350

Estimation of Power Consumption for Hybrid Control

To estimate the power consumption of the rooftop unit the following assumptions were made:

1. Processing part ("brain") of the control has similar power consumption as the Raspberry Pi model B mini-computer in operating mode.
2. Processing part of the control is always on – power saving sleep mode is not used.
3. Valve power consumption is identical to the one of the valves used for the experimental setup.
4. Idle power is assumed to be 5% of the max operating power plus the power consumption of the processing part of the controls.
5. A very efficient power supply is used, therefore power supply losses in operating mode are small compared to total power consumption of controls.
6. An average duty cycle of the rooftop unit of 30% was assumed; if the rooftop unit is in on-mode, the valve power consumption is considered.
7. To calculate the effects on COP, the total power consumption of the entire operating time is added to the 30% on cycle.

Table C 15: Power Consumption for Hybrid Control

Item	Value	Source
Processor contribution (brain), assuming Raspberri Pi model B	3.5 W	Brown (2013)
Valve (single spool)	3.1 W	Emerson (2012)
Valve (spools operating, time avg)	1.5	Emerson (2012)
Valve (operating)	4.7 W	
Valve duty (idle when not needed)	5.0%	Assumption
Number of valves	7	
Valve power, time averaged, considering duty cycle	1.6 W	
Max power (everything on)	36.3 W	
Idle power (5% of max due to transformer)	3.6 W	
Estimate for continuous power:		
assume 30% average duty cycle of RTU in AC mode		
off cycle:		
Raspberri Pi model B and idle power	7.1 W	
on - cycle:		
raspbpie and valves and idle	8.8 W	
average for on cycle (to calculate COP)		
(off cycle power · 0.7 + on cycle power · 0.3)/0.3	25.4 W	